Sensing and Actuating with Fringing Electric Field

Hsiu-Che Wang

A dissertation

submitted in partial fulfillment of the

requirements for the degree of

Doctor of Philosophy

University of Washington

2012

Reading Committee:

Ashley Emery, Chair

Dayong Gao

Karl Böhringer

Program Authorized to Offer Degree:
Mechanical Engineering

University of Washington
Graduate School

This is to certify that I have examined this copy of a doctoral dissertation by

Hsiu-Che Wang

and have found it complete and satisfactory in all respects,
and that any and all revisions required by the final
examining committee have been made.

Chair of the Supervisory Committee:

_____

Alexander V. Mamishev

Reading Committee:

_____

Karl Böhringer

_____

Ashley F. Emery

_____

Dayong Gao

Date: ____October 2012_____

In presenting this dissertation in partial fulfillment of the requirements for the doctoral degree at the University of Washington, I agree that the Library shall make its copies freely available for inspection. I further agree that extensive copying of the dissertation is allowable only for scholarly purposes, consistent with "fair use" as prescribed in the U.S. Copyright Law. Requests for copying or reproduction of this dissertation may be referred to ProQuest Information and Learning, 300 North Zeeb Road, Ann Arbor, MI 48106-1346, 1-800-521-0600, to whom the author has granted "the right to reproduce and sell (a) copies of the manuscript in microform and/or (b) printed copies of the manuscript made from microform."

Signature 

Date 10/18/2012

University of Washington

Abstract

Sensing and Actuating with Fringing Electric Field

Hsiu-Che Wang

Chair of the Supervisory Committee:

Associate Professor Alexander V. Mamishev

Department of Electrical Engineering

Many researchers worldwide have used the fringing electric field (FEF) to develop different devices and technologies to fulfill industrial requirements. In some cases, simple analytical models fulfill development requirements, whereas in other cases, complex numerical models and analytical models are required. This dissertation investigates methodologies, which involve both simple analytical models and complex numerical models to develop new devices and models through sensing and actuating with the fringing electric field.

The parallel plate sensor involves using simple analytical models to acquire data for instrument calibration and dielectric property measurement of uniform granular materials. The FEF sensor is designed through numerical modeling to acquire data for uniform materials and non-uniform materials. A parameter estimation algorithm is also developed to process data for the measurement of multilayer coating thickness and loading (percent of pure iron oxide powder that is mixed with silicone filler) of aircraft. The FEF actuators are designed through numerical modeling to controlling droplets for heat transfer enhancement. Design methodology, optimization methodology, and new models of FEF actuators for heat transfer applications are also presented.

The outcomes of this dissertation will increase our understanding on the further development of FEF actuators for different thermal management requirements of electronics, and on developing different FEF sensors and associated parameter estimation algorithms to fulfill different industrial requirements.

TABLE OF CONTENTS

LIST OF FIGURES

LIST OF TABLES

ACKNOWLEDGEMENTS

I was finally able to complete my Ph.D. at the University of Washington after five years of study. However, without support from others, this dream might still be a pie in the sky.

First, I would like to thank my academic advisor and mentor Prof. Alexander Mamishev, who has been struggling to find enough funding and resources to allow me to concentrate on research to complete this degree. While working at the Sensors, Energy, and Automation Laboratory (SEAL), I have established solid experience and knowledge about technology, technical writing, project management, and teamwork.

Second, I would like to thank my supervisor committee members, Prof. Karl Böhringer, Prof. Ashely Emery, Prof. Dayong Gao, and Prof. Sverre Vedal for their invaluable comments during my general exam and final exam. I would also like to thank Prof. Emery for his advice on revising a rejected paper, which finally, was accepted for publication in a journal that was recommended by Prof. Gao in the general exam.

Third, I would like to thank my lab mates Chih-Peng Hsu, Kishore Sundara-Rajan, Nels Jewell-Larsen, Junqing Shang, TsrongYi Wen, Aaron Zielinski, and Joshua Hutt. I really enjoyed my time at SEAL.

Fourth, I would like to thank Alexei Zyuzin, President of Illionix, George Kychakoff, President of Enertechnix, and Peter Ariessohn, Vice President of Enertechnix, for providing me with internship opportunities during my Ph.D. program, which has helped me acquire valuable experience and knowledge beyond my academic education.

Lastly, I would like to thank my parents, wife, daughters, sister, and brothers for their encouragement and their support for pursuing my dream.

DEDICATION

This thesis is dedicated to my parents, Jia-Yen Wang and Huei-Se Wang Liang, my wife, Chang-Yi, and my daughters, De-Ruie and De-Jen.

Chapter 1 **Introduction**

The work presented in this dissertation is motivated by ever increasing needs for methodologies to develop new devices and models through sensing and actuating with the fringing electric field (FEF) to overcome scientific and engineering challenges in fields related to the real time monitoring and the improvement and optimization of industrial manufacturing processes. This dissertation is an investigation in the design, modeling, and integration of fringing electric field sensors and actuators for applications in material science, manufacture process improvement, and product optimization processes. This work is based on publications [1-9] by the author.

1.1 Introduction to Sensing and Actuating with Fringing Electric Field

1.1.1 Sensing with Fringing Electric Field

Sensors with fringing electric field (FEF) have been widely used in industrial applications, such as the measurement of material properties and the control of manufacture processes. A conventional fringing electric field sensor consists of a sensor head, AC voltage source or current source, an impedance measurement circuit, and data acquisition and processing accessories. The sensor head is usually a patterned array of electrodes or windings on an electrically insulating substrate. The current or AC voltage source is applied to the electrodes and creates an electric field in the space between the electrodes or windings. Variations of dielectric properties of materials affect the distribution of the electric field. The impedance measured between the electrical terminals of the sensor head is a function of the material dielectric and geometric properties and the electrical field. The general methodology allows for the design of FEF sensors for different applications, including relating variations in electrical properties, dielectric constants, to physical properties, such as density, humidity, temperature, composition, etc.

Non-destructive sensing with fringing electric field (FEF) provides extensive information about material structural and physical properties. FEF sensors have been used in research and commercial applications to measure material properties [1-5], control manufacturing processes [10, 11], monitor chemical and physical changes of fluid and solid dielectrics [12, 13], detect

abrasion and degradation of power cables [14-16], and identify materials. In many cases, the interpretation of the sensor response depends on simple calibration procedures, whereas in other cases, it requires sophisticated signal processing algorithms [17] and a deep understanding of the physics and chemistry of the underlying phenomena [18]. Therefore, fringing electric field sensors are a viable process analytical solution for detecting the presence of a material or estimating the concentration of a material within the test environment.

Structurally, fringing electric field (FEF) sensors (Figure 1-1) can be visualized as parallel plate capacitors with opposing plates placed in a coplanar arrangement. The unidirectional periodic variation of potential gives rise to an exponentially decaying electric field perpendicular to the sensing plane. FEF sensors with the localized electric field lines penetrate a material under test placed on the sensor. A spectroscopic dielectric response of the material is measured in terms of electrical impedance, and the distribution of electrical parameters is used to obtain information about the distribution of various physical properties.

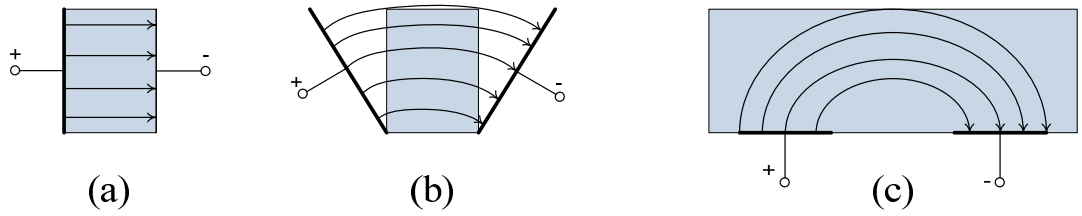

Figure 1-1. *A fringing electric field sensor can be visualized as (a) a parallel plate capacitor whose (b) electrodes open up to provide (c) a one-side access to the material under test.*

This dissertation investigates the instrumentation and data analysis of fringing electric field sensing systems and their application in granular material property measurement (Chapter 3) and coating thickness measurement (Chapter 4).

1.1.2 Actuating with Fringing Electric Field

Actuators with fringing electric field (FEF) have been widely used to control or move an object of interest, such as a fluid accelerator for microcooling [19-29], the control of the boundary layer of airflow [30-32], protein [33], RE-MEMS technology [34], etc. A conventional fringing electric field actuator consists of an actuating mechanism, an AC voltage source or a

current source, and data acquisition and processing accessories. The actuating mechanism is usually a patterned array of electrodes or windings of different arrangements on an electrically insulating substrate. The current or AC voltage source is applied to the electrodes and creates electric field in the space between the electrodes or windings. By varying the current or AC voltage source, the FEF actuator controls or manipulates objects of interest for specific purposes. The general methodology allows for the design of FEF actuators for different applications, including relating variations in electric field strength, electrical properties, to parameters of interest, such as enhanced air momentum, reduced surface temperature, enhancement in device performance, etc.

FEF actuators can be visualized as capacitors with plates of the same size or different sizes placed in either coplanar or opposite arrangements. The variation of the nonlinear distribution of potential creates an exponentially decaying electric field perpendicular to the sensing plane. FEF actuators with the localized electric field can be varied through arrangements of sensing and emitting electrodes or different driving sources for optimal process control in industrial applications [30-32, 34, 35]. It is the variation of the localized electric field that works as an actuator for process control. Figure 1-2 is an example that shows how an FEF actuator can be used for thin film formation with different deposition area.

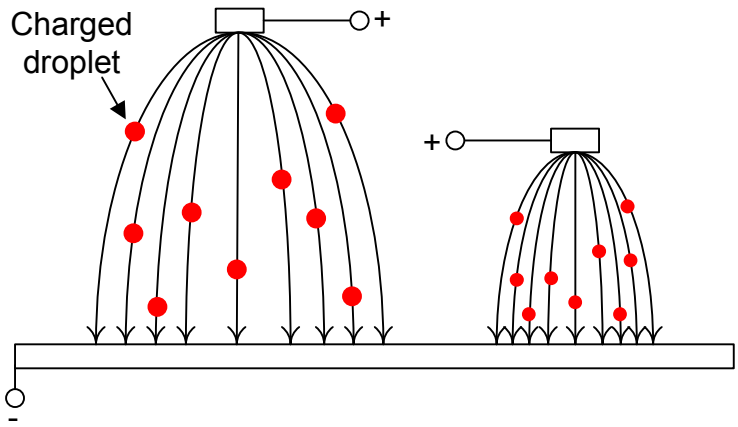

Figure 1-2. *Schematic diagram showing how a fringing electric field actuator is used for thin film deposition with different area. Charged droplets are manipulated by electric field lines to transport toward a grounded plate (sensing electrode) and deposit on the plate.*

This dissertation investigates the design methodology, optimization methodology, and empirical design model of fringing electric field actuators and their application in the fields of thermal management of electronics (Chapter 5).

1.2 Scientific and Engineering Challenges

The research work presented in this dissertation has several scientific and engineering challenges which are grouped according to three applications and discussed as follows.

1.2.1 Application in Dielectric Material Property Measurement of Granular Materials

Although the ASTM D150-98 [36] testing standard addresses the relative dielectric permittivity measurement approach for solid and liquid materials, there is currently no standard measurement approach for granular materials, in part because granular materials have a wide range of measurement challenges not encountered by other material forms. For example, the dielectric properties of granular materials strongly depend on packing density, uniformity of granule size, degree of contact between individual granules, short-term moisture and solvent diffusion (dynamics within individual granules, as opposed to the bulk of the material), contact polarization, varying degree of contact with the sensing electrodes, and, in the case of organic materials, variation of product sources. Those factors are strongly coupled, and inherently, are difficult to isolate the individual effects on the dielectric properties of a granular material.

The dielectric property measurement system used in this dissertation uses circuit impedance of the measurement system and electrical measurements to estimate dielectric properties of a material under test. To improve material property measurement accuracy, it is necessary to have a systematic calibration methodology to accurately calibrate the individual stages of the measurement circuit of the measurement system, including the meter and sensors. This systematic calibration methodology has not been proposed as a whole. Although a lot of calibration methodologies for dielectric measurement systems have been investigated [37-41], these methodologies focused on using materials with known material properties for the calibration. The calibrated measurement systems can only be used to measure limited material

properties, or to measure material properties within limited ranges. Once different sensors are used together with the same meter, whole system calibration has to be done again before any measurements.

This dissertation will investigate a systematic calibration methodology to increase the dielectric property measurement system's accuracy in the dielectric property measurement of granular materials.

1.2.2 Application in Coating Thickness Measurement

A number of methods for measuring the thickness of paint and functional coatings have been used in the industry with various levels of success. The high cost of painting processes, coupled with a need for in-process control to optimize various performance characteristics of coatings, has fueled technological advances in coating instrumentation. The current trend toward substituting metals with composite materials has further affected coating technologies. For example, some technologies, including magnetic induction and eddy-current methods, have been rendered inoperable by this transition, while the performance of others (i.e. capacitive methods) has been proven not able to provide significant signal to noise ratios. At the same time, the demands in aerospace and other industries continuously require coating thickness instrumentation with increased thickness measurement accuracy. Additionally, these industries often desire instrumentation that can measure more than a single layer thickness. Some applications require simultaneous gauging of multiple layers, while others demand monitoring of the degree of cure.

Dielectrometry is widely used for non-invasive determination of material properties. Under circumstances where direct determination of the material dielectric permittivity is difficult, an indirect parameter estimation approach based on quantitative mapping between the material property and electrical measurements can be used. The major challenge for such an approach lies in minimizing the effect of variables other than the material property under study, such as ambient temperature and sample density, which are considered here as disturbance factors. The effects of these factors should either be eliminated or accounted for in the calibration algorithm.

This dissertation will investigate an in-process coating thickness measurement technology by design a custom fringing electric field sensor associated with a parameter estimation algorithm and a calibration algorithm.

1.2.3 Application in Thermal Management of Electronics

Design and performance optimization methodologies of actuators with fringing electric field investigated for the thermal management of electronics have not been investigated yet. The fringing electric field actuator investigated in this dissertation is also called electrospray evaporative cooling (ESEC) chambers. To design and optimize the ESEC chambers' performance for the thermal management of electronics, either analytical models or multiphysics models that address full physics behind the operating principle of the ESEC are important. In general, the multiphysics can be divided into three major discrete disciplines, namely: electrohydrodynamic-assisted liquid atomization processes, dynamic transportation of charged droplets, and heat transfer of the droplets during the transportation and at the solid-liquid and liquid-gas interfaces. Depending on the applied potential between the electrospraying nozzle and the collecting elelctrode, the electrohydrodynamic (EHD) functioning modes, such as the stable cone-jet and the unstable multi-jet modes, for the electrospray processes are extremely distinct [42, 43]. Although the numerical models for the stable cone-jet [44-53] and the unstable multi-jet modes [54] have been investigated individually, the global numerical and analytical models, respectively, allowing for the transition between different electrohydrodynamic functioning modes and for both the cone-jet and unstable multi-jet modes, have not been developed yet.

Although numerical models regarding the individual physics behind the ESEC chambers have been investigated, the integrated and higher accuracy numerical and analytical models for the ESEC modeling and optimization are still limited. Higher accuracy on modeling depends heavily on the appropriate mesh definition and the complexity of the boundary conditions. That is, for the ESEC chambers, the full multiphysics modeling will be resource-consuming and time-consuming as the scale of the ESEC chamber goes down to the micro-scale, especially for complex geometries.

A simplified and efficient methodology for the practical design purpose and optimization of the ESEC chambers in any scale depends on the thorough understanding of the design trade-offs

and the fundamental principles. For the practical applications of the thermal management of electronics, the design trade-off of the ESEC is to balance the fluid properties, operation potential margin, power consumption, and fluid flow rate to achieve the best heat transfer performance among different chamber geometries.

Another approach to design ESEC chambers is to develop empirical models related to parameters of interest in such applications as mass spectroscopy [55-57], microthrusters [56], nanofibers [58], etc. Although several researchers [45, 54, 59-61] have developed numerical models for several applications, complete numerical models using electrospray technology for the thermal management of electronics are currently limited. Researchers have faced significant challenges designing and optimizing ESEC chambers for heat transfer applications in electronics. Furthermore, from our experimental observation [1], the electrified liquid jet is similar to that of the traditional free-surface impinging jet. The empirical heat transfer correlations for a traditional free-surface impinging jet [62, 63] could be a good foundation to investigate the appropriate empirical heat transfer correlations to design ESEC chambers.

This dissertation will investigate a design and optimization methodology for ESEC chambers. Empirical heat transfer correlation models will also be investigated for the practical design of ESEC chambers.

1.3 Scope of the Dissertation

This dissertation investigates developing new devices and models through sensing and actuating with the fringing electric field. Figure 1-3 shows the scope of this dissertation, which covers from a simple parallel plate sensor to a complicated fringing electric field actuator.

The parallel plate sensor focuses on acquiring data of interest that can be used for instrument calibration and be processed through different parameter estimation algorithms in real time. The parameter estimation algorithms only involve simple analytical equations for post processing. Additionally, the parallel plate sensor is used for the dielectric property measurement of uniform materials. In this dissertation, dielectric properties of several granular materials are measured by a custom-designed parallel plate sensor.

The fringing electric field (FEF) sensor focuses on acquiring data of interest that can be processed through different parameter estimation algorithms in real time. To develop a FEF sensor for a specific application, the numerical modeling based on the Maxwell equation needs to be involved. The FEF sensor is used to measure non-uniform materials. In this dissertation, functional coating thickness and loading (percent of pure iron oxide powder that is mixed with silicone filler) of aircraft is measured by a custom-designed FEF sensor.

The fringing electric field actuator focuses on controlling liquid droplets to enhance the heat transfer performance of a cooling chamber. To develop a new FEF actuator for a specific application, in some cases, multiphysics numerical modeling is necessary, but in other cases, complex analytical models can only be used for performance estimation due to limited multiphysics-coupled numerical models. Furthermore, the FEF actuator can deal with no-uniform and movable materials. In this dissertation, droplets are manipulated by several custom-designed FEF actuators with different geometry types.

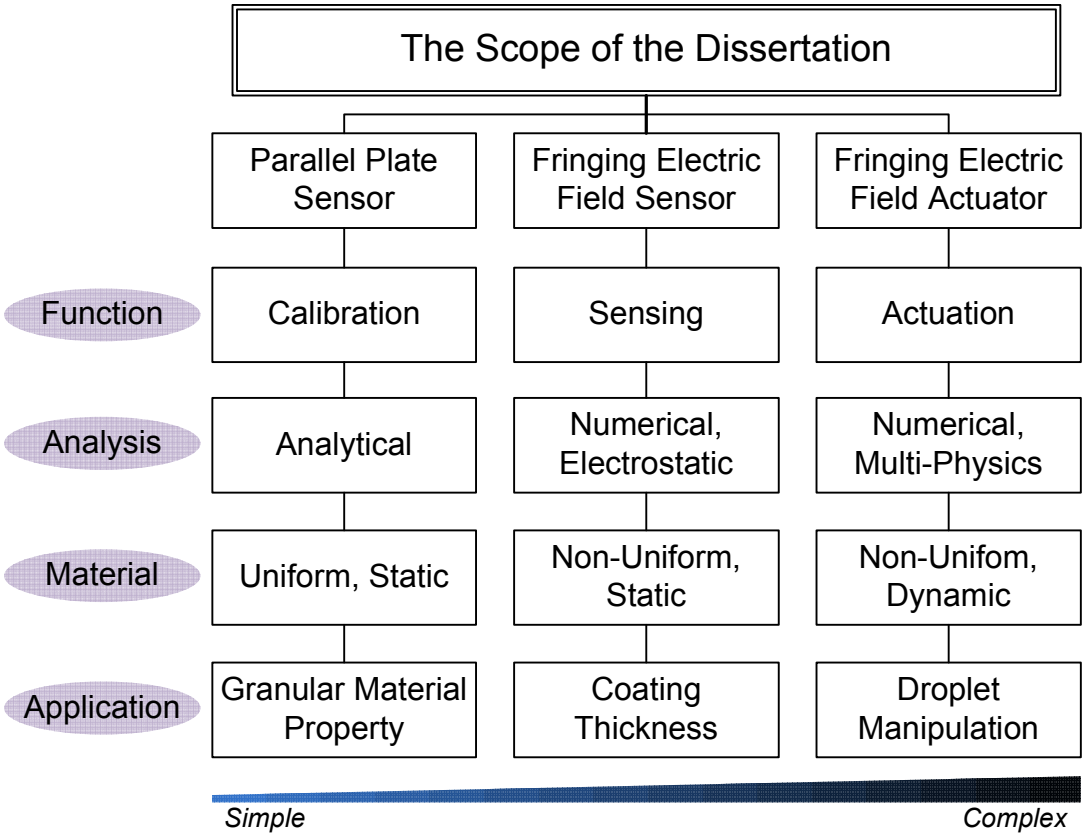

Figure 1-3. *The scope of this dissertation.*

Since this dissertation covers from a simple parallel plate sensor to a complicated fringing electric field actuator, different investigation processes are required; therefore, the detailed scope of each sensor and actuator is discussed next.

1.3.1 Dielectric Property Measurement of Materials

1.3.1.1 Granular Material Property Measurement

Figure 1-4 shows the scope of the granular material property measurement of this dissertation. This part of the dissertation focuses on the sensor design, the calibration methodology of the measurement system, and the material property measurement.

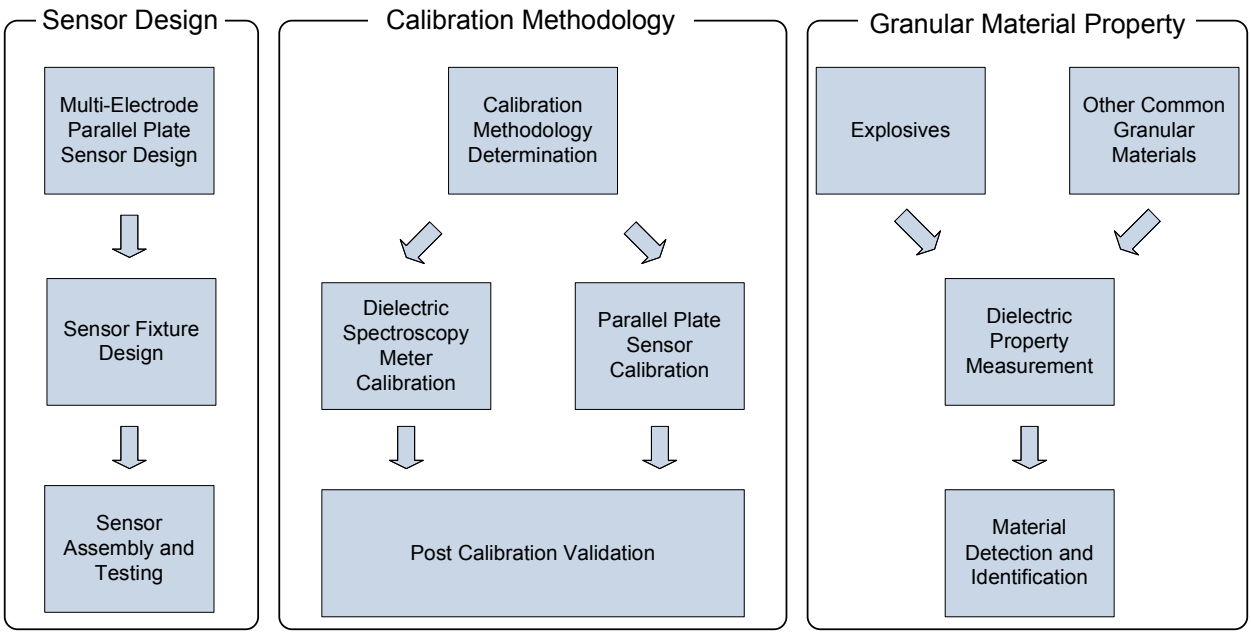

Figure 1-4. *Dissertation scope for granular material property measurement.*

The focus of sensor design is to design a new multi-electrode concentric parallel plate sensor capable of measuring dielectric properties of granular materials accurately. This sensor should also be able to provide package uniformity of a material through switching different sensing electrodes of the sensor. EM shielding and guard electrode design play an important role in the sensor design. Sensor fixture design provides two features, including the EM shielding and quantitative measurement by the package sample material in a fixed volume. The last task of the

sensor design is to assemble the sensor and the sensor fixture and to test them in order to ensure that the sensor works in the frequency domain.

The calibration methodology focuses on presenting a systematic way of calibrating the dielectric material property measurement system to increase the material property measurement accuracy of the system. The first task of this part of the dissertation is to determine the best calibration methodology for the measurement system. The proposed calibration methodology calibrates the individual stages of the measurement system, including the dielectric spectroscopy meter and the multi-electrode concentric parallel plate sensor. The second task is to calibrate the dielectric spectroscopy meter and the parallel plate sensor separately. The calibration of the meter focuses on calibrating the meter's impedances of the measurement circuit in order to ensure that the meter can precisely measure impedance of a resistor or a capacitor with a known nominal value. The parallel plate sensor estimates dielectric material properties of granular materials by converting electrical signals in the frequency domain from the sensor terminals; therefore, the calibration of the parallel plate sensor is to ensure that the sensor presents correct quantitative mapping between the dielectric material properties and electrical measurements. The last task of the calibration methodology is to validate that the fully-calibrated dielectric spectroscopy measurement system can precisely estimate dielectric material properties of a material with known dielectric material properties. Air is selected for validation.

Granular material property measurement focuses on using the fully-calibrated dielectric spectroscopy measurement system to establish database on dielectric properties of explosives and other common granular materials in frequency domains. Once this database is established, this system can then be used to detect and identify granular materials of interest.

1.3.1.2 Multi-Layer Coating Thickness Measurement

The scope of multi-layer coating thickness measurement in this dissertation focuses on using a custom-designed fringing electric field sensor for demonstration of in-process coating thickness measurement. Figure 1-5 shows the scope of the multi-layer coating thickness measurement.

Sensor design involves designing a customized concentric fringing electric field (FEF) sensor to measure a specific range of coating thicknesses of interest. Numerical modeling is used

for the sensor design. A sensor with optimal sensor geometry involves tradeoff among the penetration depth, the quantity of the ring electrodes, and the gap between ring electrodes of a sensor. These parameters are also discussed through numerical modeling results. The sensor with optimal geometry for the specific range of coating thicknesses of interest is then fabricated for experimental demonstration.

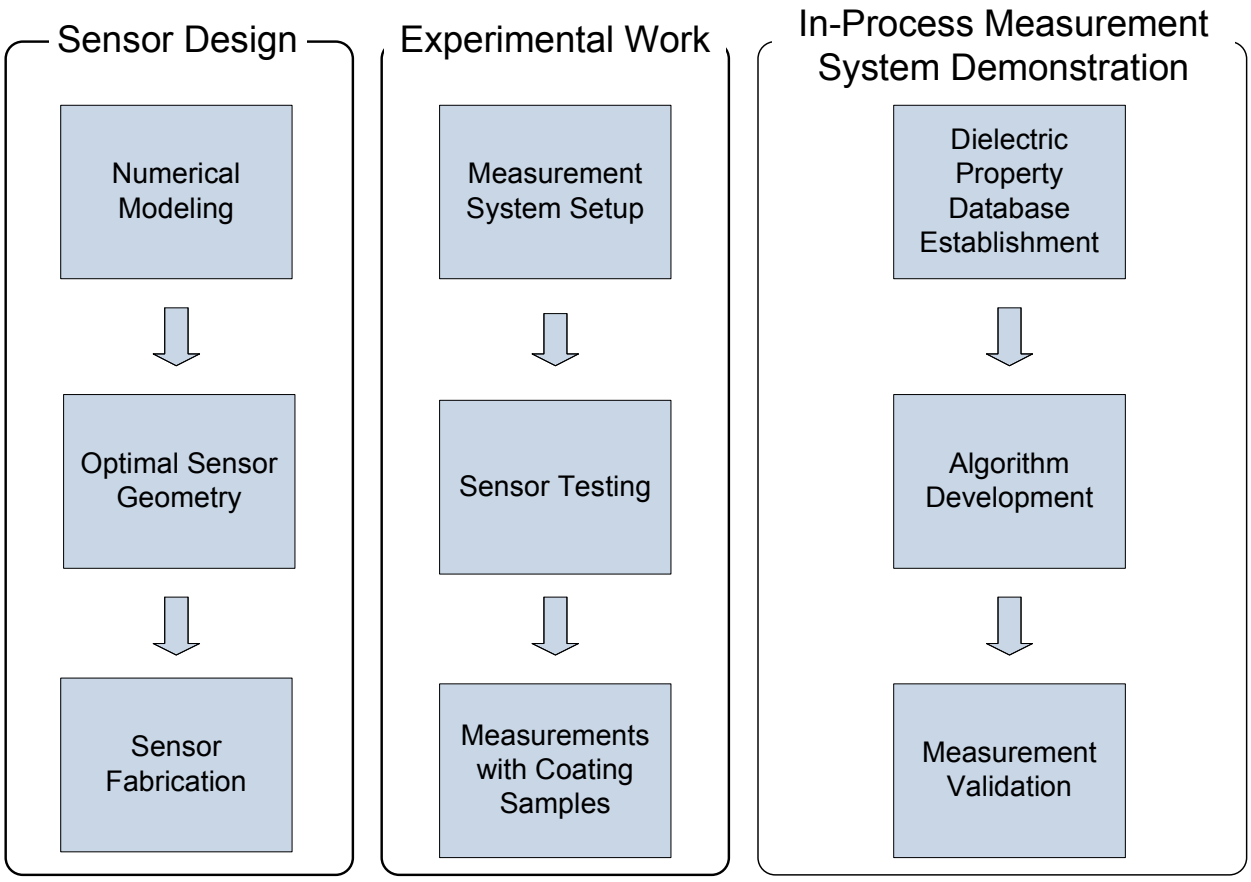

Figure 1-5. *Dissertation scope for the multi-layer coating thickness measurement.*

The experimental work focuses on validating the fabricated concentric fringing electric field (FEF) sensor's performance of quantitative mapping between coating thicknesses and electrical measurements. The measurement system setup focuses on integrating the dielectric spectroscopy meter, the fabricated concentric FEF sensor, and the associated LabVIEW program, followed by the sensor testing. The sensor testing involves two steps. The first step is to use the FEF sensor to acquire its electrical signals in the frequency domain from different samples. The second step is to validate the sensor's response trend from experimental and numerical results. Once the FEF

sensor works correctly, the sensor is used to acquire the dielectric signatures of coating samples of different coating thicknesses.

To demonstrate the ability of the sensor for in-process coating thickness measurements, the first step is to establish a sensor capacitance database with respect to the coating thickness and coating loading. Once the database is established, the second step is to develop algorithms that can real-time show a coating thickness with certain loading during the coating process. The last step is to demonstrate the sensor's performance for in-process coating thickness measurement. Several coating samples will be randomly chosen for demonstration.

1.3.2 Thermal Management of Electronics

Although the electrospray-enhanced phase change cooling solution has been investigated in the meso-scale, a practical design methodology and heat transfer performance optimization methodology are still limited. The scope of thermal management of electronics in this dissertation focuses on the design methodology, the heat transfer performance optimization methodology, and the empirical heat transfer correlations for meso-scale electrospray evaporative cooling (ESEC) chambers.

Figure 1-6 shows the scope of the thermal management of electronics in the dissertation. The way to design and optimize ESEC chambers for the thermal management of micromicroelectronics is the core of this application. For the design methodology, the miniaturization of the low nozzle density ESEC chamber focuses on using off-the-shelf micronozzles and other components to design and integrate meso-scale ESEC chambers. The characterization of the ESEC chambers is to identify the chambers' operational potential regions and the EHD functioning modes. The heat transfer performance demonstration of meso-scale ESEC chambers will be conducted according to the characterization of the ESEC chambers. Additionally, the numerical electrostatic field modeling will be used to investigate the electric field distribution of the ESEC chambers. The design rule focuses on investigating the relationship between the heat transfer performance and the electric field distribution of the ESEC chambers, in order to provide important information regarding how to design an ESEC chamber to achieve better heat transfer performance.

The focus of the optimization methodology is to investigate how an ESEC chamber can achieve optimal heat transfer performance in terms of different quantities of micronozzles, and the spacing between micronozzles. ESEC chambers with different geometry types will be designed, fabricated, and integrated. The characterization of the ESEC chambers is to identify the chambers' operational potential regions and the EHD functioning modes. The heat transfer performance of the ESEC chambers of different geometry types will be conducted, in order to investigate the effect of the geometry types of the ESEC chambers on the heat transfer performance.

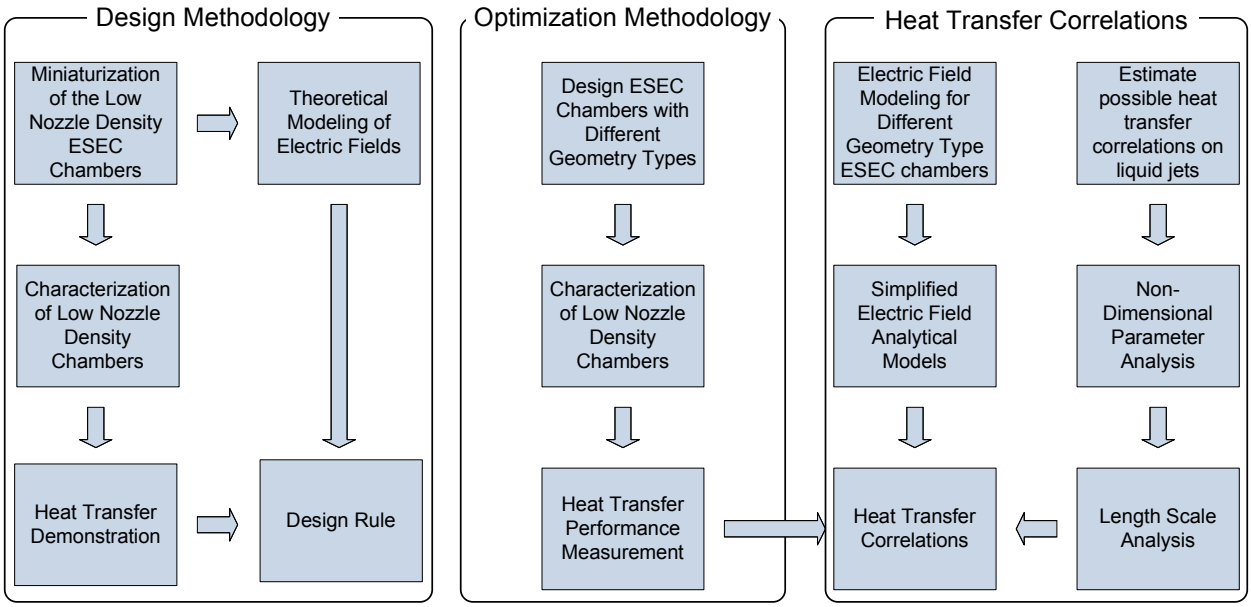

Figure 1-6. *Dissertation scope for thermal management of electronics.*

The focus of the heat transfer correlations is to investigate empirical heat transfer correlations for ESEC chambers, in order to assist the design and optimization of ESEC chambers for thermal management of electronics. The same ESEC chambers designed for optimization methodology investigation will be modeled in order to estimate the average electrostatic field distribution between the micronozzle tip and the thermal exchange surface for each ESEC chamber. The modeled electric field distribution results will be analyzed to formulate a simplified electric field analytical model which will be regressed to be function of the quantities of micronozzles and the spacing between the micronozzles. Additionally, the heat transfer correlations for traditional free-surface multiple impinging liquid jets are estimated to be

a starting foundation to investigate ESEC chambers' heat transfer correlation. Non-dimensional parameter analysis and length scale analysis according to the ESEC chambers follows the estimation results of the heat transfer correlations for traditional free-surface multiple impinging liquid jets. The final step is to combine the heat transfer results (from optimization methodology), the heat transfer correlation format for traditional free-surface multiple impinging liquid jets, and the addition of the electric field effect to investigate the heat transfer correlations for the designed ESEC chambers.

1.4 Contribution of the Dissertation

The dissertation makes two major contributions to fringing electric field sensors. First, it provides a systematic calibration methodology to fully calibrate FEF sensors, including the dielectrometry meter. Although a lot of calibration methodologies for dielectric measurement systems have been investigated, these methodologies focus on using materials with known material properties for the calibration. Thus, the calibrated measurement systems can only be used to measure limited material properties or to measure material properties within limited ranges. Once different sensors are used together with the same meter, whole system calibration must be performed again before any measurements are made. This dissertation bridges the gap by presenting a methodology to calibrate individual stages of the measurement circuit of the FEF sensors to extensively measure dielectric material properties in broad ranges for different industrial applications. Second, this dissertation demonstrates the viability of FEF sensors as a non-destructive sensing technology for material identification and coating thickness measurement. Although several sensing technologies, e.g., magnetic induction, eddy-current methods, and microwave sensing, have been widely used for material property and coating thickness measurement, the dissertation presents case studies where FEF sensors can be used and have advantages over currently used technologies due to simplicity, low cost, fast signal processing speed, and application specific algorithm development.

The dissertation makes three contributions to fringing electric field actuators. First, the dissertation presents detailed characterizations of ESEC chambers and design guidelines for the development of electrospray-based cooling technologies for the thermal management of electronics. The characterization includes operation potential margins and the corresponding heat

transfer performance. The design guidelines include the relationship between the heat transfer performance and the electric field distribution of ESEC chambers. Second, the dissertation presents a design methodology to achieve the optimal heat transfer performance of the meso-scale ESEC chambers with different geometry types, including the quantity of micronozzles and the spacing between micronozzles. Currently, the optimization methodology to boost the heat transfer performance of a meso-scale ESEC chamber has been limited. The dissertation demonstrates that increasing an ESEC chamber's quantity of micronozzles while decreasing the flow rate per nozzle might not be an effective way of improving the heat transfer performance of the ESEC chamber. Third, according to the experimental results, the dissertation presents several empirical heat transfer correlations and an analytical electric field model to design ESEC chambers. Since analytical and numerical models regarding the full multiphysics behind ESEC chambers' operating principles have been limited, the dissertation investigates empirical heat transfer correlations for ESEC chambers to bridge the gap, in order to allow for engineers to design ESEC chambers for different heat transfer cooling applications. Additionally, the correlations can be used to help researchers develop complete full multiphysics ESEC models to optimize the heat transfer performance of the meso-scale ESEC chamber and to develop and optimize a micro-scale ESEC chamber with a high micronozzle density for the thermal management of electronics. Finally, the dissertation investigates an analytical electric field model for ESEC chambers to help engineers estimate the electric field distribution of micronozzle-based ESEC chambers without needing to conduct numerical electrostatic field modeling and the following post data processing.

1.5 Outline of the Dissertation

This dissertation investigates the applications of fringing electric field on the thermal management of electronics and dielectric property measurement of materials. The outline of the dissertation is listed below:

0 describes the introduction, the motivation, the scientific and engineering challenges, the scope of this dissertation, and the contributions of this dissertation.

Chapter 2 reviews the fundamentals behind sensing and actuating with fringing electric field according to three applications. The fundamentals behind the dielectric property measurement of

materials include the governing equations, the measurement approach, the measurement circuit analysis, and the quantitative mapping between material properties and electrical measurements. The fundamentals behind the electrospray evaporative cooling chambers include electrospray cooling processes, governing equations, electrohydrodynamics functioning modes, theoretical current-voltage relationships, and applications. The non-dimensional parameters analysis is also discussed to establish empirical heat transfer correlations of the proposed ESEC chambers.

Chapter 3 focuses on the dielectric property measurement of granular materials using the concentric parallel plate sensor. The sensor design and calibration methodology for the measurement system to increase accuracy in material property measurement is discussed.

Chapter 4 focuses on demonstrating the ability of a customized concentric fringing electric field (FEF) sensor on the in-process measurement of coating thickness and coating loading of a functional coating material. The FEF sensor design, experimental apparatus and parameters, experimental results, measurement accuracy analysis, and a signal processing algorithm are discussed.

Chapter 5 focuses on developing fringing electric field actuators (electrospray evaporative cooling (ESEC) chambers) for the thermal management of electronics. The design methodology, performance optimization methodology, experimental apparatus, experimental parameters, and data reduction for ESEC chambers is discussed. Heat transfer characterization and correlations of ESEC chambers are discussed as well.

Chapter 6 outlines the future work extended from this dissertation.

Chapter 2 **Fundamentals**

2.1 Background on Fringing Electric Field Sensors

2.1.1 Maxwell's Equations

Maxwell's equations describe all electromagnetic phenomena. The differential form of Maxwell's equations in linear dielectric and magnetic media is

$$\text{Gauss's Law for } E-\text{Field}: \quad \nabla\bullet\left(\varepsilon\vec{E}\right)=\rho \tag{2.1}$$

$$\text{Gauss's Law for } H-\text{Field}: \quad \nabla\bullet\left(\mu\vec{H}\right)=0 \tag{2.2}$$

$$\text{Faraday's Law}: \quad \nabla\times\vec{E}=-\frac{\partial}{\partial t}\left(\mu\vec{H}\right) \tag{2.3}$$

$$\text{Ampere's Law}: \quad \nabla\times\vec{H}=\vec{J}+\frac{\partial}{\partial t}\left(\varepsilon\vec{E}\right) \tag{2.4}$$

$$\text{Law of Conservation of Charge}: \quad \nabla\bullet\vec{J}+\frac{\partial\rho}{\partial t}=0 \tag{2.5}$$

where $\vec{E}$ is the electric field, $\vec{H}$ is the magnetic field strength, $\vec{J}$ is the current density, ρ is the charge density, μ is the magnetic permittivity, ε is the dielectric permittivity, and t is time. The magnetic permittivity, μ, and dielectric permittivity, ε, in Eq. (2.1) - (2.5) can be a variable of time and space. Under most sensor application conditions, the electromagnetic wave radiation wavelength, $\lambda_m = c/f$ where $c = 1/\sqrt{\varepsilon\mu}$ is the speed and f is the frequency of electromagnetic waves, is much longer than sensor periodicity, λ, of the sensor geometrical structure. This is important in order to apply quasistatic approximations for the sensor applications.

2.1.2 Electroquasistatics

The electroquasistatic approximations to Maxwell's equations govern the operation of fringing electric field sensors. In this approximation, the electric field energy stored in the system is much larger than the magnetic field energy, and the electric field ($\vec{E}$) is approximately

irrotational, i.e. $\nabla \times \vec{E} = 0$. This occurs when the system is capacitive and the time variations are sufficiently slow that the time variation on the right hand side of Eq. (2.3) is neglected. Based on the electroquasistatic approximation, Maxwell's equations reduce to be the following.

$$\nabla \bullet \left(\varepsilon \vec{E} \right) = \rho \tag{2.6}$$

$$\nabla \bullet \vec{J} + \frac{\partial \rho}{\partial t} = 0 \tag{2.7}$$

$$\nabla \times \vec{E} = 0 \tag{2.8}$$

$$\nabla \times \vec{H} = \vec{J} + \frac{\partial}{\partial t}\left(\varepsilon \vec{E} \right) \tag{2.9}$$

Figure 2-1 shows a schematic diagram of a generic model-based fringing electric field sensor. The sensor is composed of a set of coplanar electrodes, including the driving electrode, the sensing electrode, the guard electrode, and the ground electrode. The driving electrode is adopted to excite the sensor. The driving electrode, in general, is connected in series to an AC voltage source (V_D in Figure 2-1). For different applications, the sensing electrode can either be connected to the current measurement circuit or a voltage measurement circuit. When a material under test is present in the vicinity of the sensor electrodes, the electric field originating from the driving electrodes penetrates through the bulk material and then terminates the sensing electrodes. The dielectric properties of the material alter the distribution of the electric field lines. Therefore, the current or potential at the sensing electrodes is a function of the material's dielectric properties as well. By investigating the variation of sensing voltage or sensing current, $I_{s,}$ in the frequency or time domain, the material's dielectric properties can then be estimated. A ground plate, which is in the plane below the driving and sensing electrodes, is to prevent interference from external stray electromagnetic fields. If there are multiple sensor heads on the same substrate, the guard electrodes are designed to prevent "cross-talk" between sensor heads. The guard electrodes are either grounded or can be maintained at the same voltage as the sensing electrodes.

The electric scalar potential follows Laplace's equation with the electric field penetration depth, of the order of $\lambda/2\pi$, where λ is the spatial periodicity of the electrode structure. Because

the electric field has zero curl in Eq. (2.8), $\vec{E} = -\nabla\Phi$, where Φ is the electric scalar potential. When $\rho = 0$ and ε is spatially uniform, Eq. (2.6) reduces to Laplace's equation.

$$\nabla^2\Phi = 0 \tag{2.10}$$

The potential as a function of position for $z > 0$ can be expressed as a Fourier series

$$\Phi(x,z) = \sum_{n=1}^{\infty} \Phi_n \cos(k_n x) e^{-k_n z} + \Phi_0 \frac{z}{\lambda}, \quad k_n = \frac{2n\pi}{\lambda} \tag{2.11}$$

The coefficient Φ_n and Φ_0 can be found by evaluating Eq. (2.11) at $z = 0$, where the potentials are constant on each driving and sensing electrodes, and must be solved by numerical techniques in the space between the electrodes.

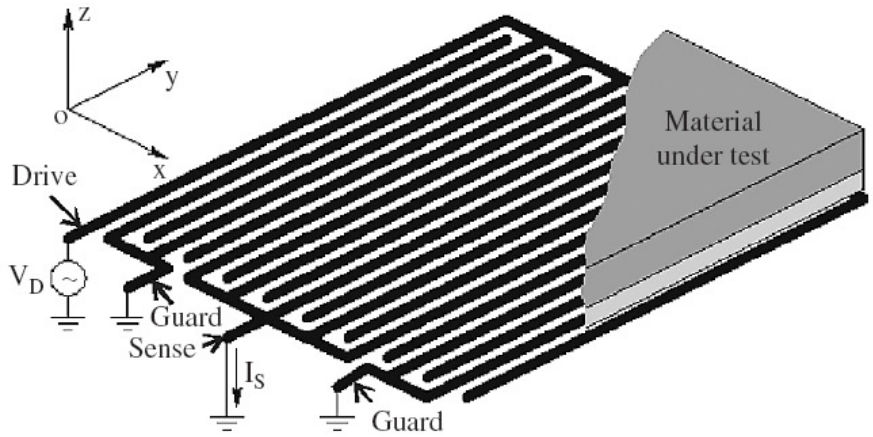

Figure 2-1. *Generic fringing electric field sensor with an interdigital pattern of electrodes [64, 65].*

2.1.3 Theory of Dielectrics

Dielectrics consist of polar molecules, non-polar molecules, or both. Due to the asymmetric configuration of polar molecules, materials consisting of these molecules have built-in dipole moments. Under influence of an external electric field, the polarized dipoles reorient in the

electric field and neutralize some of the charges on the electrodes. The common measure of material dielectric properties is the complex dielectric permittivity. It is a measure of the ability of the dielectric material to reorient and neutralize charges on the electrodes. This usually depends on how polarized the material is and the inertial force it has to overcome to reorient. Relative complex dielectric permittivity is used to describe dielectric properties of a material. It is defined as the ratio between the dielectric permittivity of the material and that of free space. The dielectric permittivity of free space is 8.85×10^{-12} F/m.

Most dielectric material's dielectric permittivity is frequency-dependent. In the presence of an alternating electric field, the dipole moments inside the material oscillate with the direction of the electric field. It is harder for the dipole moments to catch up with the variation of the field direction if the driving frequency is high, which results in a decreasing ability for the material to neutralize charges on the electrodes at high frequencies. Generally speaking, the complex dielectric permittivity ($\varepsilon^*(\omega)$) is expressed as

$$\varepsilon_r^*(\omega) = \varepsilon_r^{'}(\omega) - j\varepsilon_r^{''}(\omega) \tag{2.12}$$

where $\varepsilon_r^{'}$ is the real part of the dielectric permittivity of the material, and $\varepsilon_r^{''}$ is the dielectric loss of the material. There is currently no general model to describe the dielectric relaxation process. One of the most commonly used models for fitting dielectric relaxation data is the Havriliak-Negami (HN) function, which is expressed as

$$\varepsilon_r^*(\omega) = \varepsilon_\infty + \frac{\varepsilon_0 - \varepsilon_\infty}{\left[1+(i\omega\tau_0)\alpha\right]^\beta} \tag{2.13}$$

$$\sigma = \omega\varepsilon_r^{''} \tag{2.14}$$

where ε_0 is the dielectric permittivity at dc, and ε_∞ is its asymptotic value at infinite high frequency. The term ε_0 - ε_∞ is the total dielectric relaxation strength and τ_0 is the relaxation time

of the material. For α = 1, the Davison-Cole model emerges, where as for β = 1, the Cole-Cole model emerges.

2.1.4 Measurement Approach

Figure 2-2 (a) shows the basic measurement circuit behind the measurement system, which consists of a fringing electric field sensor and a dielectric spectroscopy meter (DS-1, Illionix). We use the sensor's dielectric response with respect to changes in the functional coating layer thicknesses in the frequency domain to measure the functional coating layer thickness and loading. When voltage, V_1, is applied between a material under test, an AC current, i, passing through the sensor also passes through the dielectric spectroscopy meter's measurement circuit and generates an output voltage, V_2. By measuring the amplitude and phase of V_1 and V_2 through the data acquisition interface (NI-6154 DAQ card and LabVIEW program), the sensor's dielectric response in the frequency domain can then be determined. Figure 2-2 (b) shows the circuit impedance of the measurement system. Circuit analysis regarding the extrapolation of the sensor's dielectric response with respect to the MUT is discussed in [66] and is summarized next.

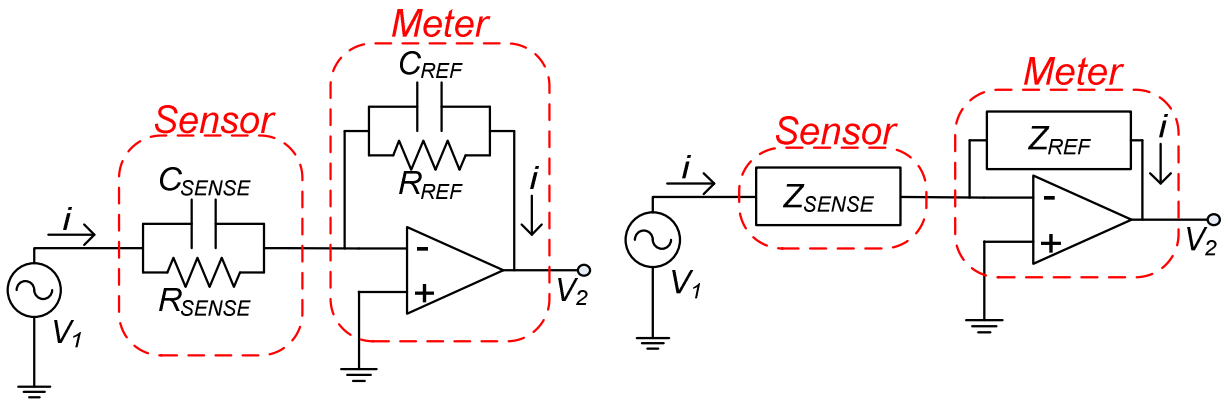

(a) Schematic circuit (b) Corresponding circuit impedance

Figure 2-2. *Schematic diagram of the basic measurement circuit of the dielectric property measurement system.*

2.1.5 Measurement Circuit Analysis

2.1.5.1 Parallel R-C Circuit Impedance

For a parallel *R*-*C* circuit, the corresponding impedance (*Z*) is

$$\frac{1}{Z} = \frac{1}{Z_R} + \frac{1}{Z_C} = \frac{1}{R} + j\omega C \tag{2.15}$$

where Z_R is impedance of a resistor, Z_C is impedance of a capacitor, R is resistance of a resistor, C is capacitance of a capacitor, and ω is the radial frequency.

2.1.5.2 Gain and Impedance

The current, i, passing through the sensor impedance (Z_{SENSE}) is

$$i = \frac{V_1}{Z_{SENSE}} \tag{2.16}$$

The same current, i, then passes through the meter's circuit impedance (Z_{REF}), which results in the voltage, V_2, on the output.

$$V_2 = -iZ_{REF} \tag{2.17}$$

Therefore, the resulting gain, G, is

$$G = \frac{V_2}{V_1} = -\frac{Z_{REF}}{Z_{SENSE}} \tag{2.18}$$

2.1.5.3 Capacitance and Resistance

From Eq.(2.15), the sensor impedance (Z_{SENSE}) is a function of the sensor parallel capacitance, $C_{SENSE,}$ and resistance, R_{SENSE}

$$\frac{1}{Z_{SENSE}} = \frac{1}{R_{SENSE}} + j\omega C_{SENSE} \tag{2.19}$$

When Eq. (2.19) is separated into real and imaginary parts,

$$\mathrm{Re}(\frac{1}{Z_{SENSE}}) + j\,\mathrm{Im}(\frac{1}{Z_{SENSE}}) = \frac{1}{R_{SENSE}} + j\omega C_{SENSE} \tag{2.20}$$

Therefore, the resistance and capacitance at the sensor terminals is

$$R_{SENSE} = \frac{1}{\mathrm{Re}(1/Z_{SENSE})} \tag{2.21}$$

$$C_{SENSE} = \frac{\mathrm{Im}(1/Z_{SENSE})}{\omega} \tag{2.22}$$

By combining Eq. (2.18), Eq. (2.21), and Eq. (2.22), the sensor's resistance and capacitance is determined by the resulting gain, G, and the dielectric spectroscopy meter's circuit impedance Z_{REF}.

$$R_{SENSE} = \frac{1}{\mathrm{Re}(-G/Z_{REF})} \tag{2.23}$$

$$C_{SENSE} = \frac{\mathrm{Im}(-G/Z_{REF})}{\omega} \tag{2.24}$$

2.1.6 Complex Dielectric Permittivity and Conductivity

To quantitatively determine the dielectric properties of a material from electrical measurements of a sensor, a formula for a specific sensor is necessary. For example, when a parallel plate sensor is used, the equation describing the relationship between the complex dielectric permittivity (ε_r^*) and the complex capacitance of the sensor using a parallel plate sensor formula [36] is

$$\varepsilon_r^*(\omega) = \frac{C_{SENSE}^*(\omega) \times d}{\varepsilon_0 \times A_s} = \varepsilon_r'(\omega) - j\varepsilon_r''(\omega) \tag{2.25}$$

where C_{SENSE}^* is the complex capacitance from the sensor, ε_0 is the vacuum dielectric permittivity, A_s is the sensing electrode area of the sensor, d is the electrode spacing between two parallel plates of the sensor, and ω is the angular frequency. $\varepsilon_r'(\omega)$ and $\varepsilon_r''(\omega)$ are the real part and imaginary part of the relative dielectric permittivity of the sample material. $\varepsilon_r'(\omega)$ is related to the electrical permittivity of the material, while $\varepsilon_r''(\omega)$ is associated with the conductivity of the material. The complex capacitance, C_{SENSE}^*, can be expressed as

$$C_{SENSE}^* = \frac{1}{j\omega Z_{SENSE}} = \frac{-G}{j\omega Z_{REF}} \tag{2.26}$$

By combining Eq. (2.25) and Eq. (2.26), the real part of the relative dielectric permittivity of the sample is

$$\varepsilon_r'(\omega) = \frac{d}{\varepsilon_0 \times A_s} \mathrm{Re}\left(\frac{-G}{j\omega Z_{REF}}\right) \tag{2.27}$$

and the imaginary part of the relative dielectric permittivity of the sample is

$$\varepsilon''_{r,}(\omega) = -\frac{d}{\varepsilon_0 \times A_s} \mathrm{Im}(\frac{-G}{j\omega Z_{REF}}) = \frac{\sigma}{\varepsilon_0 \omega} \tag{2.28}$$

where σ is the conductivity of the sample.

2.2 Background on Fringing Electric Field Actuators for Thermal Management of Electronics

2.2.1 Electrospray Cooling Processes

Figure 2-3 shows the complete electrospray cooling process. Electrospraying or electrohydrodynamics atomization (EHDA) is a process in which the free boundary surface of a liquid flowing out of a capillary tube is transformed as a result of electric stress. Electrospray is also a method of generating fine liquid droplets/aerosols in a variety of ranges through the electrostatic charging process [67, 68], which potentially shows the ability of generating mist of droplets in an optimal size for heat transfer cooling applications of microelectronics.

In the electrospray evaporative cooling (ESEC) chamber, when an electric field is applied in the vicinity of liquid flow from a capillary tube, surface charge will be induced on the liquid meniscus. The applied electric field accelerates the surface charge, reshaping the meniscus. For example, the Coulomb force acting onto the charges in the fluid causes the fluid meniscus to deform into the shape of a cone, known as the Taylor cone [43, 68, 69]. The shape and characteristic behavior of the free boundary surface will depend on the interaction of electrostatic, liquid momentum, gravity, surface tension, and viscosity forces. This interaction of forces can produce electrohydrodynamics functioning modes from dripping to multiple jets under the same flow conditions by changing the applied voltage [43]. The electric field usually has an obvious effect on the free boundary flow exiting a capillary tube within the flow rate range from 10^{-12} m^3/s to 10^{-7} m^3/s for applied voltages, up to 30 kV. Even at higher voltages, the current flow is so low (from 10^{-4} A to 10^{-6} A) that the Joule heating effect is negligible.

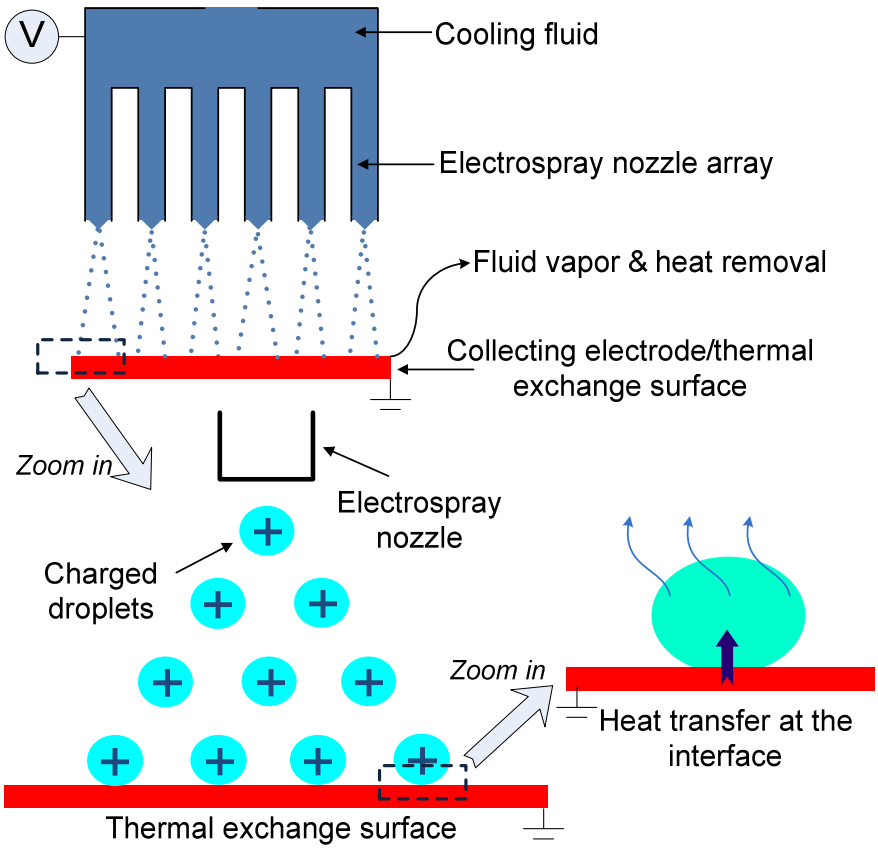

Figure 2-3. *Schematic diagram of the fluid atomization and heat transfer mechanism of the ESEC chamber using an array of electrospraying micronozzles.*

As the applied voltage increases, the electric field intensity and the charge density at the surface increase as well. The charged liquid in the capillary tube becomes unstable as it is forced to hold more and more charge. At the critical electric field intensity, the forces on the charged fluid in the Taylor cone overcome the intra-molecular forces of the fluid, such as viscosity, surface tension, and liquid momentum, and a jet of charged liquid is then sprayed from the tip of the cone. The charged fluid particles expelled from the tip of the fluid cone repel each other, generating fine aerosol droplets. The droplet diameter highly depends on the electrohydrodynamics functioning modes. Typically, for the stable cone-jet mode, the droplet size is around 10 µm in diameter [67, 68], while for the unstable multi-jet mode, the droplet size could be around 200 µm in diameter [68]. Those charged droplets are then accelerated by the electrostatic force and toward the collecting electrode surface. During the transportation, droplets rapidly shrink due to evaporation from their surface. Since it is difficult for the charge to evaporate, the distance between the electrical charges in the droplet dramatically decreases. If the

droplet cannot dissipate its charge in time during the transportation, the electrical charge could reach a critical state, and the droplet will violently blow apart again to form smaller droplets [70]. As the droplets reach the collecting electrode, which is also the thermal exchange surface, two-phase heat transfer occurs at the surface, which dissipates large amounts of heat, generated from the thermal exchange surface, because of the phase change of droplets from the liquid to the vapor phase.

2.2.2 Governing Equations for the Electrospray Process

The governing equations regarding the full multiphysics behind the electrospray evaporative cooling (ESEC) chamber is currently limited, in part due to the dependence of the complicated electrohydrodynamics (EHD) function modes on the applied electric field. The governing equations discussed in this section focus on the electrospray process.

The electrical and mechanical forces included in the mass and momentum conservation equations govern the electrospray process [43]. The mass conservation equation is

$$\frac{\partial \rho_i}{\partial t} + \nabla \bullet \left(\rho_i \mathrm{v}_i \right) = \sum_{j=1}^{n} I_{ij} \tag{2.1}$$

, and the momentum conservation equation is

$$\frac{\partial \rho_i \mathrm{v}_i}{\partial t} + \nabla \bullet \left(\rho_i \mathrm{v}_i \otimes \mathrm{v}_i \right) = \nabla \bullet \mathbf{\Pi}_l + \rho_i \boldsymbol{g} + \sum_{j=1}^{n} \mathbf{P}_{ij} + \mathbf{L}_l \tag{2.2}$$

where ρ_i is the density of the ith phase, v_i is the velocity of the ith phase, I_{ij} is the mass conservation ith to jth phase, $\mathbf{\Pi}_i$ is the stress tensor acting on the liquid surface due to the hydrostatic pressure and viscosity, $\mathbf{g}$ is the acceleration due to gravity, $\mathbf{P}_{ij}$ is the volume density of momentum conservation ith to jth phase, and $\mathbf{L}_l$ is the volume density of electromagnetic and polarization forces on the liquid phase. The subscript i refers to the gas phase, and the subscript l refers to the liquid phase. The symbol $\otimes$ represents the outer product of the vectors.

The stress tensor ($\mathbf{\Pi}_i$) on the liquid surface is due to the dynamic and hydrostatic pressure (p) on the inter-phase surface, and the liquid viscosity (η_l).

$$\mathbf{\Pi}_l = \nabla(\mathbf{1}p) + \eta_l \nabla \mathrm{v}_l \tag{2.3}$$

$$\nabla(p) = p_l - p_g \tag{2.4}$$

Where $\mathbf{1}$ is the unit tensor, which is always perpendicular to the inter-phase surface. p_l and p_g are the pressures on both sides of the interfacial surface. When Eq. (2.2), Eq. (2.3), and Eq. (2.4) are combined, the force density on the liquid jet is

$$\frac{\partial \rho_l \mathrm{v}_l}{\partial t} = \rho_l \boldsymbol{g} + \mathbf{L}_l + \nabla \bullet \left[\nabla(\mathbf{1}p) + \eta_l \nabla \mathrm{v}_l + \rho_l \mathrm{v}_l \otimes \mathrm{v}_l\right] - \mathbf{\Phi}_{\mathbf{St}} \tag{2.5}$$

where $\mathbf{P}_{ij}$ is simplified to the Strokes drag force ($\mathbf{\Phi}_{\mathbf{St}}$) on the jet due to the surrounding gas viscosity.

The volume density of the electromagnetic and polarization forces ($\mathbf{L}_l$), with magnetic component negligible, on the liquid phase is

$$\mathbf{L}_l = \rho_q \mathbf{E} + \frac{1}{2}\left(\mathbf{D}\nabla^{\mathrm{T}}\mathbf{E} - \mathbf{E}\nabla^{\mathrm{T}}\mathbf{D}\right) \tag{2.6}$$

where ρ_q is the charge density, $\mathbf{E}$ is the electric field, and $\mathbf{D}$ is the electric flux density. On the liquid-phase surface, the stress tensor balance equation is

$$\nabla \times \Xi = \nabla(\mathbf{1}p) + \eta_l \nabla \mathrm{v}_l + \rho_l \mathrm{v}_l \otimes \mathrm{v}_l + \Lambda_l \tag{2.7}$$

where Ξ is the tensor of the stress tensor, Λ_l is the tensor of the electromagnetic and polarization stresses on the inter-phase surface, and $\nabla(\mathbf{1}p)$ is the stress tensor due to the pressure difference.

$\eta_l \nabla \mathrm{v}_l$ is the stress caused by the liquid viscosity. $\rho_l \mathrm{v}_l \otimes \mathrm{v}_l$ is the stress caused by the inertial forces due to the flowing liquid. The electrodynamic stress tensor (Λ_l) on the interfacial surface is

$$\Lambda_l = \mathbf{q} \otimes \mathbf{E} + \mathbf{1} \times \frac{1}{2}\left(\mathbf{D}\nabla\mathbf{E} - \mathbf{E}\nabla\mathbf{D}\right) \tag{2.8}$$

$$\nabla\mathbf{E} = \mathbf{E}_l - \mathbf{E}_g \tag{2.9}$$

where $\mathbf{q}$ is the surface charge density. $\mathbf{E}_l$ and $\mathbf{E}_g$ are the vectors on both liquid and gas sides of the inter-phase surface, respectively. The equation describing the electrical surface charge balance is

$$\frac{\partial \mathbf{q}}{\partial t} = \nabla \bullet \mathbf{j} - \nabla \times \left(\mathbf{j}_s - \mathrm{v} \times \mathbf{q}\right) \tag{2.10}$$

$$\nabla \bullet \mathbf{j} = \mathbf{j}_g^n - \mathbf{j}_l^n \tag{2.11}$$

$$\mathbf{j}_s = \bar{\Delta}\mathbf{I} \times \mathbf{j} \tag{2.12}$$

where $\mathbf{j}$ is the density of the surface current on the inter-phase surface, $\mathbf{j}_s$ is the line current density due to charge movement on the inter-phase surface, and $\bar{\Delta}\mathbf{I}$ is the charge layer thickness close to the liquid surface. $\nabla \bullet \mathbf{j}$ is the current density, on the perpendicular components of the current vectors, through the liquid surface. $\mathrm{v} \times \mathbf{q}$ is the line current density due to the charge flowing with liquid on the surface (dynamic current).

Electric field on the liquid surface consists of two sources. The first source is the potential applied on the capillary with the charge-free interelectrode space (E_0). The second source is from the charged droplets, which include their image charge on the collecting electrode (E_k), and from the space charge of ions due to electrical discharge in gas (E_i). Therefore, the electric field on the liquid (E) is expressed as

$$\mathbf{E} = \mathbf{E}_0 + \mathbf{E}_i + \sum_k \mathbf{E}_k \tag{2.13}$$

The electric field near the capillary tip is deformed by charged droplets and space charge generated by gas ions due to electrical discharge. This phenomenon should be considered in EHD functioning mode analysis, except for the dripping mode at lower potentials.

The surface charge density vector in Eq. (2.8) and Eq. (2.10) is defined as [71]

$$\mathbf{q} = \bar{\Delta}\mathbf{I}_n \rho_q = \mathbf{I}_n q \tag{2.14}$$

where ρ_q is the space charge density in the charge layer ($\bar{\Delta}\mathbf{I}$). The surface charge density vector is always perpendicular to the inter-phase surface.

On the liquid surface, the tangential component of the stress tensor results in liquid jet elongation from the main body of liquid, which issues from the capillary, while the normal component of the electric field balances the hydrostatic pressures. Additionally, the force on the bulk jet, which results from the electric field generated by the electrodes and by the space charge of each *k*th droplet, are also important information, because they result in liquid jet movement and also participate in the formation of other droplets.

The trajectory of the *k*th droplet of mass (m_k) and charge (Q_k), is governed by the vector differential equations.

$$m_k \frac{d\mathbf{w}_k}{dt} = \frac{C_d \,\mathrm{Re}_k}{24} \mathbf{F}_{Sk} + \mathbf{F}_{ek} + m_k \mathbf{g} \tag{2.15}$$

where $\mathrm{w_k}$ is the *k*th droplet velocity, C_d is the non-Strokesian drag coefficient, $\mathrm{Re_k}$ is the Reynolds number for the *k*th droplet. F_{Sk} is the Strokes drag force on the *k*th droplet.

$$\mathbf{F}_{Sk} = \frac{6\pi\eta_g R_k \left(\mathrm{u} - \mathrm{w}\right)}{C_c} \tag{2.16}$$

where R_k is the radius of the droplet, **u** is the surrounding gas velocity, η_g is the gas viscosity, and C_c is the Cunningham correction factor. F_{ck} is the electrostatic force on the kth droplet.

$$\mathbf{F}_{ek} = Q_k \mathbf{E} + \frac{Q_k Q_j}{4\pi\varepsilon_0 \left| r_{kj} \right|^3} \mathbf{r}_{kj} \tag{2.17}$$

where r_{kj} is the distance between the kth droplet and the jth droplet centers, and ε_0 is the permittivity of the free space.

Directly solving the above-mentioned sets of governing equations are almost impossible, in part due to the difficulties in formulating the appropriate boundary conditions for free moving jets in an open electrode system. Wilhelm *et al.* [72] uses the Lagrangian single-droplet tracking of a dilute two-phase flow to quantitatively investigate the migration of droplets emitted from an electrified liquid meniscus towards a collecting electrode. He focuses on the transportation process and the evaporative process.

A force balance for transportation of droplet, i, is expressed as [44]

$$\frac{\pi}{6} d_i^3 \rho_d \frac{d\vec{\mathrm{v}}_i}{dt} = C_d \frac{\pi}{8} \rho_g d_i^2 \vec{\mathrm{v}}_i^2 \vec{e}_i + q_i \vec{E}_{ext} + \frac{1}{4\pi\varepsilon_0} \sum_{ij, i \neq j} \frac{q_i q_j}{r_{ij}^3} \vec{r}_{ij} \tag{2.18}$$

where d_i is the diameter of droplets, ρ_d is the mass density of droplets, v_i is the velocity of droplets, C_d is the coefficient of drag, ρ_g is the mass density of the air, e_i is the unit vector of velocity of droplets, q_i is the charge of droplet i, q_j is the charge of droplet j, E_{ext} is the external electric field intensity, and r_{ij} is the distance between droplet i and droplet j. The first term on the right-hand side of Eq. (2.18) represents the drag force by the surrounding gas. The second term on the right-hand side of Eq. (2.18) represents the force on the droplets due to the external electric field between the nozzle and collecting electrode. The third term on the right-hand side of Eq. (2.18) represents the mutual electric forces between the charged droplets and the induced charge on the collecting electrode by the image force from the charged droplets.

The general form describing the drag force is from Newton's resistance law.

$$C_d = \frac{24}{\mathrm{Re}}\left(1 + 0.15\,\mathrm{Re}^{0.687}\right), \quad \mathrm{Re} < 800 \tag{2.19}$$

The external electric field (E_{ext}) is calculated as that between a needle (representing a semi-infinite line of charges) and the collecting electrode (representing an infinite plane) separated by distance (H).

$$\vec{E}_{ext} = \frac{\Phi_0}{H}\nabla\Phi^* \tag{2.20}$$

where Φ_0 is the applied potential between the nozzle and the collecting electrode. Φ^* is a non-dimensional potential.

$$\Phi^*\left(r^*, z^*\right) = \frac{K_V}{\log\left(4H/R\right)}\log\left\{\frac{\left[r^{*2} + \left(1 - z^*\right)^2\right]^{1/2} + \left(1 - z^*\right)}{\left[r^{*2} + \left(1 + z^*\right)^2\right]^{1/2} + \left(1 + z^*\right)}\right\} \tag{2.21}$$

$$r^* = \frac{r}{H},\ z^* = \frac{z}{H}$$

where r is the radial component of position vector (x_i), and z is the axial component of position vector (x_i). K_v is a dimensionless parameter (from 0 to 1), which depends on the H/R ratio. Each droplet's trajectory can be followed by the velocity vector (x_i).

$$\vec{\mathrm{v}}_i = \frac{d\vec{x}_i}{dt} \tag{2.22}$$

By integrating from Eq. (2.18) to Eq. (2.22) in three dimensions, one should be able to track the transportation path of every single droplet emitted from the nozzle. The electric current between the nozzle, the spray, and the initial mean droplet diameter should also be taken into account for complete analysis and calculation. This information is discussed in Section 2.2.6.

Droplets evaporate on their way from the nozzle tip to the heated collecting electrode, which determines their final droplet diameter as they reach the heated collecting electrode. The evaporation process can be considered as the movement of droplets in a forced convection condition. The mass transfer for a droplet in a forced convection environment is [73]

$$\dot{m}_i = -\pi d_i D\left(T_{i,ref}\right)\mathrm{Sh}_0\left[c_{i,s}\left(T_{i,s}\right) - c_\infty\left(T_{g,\infty}\right)\right] \tag{2.23}$$

where D is the diffusion coefficient, $T_{i,ref}$ is the reference temperature of droplet i, $c_{i,s}$ is the vapor mass concentration at surface of droplet i, c_∞ is the vapor mass concentration outside the droplet boundary layer, $T_{i,s}$ is the surface temperature of the droplet i, and $T_{g,\infty}$ is the air temperature outside the droplet boundary layer. Sh_0 is the Sherwood number. Some Sherwood number correlations can be founded in [73-76].

When the temperature distribution between the nozzle and the heated collecting electrode is known, the transient temperature of each droplet can be calculated. The correlations for heat transfer are similar to the mass transfer correlations. The Schmidt number in the Sherwood number correlations is replaced by the Prandtl number, and the Sherwood number is replaced by the Nusselt number. The heat transfer correlation is

$$\dot{Q}_{i,s} = -\pi d_i \lambda_g\left(T_{i,ref}\right)\mathrm{Nu}_0\left[T_{i,s} - T_{g,\infty}\right] - \Delta H_V \dot{m}_i \tag{2.24}$$

where λ_g is the thermal conductivity of the air, and ΔH_V is the latent heat of vaporization. Since the surrounding air is assumed to be stagnant, the heat conduction within the droplet is much faster compared to the conduction of the surrounding air. Therefore, the temperature inside the droplet is uniformly distributed at all times [77].

2.2.3 Electrohydrodynamics (EHD) Functioning Modes

According to the investigation results from Cloupeau *et al.* [42] and Jaworek *et al.* [43], the EHD functioning modes of a single-capillary-to-plane configuration, in general, can be classified

as the dripping modes and jet modes. The dripping modes are classified because only fragments of liquid are electrified directly from the nozzle tip. The jet modes are classified because liquid is electrified directly into a long fine jet, which can be stable or can move in any regular way. The stable cone-jet and the unstable multi-jet modes are jet modes. The stable cone-jet mode has the advantage of generating uniform submicron droplets [67, 68], providing the ability to select the appropriate droplet's size for optimal heat transfer. However, the operating range of the potential required to maintain the cone-jet mode is narrow and highly influenced by the flow rate and properties of the working fluid, as well as the number and the arrangement of the electrospray nozzles. The critical voltage required for a given flow rate to change from the cone-jet to the multi-jet mode has not been quantitatively investigated.

Although the droplet control ability in multi-jet mode is poor, the electrified liquid jets can cover larger portions of the thermal exchange surface, which results in higher heat transfer performance. Therefore, in this investigation, all ESEC chambers were operated in the unstable multi-jet EHD mode, as shown in Figure 2-4.

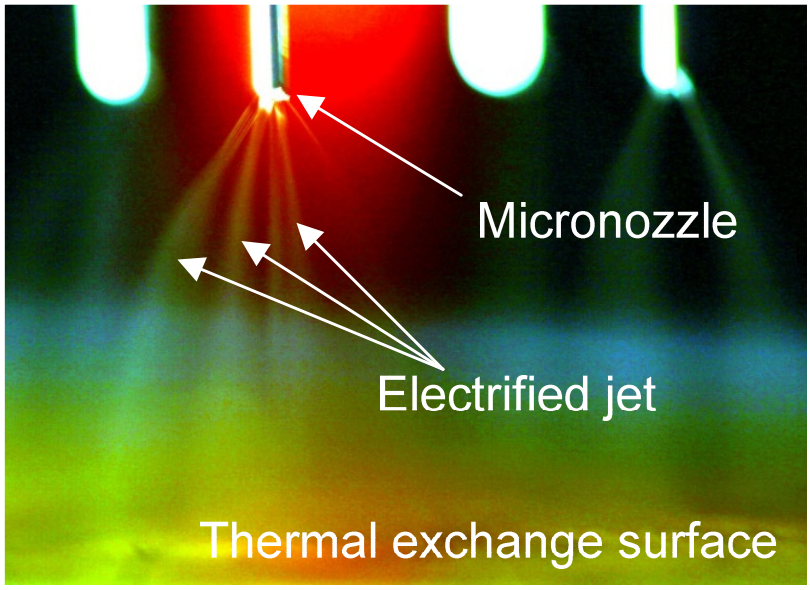

Figure 2-4. *Multi-jet EHD functioning mode of the 4-nozzle ESEC chamber with 5 mm spacing operated at 7.0 kV and the flow rate of 2 cc/hr. Four obvious ethyl alcohol jets are electrified close to the tip of the micronozzles.*

2.2.4 Qualitative Onset Voltage of the EHD Mode

The EHD mode discussed in this section is the cone-jet mode. The onset of the EHD mode highly relies on the applied potential that the electric field intensity on the liquid surface overcomes the liquid surface stress induced by liquid surface tension, σ. In general, the cone is not quite considered as equal-potential. However, it was found that the evaluated potential drop at the filament was always small compared with the onset potential and, hence, the equal-potential through the entire liquid cone is held for the qualitative analysis.

To obtain the onset potential of the EHD mode for a liquid of known surface tension, the same electric field conditions should be kept regardless of geometrical configurations. The relationship between the onset potential and the electric field (E_0) on the liquid surface formed at a capillary edge is

$$E_0\left(r_c\right)=\frac{V_0}{f\left(r_c,h\right)} \tag{2.25}$$

where V_0 is the onset potential, and $f\left(r_c\,,\,h\right)$ is the geometrical expression of the radius (r_c) of the capillary tube and the capillary-to-plane distance (h). The most appropriate form of the geometrical expression is from Jones *et al.* [78] and expressed as

$$f\left(r_c,h\right)=A_1 r_c \ln\left(\frac{4h}{r_c}\right) \tag{2.26}$$

where A_1 is a constant, and its best value should be experimentally determined.

At the onset of the EHD mode, the electric field on the liquid meniscus at the tip of the capillary tube should balance the surface tension. The electric field form assumed by Taylor [79] is

$$E_0\left(r_c\right)=\left[\frac{2\sigma Cos\theta_0}{\varepsilon_0 r_c}\right]^{1/2} \tag{2.27}$$

where θ_0 is the half angle of the liquid cone, and σ is the surface tension. This form neglects the small effect induced by hysteresis. Therefore, the onset potential of the EHD mode can be expressed by combining Eq. (2.25), Eq. (2.26), and Eq. (2.27).

$$V_0 = A_1 \left[\frac{2\sigma r_c Cos\theta_0}{\varepsilon_0} \right]^{1/2} \ln\left(\frac{4h}{r_c} \right) \tag{2.28}$$

where ε_0 is the vacuum permittivity. Figure 2-5 shows the relationship between the onset voltage and the distance (between the tube and the plate) of the single-capillary-to-plane configuration with the tube radius of 0.21 mm and A_1 of 7.07×10^{-1} [78]. For the distance of 7.5 mm, the predicted onset voltage using Eq. (2.28) is 1.38 kV.

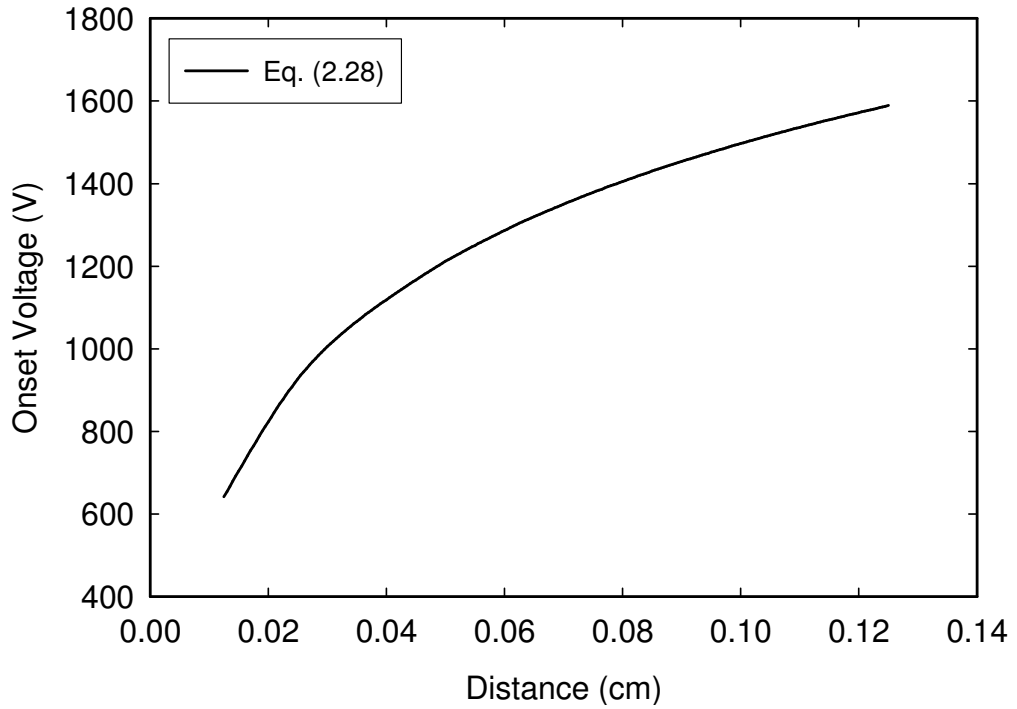

Figure 2-5. *Predicted onset voltage of the EHD mode with the single-capillary-to-plane configuration using Eq.(2.28).*

Additionally, for the same geometric configuration, the onset potential of the EHD mode is highly dependent on the surface tension of the liquid regardless of the variation on conductivity and viscosity [80]. The square of the onset potential was found to be proportional to the surface

tension of the liquid. If the liquid exhibits surface tension higher than 5×10^{-2} N/m, this liquid would not be atomized in the EHD mode.

2.2.5 Theoretical Current-Voltage Relationship

Theoretically, the generated current from the movement of charged droplets and space charged ions depends on the applied potential between the capillary tube and the collecting electrode, as well as the EHD modes of the system. Many researchers have focused on the theoretical current-voltage relationship for the stable cone-jet EHD mode. The results show that the generated current is independent of the potential [81] as the system is operated in the stable cone-jet mode. Theoretical current-voltage equations for the EHD modes other than the stable cone-jet mode are currently limited, in part due to limited theoretical modes describing the complicated multi-jet EHD modes. More experimental investigations on this issue would be necessary to establish empirical current-voltage correlations.

2.2.6 Theoretical Current-Volume-Flow-Rate Relationship

For the electrospray mechanism, power consumption is the product of the induced current (I) and applied potential (V). This current strongly depends on the generated droplet size (d), and is generally on the order of several nanoamperes [82].

The first scaling law regarding the current generated from the electrified conical meniscus in the stable cone-jet EHD mode for a needle-to-plate configuration was presented by De La Mora and Loscertales [83] in the form of

$$I \sim Q^{1/2} \tag{2.29}$$

Another scaling law of current versus volumetric flow rate of liquids with low polarity was reported by Ganan-Calvo *et al.* [84, 85] in the form of

$$I \sim Q^{1/4} \tag{2.30}$$

Ganan-Calvo *et al.* [85] have developed a scaling law describing the relationship among the flow rate (Q) of different working fluids, the generated droplet size, the corresponding ionic current (I), and the dimensionless charge density of the droplets (q). The system of equations describing this scaling law is as follows.

For $\delta_\mu \delta \leq 1$,

$$\frac{I}{I_0} = 6.2\left[\frac{Q}{Q_0(\beta-1)^{\frac{1}{2}}}\right]^{\frac{1}{2}} - 2.0 \tag{2.31}$$

$$\frac{d}{d_o(\beta-1)^{\frac{1}{3}}} = 1.6\left[\frac{Q}{Q_o(\beta-1)^{\frac{1}{2}}}\right]^{\frac{1}{3}} - 1.0 \tag{2.32}$$

$$q = 12.6\left[\frac{d}{d_o(\beta-1)^{\frac{1}{3}}} + 1.0\right]^{\frac{-2}{3}} \times \left[1 - 0.6\left(\frac{d}{d_o(\beta-1)^{\frac{1}{3}}} + 1.0\right)^{\frac{-2}{3}}\right] \tag{2.33}$$

For $\delta_\mu \delta \gg 1$,

$$\frac{I}{I_0} = 11\left[\frac{Q}{Q_0}\right]^{\frac{1}{4}} - 5.0 \tag{2.34}$$

$$\frac{d}{d_o} = 1.2\left[\frac{Q}{Q_o}\right]^{\frac{1}{2}} - 0.3 \tag{2.35}$$

$$q = 14.0\left[\frac{d}{d_o} + 0.3\right]^{\frac{-2}{3}} \times \left[1 - 0.5\left(\frac{d}{d_o} + 0.3\right)^{\frac{-1}{2}}\right] \tag{2.36}$$

where the scaling quantities are

$$I_o = \left(\frac{\varepsilon_o \gamma^2}{\rho} \right)^{\frac{1}{2}} \qquad Q_o = \frac{\varepsilon_o \gamma}{\rho K} \qquad d_o = \left(\varepsilon_o^2 \gamma \rho K^2 \right)^{\frac{1}{3}} \tag{2.37}$$

where γ is surface tension, ε_0 is the vacuum permittivity, μ is the viscosity, ρ is the relative permittivity, and K is the electrical conductivity. Equation (2.31) holds only when the viscosity and conductivity of the working fluid is bigger. For fluid with smaller viscosity and conductivity, I/I_0 is suggested to be proportional to $(Q/Q_0)^{1/4}$. Figure 2-6 shows the estimated theoretical current of the ESEC chambers when they are operated at the stable cone-jet mode with different volumetric flow rates. Water and the ethanol alcohol are the working fluids for the estimation of the theoretical current.

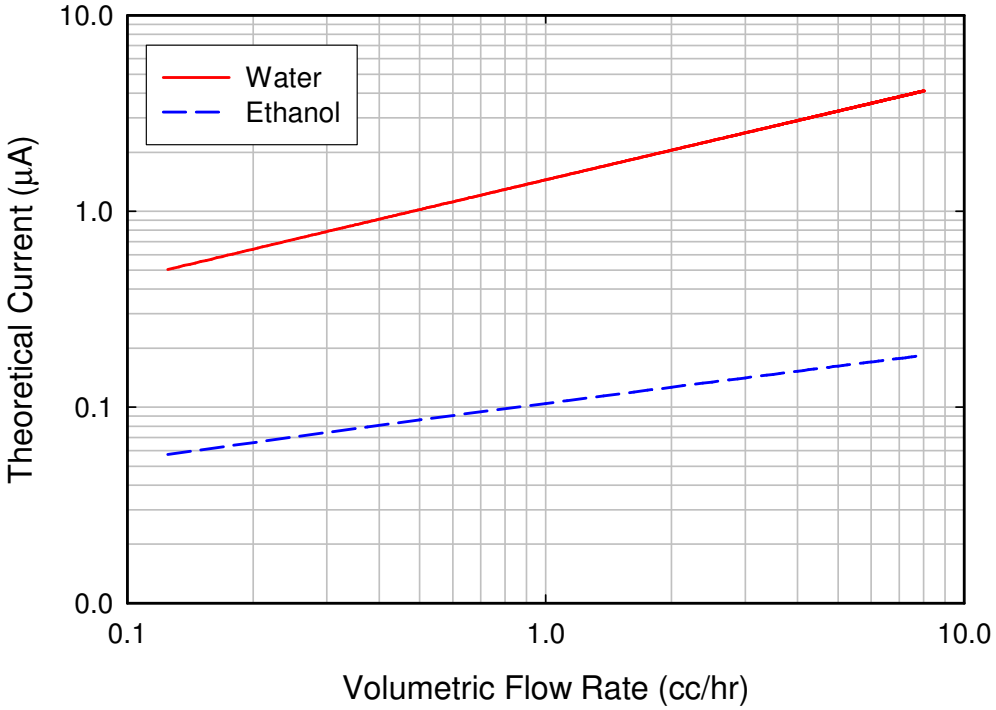

Figure 2-6. *Comparison of the theoretical current of the ESEC chambers at different volumetric flow rates using water and ethanol alcohol as working fluids. The EHD mode is the stable cone-jet mode.*

For a multi-capillary nozzle emitter system operated at the cone-jet EHD mode, Tatemoto *et al.* [68] have shown that the current-to-volumetric-flow-rate scaling law obtained from the experimental results of the single capillary system is still applicable when the number of the capillary nozzles is less than seven.

2.2.7 Applications

Mass Spectroscopy: The electrospray process has profoundly affected the field of mass spectrometry [55-57] by allowing structural analysis of unlimited molecular weight, e.g., large biomolecules, and being directly compatible with liquid chromatography methods. The most common electrospray apparatus used by mass spectrometrists uses a sharply pointed hollow metal tube (i.e., a syringe needle) with liquid pumped through the tube. A high-voltage power supply is connected to the outlet of the tube and the tube is positioned in front of a plate (counter-electrode) held at ground potential. When the power supply is turned on and adjusted for the appropriate voltage, the liquid being pumped through the tube transforms into a fine continuous group of droplets that transport rapidly toward the counter-electrode.

The electrospray process, which occurs at the tip of the emitter, can be viewed through a high-powered microscope. In general, as the liquid begins to exit the needle, it charges up and assumes a conical shape (Taylor cone [43, 68, 69]). The liquid assumes this shape because when the liquid is charged up, a cylindrical shape can hold more charge than a spherical shape. At the tip of the cone, the liquid again changes shape into a fine jet. This jet, however, then becomes unstable, breaking up into the mist of fine droplets. Since these droplets are all highly charged with the same electrical charge, they repel each other very strongly. Thus, the droplets fly apart from each other and cover a wide surface area.

Coatings and Paints: On the industrial scale, electrospray is used in the application of paints and coatings to metal surfaces. The fine spray results in very smooth even films with the paint actually attracted to the metal, so the paint material is used more efficiently. This technology lowers the cost, cuts down on the amount of organic solvents required, and reduces environmental impact.

Microthruster: Miniaturized versions of electrospray are even finding their way into the next generation of micro-satellites. The electrostatic plume makes an efficient ion propulsion engine, although it provides very low power [56].

Chemical Analysis: When electrospray is used as a soft ionization method for chemical analysis, the more generally accepted term is "electrospray ionization" (ESI). Ionization is the process of generating a gas phase ion from a typically solid or liquid chemical species. It is called "soft" since the molecule being ionized does not fall apart or break-up during the process. Ionization is a critical event in mass spectrometry, as only ions can be accurately measured. Once we know an ion's mass, the chemical composition can be determined. When combined with mass spectrometry, the value of ESI is unparalleled, especially in the analysis of such large biological molecules as proteins and DNA.

Thermal Management of Electronics: The application of electrospray in the thermal management of microelectronics is currently limited, in part due to the limited practical design methodology and the heat transfer performance estimation methodology. Feng and Bryan [86] investigated the heat transfer performance enhancement through the application of the electrohydrodynamics (EHD) on traditional impinging liquid jets over a thermal exchange surface by using the cooling chambers of a different number of capillary tubes in an enclosed cooling loop system. Their experimental result shows that the application of the potential on the traditional impinging liquid jets can enhance the heat transfer rate of the cooling chamber by approximately 1.7. The best heat transfer enhancement is primarily at a heat flux of less than 30 W/cm^2 and a critical heat flux (CHF) of approximately 70 W/cm^2. Better enhancement in the heat transfer rate is also achieved by the chamber with multiple capillary tubes at a lower heat flux condition.

2.2.8 Non-Dimensional Parameter Analysis

To investigate the empirical heat transfer correlations for electrospray evaporative cooling (ESEC) chambers of different geometry types and operational parameters, non-dimensional analysis is necessary. We use the Buckingham pi theorem [87] to relate heat transfer performance to the physical mechanism behind the ESEC chamber. Figure 2-7 shows the electrospray region in which the Buckingham pi theorem was applied. The electrospray

processes are highly influenced by the fluid flow rate, the applied potential, the spacing between the center of the array and the center of an electrospraying micronozzle, the quantity of micronozzles, the outer and inner diameter of the micronozzle, and the thermal properties of the fluid, which includes surface tension, dynamic viscosity, liquid density, thermal conductivity, specific heat, and relative permittivity. Table 2.1 shows the variables used for non-dimensional parameter analysis. Since twelve variables were used and six dimensions (L, s, C, kg, J, and K) were used for analysis, six pi-groups should be generated to relate to heat transfer performance. The relationship between heat transfer performance, *h*, and six pi-groups can be expressed as

$$h = h\left[Q, V, s, \sigma, \mu, \rho_l, \varepsilon, N, c_p, k, D_o, D_i\right] \tag{2.38}$$

By defining the appropriate dimensionless parameters, the non-dimensional heat transfer performance is expressed as

$$\frac{hl}{k} = \mathrm{Nu_l} = f\left[\mathrm{We}, \mathrm{We_E}, \mathrm{Re}, \mathrm{Pr}, \frac{L^*(s)}{D_i}, N\right] \tag{2.39}$$

where N_{ul} is the Nusselt number, W_e is the Weber number, W_{eE} is the Electric Weber number [88], R_e is the Reynolds number, and P_r is the Prandtl number. $L^*(s)$ is the characteristic length, which is a function of the spacing between the center of the array and the center of an electrospraying micronozzle. These numbers are discussed in more detail in the following sections.

Nusselt Number: The general form for the Nusselt number is

$$\mathrm{Nu_l} = \frac{hl}{k} \tag{2.40}$$

where *k* is the thermal conductivity of the fluid, *h* is the convective heat transfer coefficient, and *l* is the characteristic length.

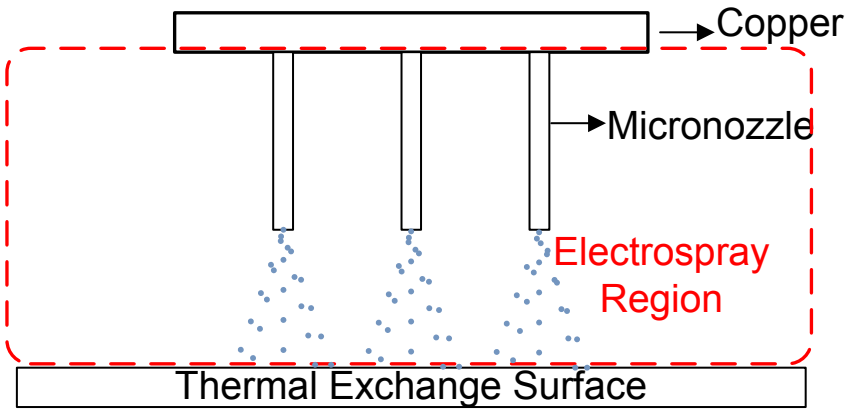

Figure 2-7. *Schematic diagram showing where the Buckingham theorem was applied for dimensionless analysis.*

Table 2.1. *Variables adopted for dimensionless analysis of physical mechanism of electrospray processes.*

Variable	Symbol	Unit	Dimension
Potential	V	V	J/C
Flow rate	Q	cc/min	L^3/s
Spacing	s	mm	L
Number of nozzles	N	--	--
Outer diameter of the nozzle	D_o	mm	L
Inner diameter of the nozzle	D_i	mm	L
Surface tension	σ	N/m	kg/s^2
Dynamic viscosity	μ	kg/ms	kg/Ls
Density	ρ	kg/m^3	kg/L^3
Thermal conductivity	k	W/mK	J/sLK
Specific heat	c_p	J/kgK	J/kgK
Relative permittivity	ε	F/m	$(C/s)^2s^4/kgL^4$

Weber Number: The general form for the Webber number (We) is

$$\mathrm{We} = \frac{\rho l u^2}{\sigma} \tag{2.41}$$

where ρ is the fluid density, l is the characteristic length, u is the average fluid velocity, and σ is the fluid surface tension. When D_0, the outer diameter of the micronozzle, is adopted as the characteristic length, the modified Weber number is expressed as

$$\mathrm{We} = \frac{16\rho D_0}{\sigma} \times \frac{Q^2}{\left(N\pi D_i^2\right)^2} \tag{2.42}$$

where ρ is the fluid density, D_0 is the outer diameter of the micronozzle, σ is the fluid surface tension, Q is the total volumetric flow rate, D_i is the inner diameter of the micronozzle, and N is the quantity of micronozzles of an ESEC chamber.

Electric Weber number: The electric Weber number ($\mathrm{We_E}$) is the ratio of electric pressure and surface tension, and its general form is defined as [89]

$$\mathrm{We_E} = \frac{\varepsilon E_0^2 D_0}{2\sigma} \tag{2.43}$$

where ε is the fluid relative permittivity and E_0 is the average electrostatic field. The characteristic length used here is the outer diameter (D_o) of the micronozzle.

Reynolds Number: The general form for the Reynolds number (Re) is

$$\mathrm{Re} = \frac{\rho u l}{\mu} \tag{2.44}$$

where ρ is the fluid density, u is the average fluid velocity, and μ is the fluid dynamic viscosity. According to the quantity of micronozzle of an ESEC chamber, the Reynolds number is modified as

$$\mathrm{Re} = \frac{4Q}{\nu\pi D_i} \tag{2.45}$$

where ν is the kinematic viscosity of the working fluid. The characteristic length used here is the inner diameter (D_i) of the micronozzle.

Prandtl Number: The general form for the Prandtl number (Pr) is

$$\mathrm{Pr} = \frac{\mu c_p}{k} \tag{2.46}$$

where μ is the fluid dynamic viscosity, C_p is the fluid specific heat, and k is the thermal conductivity of the fluid.

Chapter 3 **Dielectric Property Measurement of Granular Materials**

3.1 Motivation

Many fields, including forensics, pharmacology, agriculture, and construction, require accurate information about the dielectric properties of granular materials and powders. The dielectric properties of granular materials strongly depend on material composition, packing density, uniformity of granule size, degree of contact between individual granules, short-term moisture and solvent diffusion (dynamics within individual granules, as opposed to the bulk of the material), contact polarization, varying degree of contact with the sensing electrodes, and, in case of organic materials, variation of product sources.

Since they contain extensive information about material structural, physical, and chemical properties, non-destructive dielectric sensors have been broadly used in research and commercial applications to measure solid material properties [90-94], control manufacturing processes [10, 11], monitor chemical and physical changes of fluid and solid dielectrics [12, 13], detect abrasion and degradation of power cables [14-16], and identify materials. In many cases, the interpretation of the sensor response depends on simple calibration procedures, while in other cases, it requires sophisticated signal processing algorithms [17] and a deep understanding of the physics and chemistry of the underlying phenomena [18]. In this dissertation, we focus on a multi-electrode concentric parallel plate dielectric sensor.

Figure 3-1 shows the schematic diagram of how the parallel plate sensor measures granular material properties. The measurement approach behind the parallel plate sensor is that when potential ($\hat{V}$) is applied between two plates of the sensor, an electric field is created between these two plates. When a granular material under test is placed under the electric field, an AC current ($\hat{i}$) passes through the material under test. The magnitude of the current ($\hat{i}$) depends on dielectric properties of the material. By measuring the output potential and current in the frequency domain, the measurement system can eventually estimate the material's dielectric properties.

The measurement system discussed in this dissertation consists of two parts, a dielectric spectroscopy meter and the multi-electrode concentric parallel plate dielectric sensor. The individual stages of the measurement circuit influences the measurement system's accuracy in

dielectric material property measurement. Therefore, an adequate methodology to calibrate the measurement circuit of the system is imperative.

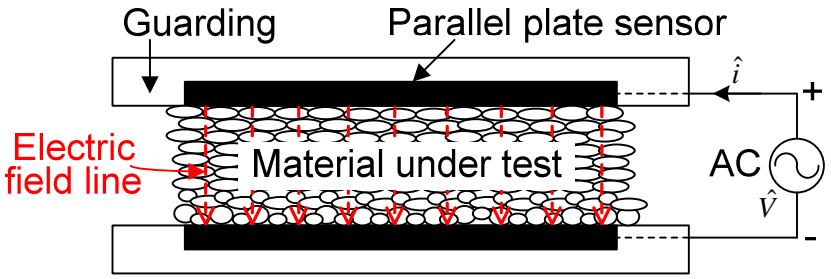

Figure 3-1. *Schematic diagram showing material property measurement using the parallel plate sensor.*

In general, there are two methods to calibrate a material property measurement system. The first method involves calibrating the whole measurement system. By using this method, investigators can use reference materials of known material properties that are close to those of a material under test to establish the system's calibration curves [37, 38, 95] by quantitative data mapping between the known material properties and the electrical measurements. This calibration method is only convenient for the same meter and sensor. Different sensors combined with the same meter require different calibration curves for data interpretation. The second method involves calibrating the individual stages of the measurement circuit, thus calibrating meters [40, 41] and sensors [38, 39] independently.

This dissertation presents the systematic iterative calibration methodology to calibrate the individual stages of the measurement circuit, in order to improve the measurement system's accuracy in granular material property measurement. Additionally, this dissertation uses the fully calibrated measurement system to investigate dielectric signatures of granular materials in the frequency domain.

3.2 Multi-Electrode Concentric Parallel Plate Sensor Design

Figure 3-2 shows the multi-electrode concentric parallel plate sensor and the sensor fixture. The sensor's two parallel plates are mounted inside the sensor fixture. The material under test is placed between two plates of the parallel plate sensor. One of the plates acts as a driving

electrode and the other one acts as the sensing electrode. The plate consists of one square electrode (center electrode) surrounded by three ring electrodes with different sizes. The ring electrodes can be used as guarding shield electrodes, and for measuring material samples with different quantities. Smaller quantities of materials require sample to be suspended or supported in the center of the sensor fixture. By varying electrical assignments of different ring electrodes on the sensing plate, the multi-electrode concentric parallel plate sensor can be used to determine the material compositions, uniformity, and the packing density. A tri-state DIP switch array on the backside of the sensor fixture is designed to be able to select different electrodes for driving, sensing, and guarding. Available areas for both driving and sensing electrodes are 25 cm^2, 47 cm^2, 81 cm^2, and 121 cm^2. The designed electrode spacing between two plates of the parallel plate sensor is 3 cm.

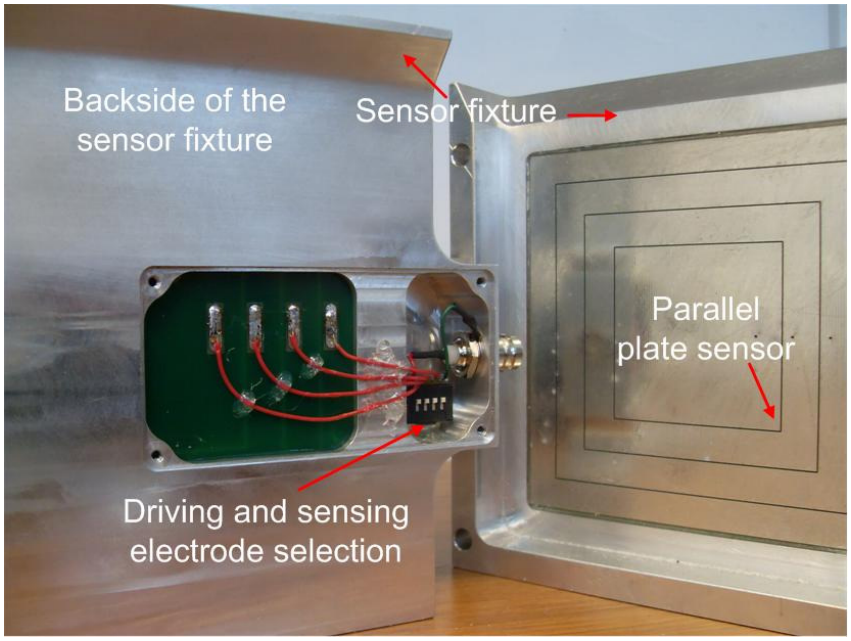

Figure 3-2. *Snapshot of the parallel plate sensor and its fixture.*

To precisely measure the dielectric properties of granular materials, the guarding design on the parallel plate sensor is necessary. Figure 3-1 shows the schematic diagram. The guarding enclosure surrounding the entire plates of the parallel plate sensor improves the linearity of the electric field and minimized EMF interference, which ensures the parallel plate sensor can accurately measure material properties of the material under test. The guarding surface which faces the material under test is in-plane with the surface of the plate of the parallel plate sensor.

The parallel plate sensor electrodes (plates) are electrically isolated by a thin insulating layer. The internal surfaces of the parallel plate fixture are smoothed out where necessary for more uniform stacking and easy removing of sample granules. The granular material rests close to the edge of the plate of the parallel plate sensor and induces high uncertainty in quantitative dielectric property measurement.

3.3 Measurement System

Figure 3-3 shows the dielectric property measurement system, consisting of the dielectric spectroscopy meter (DS-1, Illionix), the multi-electrode concentric parallel plate sensor, and the sensor fixture.

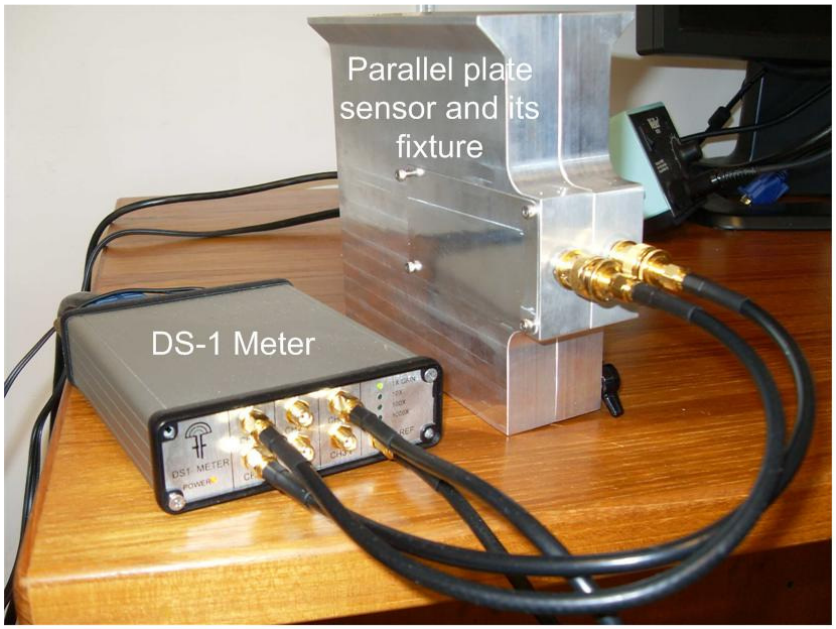

Figure 3-3. *The material property measurement system which consists of the dielectric spectroscopy meter (left) as well as the parallel plate sensor and its fixture (right).*

Figure 3-4 shows the top view of the circuit board of the dielectric spectroscopy meter (DS-1). The dielectric spectroscopy meter (DS-1) from Illionix, LLC has three isolated channels for simultaneous measurement. Figure 3-5 shows that each channel consists of an ultra-low bias operational amplifier, four reference capacitors (1 pF, 10 pF, 100 pF, and 1,000 pF), and one reference resistor (1 GΩ). For each channel, the four reference capacitors (also called gain

setting capacitors) were designed to target different sensor capacitances (0.1 pF to 0.1 µF) which can then be converted to the dielectric properties of the material under test. The meter's accuracy in sensor capacitance measurement is less than ± 1.0 %.

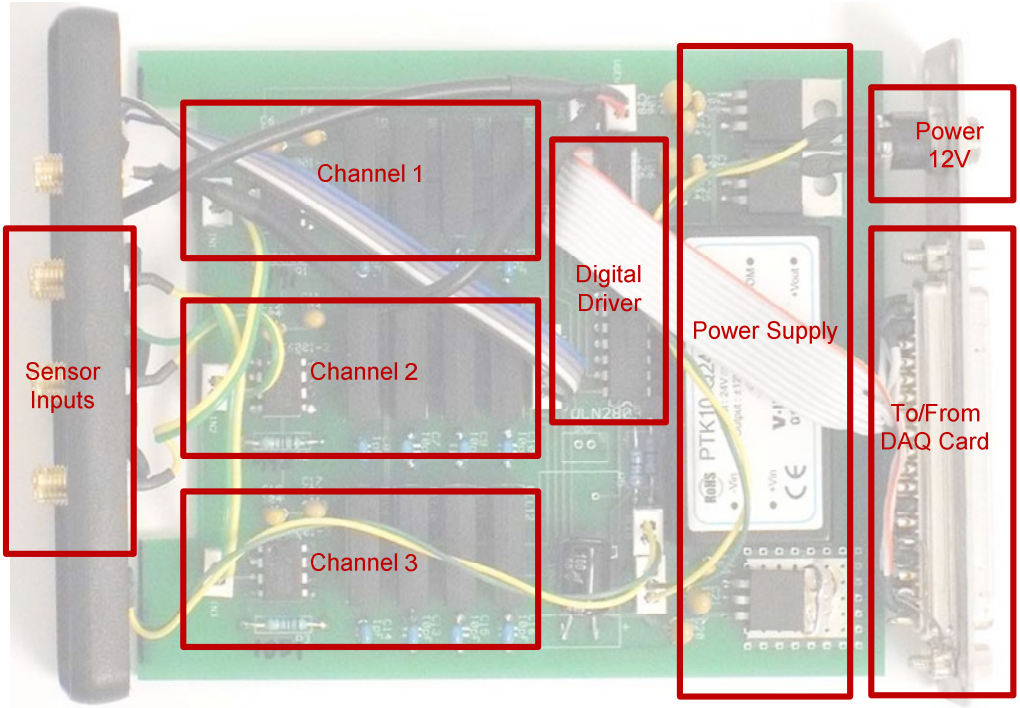

Figure 3-4. *Schematic Top view of the dielectric spectroscopy meter circuit board (not to scale).*

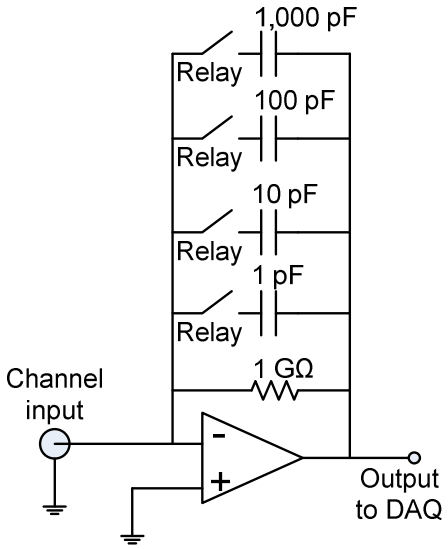

Figure 3-5. *Schematic diagram of one of the DS-1 channels with four default reference capacitors and one default reference resistor.*

3.4 Calibration Methodology for the Measurement System

The systematic iterative calibration process consists of two parts. The first part is the dielectric spectroscopy meter's circuit calibration, which involves calibrating the corresponding reference capacitance and reference resistance. The corresponding reference capacitance is the circuit capacitance between a channel input and a channel output. The corresponding reference resistance is the circuit resistance between a channel's input and output terminals. The reference capacitance and reference resistance are used to represent the corresponding reference capacitance and resistance for the rest of the investigation. The second part is the parallel plate sensor calibration, which involves compensating for mechanical defects due to sensor manufacturing and assembly, and for any fringing in the electric field inside the sensor fixture. Detailed calibration methodology is discussed in the following.

3.4.1 Circuit Calibration of the Dielectric Spectroscopy Meter

3.4.1.1 Calibration Process

The primary purpose of the circuit calibration of the dielectric spectroscopy meter is to ensure that the meter measures correct capacitance and resistance at the meter's output and input terminals. We focus on calibrating the reference capacitances and reference resistance in the feedback loop of the DS-1 meter circuit. According to the measurement approach behind the measurement system (Section 2.1.4 and Section 2.1.5), the reference capacitance and resistance of the meter circuit determine how precisely the meter measures capacitance and resistance at the meter's input and output terminals. Therefore, obtaining the reference capacitance and resistance of the meter circuit is an important way of improving the meter's measurement accuracy.

We present two calibration processes (Figure 3-6 (a) and (b)) to calibrate the meter's measurement circuit. The calibration processes use several nominal capacitors and resistors for the circuit calibration. The tolerance of the nominal capacitance value of the selected nominal capacitor should be less than ± 5.0%, and so does the nominal resistance value of the selected nominal resistor. In principle, one can achieve a better meter circuit calibration result if a larger number of nominal capacitors and resistors are used for the iterative circuit calibration processes.

In this investigation, we used ten nominal capacitors (10 pF) and resistors (1 GΩ) for the calibration.

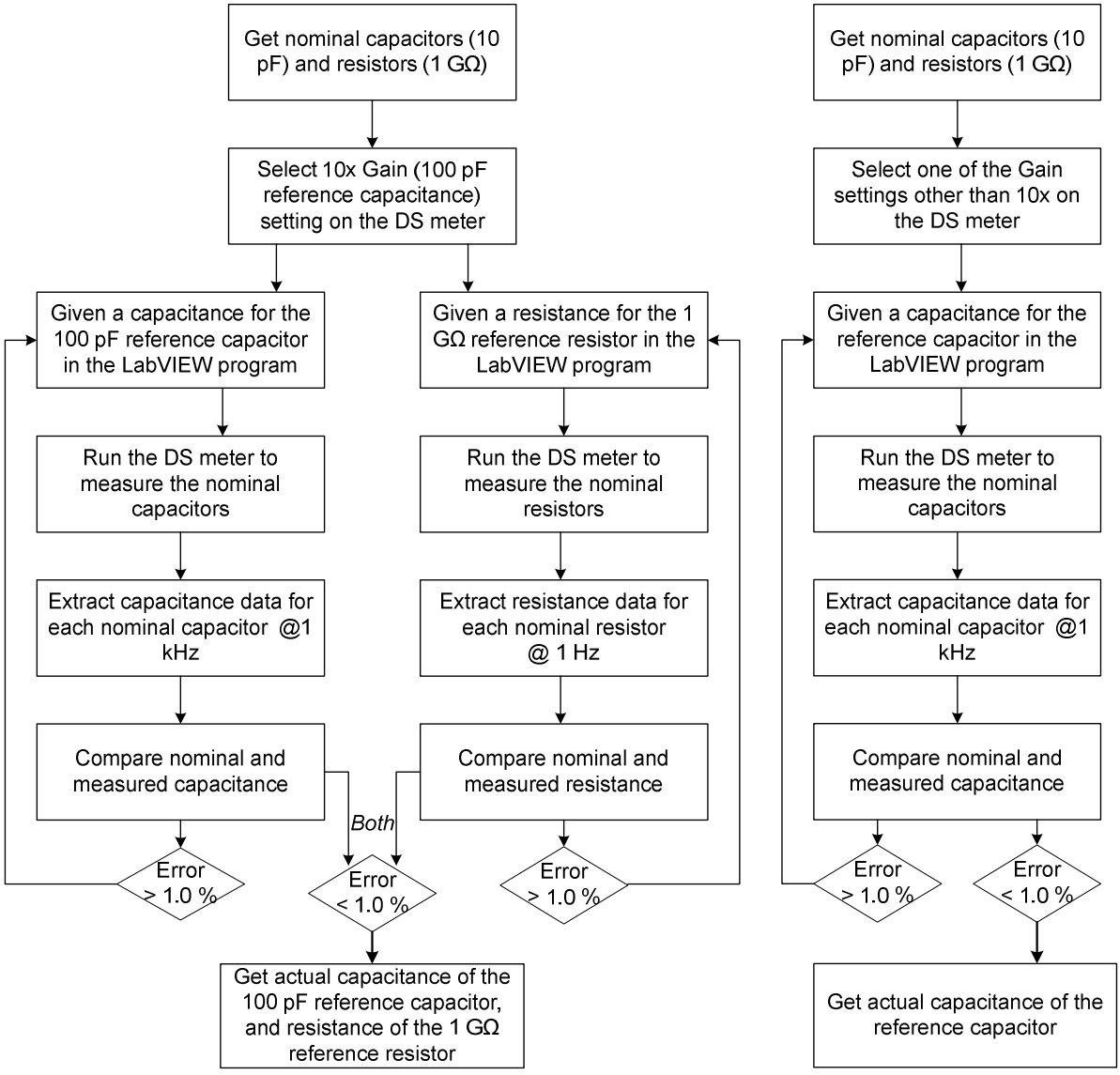

(a) Calibration procedures for 100 pF reference capacitor, 1G Ohm reference resistor, and the associated circuit

(b) Calibration procedures for 1 pF, 10 pF, and 1,000 pF reference capacitors and associated circuits

Figure 3-6. *Circuit calibration processes. The tolerance of the selected 10 pF capacitor should be less than ± 5.0%.*

Figure 3-6 (a) shows that the first circuit calibration process is to simultaneously calibrate the DS-1 measurement channel, which consists of the 100 pF reference capacitor, the 1 GΩ

resistor, and the associated circuit impedance between the channel's input and output terminals. . The capacitance of the measurement circuit is calibrated at 1 kHz (standard capacitance measurement frequency), and the resistance of the measurement circuit is calibrated at one Hz. The main point behind this circuit calibration process is to ensure that deviations between the average value of ten nominal capacitors (from the selected nominal capacitors) and the measured average capacitances of the same nominal capacitors are within defined 1.0%. Similarly, deviations between nominal resistances (from selected nominal resistors) and the measured average resistance for the same nominal resistors should be less than defined 1.0% as well. The reference resistance of the channel's measurement circuit is only calibrated in the first calibration process, because the measurement circuit regarding the reference resistor remains the same for other channels of the meter.

The second circuit calibration process shown in Figure 3-6 (b) is to calibrate the rest of the DS-1 measurement channels with different reference capacitors. In this calibration process, the only requirement is to ensure that deviations between the average values of ten nominal capacitors (from the selected nominal capacitors) and the measured average capacitances of the same nominal capacitors are also within defined 1.0%.

3.4.1.2 Capacitor and Resistor Calibrator

Figure 3-7 shows the schematic diagram of the capacitance calibrator circuit. We design this calibrator based on the presented calibration processes shown in Figure 3-6 to calibrate reference capacitances of the dielectric spectroscopy meter. This calibrator communicates with the NI-6154 DAQ card and the control logic through a LabVIEW VI. The LabVIEW VI sends a binary message to the control logic through the DAQ card, and the control logic converts the message to trigger one of ten relays. Once a relay is triggered, the LabVIEW VI outputs a 1 kHz AC voltage to the 10 pF capacitor through one of the analog output channels on the DAQ card. The current passing through the 10 pF capacitor then passes through the reference capacitor and resistor and one of the reference capacitors of the dielectric spectroscopy meter. The meter then outputs a different 1 kHz AC voltage to the LabVIEW VI through one of the analog input channels on the DAQ card. Once all the ten relays are triggered in sequence, the average capacitance of the ten nominal 10 pF capacitors in the capacitance calibrator can be calculated and averaged. To

calibrate the reference resistance of the dielectric spectroscopy meter, we replace ten 10 pF capacitors with ten 1 GΩ resistors. The same LabVIEW VI is also applicable to reference resistance calibration except for that the AC driving frequency is switched to one Hz.

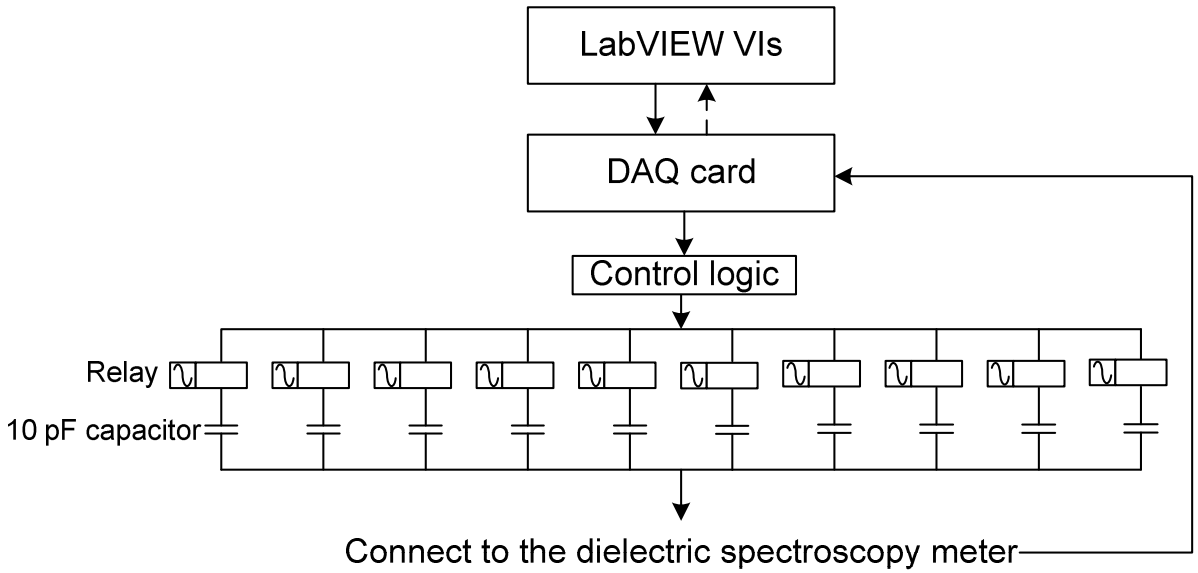

Figure 3-7. *Schematic diagram showing the capacitance calibrator circuit. This calibration circuit is also applicable to calibrate reference resistance of the dielectric spectroscopy meter by replacing ten 10 pF nominal capacitors with ten 1 GΩ nominal resistors.*

3.4.1.3 Measurement Results Using the Calibrated Meter

Figure 3-8 shows the air's relative dielectric permittivity obtained by using the non-calibrated dielectric spectroscopy meter and the non-calibrated parallel plate sensor. Theoretically, the air's relative dielectric permittivity is one in the frequency range from 10 Hz to 100 kHz. However, at 1 kHz frequency, the calculated relative dielectric permittivity of the air is actually lower than one. Deviations on the air's relative dielectric permittivity measurement are above 30% in the non-calibration mode. To improve the dielectric property measurement accuracy, calibration on the dielectric spectroscopy meter's circuit is necessary.

To follow the calibration processes shown in Figure 3-6, we used ten 10 pF nominal capacitors and ten 1GΩ nominal resistors to calibrate reference capacitances and reference resistance of the dielectric spectroscopy meter. Table 3.1 shows the comparisons between the nominal capacitances and resistance and the calibrated values. The reference capacitance is

calibrated at 1 kHz and the reference resistance is calibrated at one Hz. The deviations between the nominal values and the calibrated values are likely due to: (1) the tolerance of the nominal values of the selected capacitors and resistors, and (2) the parasitic contribution of the associated measurement circuit, i.e., capacitance between the component leads, the PCB traces, and the op-amp input to output capacitance. The deviation is more noticeable for such smaller capacitors as the 1 pF capacitor. error is higher for smaller reference capacitors because there is parasitic capacitance between the measurement circuit input and output. For example, 0.78 pF parasitic capacitance for the 1 pF and 10 pF reference capacitors is a reasonable value due to parasitic capacitance between traces and leads of the components and capacitance in the op-amp itself.

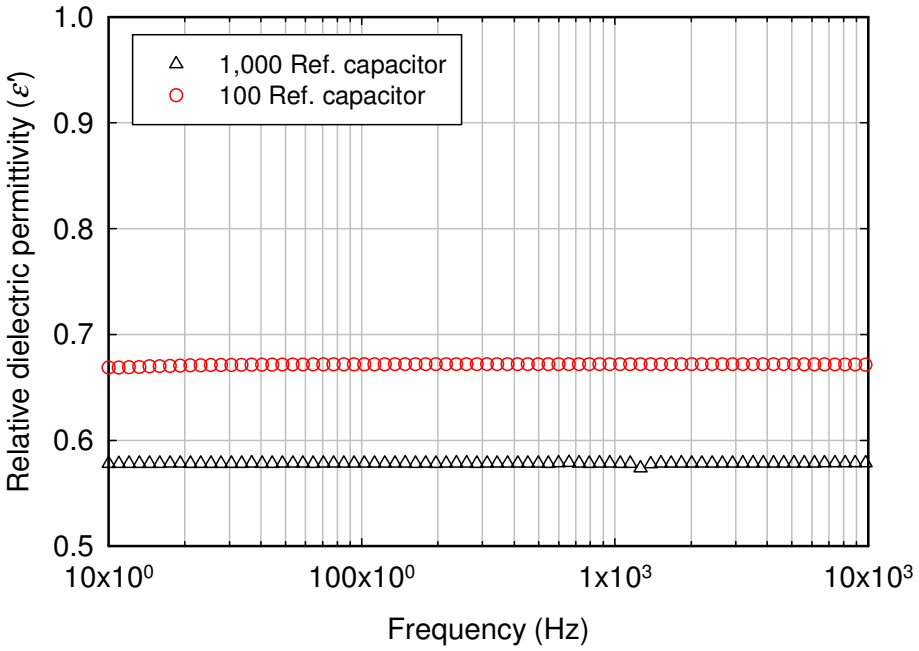

Figure 3-8. *Relative dielectric permittivity of the air measured by using the parallel plate sensor and the non-calibrated dielectric spectroscopy meter.*

Table 3.1. *Summary of calibrated values of four reference capacitors, one reference resistor, and associated circuit in the dielectric spectroscopy meter*

	Reference capacitance*(pF)				Reference resistance**(GΩ)
Nominal	1	10	100	1,000	1.0000
Calibrated	1.7818	10.74	99.6	1,009.8	1. 0083

*: measured at 1 kHz.
**: measured at one Hz.

Figure 3-9 shows measured capacitances of the ten 10 pF nominal capacitors after the meter was calibrated. At frequencies around 1 kHz, measured capacitance of the ten 10 pF nominal capacitors is fairly flat with errors within ± 0.5%; this indicates that the reference capacitors and the reference resistor were well calibrated. At low frequency, the current in the measurement circuit is primarily resistive because capacitance impedance drops at low frequency. Capacitance measurement error is higher at low frequencies because capacitance influence on the resulting AC voltage waveform is minimal.

Figure 3-10 shows air capacitance measurement results using the circuit-calibrated dielectric spectroscopy meter. A parallel plate sensor was connected to the first channel of the dielectric spectroscopy meter. Settings for the dielectric spectroscopy meter and the parallel plate sensor are listed in Table 3.2.

Figure 3-11 shows the relative dielectric permittivity of the air obtained by using the circuit-calibrated dielectric spectroscopy meter and the non-calibrated parallel plate sensor. The deviation between theoretical and measured relative dielectric permittivity of the air is significantly reduced to 6.73%. If we choose the central square electrode (5 cm × 5 cm) as the sensing electrode, the deviation between the theoretical and the measured relative dielectric permittivity of the air is significantly reduced to be less than 0.10% at frequencies less than 10 kHz. In reality, for fixed electrode spacing between two plates of the parallel plate sensor, measured relative dielectric permittivity of the air is always equal to one at frequencies from 10 Hz to 100 kHz, and should be independent of the sensing electrode area of the sensor The dependence of the deviation in measurement of relative dielectric permittivity of the air and the sensing electrode area selection is primarily due to the fringing field in the electric field inside the sensor fixture, and in part due to the non-uniform distance between two plates of the parallel plate sensor. This issue is discussed in Section 3.4.2.

Figure 3-12 shows the analysis of how variations in reference capacitance of the measurement circuit affect the meter's capacitance and resistance measurements. The relationships are linear for both capacitance and resistance measurement. Resistance measurement is more sensitive to the variation in reference capacitance of the measurement circuit.

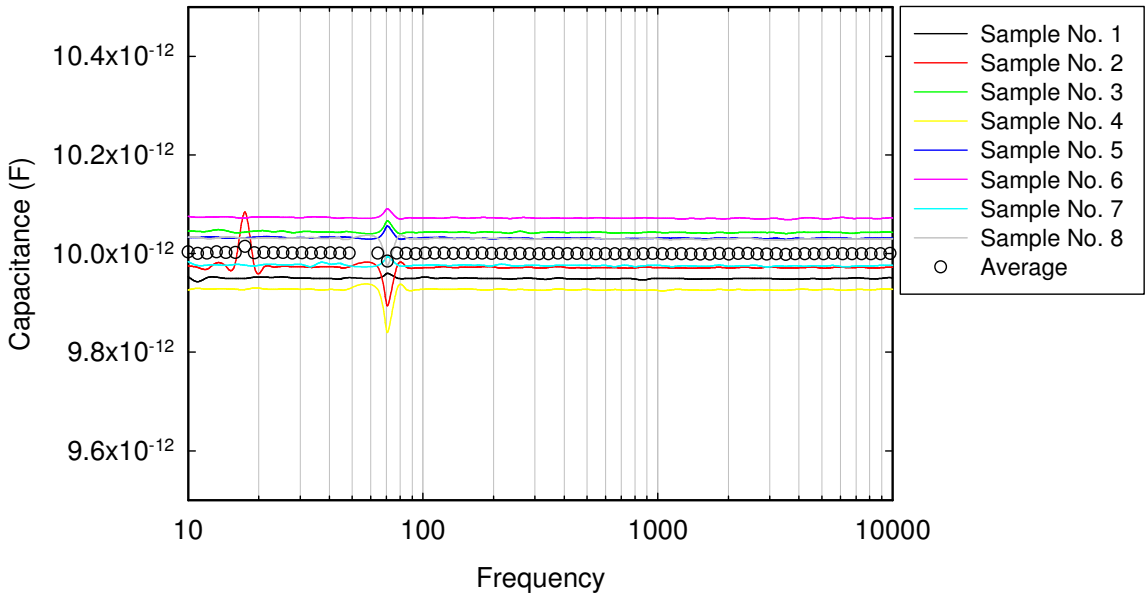

(a) 1000 pF reference capacitor

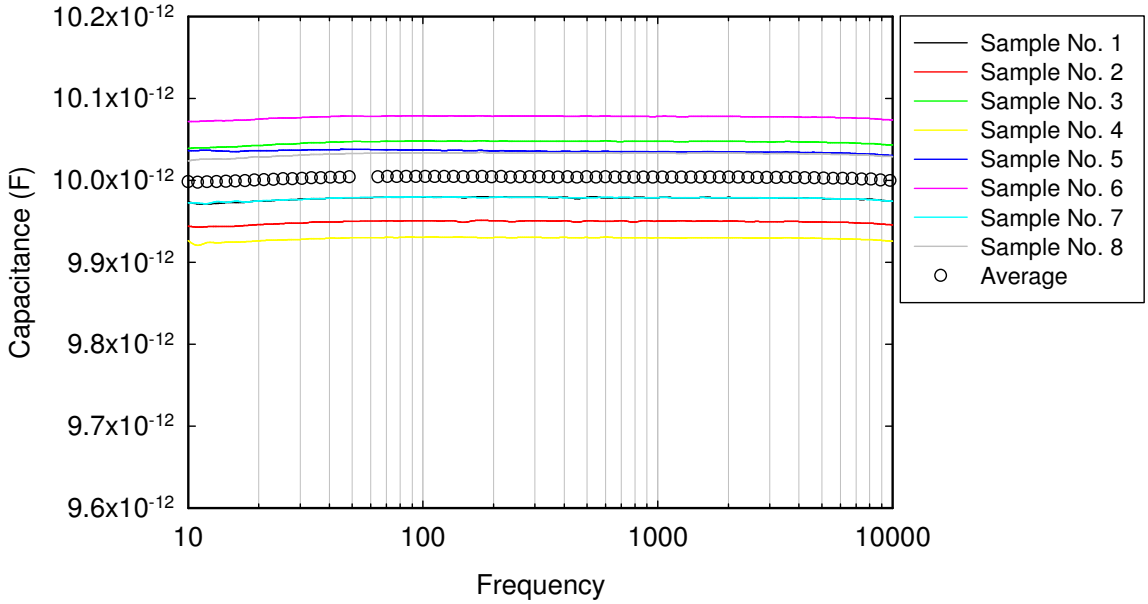

(b) 100 pF reference capacitor

Figure 3-9. *Capacitance obtained by using the circuit-calibrated dielectric spectroscopy meter. The 100 pF reference capacitor was selected for measurement.*

The calibration processes were also used to calibrate fifty single-channel dielectric spectroscopy meters for high voltage multi-channel applications [96]. After completing the calibration for the fifty single-channel dielectric spectroscopy meters, we used a ± 5% 100 pF nominal capacitor to test the accuracy these meters achieve. The average capacitance of the 100 pF capacitor measured by these fifty meters is 97.75 pF, and the measurement error (defined as a

deviation between a nominal capacitance and a measured capacitance) was ± 0.5%. The capacitance measurement uncertainty [97] is within ± 0.33%.

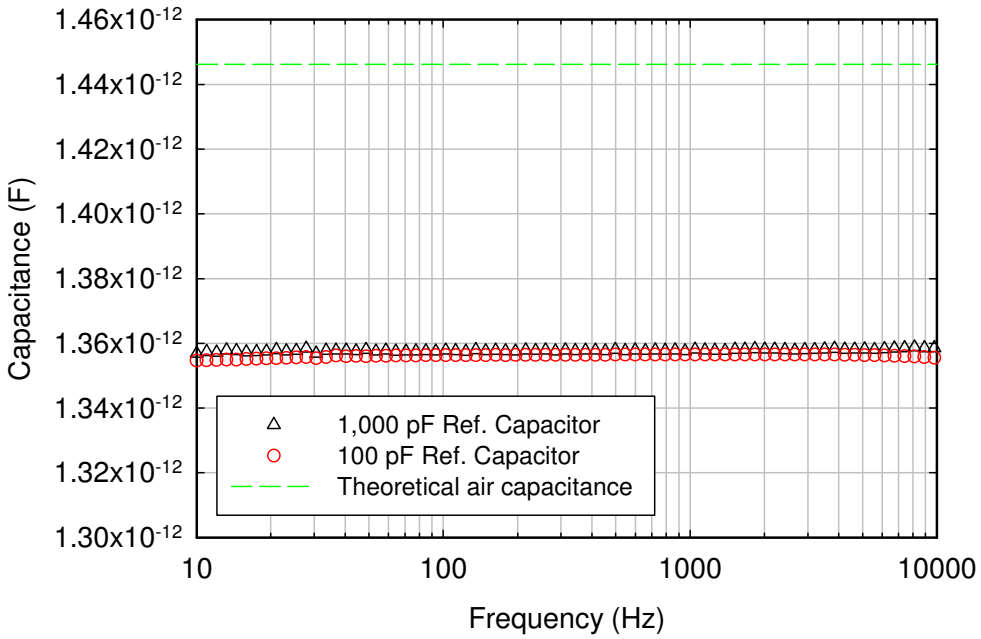

Figure 3-10. *Measured sensor capacitance of the air using the circuit-calibrated dielectric spectroscopy meter.*

Table 3.2. *Settings for the Dielectric spectroscopy meter and the parallel plate sensor.*

Dielectric spectroscopy meter	Parallel plate sensor
Amplitude: 10 V	Driving electrode: 4 rings selected
Start frequency: 10 Hz	Sensing electrode: 2 rings selected
Stop frequency: 100k Hz	Sensing electrode size: 7 cm × 7 cm
Integration time: 10.0 s	Spacing between two electrodes: 3 cm

At one Hz measurement frequency, the sensor conductance of the air obtained by using the circuit-calibrated dielectric spectroscopy meter with the 100 pF reference capacitor selected and the non-calibrated parallel plate sensor is 6.13×10^{-14} S. According to the sensing electrode area and the distance between two plates of the parallel plate sensor, sensor conductance of the air at sea level for low aerosol concentration is 4.82×10^{-16} S [98]. Although the measurement circuit of the dielectric spectroscopy meter has been calibrated, sensor conductance of the air measured is still higher than the normal value. The impedance of a capacitor is $1/\omega C$, and the impedance of a resistor is R. At one Hz measurement frequency, the measured sensor capacitance of the air is

1.44 pF, and the corresponding real part of the impedance is 1,100 GΩ. At the same measurement frequency, the measured real part of the impedance of the air is 0.6 GΩ. Noticeably, the uncertainty in measuring the current passing through the resistor is so high that the current cannot be measured precisely. This is because that most contributing factor in measuring high values of impedance is non-idealities and non-zero noise levels in the measurement circuits.

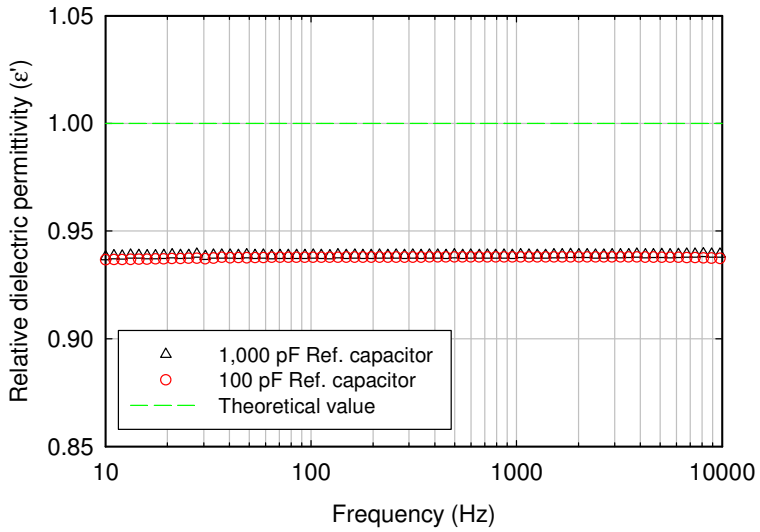

Figure 3-11. *Relative dielectric permittivity of the air obtained by using the circuit-calibrated dielectric spectroscopy meter and the non-calibrated parallel plate sensor.*

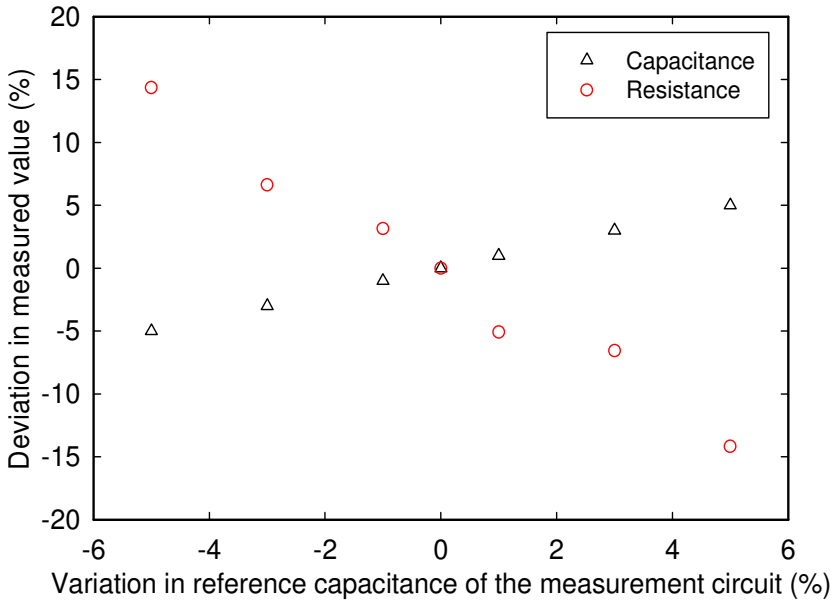

Figure 3-12. *Effect of variations in reference capacitance of the measurement circuit on deviations in capacitance and resistance measurements.*

3.4.2 Parallel Plate Sensor Calibration and Result

3.4.2.1 Calibration Process

Although we have successfully calibrated the measurement circuit of the dielectric spectroscopy meter to ensure that the meter can measure precise capacitance and resistance, Figure 3-11 indicates that measurement deviations are still there. Therefore, we developed the parallel plate sensor calibration process to compensate for the non-uniform electrode spacing between two plates of the parallel plate sensor due to assembly and manufacturing, and any fringing in the electric field inside the sensor fixture. We also use air to calibrate the parallel plate sensor.

Figure 3-13 shows the recommended parallel plate sensor calibration procedure. The first two steps are to connect the parallel plate sensor to one of the channels of the dielectric spectroscopy meter, followed by selecting and running the calibration part of a LabVIEW program. During the calibration, both calculated and theoretical relative dielectric permittivity of the air (Eq. (3.27)) is simultaneously recorded. The data at 1 kHz driving frequency are, then, extracted to estimate the actual average electrode spacing between two plates of the parallel plate sensor.

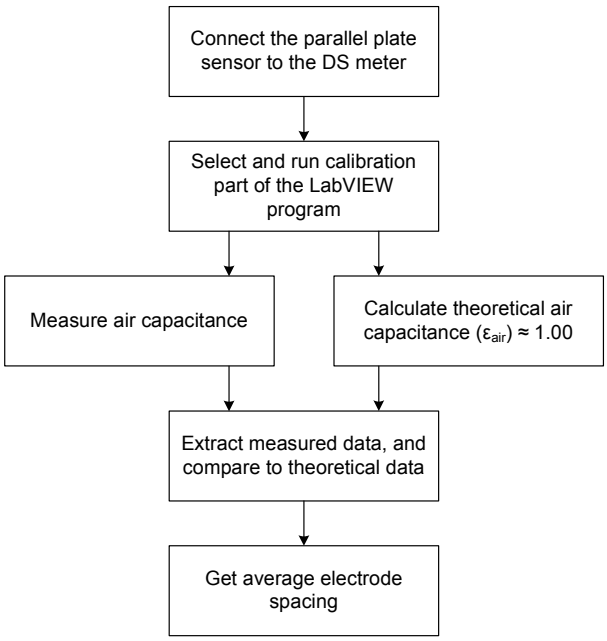

Figure 3-13. *Parallel plate sensor calibration procedures.*

3.4.2.2 Real Part of Relative Dielectric Permittivity of the Air

Theoretically, for a parallel plate sensor, air capacitance (C_{air}) between two plates of the parallel plate sensor (Eq. (3.25)) is

$$C_{air} = \frac{\varepsilon_0 \times \varepsilon_{air} \times A_s}{d} = \frac{\varepsilon_0 \times A_s}{d} \tag{3.47}$$

where ε_0 is vacuum dielectric permittivity, ε_{air} is relative dielectric permittivity of air, A_s is the sensing area of the parallel plate, and d is the electrode spacing between two parallel plates. Since relative dielectric permittivity of air (ε_{air}) is one, the capacitance measurement result is a function of the parallel plate sensor geometry (A_s/d). Furthermore, if the sensor geometry is also fixed, the capacitance measurement result is a constant value.

3.4.2.3 Parallel Plate Sensor Calibration Result

Equation (3.47) shows that the product of sensor capacitance of the air (C_{air}) and the electrode spacing (d) between two plates of the parallel plate sensor for a fixed sensing electrode area (A_s) is a fixed value. According to the parallel plate sensor setting (Table 3.2), the effective average electrode spacing (d_{eff}) between two plates of the parallel plate sensor is

$$d_{eff} = \frac{C_t}{C_m} \times d_t \tag{3.48}$$

where C_t is the theoretical sensor capacitance of the air, C_m is the measured sensor capacitance of the air, and d_t is the designed electrode spacing (3 cm). The theoretical sensor capacitance of the air, C_t, is 1.45 pF according to Table 3.2.

Table 3.3 shows the calibrated effective average electrode spacing (d_{eff}) between two plates of the parallel plate sensor for different sensing electrode areas. According to Eq. (3.48), the C_t/C_m ratio should be independent of the selected sensing area on the sensing plate of the parallel plate sensor. However, as shown in Table 3.3, as a larger sensing area on the sensor's sensing

plate is used for measurement, the deviation between the actual average electrode spacing and the d_{eff} becomes larger, which in some cases, is already beyond the physical electrode spacing in the sensor fixture where the parallel plate sensor is mounted. We measured the actual spacing between two electrodes with a micrometer at multiple points along the electrodes. The deviation in measured and designed average electrode spacing between two plates of the parallel plate sensor is approximately 3%; therefore, the non-uniform electrode spacing between two plates of the parallel plate sensor is not the major reason resulting in a higher than expected deviation in the sensor capacitance measurement.

To discuss the effect of fringing in the electric field inside the sensor fixture, we used Ansoft Maxwell software to simulate a 2D electric field line distribution between two plates of the parallel plate sensor mounted in the sensor fixture. The parallel plate sensor geometry is shown in Table 3.2. Figure 3-14 shows the simulation results. Fringing appears between the sensor fixture and the outer most part of the driving electrode close to the sensor fixture (right hand side in Figure 3-14), while the electric field lines close to the central part (left hand side in Figure 3-14) of the sensing area is approximately perpendicular to the electrode surface. When a larger sensing area (i.e., 121cm^2) is used, most of the electric field lines passing through the material under test will reach the sensor fixture instead of the outer most part of the sensing area close to the sensor fixture. Therefore, the simulation results demonstrate that the fringing inside the sensor fixture is the primary reason resulting in larger deviations in the sensor capacitance measurement for a larger sensing area.

Table 3.3. *Calibrated sensing electrode spacing between two plates of the parallel plate sensor.*

Sensing area (cm^2)	25	49	81	121
d_{eff} (cm)	3.01	3.20	3.45	4.00
Deviation in d_{eff} (%)*	0.33	6.67	15	33
Deviation in capacitance measurement (%)*	0.08	-6.14	-14.15	-26.46

*: experimental data

To compensate for the fringing effect on the parallel plate sensor and the non-uniform distance between two plates of the parallel plate sensor, we suggest that the ratio d_{eff}/d_t is a correction factor to eliminate the dependence of the deviation in relative dielectric permittivity of the air and the selected sensing area. According to the experiments, d_{eff}/d_t is independent of the

measurement frequency. The product of the correction factor and the designed electrode spacing of 3 cm are defined as the average virtual electrode spacing.

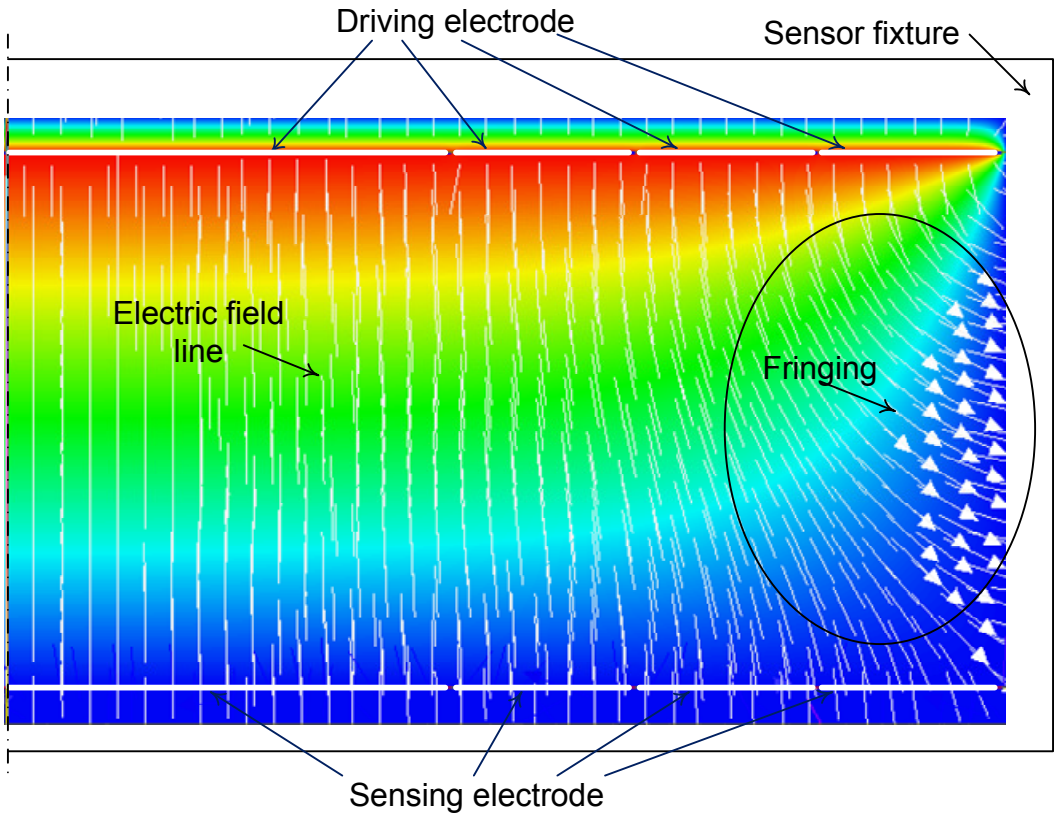

Figure 3-14. *Parallel plate sensor simulation results. The effective average electrode spacing between the driving electrode and the sensing electrode is 3 cm.*

Figure 3-15 shows the sensor capacitance of the air obtained by using the fully calibrated dielectric measurement system, including the circuit-calibrated meter and the average virtual electrode spacing-calibrated parallel plate sensor. The parallel plate sensor's sensing area is 49 cm^2. The sensor capacitance of the air is between 1.448 pF and 1.445 pF for two reference capacitors selected. Figure 3-16 shows the corresponding relative dielectric permittivity of the air according to data shown in Figure 3-15. The deviation in the measurement of the relative dielectric permittivity of the air is now significantly further reduced to less than 0.5% on different days with temperature and humidity changes.

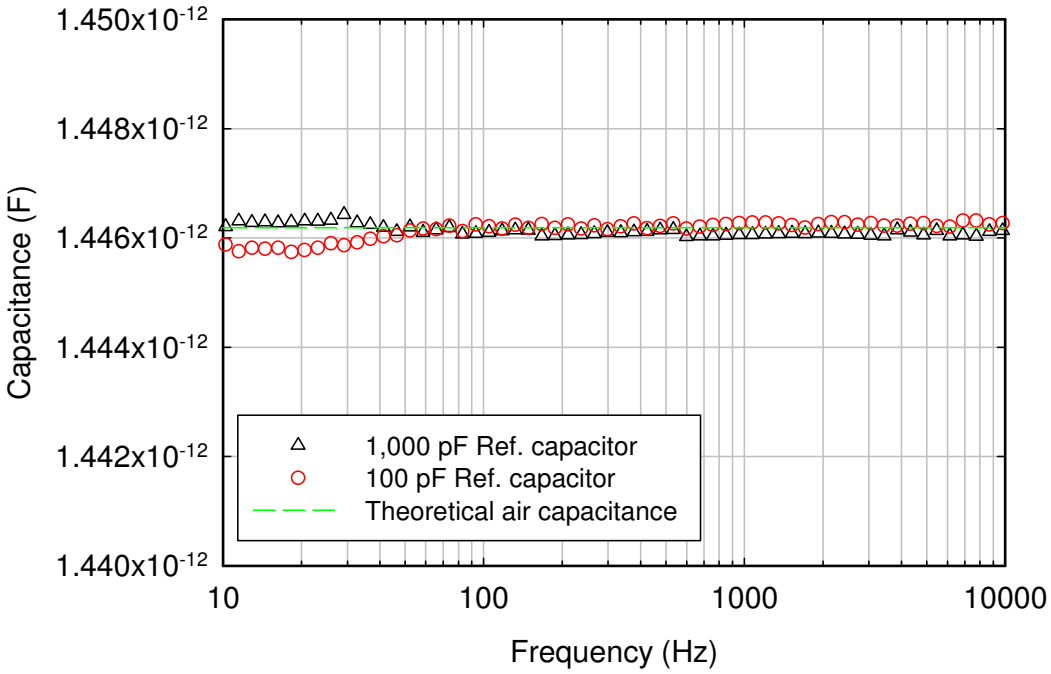

Figure 3-15. *Sensor capacitance of the air obtained by using the circuit-calibrated dielectric spectroscopy meter and the average virtual electrode spacing-calibrated parallel plate sensor.*

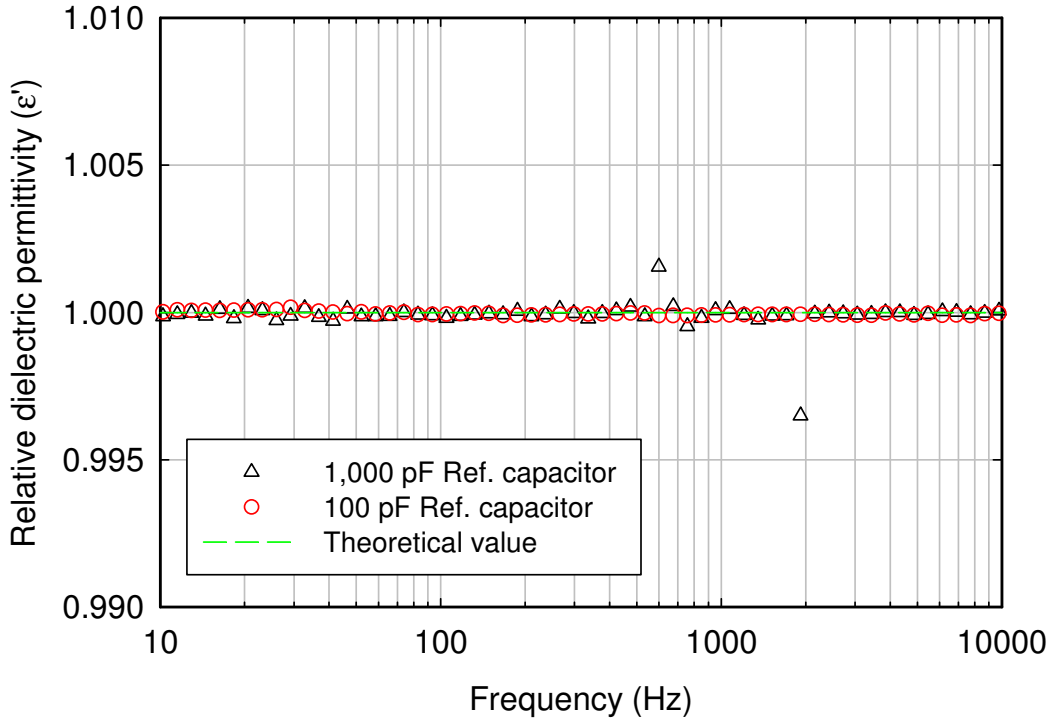

Figure 3-16. *Relative dielectric permittivity of the air obtained by using the fully calibrated dielectric measurement system.*

3.5 Granular Material Property Measurement

Explosive materials are composed of different discrete solids and macroscopic particles, such as plasticizers and binders. The same combination of compositions, but with a different granulation profile (e.g., moisture content, packing density) would result in different dielectric material properties. The dielectric properties are a function of many variables, but at least to our understanding, are only loosely related to the chemical composition of the material under test. This information is currently unavailable in research literature. Therefore, it is important and necessary to investigate the dielectric material property spectrum of common explosive materials.

Measurement systems operated in microwave ranges (300 MHz to 300 GHz) have been used to measure granular materials' relative dielectric permittivity [99-101]. Common measurement methods are: the perturbation method using a cavity, the dielectric rod resonance method, and the s-parameter method [99]. Regardless of the measurement methods, the measurement principle behind the measurement systems is that the system needs a microwave frequency or a light source (i.e., laser pulse) projected onto the granular materials, and detectors to receive a reflected or scattered microwave signal, or light for post data processing. The optical accessories limit the measurement systems' flexibility and applications for on-site detection and identification of granular materials [102].

Unlike the optics and microwave-based material property measurement systems mentioned above, we use the circuit-calibrated dielectric spectroscopy meter and the average virtual electrode spacing-calibrated parallel plate sensor, which allows the electric field to penetrate through a material for accurate, non-destructive measurement. This method largely simplifies the measurement system.

Figure 3-17 shows the real part of the complex dielectric permittivity of explosives obtained by using the fully calibrated measurement system in the frequency domain of 10 Hz to 70 kHz. We did not control for granulation size or form. For example, Composition B is composed of big chunks and the Semtex and C4 are putty-like materials. The red dot, detagel and dyno are ammonium nitrate-based materials that are gelled and formed into sticks that do not pack well into the fixture. We classify these explosives into three groups according to their relative dielectric permittivity and will subsequently draw conclusions based on the similarity or non-similarity of the chemical compositions.

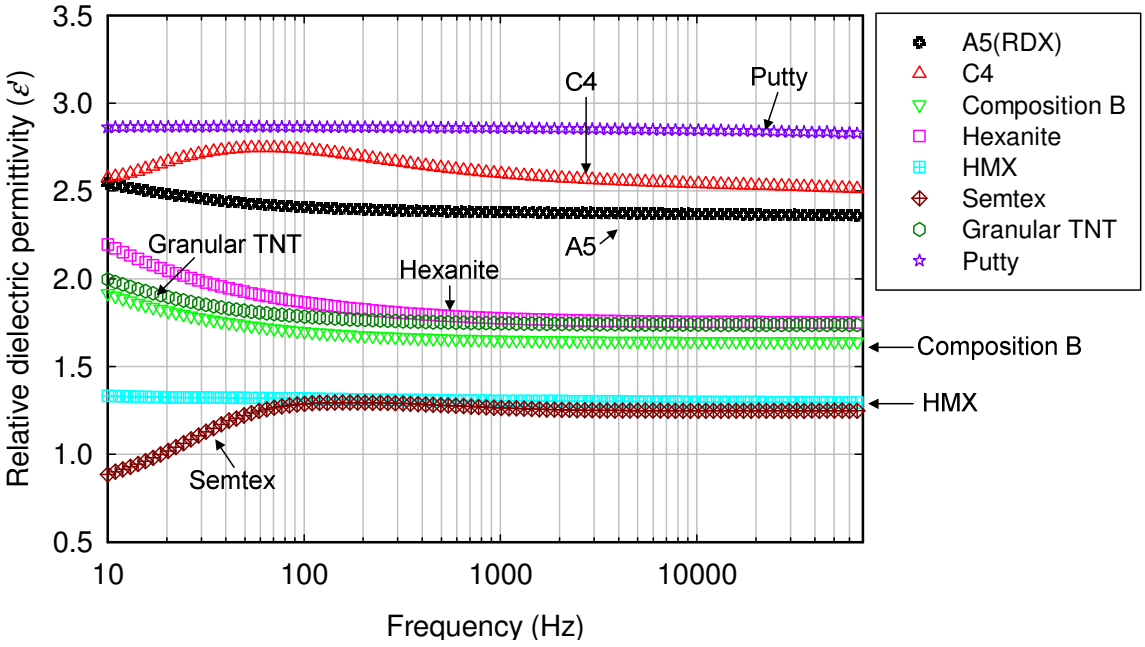

(a) Materials with relative dielectric permittivity less than 10

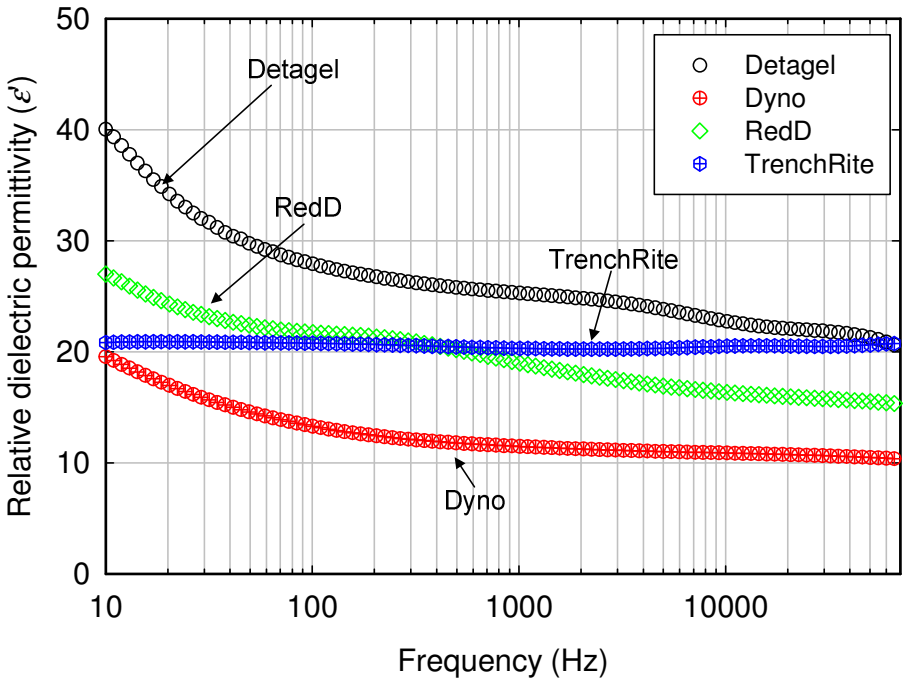

(b) Materials with relative dielectric permittivity higher than 10

Figure 3-17. *Relative dielectric permittivity measurement of explosives obtained by using the fully calibrated dielectric measurement system. All data are average values from six tests.*

The first group is Semtex[1] and HMX[2]. The measured real part of the complex dielectric permittivity of Semtex and HMX is between 1.00 and 1.50. These two materials are not distinguishable at frequencies between 60 Hz and 1 kHz. It is interesting that Semtex and HMX, both of which are chemically related to RDX and C4, evince significantly different dielectric properties. This could be because the sample of semtext was relatively small and did not fill the text fixture volume. The second group is granular TNT[3], Hexanite [4], and Composition B[5]. The measured real part of the complex dielectric permittivity of granular TNT, Hexanite, and Composition B is between 1.75 and 2.25. CompB has the lowest real part of complex dielectric permittivity at all frequencies in this group and can be distinguished from granular TNT and Hexanite at all frequencies. There compounds are the TNT group and cluster. The real part of the complex dielectric permittivity difference between granular TNT and Hexanite is noticeable at frequencies less than 110 Hz. The third group is materials with relative dielectric permittivity between 2.25 and 3.00. These materials are malleable inert putty consisting of dimethyl siloxane silica and Thixatrol ST, C4[6], and RDX[7]. The measurement results show that these three materials are distinguishable in the investigated frequency domain. It is not surprising that A5 (also known as RDX) and C4 have close dielectric profiles; it is surprising that the inert putty is so similar.

Figure 3-17 (b) shows the measured real part of the complex dielectric permittivity of explosives (higher than 10) obtained by using the fully calibrated measurement system in the frequency domain from 10 Hz to 70 kHz. Noticeably, the results indicate that these materials are distinguishable at all frequencies except for some overlap regions. For example, trenchite and redD cannot be reliably distinguished at frequencies between 200 Hz and 400 Hz. Red dot, detagel, and dyno are commercial blasting gels available in sticks. The packing density of these sticks in the fixture was poor, which could result in large measurement errors.

---

[1] **Semtex** is a general-purpose plastic explosive containing RDX and PETN.

[2] **HMX** is a powerful and relatively insensitive nitroamine high explosive, also known as cyclotetramethylene-tetranitramine, tetrahexamine tetranitramine, or octahydro-1,3,5,7-tetranitro-1,3,5,7-tetrazocine, HMX is chemically related to RDX.

[3] **Trinitrotoluene** is a castable solid. The measurements taken here were of granular TNT with an unrecorded size distribution.

[4] **Hexanite** was a castable military explosive, now obselete, consisting of 60% TNT and 40% hexanitrodiphenylamine.

[5] **Composition B**, colloquially "comp B", is an explosive consisting of castable mixtures of RDX and TNT..

[6] **C4** is a plastic explosive consisting of a mixture of RDX and diethylhexyl or dioctyl sebacate

[7] **RDX** is a nitroamine explosive cyclotrimethylene trinitramine

3.6 Conclusion

The circuit calibration of the dielectric spectroscopy meter includes calibrating the meter's circuit impedance to ensure that the meter can precisely measure capacitance and resistance at the meter's output terminals. As the results shows, after completing the circuit calibration for the dielectric spectroscopy meter, the measurement deviation in the relative dielectric permittivity of the air is significantly reduced to 7% from 30% in the non-calibration mode, at 1 kHz.

The parallel plate sensor calibration compensates for the non-uniform electrode spacing between two plates of the parallel plate sensor due to the assembly and manufacturing and the fringing of the electric field in the sensor fixture. The parallel plate sensor calibration results show that the measurement deviation in the relative dielectric permittivity of the air is significantly reduced to 0.5% from 7% at frequencies from 1 Hz to 100 kHz. The simulation results demonstrate that the fringing inside the sensor fixture is the primary reason resulting in large deviations in the sensor capacitance measurement.

The granular material property's response in the frequency domain shows that the fully calibrated dielectric spectroscopy measurement system can be used to identify different classes of explosives, such as granular TNT, RDX, and Detagel.

Chapter 4 **Measurement of Multi-Layer Coating Thickness**

4.1 Motivation

Coatings applied to aircraft's body and parts are mainly used as a defense against corrosion, abrasion, and degradation caused by chemical contamination and UV radiation. Therefore, the in-process measurement of the individual coating layer thickness of a multi-layer coating stack-up on aircraft is imperative for both commercial and military aircraft. For commercial aircraft, precise coating thickness control not only reduces the amount of paint, but also reduces the total aircraft weight. For military aircraft, precise coating thickness not only reduces weight significantly, but also minimizes the reflected electromagnetic signature.

Signal processing plays a critical role in the fringing electric field (FEF) sensing measurement, especially for multiple-penetration depth sensing. Figure 4-1 shows the conceptual view of a multi-penetration depth fringing electric field sensor. One of the most attractive features of multi-penetration depth dielectrometry is the ability to measure (from one side) the complex spatially inhomogeneous distributions of properties. The types of spatial distributions includes, but are not limited to, homogeneous materials, multiple layer materials, local discontinuities (i.e., cracks and electrical trees), global discontinuities in microstructure (i.e., grains or fibers forming the material), and smoothly varying properties.

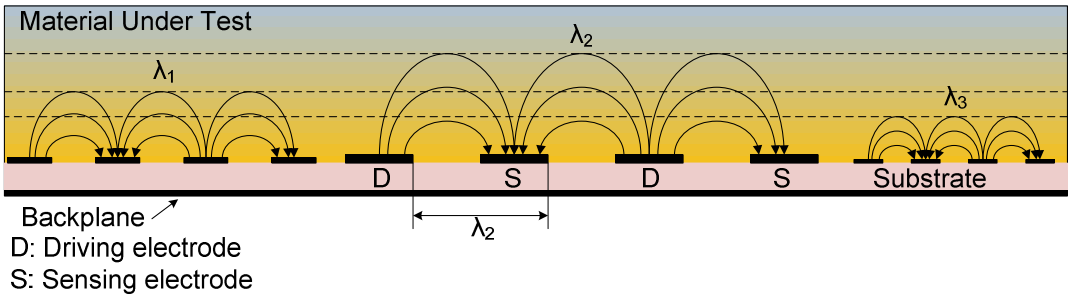

Figure 4-1. *A concept of a multiple-penetration depth fringing electric field sensor.*

This dissertation investigates the feasibility of using the customized concentric fringing electric field sensor and the dielectric spectroscopy meter for the measurement of aircraft functional coating layer thickness and coating loading (percent of pure iron oxide powder that is mixed with silicone filler). This dissertation also develops a coating layer stripping algorithm for

the in-process aircraft functional coating layer thickness and loading measurement. The capacitance discussed in this dissertation is the value, in units, of farads per meter.

4.2 Multi-Layer Coating Stack-up

Figure 4-2 shows the schematic diagram of a multi-layer aircraft coating stack-up. Among the coating stack-up, the functional coating layer is the most interesting of all because it is the primary functioning coating layer, and it is the thickest coating layer in the coating stack-up. Therefore, we focus on measuring the functional coating layer thickness.

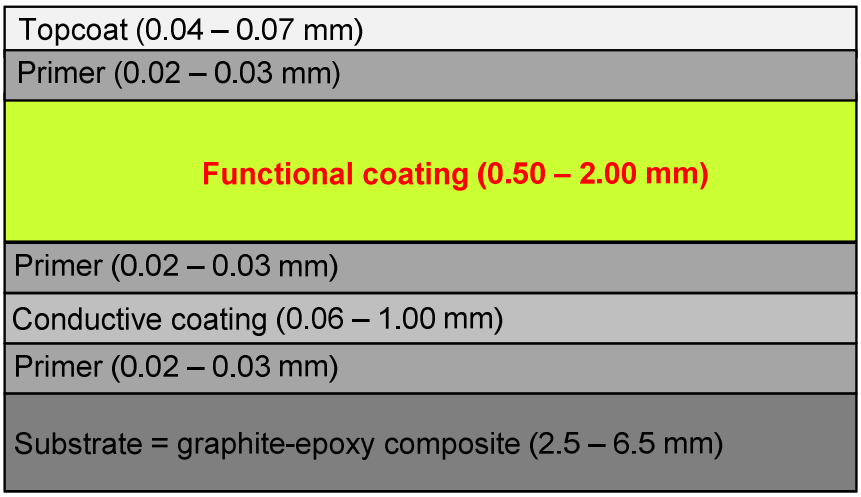

Figure 4-2. *Schematic diagram of a multi-layer aircraft coating stack-up (not to scale).*

Figure 4-3 shows the cutaway of the simplified coating stack-up. The coating stack-up consists of two layers, including graphite and the functional coating layer. The substrate is graphite with a thickness of 2.0 mm. The thickness of the functional coating varies from 0.05 mm to 4.00 mm.

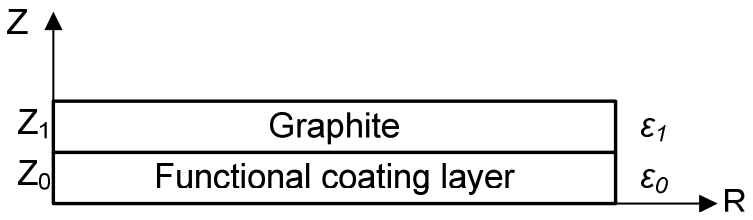

Figure 4-3. *Cutaway of the coating stack-up.*

Table 4.1 shows the material properties of the simplified multi-layer coating stack-up for the modeling. The electrical conductivity of the functional coating layer is zero, and its dielectric permittivity is 13.5 [103].

Table 4.1. *Material properties of the coating stack-up in the simulation.*

Material	Position	Relative dielectric permittivity (ε)	Electrical conductivity (σ, siemens/m)
Graphite	Sample substrate	12.5	7×10^4
Polyurethane	Functional coating layer	13.5	0

4.3 Numerical Modeling for Fringing Electric Field Sensor Design

The numerical modeling was conducted to optimize the design of the fringing electric field sensor to measure aircraft's functional coating layer thickness and loading.

4.3.1 Geometry of Fringing Electric Field Sensors

The purpose of the numerical modeling is to design and fabricate a customized fringing electric field (FEF) sensor for the functional coating layer thickness and loading measurement of aircraft's multi-layer coating stack-up. We model five concentric FEF sensors' capacitance response to different functional coating layer thicknesses. Table 4.2 shows these five FEF sensors' specifications. Simulations were performed in Ansoft Maxwell 2D EM simulation software in the RZ coordinates. R is the radius of the simulation domain, and Z is the height of the simulation domain.

Table 4.2. *Fringing electric field sensor specifications for modeling.*

Sensor	Penetration depth (mm)	# of rings	Electrode width (mm)	Gap between Electrodes (mm)
Sensor-1	4.00	8	3.00	3.00
Sensor-2	2.00	8	1.50	1.50
Sensor-3	2.00	6	1.50	1.50
Sensor-4	1.00	9	0.75	0.75
Sensor-5	0.43	15	0.32	0.32

Both contact and non-contact configurations were used in modeling. For the contact configuration, the fringing electric field sensor head (electrode) directly touches the top surface of the functional coating layer. For the non-contact configuration, air is the media in between the fringing electric field sensor head and top surface of the functional coating layer samples.

Figure 4-4 shows the cross section of the concentric fringing electric field sensor for numerical modeling. The sensor consists of driving electrodes, sensing electrodes, a substrate, and a guard electrode. The FEF sensor's outer most electrode is the driving electrode, followed by the sensing electrode, and the electrodes alternate between driving and sensing after that.

Table 4.3 shows the general materials and the dimensions of the concentric fringing electric field sensor. The substrate is made of FR-4 (woven glass and epoxy), and the standard thickness is 1.55 mm. The material of the electrode is copper, and the thickness of the electrode is 3.5×10^{-2} mm.

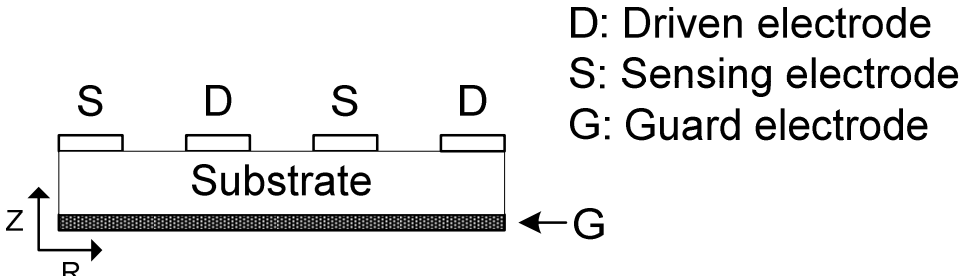

Figure 4-4. *Cross section of the concentric fringing electric field sensor.*

Table 4.3. *Materials and dimensions of the fringing electric field sensor for the simulation.*

Part	Material	Thickness (mm)
Sensor substrate	FR-4 (woven glass and epoxy)	1.55
Driving/Sensing electrode	Copper	3.5×10^{-2}
Guard electrode	Copper	3.5×10^{-2}

4.3.2 Boundary Conditions

Figure 4-5 shows the applied boundary conditions for the simulation. The zero voltage (ground) boundary condition was applied to the sensing electrodes and the guard electrode. DC voltage (2V) was applied to the driving electrodes. The substrate (graphite) was grounded. The

balloon boundary condition was applied on the surrounding environment. The symmetry boundary condition was applied on the boundaries on the Z axis.

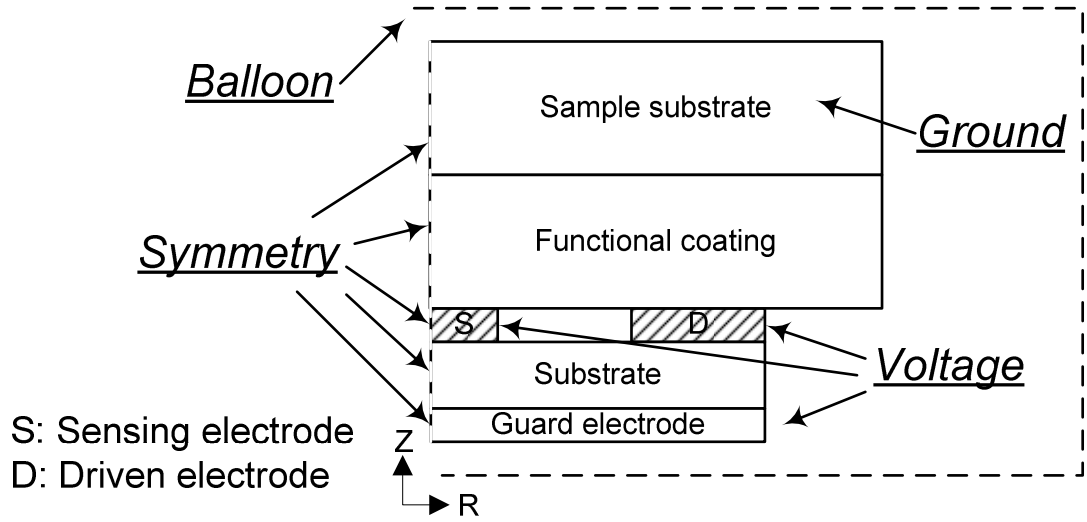

Figure 4-5. *Boundary conditions for the simulation (not to scale).*

4.3.3 Numerical Modeling Results

The numerical modeling was conducted to optimize the design of the fringing electric field sensor to measure aircraft's functional coating layer thickness and loading.

4.3.3.1 Contact Configuration Simulation

Figure 4-6 shows the sensor capacitance obtained by five different penetration depth fringing electric field sensors with respect to different functional coating layer thickness painted on the grounded graphite substrate. In general, increasing the functional coating layer thickness results in larger sensor capacitance, because when the functional coating layer is thicker, more fringing electric field lines passing through the functional coating layer reach the sensing electrodes (Figure 4-7). For some sensors, the capacitance with respect to increased functional coating layer thickness then approaches constant values (except for data from sensor-1 and sensor-2), regardless of further increases in the functional coating layer thickness. This is

because some fringing electric field sensors were operated close to the limitation in the penetration depth.

Figure 4-8 indicates that a FEF sensor shows a maximum sensitivity in sensor capacitance to change in the functional coating layer thickness when the sensor is used to measure a coating thickness that is approximately half of the sensor's penetration depth. The sensitivity in sensor capacitance means how a sensor's capacitance responds to a small amount of change in the functional coating layer thickness. For example, sensor-1 shows the maximum sensitivity in sensor capacitance to change in the functional coating layer thickness when the sensor is used to measure a 2.1 mm functional coating layer, which is about half of the sensor-1's penetration depth.

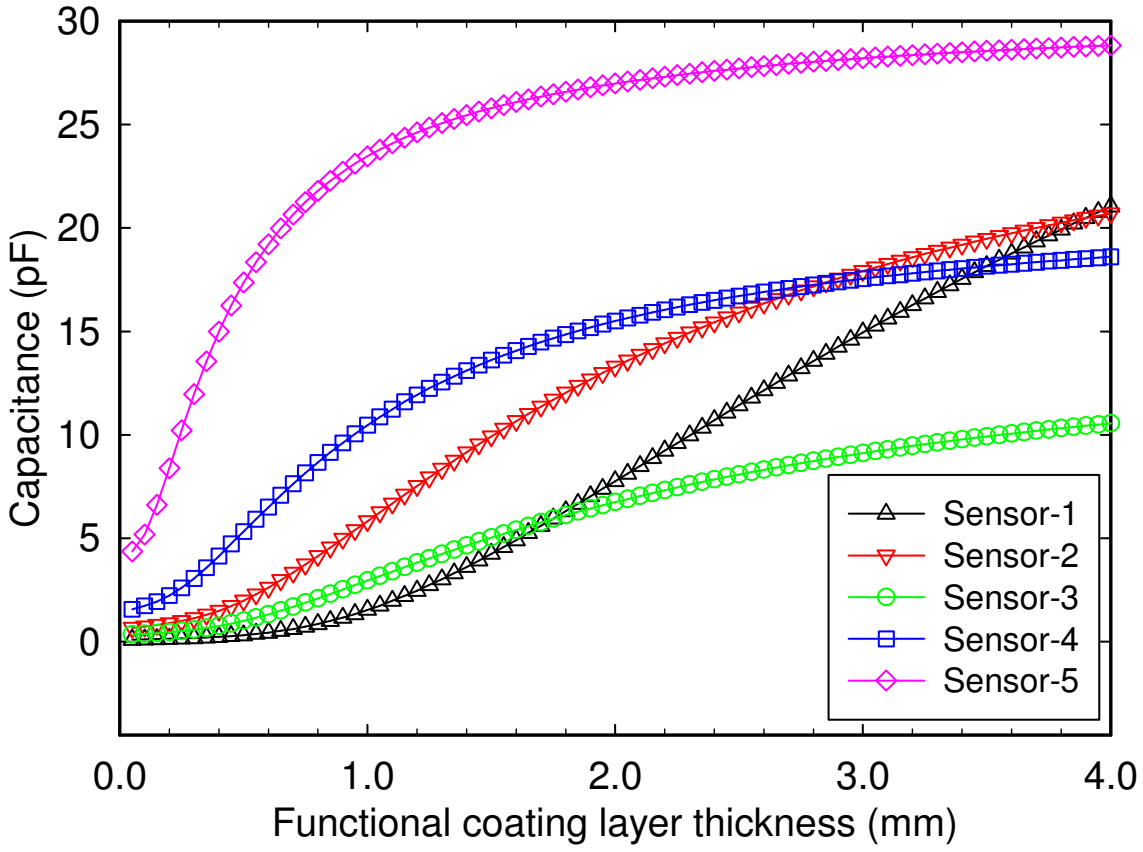

Figure 4-6. *Capacitance of five FEF sensors with different penetration depths as a function of functional coating layer thicknesses on the grounded graphite substrate. Sensor capacitance for the air is between 2.31 pF and 8.53 pF, which depends on the sensor geometry (Table 4.2).*

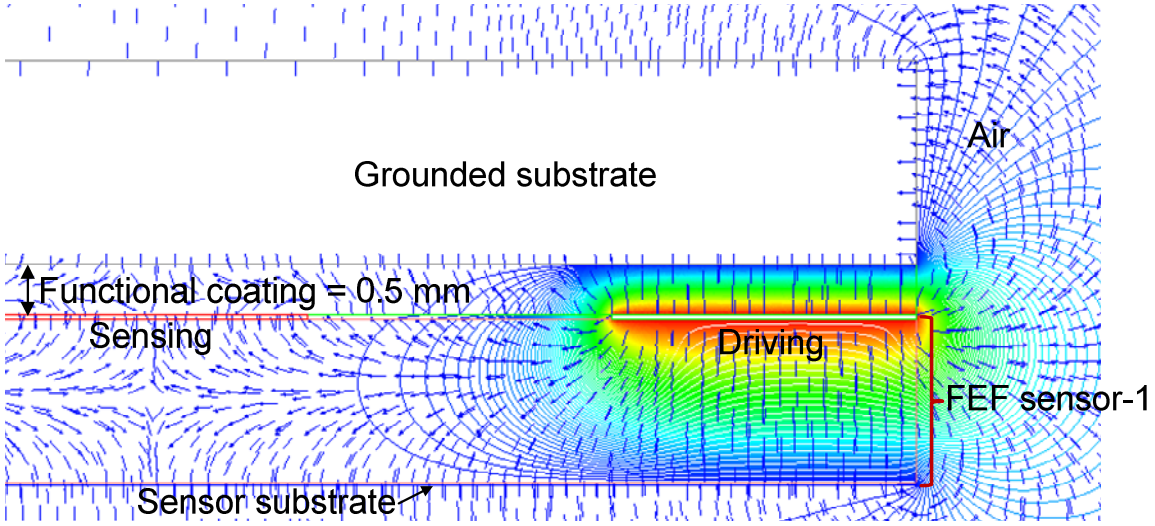

(a) 0.5 mm functional coating layer thickness

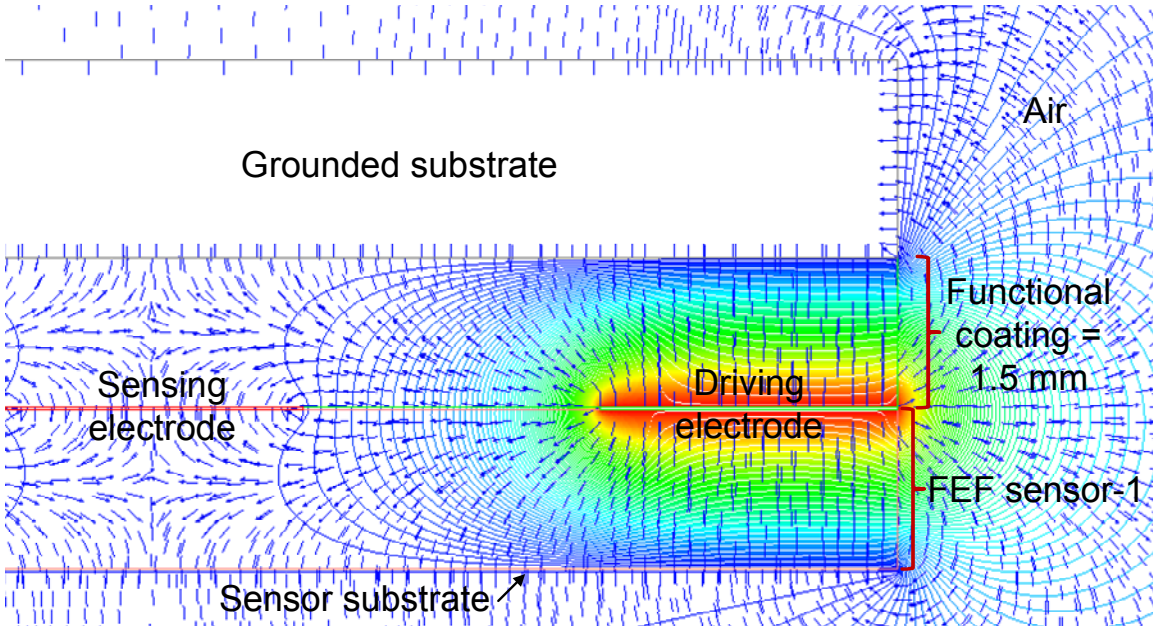

(b) 1.5 mm functional coating layer thickness

Figure 4-7. *Fringing electric field (arrow) and potential distributions (color) for sensor-1 measuring the functional coating layer with different thickness (Color picture is available in digital copy).*

In addition, Figure 4-8 shows that a sensor with a larger penetration depth can be used to measure a broad range of the functional coating layer thickness while still showing the sensitivity in sensor capacitance measurement within 10% of the sensor's maximum sensitivity in capacitance measurement. Sensors with the same penetration depth but different number of rings

also show different sensitivity in capacitance measurement. For example, sensor-2 and sensor-3 have the same penetration depth of 2 mm. However, the simulation results show that for the same functional coating layer thickness, sensor-2's sensitivity in capacitance measurement is higher than that of sensor-3, because sensor-2 has two additional rings for measurement; therefore, sensors with the same penetration depth but with a higher number of rings can increase the sensors' sensitivity in capacitance measurement.

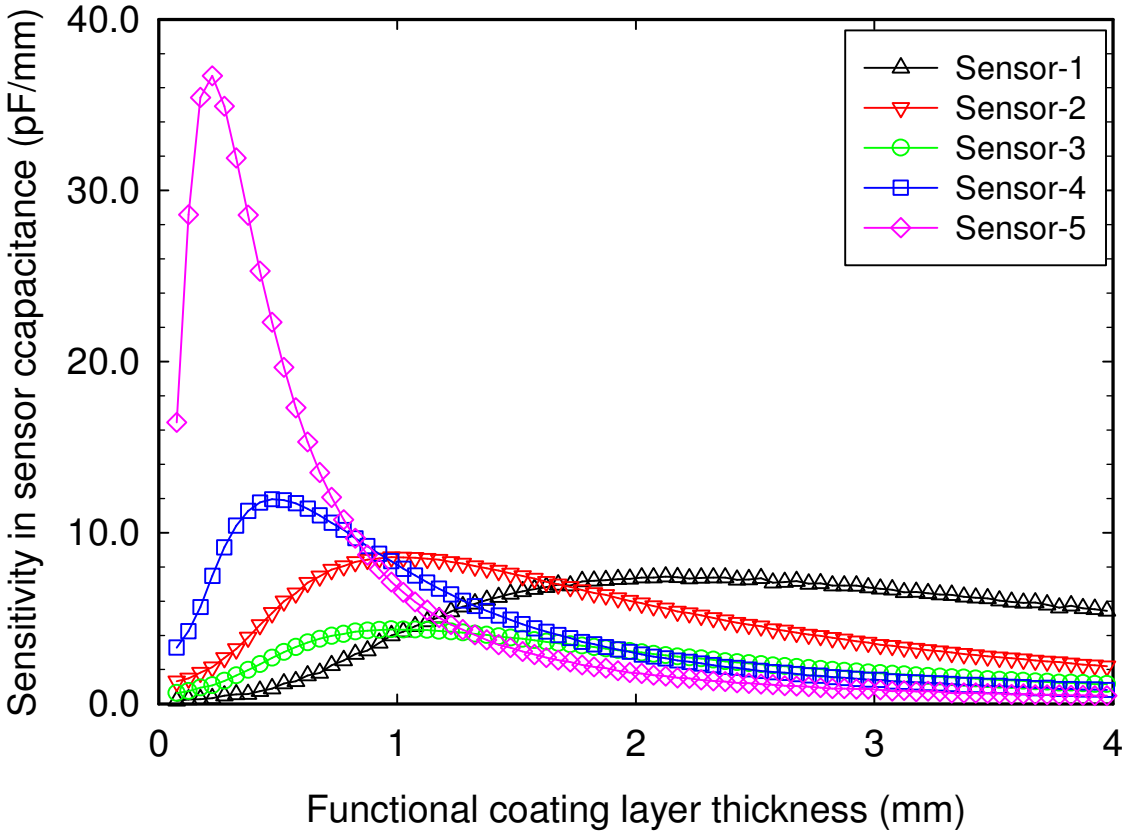

Figure 4-8. *Sensitivity in capacitance measurement of five FEF sensors as a function of functional coating layer thicknesses on grounded substrates.*

Since the simulation results indicate that sensor-1 (4 mm penetration depth) has a higher sensitivity in capacitance measurement to change in the functional coating layer thickness of interest (between 1.5 mm to 4 mm), this sensor is used for simulations of non-contact configuration cases, and is optimized for experiments.

4.3.3.2 Non-Contact Configuration Simulation

We used the fixed total distance (Figure 4-9) and fixed air gap (Figure 4-10) configurations for non-contact configuration simulations.

Fixed total distance cases. The fixed total distance (Figure 4-9) means the distance between the sensor electrode and the bottom of the grounded sample substrate is fixed.

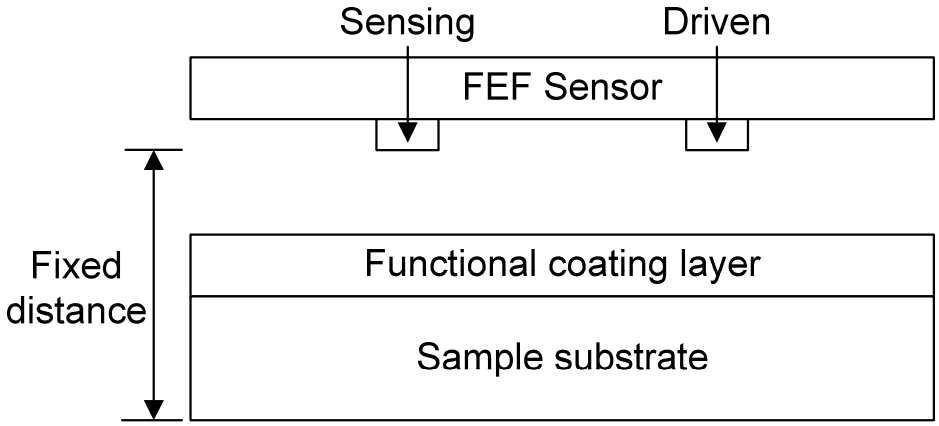

Figure 4-9. *Non-contact fixed total distance configuration for simulations.*

Figure 4-10 shows that for the same fixed total distance, increasing the functional coating layer thickness decreases the measured sensor capacitance because more fringing electric field lines passing through a thicker functional coating layer reach a grounded sample substrate instead of a sensor's sensing electrode. It is the reduced amount of fringing electric field lines reaching the sensor's sensing electrode that results in a decreased capacitance at the sensor's terminals. In addition, for the same functional coating thickness, a large fixed total distance increases the sensor capacitance because a thicker air gap between the sensor electrode and the top surface of the functional coating layer allows for more fringing electric field lines reaching the sensor's sensing electrode.

Figure 4-10 also shows that sensor-1 is more sensitive to variation in the functional coating thickness as the fixed total distance is reduced from 7.5 mm to 6.5 mm. For the same coating thickness, a small fixed total distance indicates a small air gap between the top surface of a coating sample and the sensor electrode; therefore, the sensor is more sensitive to the variation of the amount of fringing electric field lines that reach the sensor's sensing electrode.

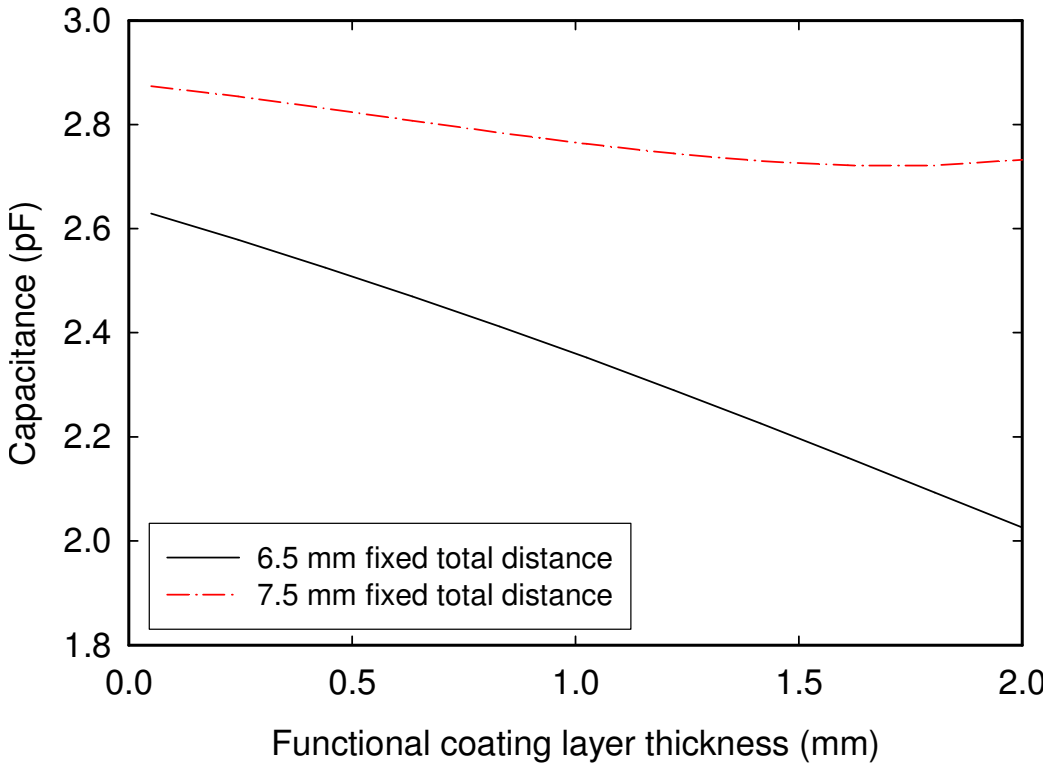

Figure 4-10. *Capacitance of sensor-1 for the fixed total distance configuration. The simulated capacitance of the air (without the coating stack-up on top of the sensor) is around 4.2 pF.*

Fixed air gap cases. The fixed air gap (Figure 4-11) means the air gap between the sensor electrode and the top surface of the functional coating layer is fixed.

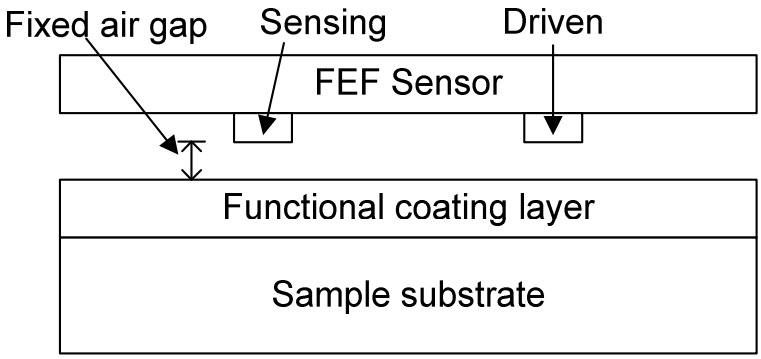

Figure 4-11. *Non-contact fixed air gap configuration for simulations.*

Figure 4-12 shows that the smaller the air gap is between the functional coating layer and the sensor electrode, the more sensitive the sensor is to change in the functional coating layer thickness. When the fixed air gap is larger than 2.0 mm, the sensor becomes insensitive to further increases in the functional coating layer thickness, because the sensor approaches its limitation (penetration depth) in the thickness measurement.

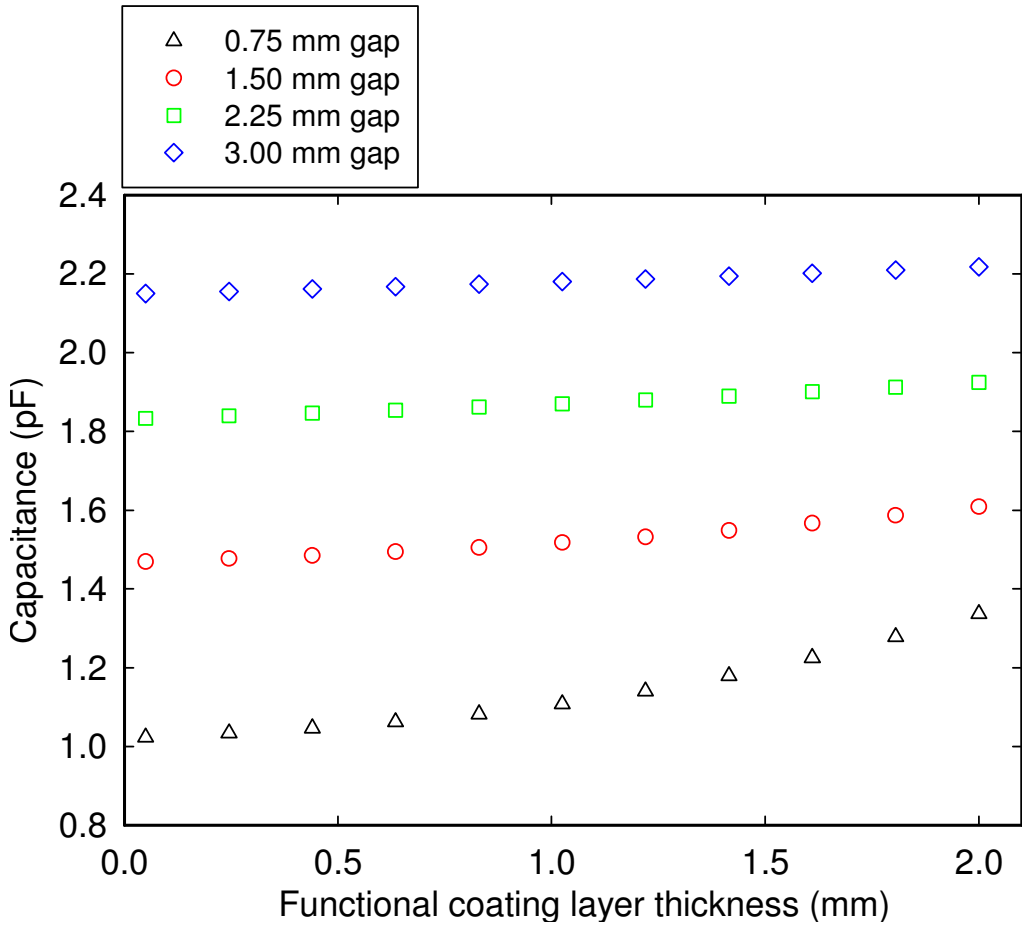

Figure 4-12. *Sensor capacitance for different fixed air gaps. The sensor capacitance of the air (without the coating stack-up on top of the sensor) is around 4.2 pF.*

4.4 Experimental Apparatus

4.4.1 Measurement System

Figure 4-13 shows the functional coating layer thickness measurement system, which consists of the 4 mm penetration depth (PD) concentric fringing electric field (FEF) sensor, the dielectric spectroscopy meter (DS-1, Illionix), a USB-6356 DAQ card, a laptop, and a LabVIEW program. The dielectric spectroscopy meter (DS-1) can measure capacitance from 0.1 pF to 0.1 μF with the accuracy of less than ± 1.0%. A detailed discussion on the FEF sensor is in Section 4.3.1. All measurements were conducted in the contact configuration and the fixed total distance configuration (Figure 4-9). The substrate that the functional coating layer is on was grounded.

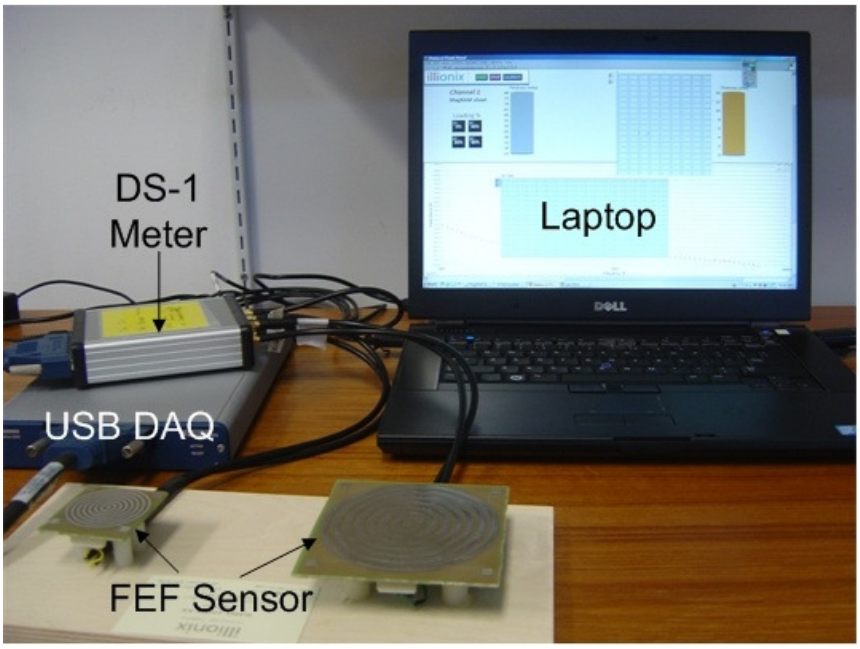

Figure 4-13. *Measurement system consists of fringing electric field sensors, dielectric spectroscopy meter (DS-1), DAQ card, and a laptop.*

4.4.2 Fringing Electric Field Sensor

According to the numerical modeling results, we optimized and fabricated the 4 mm penetration depth (PD) concentric fringing electric field sensor for all measurements. The geometry of the sensor is the same as that of sensor-1 (Table 4.2 and Table 4.3).

4.4.3 Different Functional Coating Samples

We used both rigid and flexible functional coating layer samples for experiments.

4.4.3.1 Rigid Functional Coating Layer Samples

Rigid functional coating layer samples were made by the company Millimeter Wave Technology, Inc (MWT). The functional coating is made of a carbonyl iron base (46% volume) in a urethane acrylic resin (54% volume). The samples are 4 × 4 inches. The nominal functional coating layer thicknesses on the substrates are 0.5, 1.0, 1.5, and 2.0 mm. Thicknesses of the metal substrate are 3 mm. Table 4.4 shows the actual thickness of the functional coating layer on the metal substrate. The actual thickness was averaged by taking the thickness measurement at the four corners of each sample with a micrometer. Sensor capacitance about the rigid functional coating layer samples was obtained with the contact configuration and with the fixed total distance of 7.5 mm (Figure 4-9). Each sample was placed in four different orientations (90 degree between each orientation). Measurements were taken in the frequency domain from 1 Hz to 10 MHz.

Table 4.4. *Actual thickness of the functional coating layer of the samples.*

Labeled thickness (mm)	Actual thickness (mm)	Standard deviation
0.5	0.41	0.03
1.0	0.93	0.11
1.5	1.24	0.05
2.0	1.88	0.15

4.4.3.2 Flexible Functional Coating Sheets

The flexible functional coating sheets were made by the company, SRC Cables, with three loading levels and five thicknesses for each loading level. The loading level refers to the percent of pure iron oxide powder that is mixed with silicone filler. Table 4.5 shows the thicknesses of the samples cured at each loading level. The sensor capacitance about the flexible functional

coating layer samples was obtained in several ways. First, the sheets were placed on top of the sensor electrode (contact configuration) for measurement. Second, the flexible functional coating sheets were sandwiched between the sensor electrode and a grounded aluminum substrate for measurement. Third, to determine the sheet's relative dielectric permittivity, a parallel plate sensor was used. For all measurements, each sample was placed in four different orientations (90 degree between each orientation), so that four measurements were taken in four different orientations. Measurements were taken in the frequency domain from 1 Hz to 10 MHz.

Table 4.5. *Loadings and thicknesses of the flexible functional coating sheets.*

Loading (%)		Thickness (mm)				
40	Labeled	0.75	1.00	1.25	1.50	1.88
	Actual	0.77	1.01	1.24	1.43	1.79
	STDEV	0.01	0.02	0.00	0.04	0.02
60	Labeled	0.75	1.00	1.25	1.50	1.88
	Actual	0.77	1.04	1.19	1.47	1.87
	STDEV	0.01	0.05	0.04	0.01	0.01
80	Labeled	0.75	1.00	1.25	1.50	1.88
	Actual	0.78	1.08	1.28	1.50	1.89
	STDEV	0.01	0.02	0.03	0.02	0.05

4.5 Experimental Results

4.5.1 Rigid Functional Coating Layer Samples

4.5.1.1 Contact Measurement

Figure 4-14 shows the capacitance obtained by the 4 mm penetration depth fringing electric field sensor with the contact measurement configuration. The rigid functional coating layer samples were used. In general, the sensor capacitance as a function of the functional coating layer thickness is in order, meaning that a thick functional coating layer results in a high sensor capacitance. This trend was also indicated in numerical modeling results, as shown in Figure 4-6. The sample with 0.93 mm coating thickness was not measured, because we visually observed that the color and brightness of this sample is different than that of other samples.

Sensor capacitance response in the contact measurement mode is highly influenced by the surface roughness of the samples. When the sensor's electrodes contact the sample's surface, the

sensor is more sensitive to the sample's surface roughness and non-flatness [104, 105]. We visually observed that the surface of the samples is not perfectly flat. There are some surface extrusions on the sample's surface. When the sensor's electrodes contact the sample, there are different amounts of air between the sensor electrodes and the sample surface. Non-uniform distributions in the amount of air cause the sensor to measure different capacitances. Whether the sensor electrode edge touches the sample's surface extrusions or not, the potential intensity distribution close to the sensor electrode and the contacted sample surface changes significantly, which can also cause different sensor capacitances at the sensor terminals.

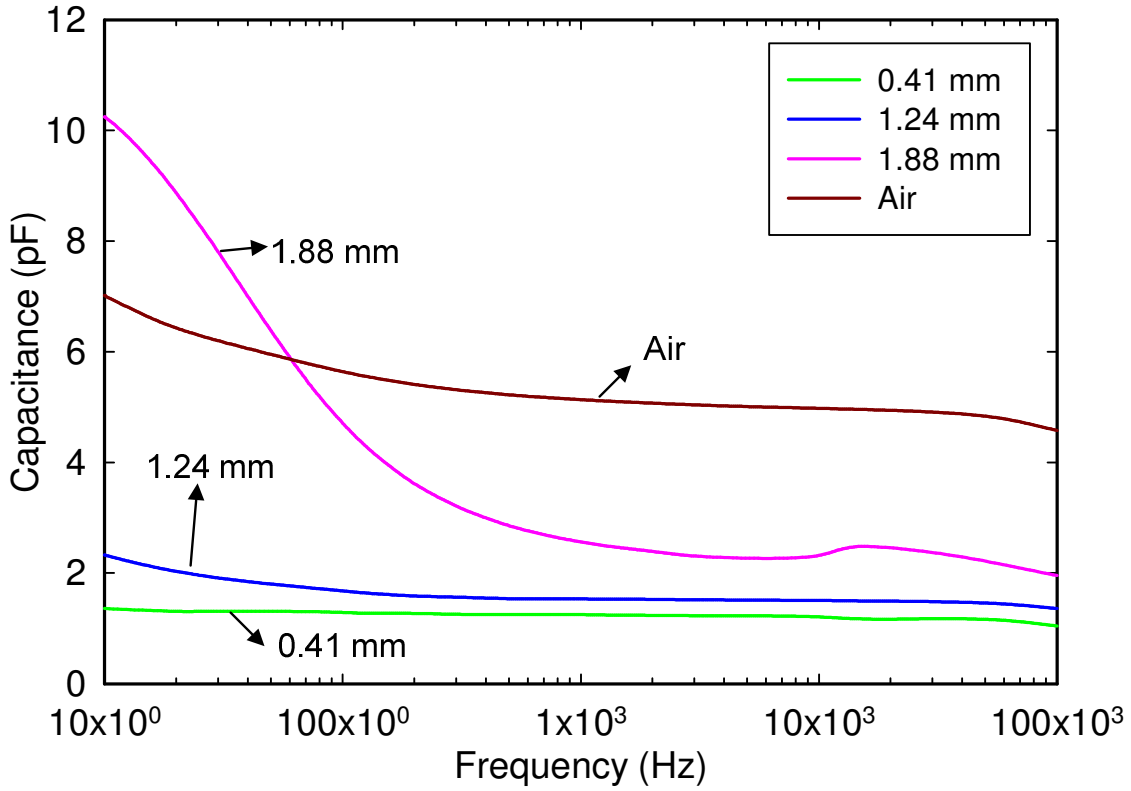

Figure 4-14. *Experimental data showing the sensor capacitance in the frequency domain as a function of the functional coating layer thicknesses on the grounded aluminum substrates.*

Furthermore, the coating uniformity should also be taken into account. Noticeably, the color and brightness on all samples are different, which means that some of these coating samples were not mixed uniformly and not dried in the same way. The sample's non-uniformity could also result in different sensor capacitances at the sensor terminals at the same driving frequency. The experimental data shown in Figure 4-15 demonstrates that the sensor capacitance of the

uniform poly(methyl methacrylate) (PMMA) with different thicknesses in the same frequency domain are in order and in parallel with respect to the thicknesses. These samples also have smooth surfaces.

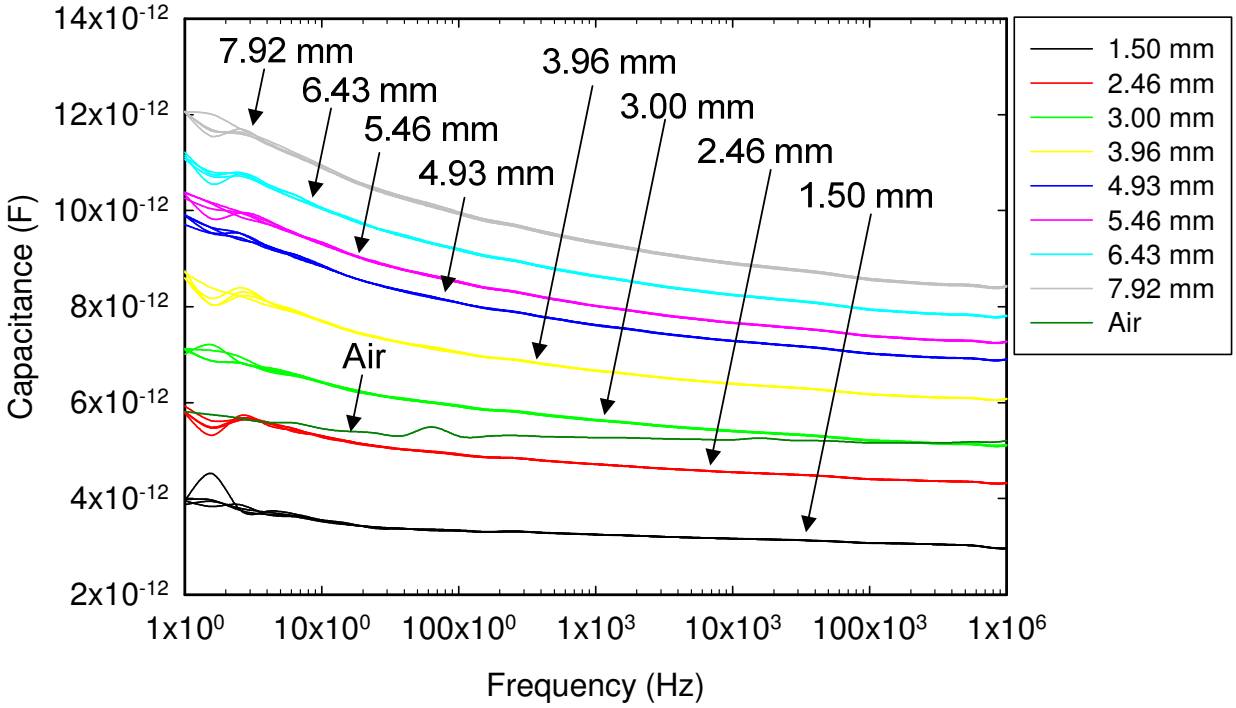

Figure 4-15. *Experimental data showing the effect of sample uniformity on the sensor capacitance measurement. Sensor capacitance in the frequency domain as a function of the thicknesses of uniform poly(methyl methacrylate) (PMMA) on the grounded aluminum substrates.*

Although sensor capacitance and conductance should be taken into account in numerical modeling, our experimental results show that the sensor capacitance already provides sufficient information, allowing us to investigate the relationship between the functional coating layers and the sensor capacitance. Therefore, we hereafter use the sensor capacitance for analysis.

4.5.1.2 Fixed Total Distance between Sensor and Platform that Functional Coating Layer Sample is on

Figure 4-9 shows the experimental configuration. Figure 4-16 shows the relationship between the measured sensor capacitance and the functional coating layer thickness. The thicker

the functional coating layer on the grounded sample substrate is, the lower the sensor capacitance is measured. This is because more fringing electric field lines passing through the thicker functional coating layer reach the grounded substrate, which reduces the amount of the fringing electric field lines reaching the sensor's sensing electrode.

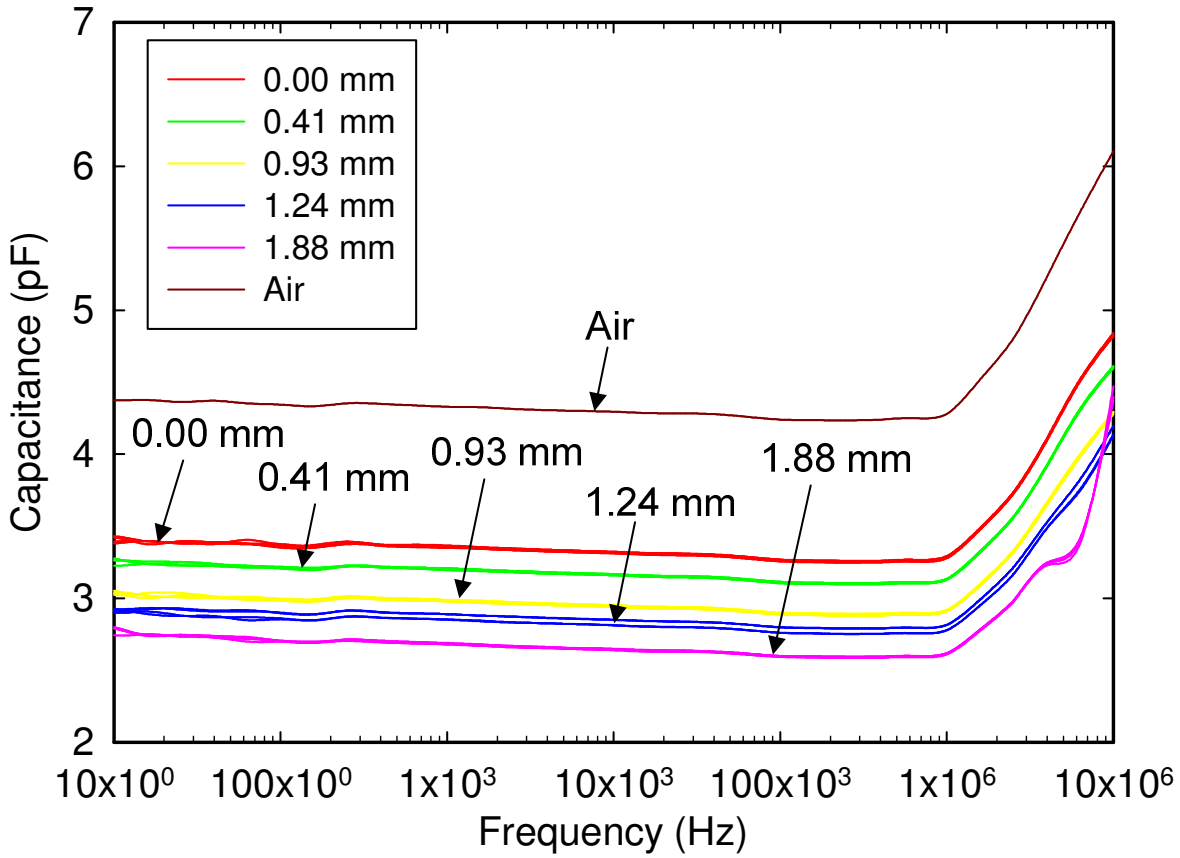

Figure 4-16. *Sensor capacitance with respect to different functional coating layer painted on the grounded substrates.*

Figure 4-17 shows that at four specific frequencies, the measured sensor capacitance decreases linearly as the functional coating layer thickness is increased. Additionally, Figure 4-16 and Figure 4-17 show that all the measured sensor capacitance about the functional coating samples are smaller than that of the air. This effect is due to the grounded metal substrate, and not because the functional coating has a smaller relative dielectric permittivity than the air. Numerical modeling results shown in Figure 4-10 also indicate the same trend as the

experimental results shown in Figure 4-16 and Figure 4-17. More fringing electric field lines reach the grounded substrate as the functional coating layer is thicker.

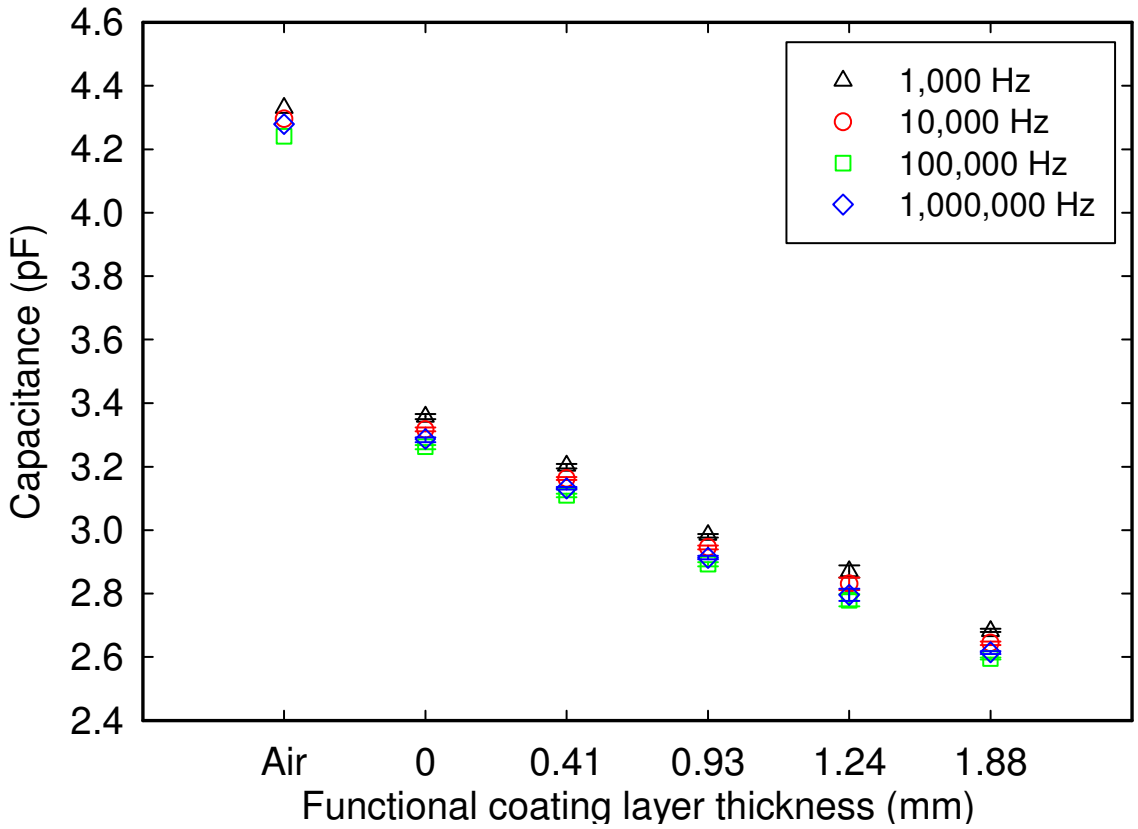

Figure 4-17. *Sensor capacitance at four frequencies as a function of the functional coating layer thicknesses. Error bars show maximum and minimum sensor capacitance at each thickness. The symbols show the mean sensor capacitance.*

4.5.2 Flexible Functional Coating Sheets

The flexible functional coating sheets investigated in this section are with 40% loading.

4.5.2.1 Contact Measurement

Figure 4-18 shows that a thick functional coating sheet results in a high sensor capacitance, because more fringing electric field lines passing through the thick functional coating layer reaches the sensor's sensing electrode. Additionally, the sensor capacitance about the functional coating sheet is always higher than that about the air, because the functional coating sheet has

larger relative dielectric permittivity. At four different frequencies, Figure 4-19 shows that the sensor capacitance relates linearly to the functional coating sheet's thickness.

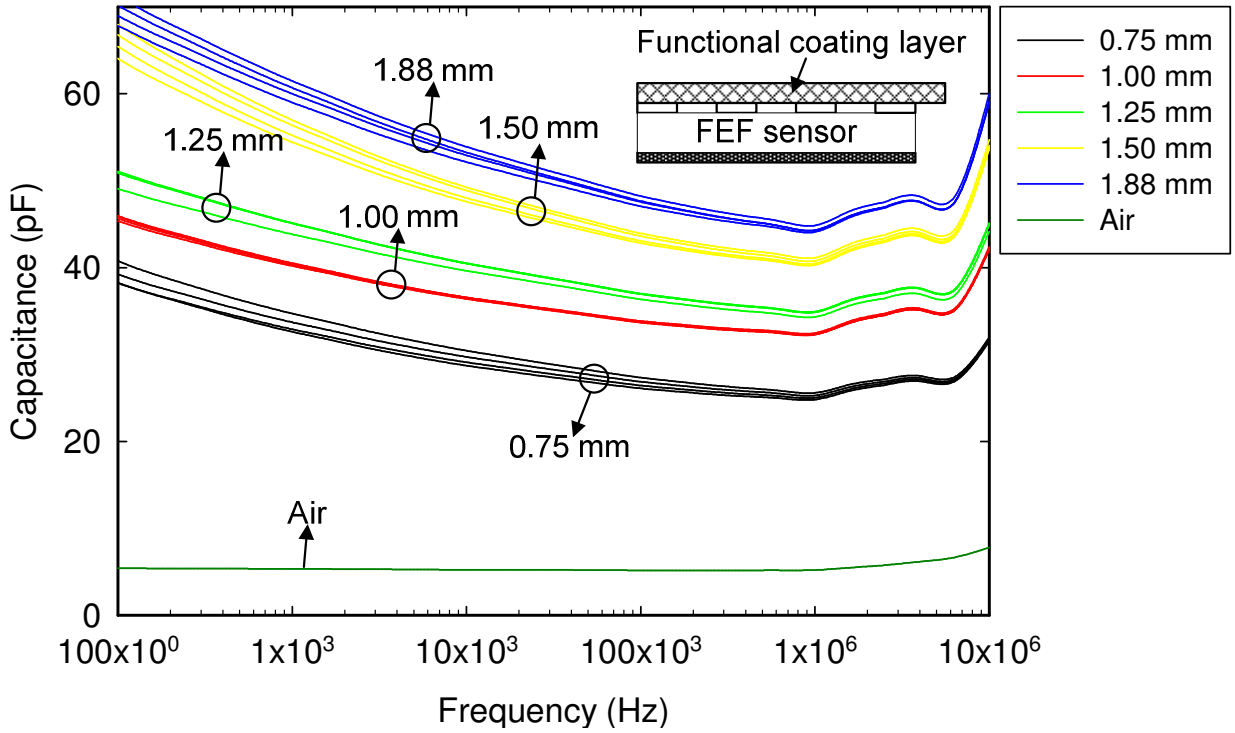

Figure 4-18. *Sensor capacitance about different thickness of the flexible functional coating sheets with the same loading (40%).*

When the flexible functional coating sheets are sandwiched between a grounded substrate and the FEF sensor, the sensor capacitance (contact measurement) of the flexible functional coating sheets in the frequency domain shows two different behaviors. For frequencies lower than 1 MHz, Figure 4-20 (a) shows that a thick functional coating sheet results in a high sensor capacitance. This trend is also consistent with the modeling results shown in Figure 4-6. However, the trend reverses for frequencies higher than 1 MHz. The measured sensor capacitance decreases as the functional coating thickness increases (Figure 4-20 (b)). This phenomenon is similar to the experimental results obtained from the sensor capacitance measurement of the rigid functional coating samples shown in Figure 4-14. The frequency where the sensor capacitance of the functional coating sheet reverses highly depends on the thickness of the functional coating sheets.

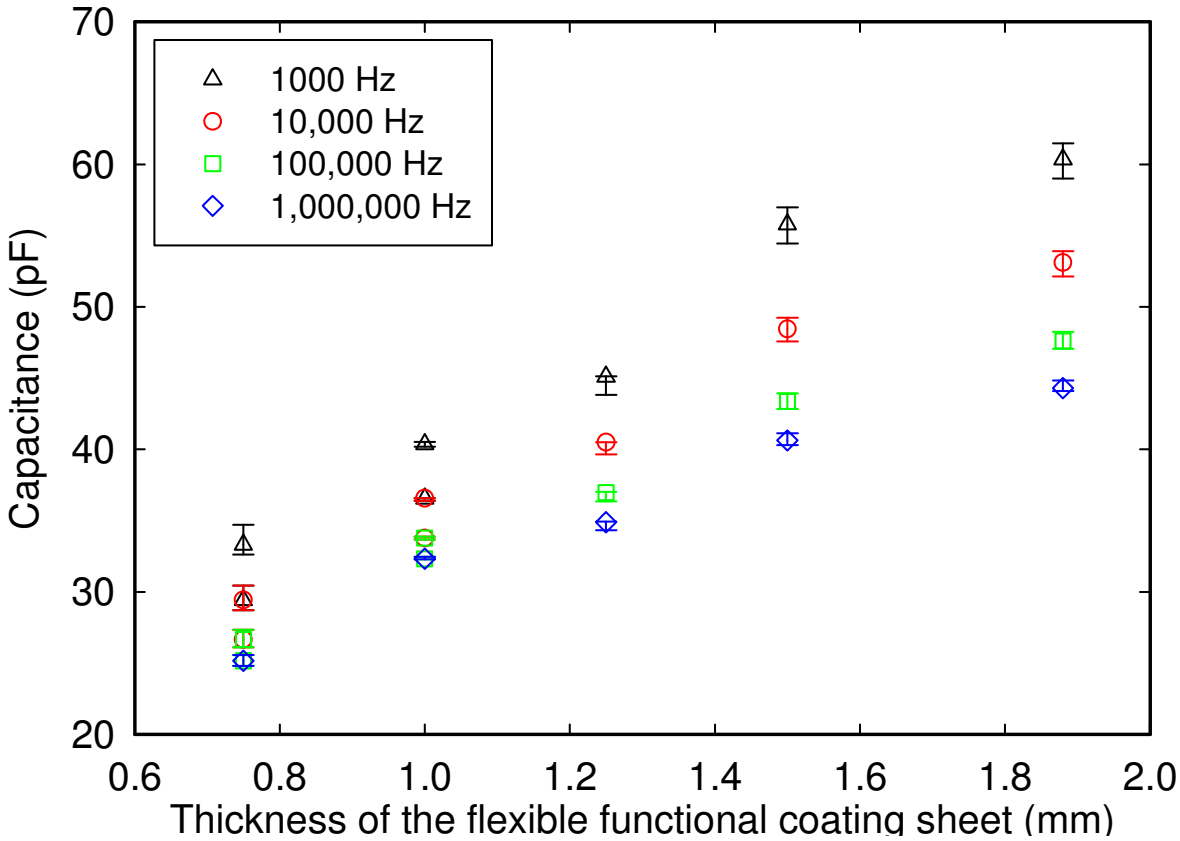

Figure 4-19. *Sensor capacitance of the 40% loading flexible functional coating sheets measured at four different frequencies. Error bars show maximum and minimum sensor capacitance at each thickness. The symbols show the mean sensor capacitance.*

Figure 4-21 shows that the measured sensor capacitance of the functional coating sheet with a thinner thickness reverses at a relatively lower driving frequency. For example, the sensor capacitance of the 0.75 mm thickness functional coating sheet reverses at 0.6 MHz, whereas the sensor capacitance of the 1.00 mm thickness functional coating sheet reverses at 1.5 MHz. The functional coating sheet's uniformity and surface roughness should not be responsible for entirely different trends in sensor capacitance in the frequency domain, because the transitions in the sensor capacitance are not shown in Figure 4-18. The discontinuous interface and possible small voids between the grounded substrate and the functional coating sheet might result in transitions in sensor capacitance near 1 MHz. Further investigations are necessary to clarify why entirely different trends occur near 1 MHz.

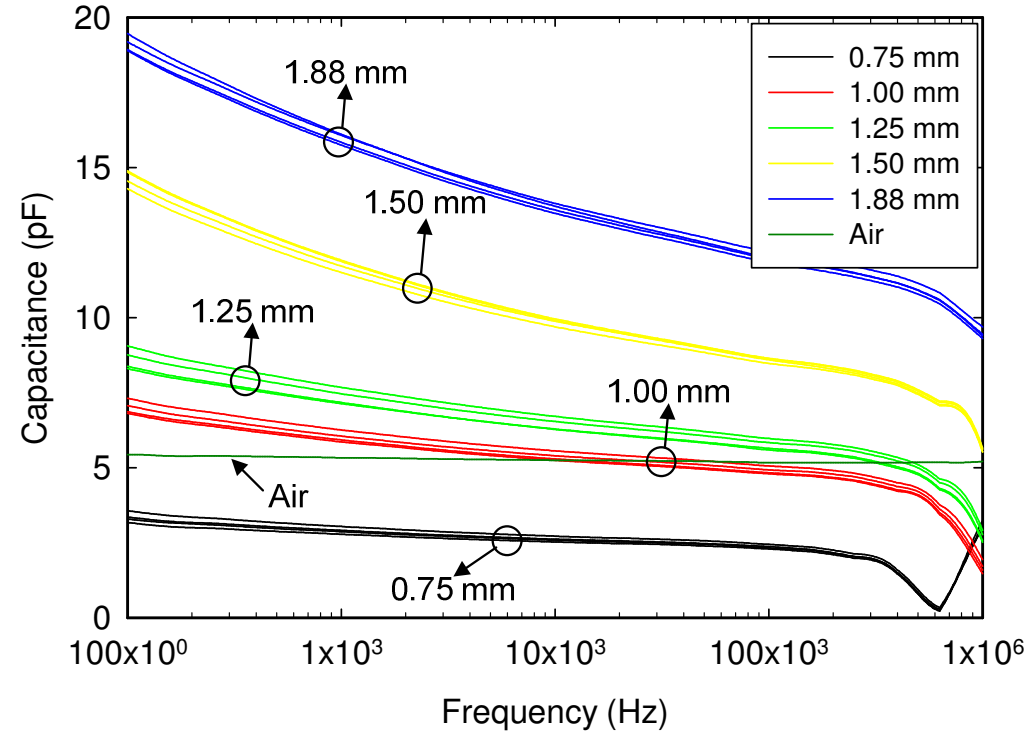

(a) Frequencies lower than 1 MHz

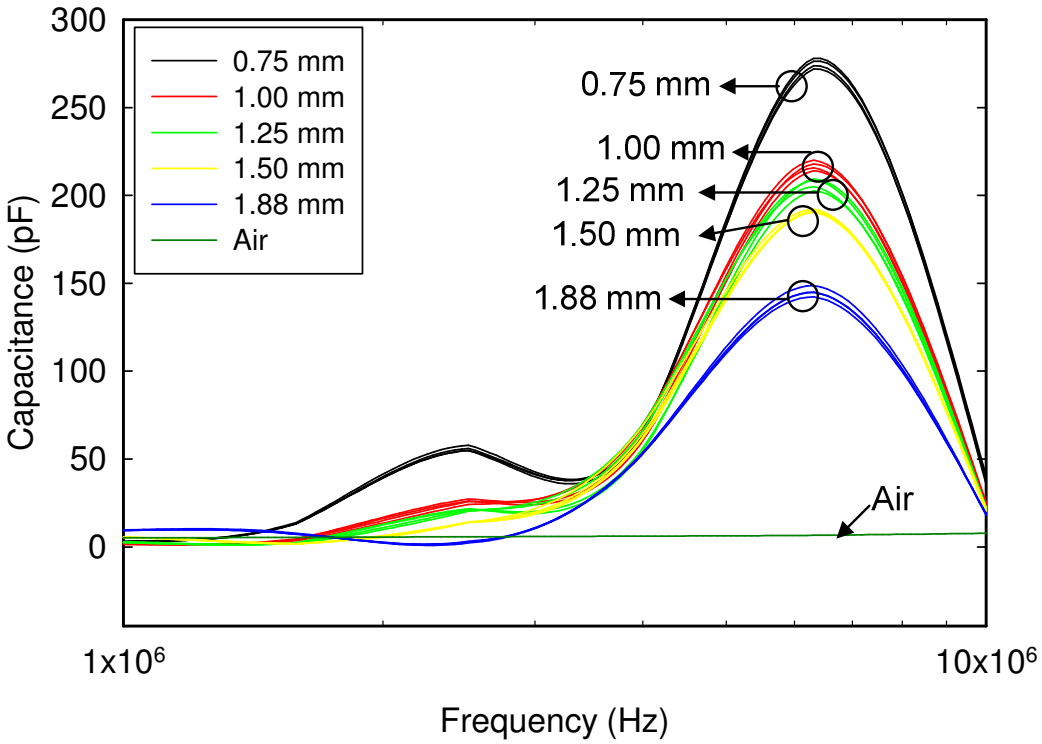

(b) Frequencies higher than 1 MHz

Figure 4-20. *Measured sensor capacitance for the 40% loading flexible functional coating sheets attached to a grounded aluminum substrate.*

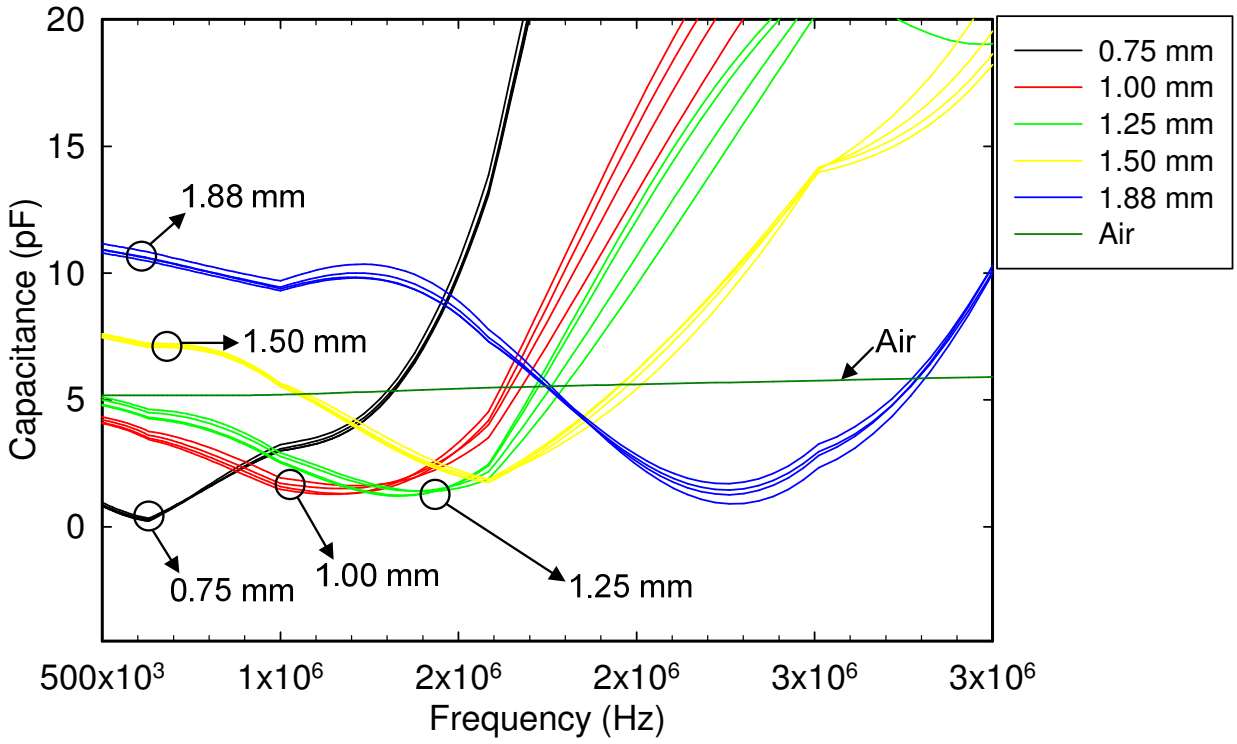

Figure 4-21. *Frequencies where reverse trends in sensor capacitance occur.*

4.5.2.2 Relative Dielectric Permittivity

Figure 4-22 shows the relative dielectric permittivity of the flexible functional coating sheet. The measurement configuration is also shown in Figure 4-22. We used two flat aluminum plates as the sensing and driving electrodes to measure the functional coating sheet's relative dielectric permittivity. The sensing electrode is 2.54 mm × 2.54 mm, and the driving electrode is 10.16 mm × 10.16 mm. The data for each thickness should overlap, and it is expected that the relative dielectric permittivity should vary with the frequency. However, it is not expected that it varies with the coating thickness. Visual inspection of these samples indicates that the top and the bottom surface of the sample with a high thickness are in different colors and brightness. The top surface is dark, while the bottom surface is gray. The cross section of the sample also shows a sandwich-like profile. The sample's non-uniformity and degree of curing during the manufacturing processes should be a possible reason for causing dependence between the relative dielectric permittivity and the coating thicknesses.

When we measured the relative dielectric permittivity of the single 1.5 mm sheet with two 0.75 mm sheets stacked up together, the result shows a significant difference. The deviation of

the dielectric permittivity between the 1.5 mm sheet and the 0.75 mm sheet is more than 55%, while between the two 0.75 mm stack-up (1.5 mm thick) and the 0.75 mm sheet is less than 16%. This demonstrates that the non-uniformity of the sample is a possible reason for causing the dependence between the relative dielectric permittivity and the coating thicknesses.

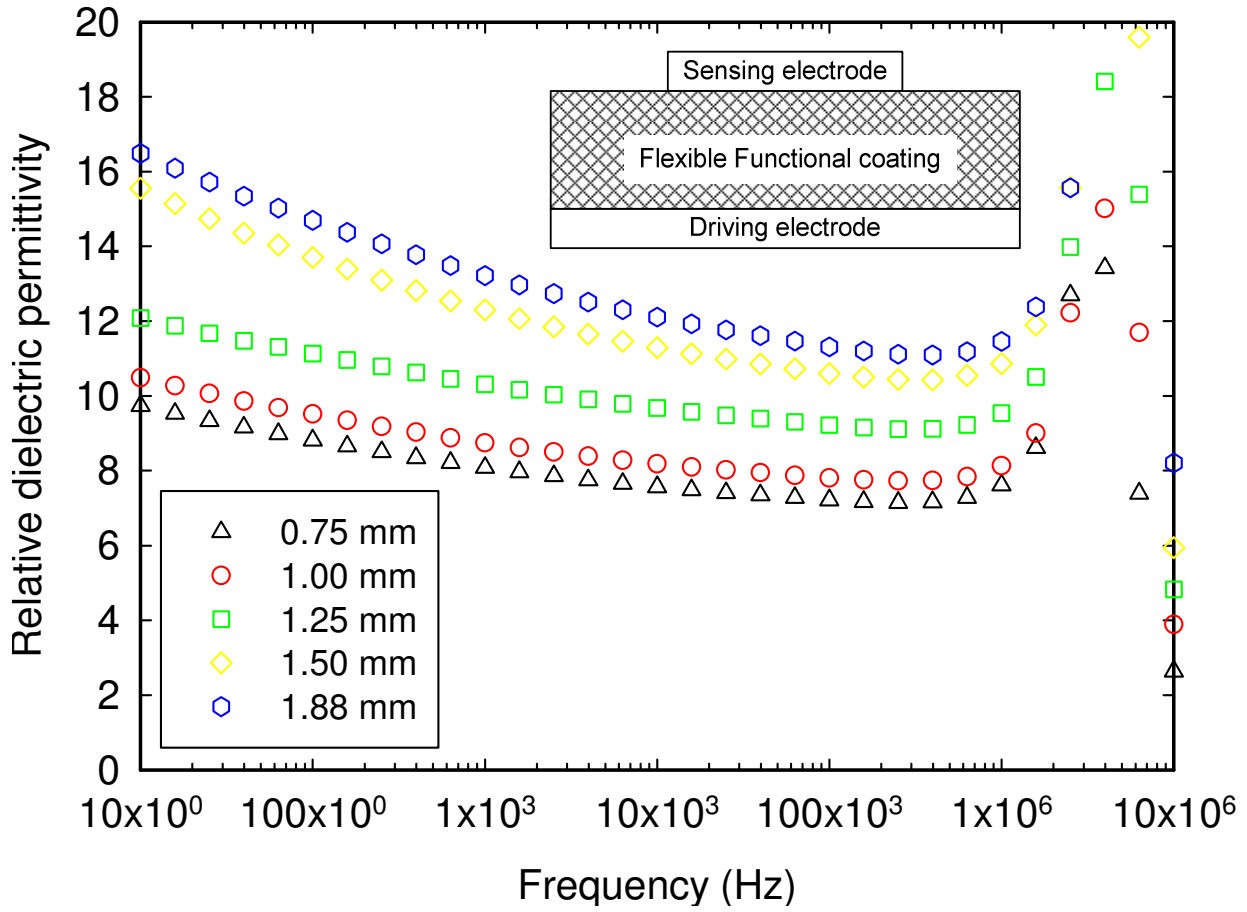

Figure 4-22. *Relative dielectric permittivity of the 40 % loading flexible functional coating sheets.*

4.5.2.3 Flexible Functional Coating Sheets with Different Loading

Figure 4-23 and Figure 4-24 show the measured sensor capacitance of the flexible functional coating sheets with varying thicknesses and loadings. The contact measurement configuration was used. In general, the measured sensor capacitance of the sheets in each loading group is in order with the sheet's thickness. In each loading group, a thick functional coating layer results in

a high sensor capacitance. Additionally, for the sheets with the same thickness but different loadings, a high coating loading results in a high sensor capacitance as well.

Theoretical expressions relating the coating thickness and different percentages of functional coating loading to the sensor capacitance have not been thoroughly investigated, and therefore, are not well understood. Equation (4.1) is the empirical expression relating the coating thickness, the coating loading, and the measurement frequency to the sensor capacitance of the fringing electric field sensor.

$$C = C(x, y) = -z_0 \times 10^{11} + 7.93 \times 10^{-13} x + 1.01 \times 10^{-11} y \tag{4.1}$$

$$z_0 = z_0(f) = \frac{3.81 \times f}{54.56 + f} + 3.45 \times 10^{-6} \times f \tag{4.2}$$

where x is the coating thickness (mm), y is the coating loading (%), and f is the driving frequency (Hz). This equation indicates that the sensor capacitance is more sensitive to the variation in coating loading than that of the coating thickness. This is because the 4 mm penetration depth sensor is not sensitive to a small thickness change. It is expected that a sensor with a small penetration depth will have a coefficient showing the sensor's high capacitance response to the coating thickness change.

Additionally, Figure 4-24 also shows that there is very little overlap between different loadings. Although overlap does occur for the 60% (0.75 mm thickness) and 40% (1.50 mm and 1.88 mm thickness) loading sheets, their sensor capacitance in the frequency domain is different, which indicates that with an appropriate algorithm, the 4 mm penetration depth fringing electric field sensor can be used to measure in-process functional coating layer thickness with different loadings. The algorithm developed in this investigation is discussed in Section 4.7.

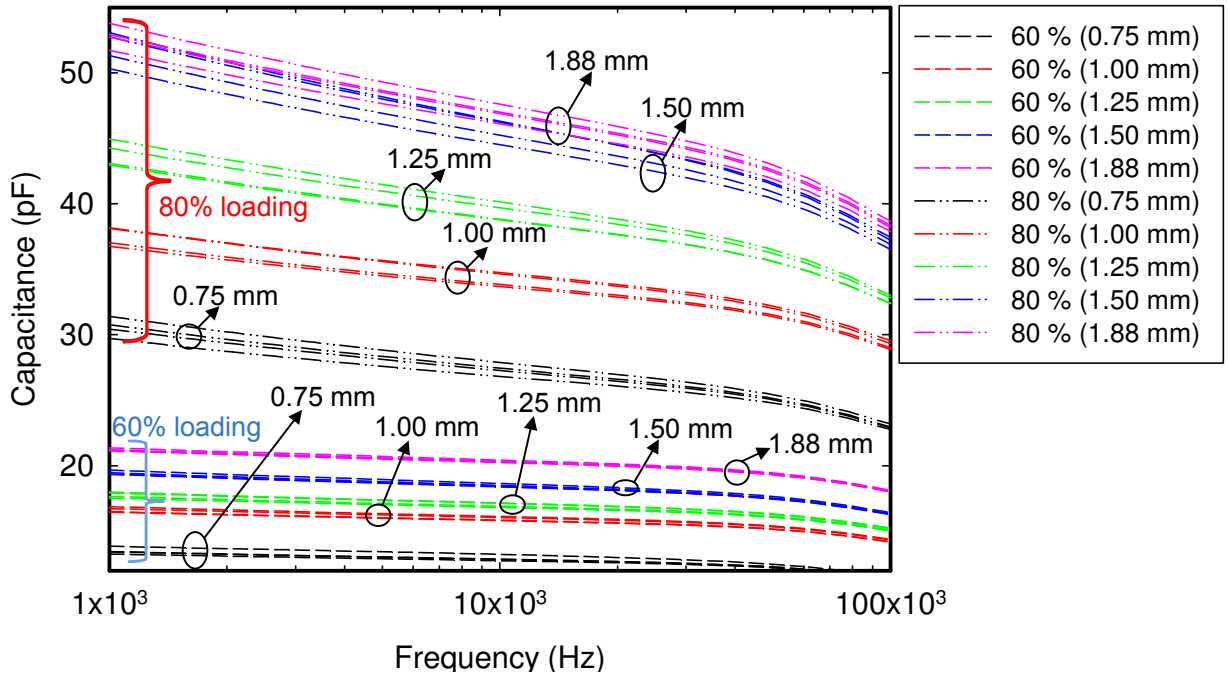

Figure 4-23. *Sensor capacitance for the flexible functional coating sheets with different loadings and thickness (60 % loading and 80 % loading).*

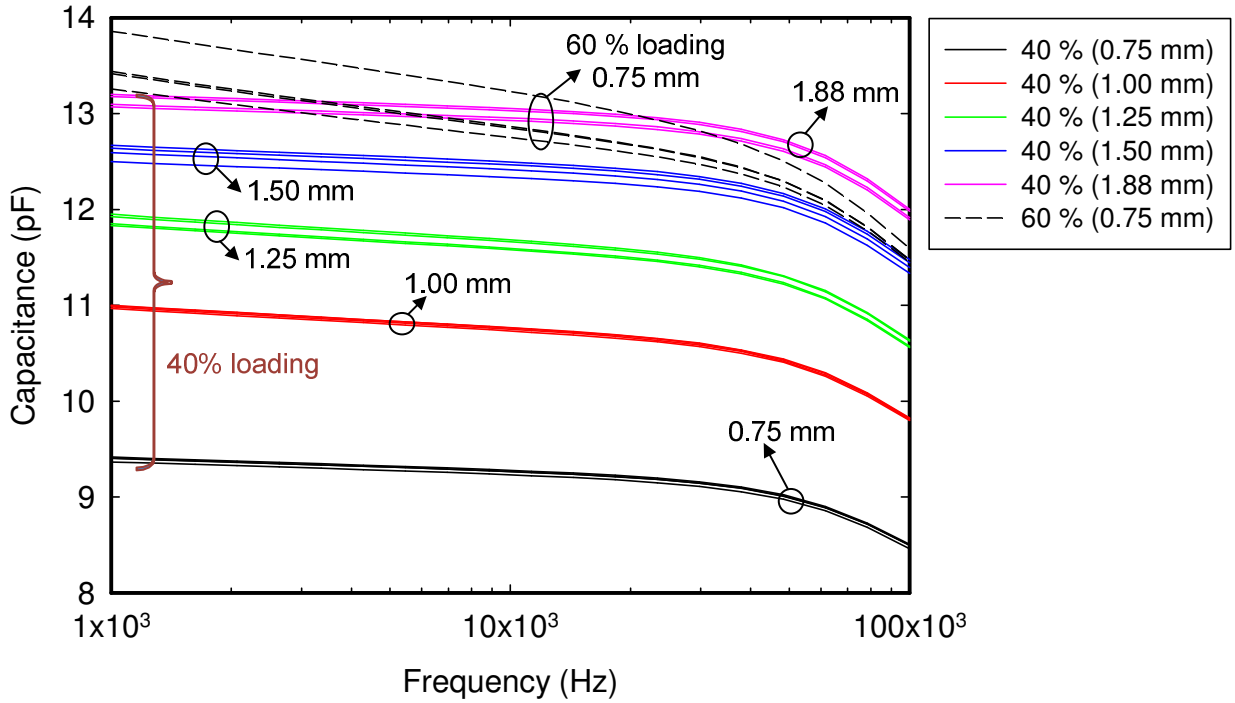

Figure 4-24. *Sensor capacitance for the flexible functional coating sheets with different loadings and thicknesses (40% loading).*

4.6 Measurement Accuracy Analysis

4.6.1 Source of Errors in Measurement

In general, sources of error in the sensor capacitance measurement system include the geometry of the measurement setup configuration, precision of manufacturing of sensor heads, the environmental conditions, and the instrumentation error from the dielectric spectroscopy meter. These sources of error are discussed next.

The measurement error in the contact measurement mode is highly dependent on the surface roughness of a sample and the quality of physical contact. Changes in pressure change the intimacy of contact, affecting the dielectric permittivity in the field enhancement region, in the corners of electrodes, where most electric field energy is stored. In the non-contact measurement mode, the field enhancement region is always in the air, and thus the surface roughness does not introduce a significant error. In this investigation, we used the contact measurement mode with the flexible functional coating sheet (flat surface) to minimize the measurement error, and maintained the same pressure for all measurements.

Since the same sensor head was used here for the reported measurements, the source of error due to using different sensor heads is eliminated.

Furthermore, the dielectric properties of a coating material vary according to the ambient temperature. Our experimental results discussed in Section 4.7.2.3 indicate that temperature variation of around 3° C results in a measurement error of less than 1%. One practical way to eliminate this source error is to calibrate the measurement system before each measurement. The other practical way to avoid the source of error due to the temperature effect is to keep the temperature stable.

According to [7], the source of error of the fully calibrated dielectric spectroscopy meter in the sensor capacitance measurement is less than ± 1.0% [7].

Based on these considerations, we assumed ± 1.0% measurement accuracy to estimate the fringing electric field sensor's measurement accuracy for the functional coating sheet thickness and loading.

4.6.2 Accuracy Analysis for Functional Coating Sheet Thickness

Figure 4-25 shows the schematic diagram of how we estimate the measurement accuracy in the thickness of the functional coating sheets. The relationship between the sensor capacitance and the functional coating sheet thickness can be regressed with a polynomial equation. For a thickness (t_1), the sensor capacitance is C_1, and the corresponding sensor capacitance accounting for the measurement accuracy is $C_{1,max}$ and $C_{1,min}$. Let us place another functional coating sheet with a thicker thickness (t_2.). The sensor capacitance is C_2, and the corresponding sensor capacitance accounting for the measurement accuracy is $C_{2,max}$ and $C_{2,min}$. If $C_{2,min} \approx C_{1,max}$, then the minimum thickness (t_{min}) the system can measure is

$$t_{\min} = t_2 - t_1 \tag{4.3}$$

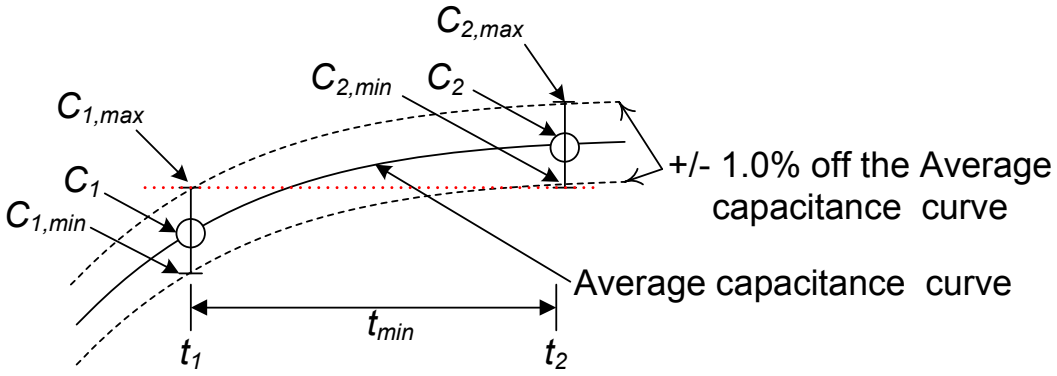

Figure 4-25. *Schematic diagram showing the definition of the minimum measurable thickness of functional coating sheets.*

Table 4.6 shows the thickness measurement accuracy of the functional coating sheets achieved by the measurement system. Regardless of the loading, the system achieves a better accuracy in thickness measurement when the sheet is thinner. This is in part influenced by the sensor's penetration depth. The sensor becomes insensitive to changes in the thickness of the sheets as the thickness of the sheets is close to the sensor's penetration depth. For the sheets with the same thickness, the measurement system provides better thickness measurement accuracy when the functional coating layer has a higher loading. This is because a sheet with a higher

loading is expected to have higher relative dielectric permittivity, which allows for more fringing electric field lines passing through the sheet to reach the sensor's sensing electrode.

Table 4.6. *Accuracy of thickness measurement in different loadings.*

Loading (%)	Thickness (mm)	Accuracy of thickness measurement at 1 kHz (mm)
40	0.75 to 1.00	3.1×10^{-2}
	1.00 to 1.25	5.0×10^{-2}
	1.25 to 1.50	8.0×10^{-2}
	1.50 to 1.88	1.3×10^{-1}
60	0.75 to 1.00	2.2×10^{-2}
	1.00 to 1.25	4.4×10^{-2}
	1.25 to 1.50	6.5×10^{-2}
	1.50 to 1.88	7.3×10^{-2}
80	0.75 to 1.00	2.7×10^{-2}
	1.00 to 1.25	2.6×10^{-2}
	1.25 to 1.50	3.5×10^{-2}
	1.50 to 1.88	8.0×10^{-2}

4.6.3 Accuracy Analysis for Functional Coating Sheet Loading

Figure 4-26 shows the schematic diagram of how we estimate the measurement accuracy in the loading of the functional coating sheets. The relationship between the sensor capacitance and the loading of the functional coating sheet can be regressed with a polynomial equation. For a loading L_1, the sensor capacitance is C_1, and the corresponding sensor capacitance accounting for the measurement accuracy is $C_{1,max}$ and $C_{1,min}$. Let us place another functional coating sheet with a higher loading (L_2). The sensor capacitance is C_2, and the corresponding sensor capacitance accounting for the measurement accuracy is $C_{2,max}$ and $C_{2,min}$. If $C_{2,min} \approx C_{1,max}$, then the minimum loading (L_{min}) the system can measure is

$$L_{\min} = L_2 - L_1 \tag{4.4}$$

Table 4.7 shows the loading measurement accuracy of the functional coating sheets achieved by the measurement system. For the sheets with the same thickness, the measurement system achieves a higher accuracy in the loading measurement when the coating loading is higher. For sheets within the same loading levels, the measurement system achieves the same accuracy in the loading measurement regardless of variations in the thickness of the sheet.

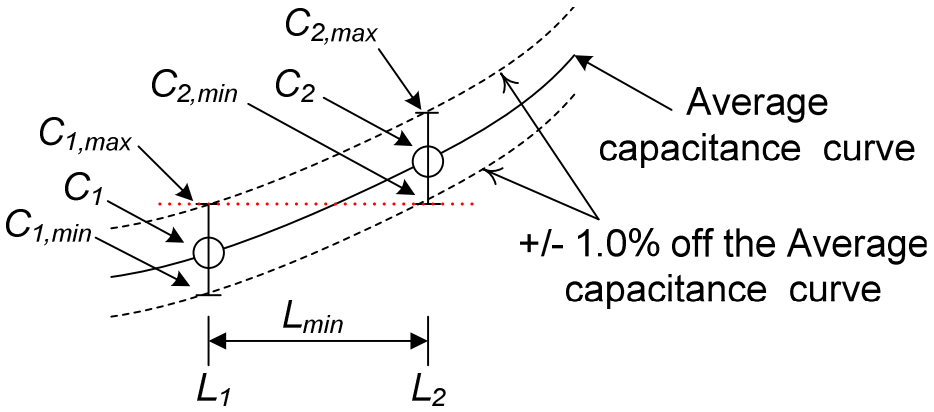

Figure 4-26. *Schematic diagram showing the definition of the minimum measurable loading of flexible functional coating sheets.*

Table 4.7. *Accuracy of loading measurement in different thicknesses.*

Thickness (mm)	Loading (%)	Accuracy of loading measurement at 1 kHz (%)
0.75	40 to 50	1.6
	50 to 60	0.6
	60 to 80	0.5
1.00	40 to 50	1.6
	50 to 60	0.6
	60 to 80	0.5
1.25	40 to 50	1.6
	50 to 60	0.5
	60 to 80	0.4
1.50	40 to 50	1.3
	50 to 60	0.5
	60 to 80	0.4
1.88	40 to 50	1.3
	50 to 60	0.5
	60 to 80	0.4

4.7 Algorithm for In-Process Coating Thickness Measurement

4.7.1 Sensor Capacitance Database

The sensor capacitance database for the flexible functional coating sheets with different loadings and thicknesses is shown in Figure 4-23 and Figure 4-24. To match the algorithm (discussed in Section 4.7.2) that we developed for the in-process functional coating layer thickness measurement, the sensor capacitance database needs to be converted into three matrices.

Matrix A, the sensor capacitance matrix (Figure 4-27), contains the sensor capacitance of the functional coating sheets in the frequency domain. Matrix B, the class matrix (Figure 4-28), relates the sensor capacitance (Matrix A) to a corresponding loading and thickness (Matrix C). Matrix C, the thickness and loading matrix (Figure 4-29), contains thickness and loading information. These three matrices can be replaced if the relationship among the sensor capacitance, the thickness, and the loading of the samples can be regressed as equations.

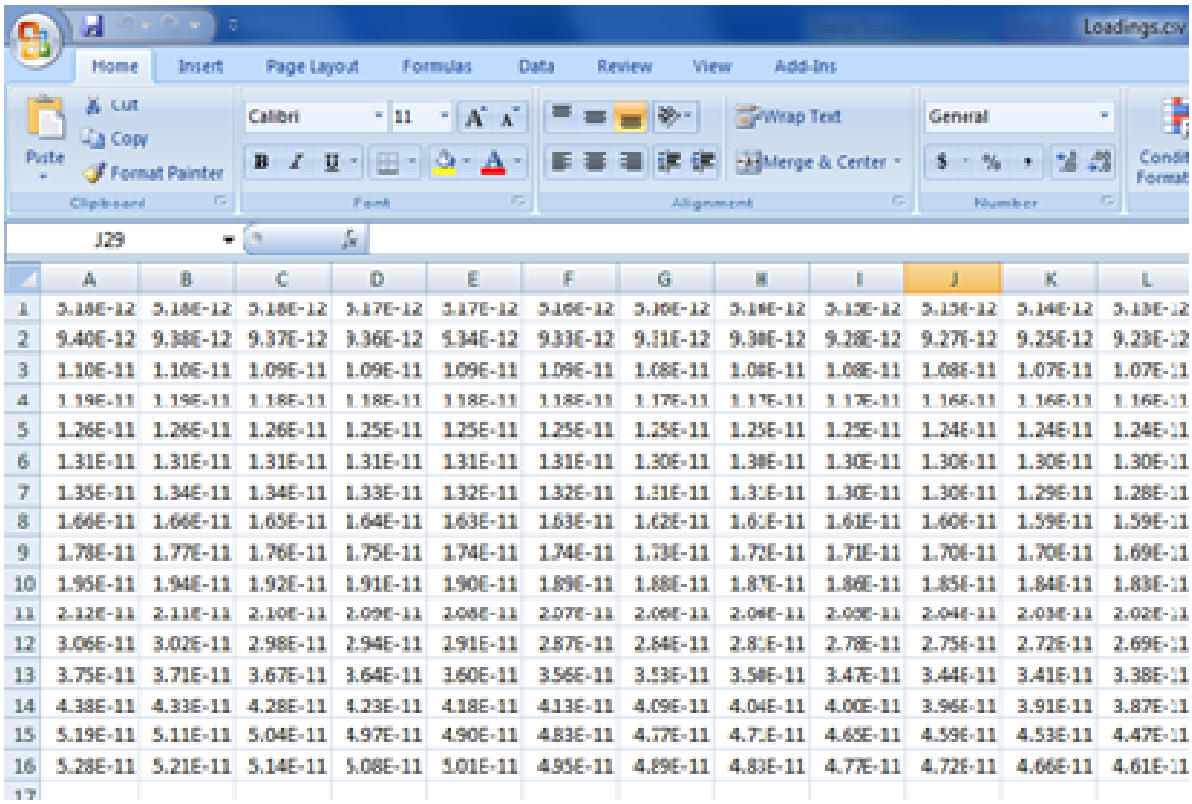

Figure 4-27. *Sensor capacitance matrix.*

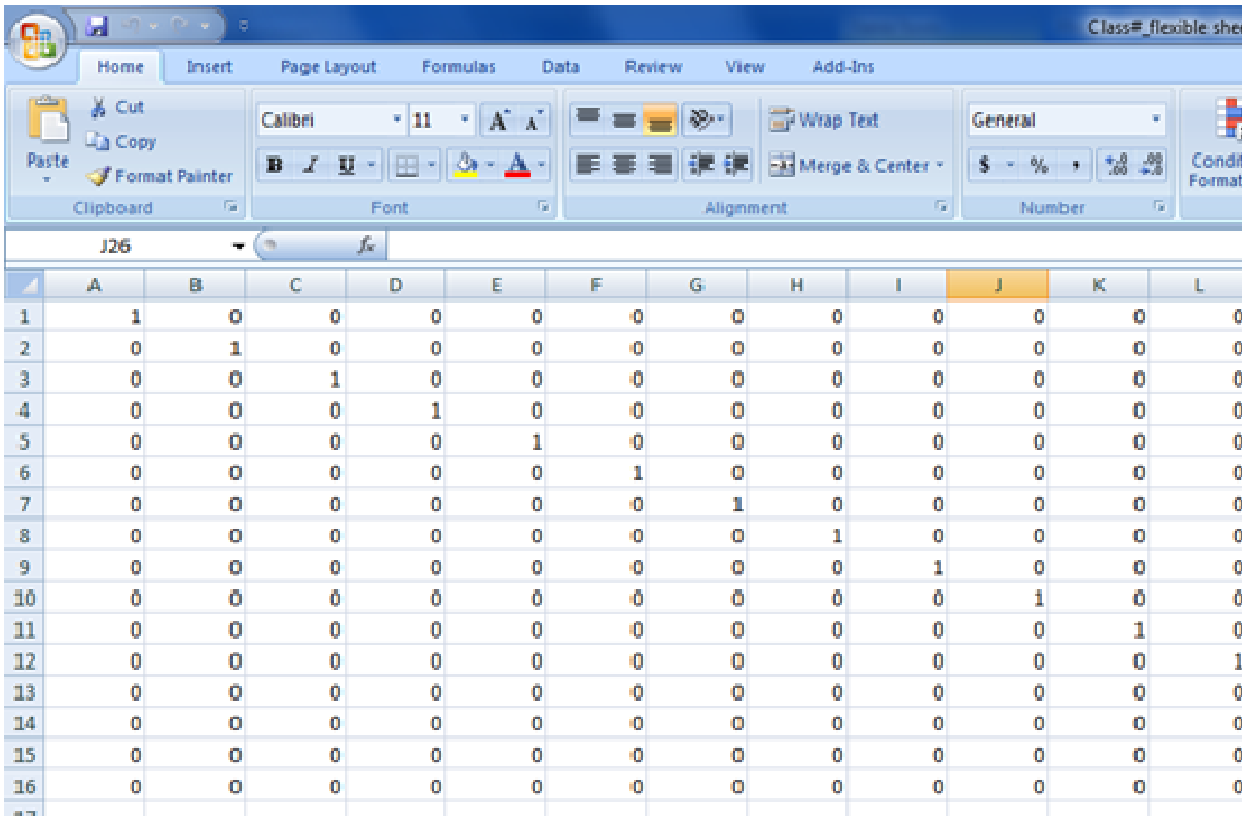

	A	B	C	D	E	F	G	H	I	J	K	L
1	1	0	0	0	0	0	0	0	0	0	0	0
2	0	1	0	0	0	0	0	0	0	0	0	0
3	0	0	1	0	0	0	0	0	0	0	0	0
4	0	0	0	1	0	0	0	0	0	0	0	0
5	0	0	0	0	1	0	0	0	0	0	0	0
6	0	0	0	0	0	1	0	0	0	0	0	0
7	0	0	0	0	0	0	1	0	0	0	0	0
8	0	0	0	0	0	0	0	1	0	0	0	0
9	0	0	0	0	0	0	0	0	1	0	0	0
10	0	0	0	0	0	0	0	0	0	1	0	0
11	0	0	0	0	0	0	0	0	0	0	1	0
12	0	0	0	0	0	0	0	0	0	0	0	1
13	0	0	0	0	0	0	0	0	0	0	0	0
14	0	0	0	0	0	0	0	0	0	0	0	0
15	0	0	0	0	0	0	0	0	0	0	0	0
16	0	0	0	0	0	0	0	0	0	0	0	0

Figure 4-28. *Class # matrix.*

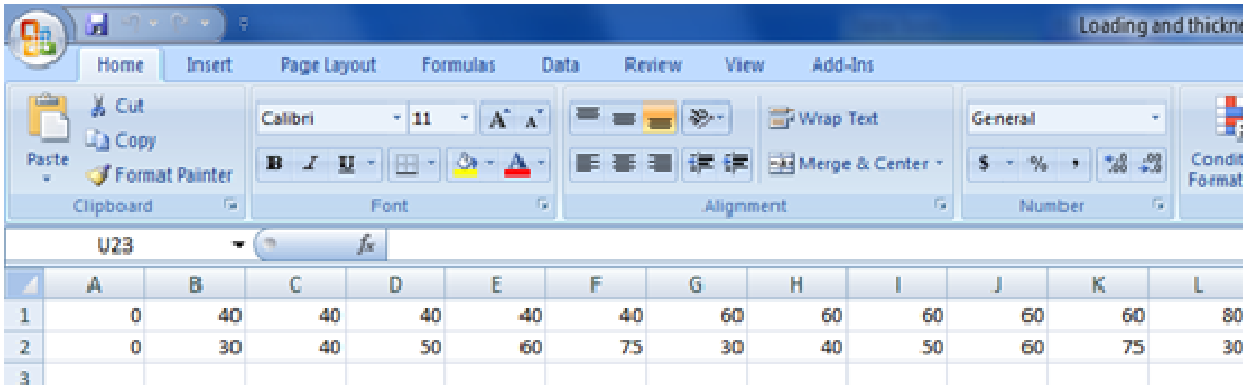

	A	B	C	D	E	F	G	H	I	J	K	L
1	0	40	40	40	40	40	60	60	60	60	60	80
2	0	30	40	50	60	75	30	40	50	60	75	30
3												

Figure 4-29. *Thickness and loading information matrix.*

4.7.2 Algorithm and Measurement Procedures

4.7.2.1 Algorithm for Loading and Thickness Measurement

The algorithm developed in this investigation for the functional coating sheet loading and thickness measurement is based on the kNN algorithm, developed by researchers at Illionix, LLC.

[106]. The kNN means the number of nearest neighbors. Figure 4-30 shows the approach behind the kNN algorithm.

When in-process sensor capacitance for a coating sample is compared to information on the sensor capacitance database, the capacitance difference (Δ) between the measured data and the data on the database at each frequency is expressed as:

$$\Delta = \sum_{f} \left| \Delta_f^{\,2} \right| \tag{4.5}$$

where f is a driving frequency. After the algorithm completes the capacitance difference calculations, a minimum Δ, which corresponds to a known coating thickness and loading, will be shown at the end of the algorithm.

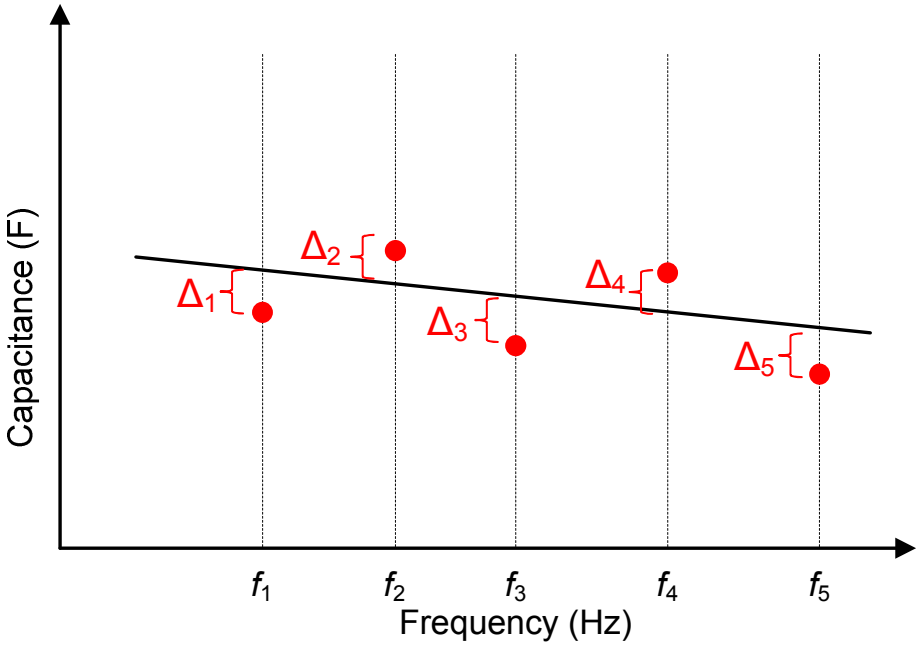

Figure 4-30. *Approach behind the kNN algorithm. Dots represent data from in-process measurements. The line represents capacitance in the sensor capacitance database.*

4.7.2.2 Measurement Procedure

Figure 4-31 shows the measurement procedures for the in-process loading and thickness measurement of the flexible functional coating sheet. The measurement procedure behind the

measurement system contains two processes, including the calibration process and the in-process measurement process. These processes are discussed in the next section.

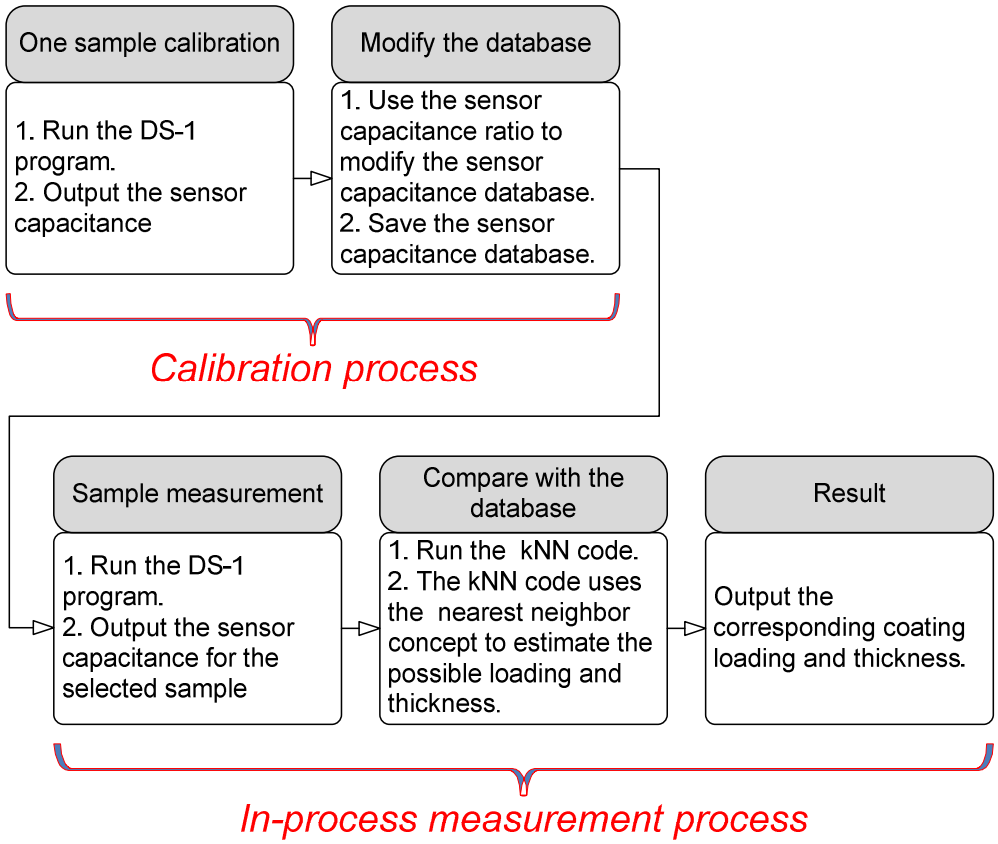

Figure 4-31. *Flowchart showing the measurement procedure.*

4.7.2.3 Calibration Process

Since the sensor capacitance is sensitive to temperature, a calibration process is necessary for temperature compensation. Our experimental results show that when the room temperature decreases from 22.3˚C to 19.7˚C, variation in the sensor capacitance ratio (sensor capacitance measured at 22.3˚C, divided by the new measured sensor capacitance of 19.7˚C) is less than 1%; that is, the sensor capacitance ratios can be regarded as constants for temperatures from 22.3˚C to 19.7˚C.

To calibrate the sensor capacitance database, our approach is to normalize the entire sensor capacitance database by using the sensor capacitance on the 1st column of the sensor capacitance database (Matrix A). Data for this column is obtained from the measurement results for the 40%

loading 0.75 mm thickness functional coating sheet. Figure 4-32 shows how the sensor capacitance database is calibrated. The capacitance values in the original database were taken at 22.3 ˚C.

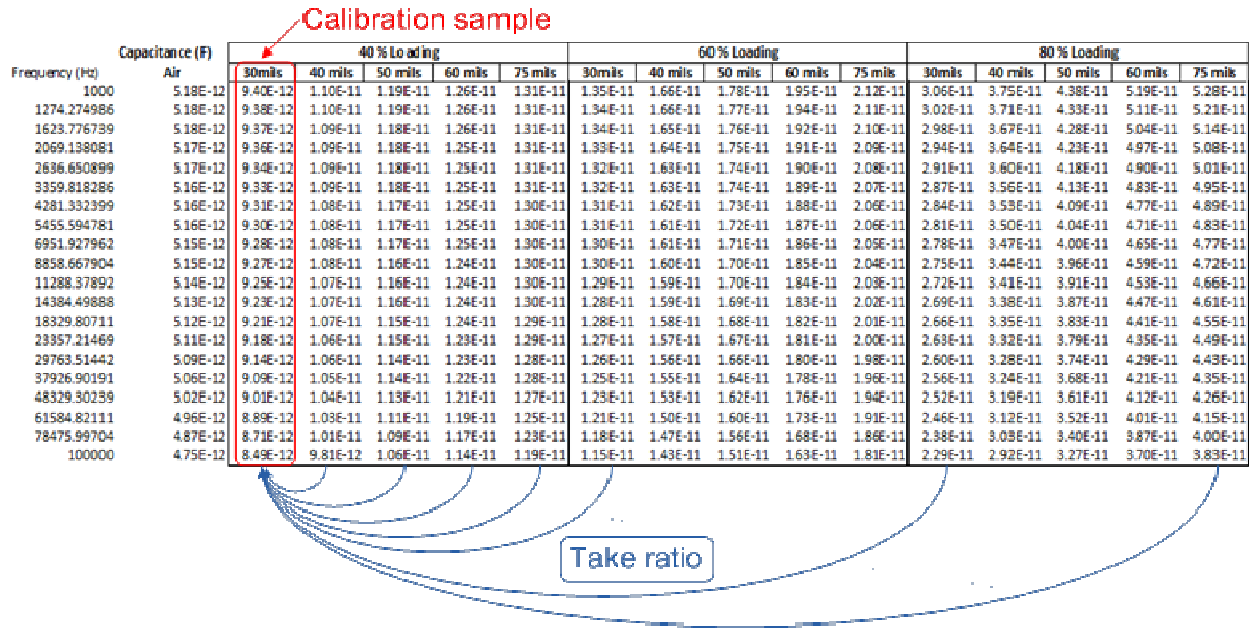

Frequency (Hz)	Capacitance (F) Air	40 % Loading 30mils	40 mils	50 mils	60 mils	75 mils	60 % Loading 30mils	40 mils	50 mils	60 mils	75 mils	80 % Loading 30mils	40 mils	50 mils	60 mils	75 mils
1000	5.18E-12	9.40E-12	1.10E-11	1.19E-11	1.26E-11	1.31E-11	1.35E-11	1.66E-11	1.78E-11	1.95E-11	2.12E-11	3.06E-11	3.75E-11	4.38E-11	5.19E-11	5.28E-11
1274.274986	5.18E-12	9.38E-12	1.10E-11	1.19E-11	1.26E-11	1.31E-11	1.34E-11	1.66E-11	1.77E-11	1.94E-11	2.11E-11	3.02E-11	3.71E-11	4.33E-11	5.11E-11	5.21E-11
1623.776739	5.18E-12	9.37E-12	1.09E-11	1.18E-11	1.26E-11	1.31E-11	1.34E-11	1.65E-11	1.76E-11	1.92E-11	2.10E-11	2.98E-11	3.67E-11	4.28E-11	5.04E-11	5.14E-11
2069.138081	5.17E-12	9.36E-12	1.09E-11	1.18E-11	1.25E-11	1.31E-11	1.33E-11	1.64E-11	1.75E-11	1.91E-11	2.09E-11	2.94E-11	3.64E-11	4.23E-11	4.97E-11	5.08E-11
2636.650899	5.17E-12	9.34E-12	1.09E-11	1.18E-11	1.25E-11	1.31E-11	1.32E-11	1.63E-11	1.74E-11	1.90E-11	2.08E-11	2.91E-11	3.60E-11	4.18E-11	4.90E-11	5.01E-11
3359.818286	5.16E-12	9.33E-12	1.09E-11	1.18E-11	1.25E-11	1.31E-11	1.32E-11	1.63E-11	1.74E-11	1.89E-11	2.07E-11	2.87E-11	3.56E-11	4.13E-11	4.83E-11	4.95E-11
4281.332399	5.16E-12	9.31E-12	1.08E-11	1.17E-11	1.25E-11	1.30E-11	1.31E-11	1.62E-11	1.73E-11	1.88E-11	2.06E-11	2.84E-11	3.53E-11	4.09E-11	4.77E-11	4.89E-11
5455.594781	5.16E-12	9.30E-12	1.08E-11	1.17E-11	1.25E-11	1.30E-11	1.31E-11	1.61E-11	1.72E-11	1.87E-11	2.06E-11	2.81E-11	3.50E-11	4.04E-11	4.71E-11	4.83E-11
6951.927962	5.15E-12	9.28E-12	1.08E-11	1.17E-11	1.25E-11	1.30E-11	1.30E-11	1.61E-11	1.71E-11	1.86E-11	2.05E-11	2.78E-11	3.47E-11	4.00E-11	4.65E-11	4.77E-11
8858.667904	5.15E-12	9.27E-12	1.08E-11	1.16E-11	1.24E-11	1.30E-11	1.30E-11	1.60E-11	1.70E-11	1.85E-11	2.04E-11	2.75E-11	3.44E-11	3.96E-11	4.59E-11	4.72E-11
11288.37892	5.14E-12	9.25E-12	1.07E-11	1.16E-11	1.24E-11	1.30E-11	1.29E-11	1.59E-11	1.70E-11	1.84E-11	2.03E-11	2.72E-11	3.41E-11	3.91E-11	4.53E-11	4.66E-11
14384.49888	5.13E-12	9.23E-12	1.07E-11	1.16E-11	1.24E-11	1.30E-11	1.28E-11	1.59E-11	1.69E-11	1.83E-11	2.02E-11	2.69E-11	3.38E-11	3.87E-11	4.47E-11	4.61E-11
18329.80711	5.12E-12	9.21E-12	1.07E-11	1.15E-11	1.24E-11	1.29E-11	1.28E-11	1.58E-11	1.68E-11	1.82E-11	2.01E-11	2.66E-11	3.35E-11	3.83E-11	4.41E-11	4.55E-11
23357.21469	5.11E-12	9.18E-12	1.06E-11	1.15E-11	1.23E-11	1.29E-11	1.27E-11	1.57E-11	1.67E-11	1.81E-11	2.00E-11	2.63E-11	3.32E-11	3.79E-11	4.35E-11	4.49E-11
29763.51442	5.09E-12	9.14E-12	1.06E-11	1.14E-11	1.23E-11	1.28E-11	1.26E-11	1.56E-11	1.66E-11	1.80E-11	1.98E-11	2.60E-11	3.28E-11	3.74E-11	4.29E-11	4.43E-11
37926.90191	5.06E-12	9.09E-12	1.05E-11	1.14E-11	1.22E-11	1.28E-11	1.25E-11	1.55E-11	1.64E-11	1.78E-11	1.96E-11	2.56E-11	3.24E-11	3.68E-11	4.21E-11	4.35E-11
48329.30239	5.02E-12	9.01E-12	1.04E-11	1.13E-11	1.21E-11	1.27E-11	1.23E-11	1.53E-11	1.62E-11	1.76E-11	1.94E-11	2.52E-11	3.19E-11	3.61E-11	4.12E-11	4.26E-11
61584.82111	4.96E-12	8.89E-12	1.03E-11	1.11E-11	1.19E-11	1.25E-11	1.21E-11	1.50E-11	1.60E-11	1.73E-11	1.91E-11	2.46E-11	3.12E-11	3.52E-11	4.01E-11	4.15E-11
78475.99704	4.87E-12	8.71E-12	1.01E-11	1.09E-11	1.17E-11	1.23E-11	1.18E-11	1.47E-11	1.56E-11	1.68E-11	1.86E-11	2.38E-11	3.03E-11	3.40E-11	3.87E-11	4.00E-11
100000	4.75E-12	8.49E-12	9.81E-12	1.06E-11	1.14E-11	1.19E-11	1.15E-11	1.43E-11	1.51E-11	1.63E-11	1.81E-11	2.29E-11	2.92E-11	3.27E-11	3.70E-11	3.83E-11

Figure 4-32. *Capacitance database of the flexible MagRAM sheets of different loadings measured at 22.3 ˚C.*

4.7.2.4 In-Process Measurement Process

Once the sensor capacitance database is calibrated, the second process is to perform an in-process measurement for a randomly selected flexible functional coating sheet. Once the measurement system obtains the sensor capacitance for the selected sample sheet, the algorithm, then, goes through the in-process measurement process to estimate loading and thickness of the sample sheet. Figure 4-33 shows the screenshot of the program GUI. We implemented simultaneous measurement of two different coating samples with functional coatings in different levels.

Figure 4-33. *Screenshot of the in-process measurement program GUI.*

4.8 Conclusion

According to the numerical modeling results, we optimized and fabricated the 4 mm penetration depth concentric fringing electric field sensor for experiments. This sensor shows a higher sensitivity in the capacitance measurement to variations in the functional coating thickness of interest.

The experimental results show that for the contact measurement configuration, a sample's surface roughness and non-flatness influence the functional coating layer thickness measurement. A sample with better surface qualities will improve the thickness measurement. For the non-contact measurement configuration, the air gap between the coating sample and the fringing electric field sensor electrodes benefits the coating thickness measurement.

The capacitance of the functional coating sheets with different loadings and thicknesses in the frequency domain obtained by the FEF sensor indicates this FEF sensor is applicable for in-process functional coating layer thickness and loading measurements. Measurement accuracy analysis shows that the coating thickness measurement accuracy is better than 0.1 mm and the coating loading measurement accuracy is better than 1.5%. In addition, we demonstrate that the developed loading and thickness measurement algorithm has been successfully used to measure the functional coating layer thicknesses and loadings.

Chapter 5 **Thermal Management of Electronics**

5.1 Motivation

Thermal management in electronics is facing a critical challenge because of rapid technology advancement, which has led to enormous component density and heat flux generation, leaving only small physical room for thermal engineers to work. Although conventional rotary fan cooling technology has been widely adopted for industrial users and consumers because of its simplicity for large form factor microelectronics, it is no longer considered a viable thermal management solution for advanced microelectronics [107].

State of the art power delivery components occupy up to 30% surface area of the printed circuit board (PCB) or printed wire board (PWB) for a computer [108]. As the scale of the computer goes down, namely smaller form factor chambers, power delivery components are expected to cover more than 30% of the surface area of the PCB/PWB. The increased power component density will lead to larger heat flux density than it has generated today and, thus, relies on a more efficient thermal module to allow for the normal function of the electronic chambers. Additionally, the amount of the anticipated transistor density will be more than 1010 per die [108] by 2010, as shown in Figure 5-1. As the CMOS fabrication process technology is improved and switched from 90 nm to 16 nm, the predicted power density will grow up exponentially by approximately 13 times [108], as shown in Figure 5-2. This growing upwards trend will lead to a large amount of heat flux, which needs to be transferred to ensure the normal operation of the future electronic chambers.

Electrostatic fluid accelerators (EFAs), also known as ionic wind pumps or corona wind pumps, have been developed to overcome the disadvantages of the conventional rotary fan cooling technology and have achieved comparable and better heat transfer performance than the conventional rotary fan cooling technology for the thermal management of small form factor electronics [25, 109, 110] and microelectronics [19-23, 26, 27]. To dissipate higher heat flux generated from future microelectronics, liquid-driven techniques, such as spray cooling [86, 111, 112], liquid jet cooling [62, 63], microchannel [113-122], and micro pump [113, 123-130] are the most potential solutions and have been widely investigated as a result.

Among the liquid cooling technologies, conventional evaporative spray cooling is one of the most potential solutions for microelectronics [111, 112, 131-133], due to its ability to dissipate heat fluxes [134-136] in a broad variety of ranges in microprocessors using a combination of convection and evaporation at the solid-liquid interface. However, several technology barriers exist to be overcome in conventional spray cooling technologies, including the requirement of a high performance mechanical pump for the fluid atomization processes, the limited droplet transportation abilities, and the poor droplet size control.

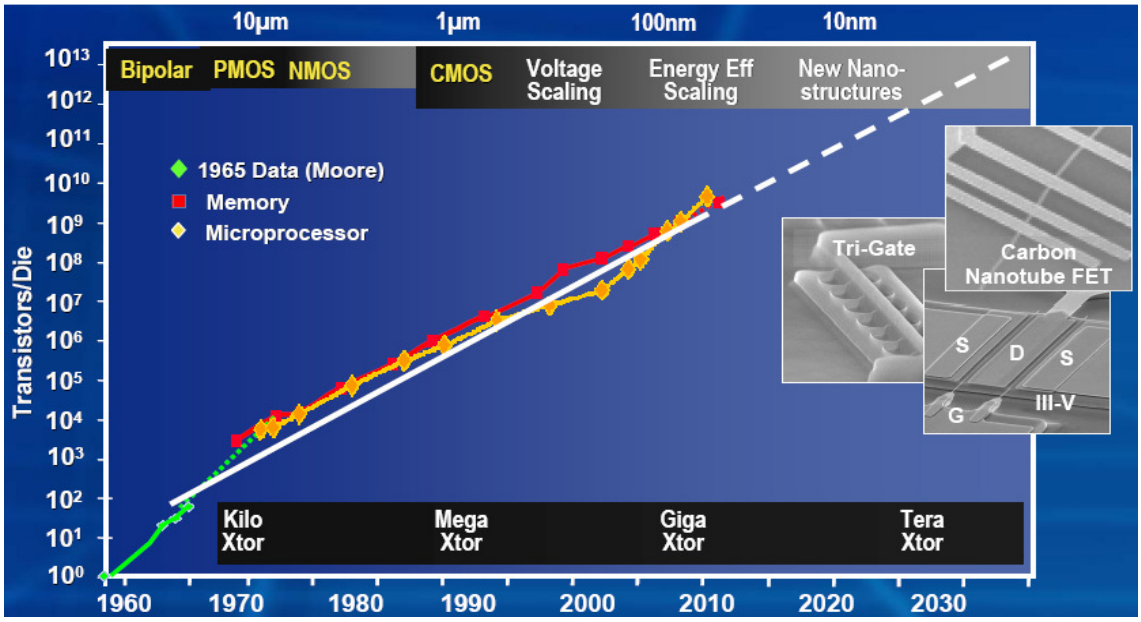

Figure 5-1. *Trend of number of transistors per die for micromicroelectronics through the next decade and beyond [108].*

Electrospray evaporative cooling (ESEC), which is also called a fringing electric field (FEF) actuator, which relies on Coulomb force for energy-efficient fluid atomization, has great potential to precisely control the formation of droplet sizes and droplet distribution, and hence can be adapted to create a uniform temperature over the surfaces of integrated circuit components of microelectronics. In the past, the electrospray technology was primarily used for application in areas such as mass spectroscopy [55-57], microthruster [56], and nanofibers [58]. The application of electrospray in thermal management of microelectronics is currently limited, in part due to limited practical design methodology and heat transfer performance optimization methodology.

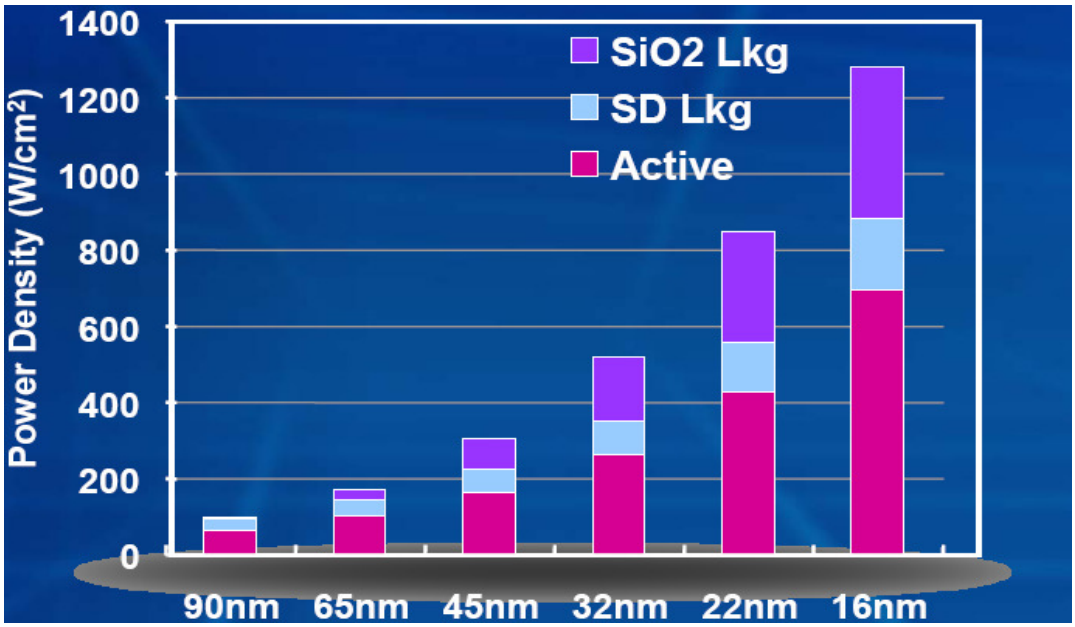

Figure 5-2. *Increase in power density of micromicroelectronics with direct CMOS scaling relationships [108].*

Feng and Bryan [86] investigated the heat transfer performance enhancement through the application of the electrohydrodynamics (EHD) on traditional impinging liquid jets over a thermal exchange surface by using the cooling chambers of a different number of capillary tubes in an enclosed cooling loop system. Their experimental result shows that the application of the potential on the traditional impinging liquid jets can enhance the heat transfer rate of the cooling chamber by approximately 1.7 at the lower heat flux (less than 30 W/cm^2). The critical heat flux (CHF) was approximately 70 W/cm^2. The critical heat flux defined in their publication was the heat flux, which makes the heat transfer enhancement below one. Better enhancement in the heat transfer rate is also achieved by the chamber with multiple capillary tubes at a lower heat flux condition.

Deng and Gomez [137] have achieved a heat dissipation of 96 W/cm^2 with a cooling efficiency of 97% by operating a microfabricated multiplexed electrospray system (MES) in the cone-jet mode. The MES uses 19 and 37 nozzles with a packing density of 253 nozzles/cm^2. The results also suggest that an increase in the number of electrospray nozzles per unit area is feasible for cooling of microelectronics in a broad range of applications.

Although heat transfer cooling capability of ESEC chambers over a CPU-size thermal exchange surface has been demonstrated experimentally, the potential design methodology,

performance optimization methodology, and empirical heat transfer correlations to estimate the heat transfer characteristic of the micronozzle-based ESEC chambers still have not been presented as a whole. This dissertation investigates the design methodology, performance optimization methodology, and the empirical heat transfer correlations for the ESEC chambers in terms of the number of micronozzles, total volume flow rates of the working fluid, applied DC potentials, and the gaps between the electrospraying micronozzle and a thermal exchange surface.

5.2 Design Methodology of the ESEC Chambers

5.2.1 Design Criterion

The objective of designing electrospray evaporative cooling (ESEC) chambers is to optimize the heat transfer performance of ESEC chambers through the optimization of the distribution of the electric field intensity between the tip of the micronozzle and the thermal exchange surface (TSE), which is also the collecting electrode. Electric field intensity optimization results in the energy-efficient EHD processes and forces a lot of charged droplets to transport along the spatially-optimized trajectory to cover a larger surface area on the thermal exchange surface, which allows for higher heat transfer rates and lowers the surface temperature over the thermal exchange surface. Following this, the major design methodology is to create, improve, and optimize the electric field distribution of ESEC chambers.

In general, Figure 5-3 shows that the key parameters affecting the electric field distribution of ESEC chambers can be categorized into four major groups, including the geometry of the ESEC chambers, the materials consisting of the ESEC chambers, the working fluid property, and the movement of the electrified droplets (or charged droplets). The first three groups are discussed in this chapter.

5.2.1.1 Geometry of the ESEC chambers

Packaged dimension of the central processing unit (CPU), the graphic processing unit (GPU), or the accelerated processing unit (APU) is approximately 3 cm by 3 cm. The proposed maximum diameter of the ESEC chambers is limited by this factor.

Figure 5-4 shows the overall dimensions and components of the proposed ESEC chambers. The chamber consists of four major components, namely: a fluid chamber, a cover, a metal plate, and several micronozzles. The material of the chamber is acrylic. The exterior dimension of the chamber was designed to be 24 mm in diameter and 20 mm in length. The inner diameter and the thickness of the chamber wall are 20 mm and 2 mm, respectively. The top of the chamber is covered by a circular cover, also made of acrylic, with an o-ring and a 1/8″ NPT hole on top of the cover. The o-ring was used to seal the chamber, and the hole was connected to a NPT Swagelok nut connector for the working fluid supply and temperature measurement of the working fluid. The bottom of the chamber was drilled with certain quantities of micro-scale channels to allow for the penetration of micronozzles.

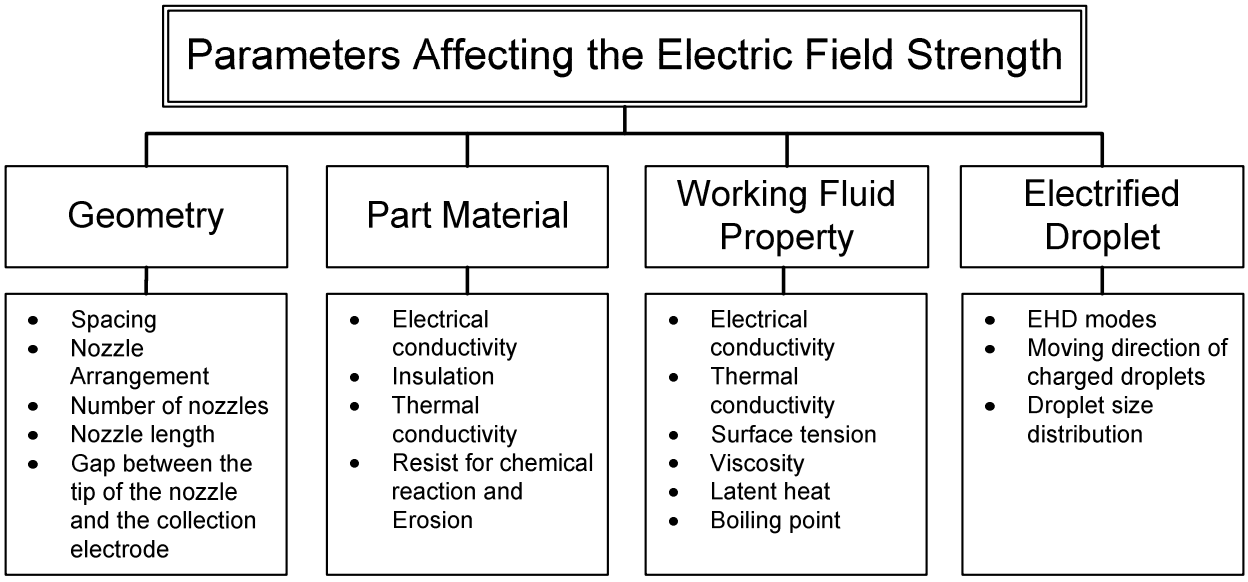

Figure 5-3. *Schematic diagram showing the parameters affecting the electric field intensity of the proposed ESEC chambers.*

The inside bottom of the chamber is placed with a copper plate which is connected to a high positive DC potential. The copper plate is 20 mm in diameter and 3 mm in thickness and was drilled with a certain number of microchannels to secure the micronozzles.

The relative position of microchannels is the key geometric parameter discussed in this dissertation. To present the geometry difference among the designed ESEC chambers, a parameter, spacing, was defined and shown in Figure 5-5. The spacing is the distance between

the center of the cooper plate and the center of one of the micronozzles of the chamber. Seven chambers with different spacing and different quantities of micronozzles were designed and fabricated, including one 1-nozzle chamber, three 4-nozzle chambers, and three 8-nozzle chambers. Table 5.1 shows the respective spacing among three types of the chambers. The spacing for the 1-nozzle chamber is zero, while that of the other two types of the chambers are 4, 5, and 6 mm. The spacing selection of 4, 5, and 6 mm was decided according to the numerical modeling results of the electrostatic field distribution, which is thoroughly discussed in 5.3.

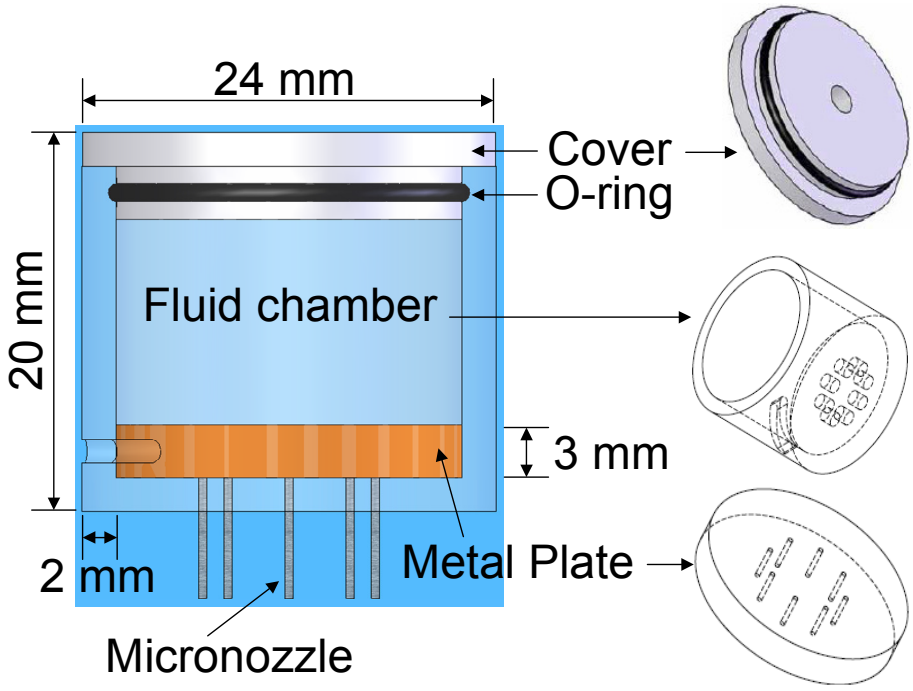

Figure 5-4. *Schematic diagram of the components and overall dimensions of the proposed ESEC chambers.*

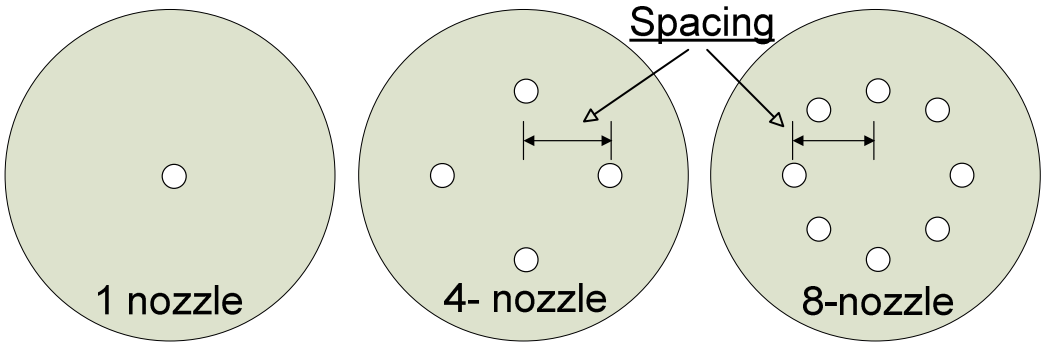

Figure 5-5. *Definition of the spacing of the chambers.*

Table 5.1. *Summary of the seven chambers designed with different spacing.*

	1-nozzle chamber	4-nozzle chamber	8-nozzle chamber
Spacing (mm)	0	4, 5, 6	4, 5, 6

Figure 5-6 shows the assembled 1-nozzle chamber, 4-nozzle chamber, and 8-nozzle chamber. The spacing for the 4-nozzle chamber and the 8-nozzle chamber is 5 mm. The interfaces among the inner wall of the chamber, the microchannel-based copper plate, and the micronozzles were secured by a specific epoxy which should not be able to react with the physical properties of the working fluid used for the experiment. The epoxy used is J-B WELD.

Figure 5-6. *The assembled 1-nozzle chamber, 4-nozzle chamber (5 mm spacing), and 8-nozzle ESEC chamber (5 mm spacing).*

5.2.1.2 Part Material

Material selection for the ESEC chambers highly depends on the working environment and the working fluid. Table 5.2 shows the potential materials and restrictions for material selection of the components of the ESEC chambers. In general, since the fluid chamber and the cover are exposed to a relative higher temperature environment, the material for the chamber and the cover should have the property of a lower thermal conductivity, in order to maintain stable working fluid temperature during operation. Furthermore, chemical reaction and erosion between the chamber and the working should also be considered and prohibited, in order to maintain the reliability of the fluid chamber and the physical quality of the working fluid. The potential material for the fluid chamber and the cover is acrylic and polycarbonate.

The primary function of the metal plate inside the fluid chamber is to conduct the high DC potential to the working fluid, in order to generate the EHD processes; therefore, the material with high electrical conductivity is required. Copper is suggested and used because it has been used and compatible with the fabrication of the electronic components in the industry, worldwide. The electrical-grade copper is even better.

Table 5.2. *Restrictions and potential material for the components of the ESEC chambers.*

Component	Fluid chamber & Cover	Metal plate	Micronozzle
Restriction	• Low thermal conductivity • Low electrical conductivity • Chemical reaction and erosion resist	• High electrical conductivity	• Low electrical conductivity • Low thermal conductivity • Chemical reaction and erosion resist
Potential material	• Acrylic • Polycarbonate	• Copper	• Stainless steel • Acrylic

EHD processes happen near the tip of the micronozzles, and they are also directly exposed to a higher temperature and a higher vapor concentration environment; therefore, the material for the micronozzles should be able to resist erosion and chemical reaction, in order to retain the best designed heat transfer performance for long operation periods. Additionally, lower electrical conductivity and thermal conductivity are preferred because of the demand of higher EHD efficiency and lower conductive heat transfer through the micronozzles to the working fluid inside the micronozzle and inside the fluid chamber. Potential material is stainless steel and acrylic capillary. These two materials are available in micro-scale in diameter, and the length of interest can be customized. Since the heat transfer enhancement of the ESEC chamber using stainless steel micronozzles is higher than that of using acrylic micronozzles [86], customized stainless steel micronozzles from MicroGroup, Inc. were used. The inner diameter (ID) of the micronozzle is 210 μm, the outer diameter (OD) of the micronozzle is 410 μm, and the length of the micronozzle is 9.98 mm.

5.2.1.3 Working Fluid Property

Working fluid selection highly depends on the compatibility between the liquid and the specific material composition of such microelectronic components as silicon, gold, copper, epoxy, glass, and etc. Table 5.3 shows four potential working fluids (two dielectric liquids, ethanol alcohol, and water) that have been broadly used in electronic cooling modules.

Water has the highest thermal physical properties and surface tension. Higher thermal physical properties are good for phase-change heat transfer; however, higher surface tension largely restricts the EHD process operation region and increases the onset voltage of the EHD process.

Table 5.3. *The physical properties of potential working fluids at 25°C.*

Property	Unit	HFE-7100	FC-72	C_2H_5OH	H_2O
Liquid specific heat	J/kg·℃	1183	1100	2480	4179
Liquid density	kg/m^3	1481.6	1680	804.4	997
Vapor density	kg/m^3	10.2	13.9	1.4×10^{-1}	2.3×10^{-2}
Surface tension	dynes/cm	13.6	10	22.3	72.0
Boiling point	℃	61	56	78.3	100
Thermal conductivity	W/m·K	6.9×10^{-2}	5.7×10^{-2}	1.8×10^{-1}	6.1×10^{-1}
Electrical conductivity	S/m	7×10^{-10}	10^{-12}	1.0×10^{-9}	5×10^{-4}
Dynamic Viscosity	kg/m·s	3.8×10^{-1}	6.4×10^{-4}	1.1×10^{-3}	1.0×10^{-3}
Dielectric constant		7.39	1.75	24.3	78.0
Heat of vaporization	kJ/kg	111.6	87.92	837.4	2438.0

Dielectric liquids have been used for direct cooling of microelectronic components because of the features of stringent thermal, electrical, and chemical properties. The perfluorocarbons (FCs) and hydro-fluoro-ethers (HFEs) series dielectric liquids made from the 3M Corporation are the most well known coolants for liquid cooling of microelectronics, and they have been successfully adopted for the cooling of electronic components in several supercomputers [138]. The thermal physical properties of the dielectric liquids are the lowest among the four potential working fluids, and would not benefit the phase-change heat transfer requirement, although their surface tension is also the lowest, which would lower the onset voltage of the EHD process and increase the operational region of the EHD process.

Ethanol alcohol has moderate thermal physical properties and surface tension among the four potential working fluids and has been adopted for EHD-related research [67, 86]. Since the ESEC chambers investigated in this dissertation is an open loop system, 99.99% ethanol alcohol was adopted.

5.2.2 Design Procedures

Figure 5-7 shows the design procedures of ESEC chambers. The detailed description is as follows.

(1) The overall dimension of the ESEC chamber is confined by the specific application, namely, the size of the electronic components. In addition, the components consisting of the ESEC chamber are subject to be compatible with applicable fabrication and installation requirements.

(2) The selection of the working fluid and the material for the components of the chamber should be parallel decided for material compatibility.

(3) The components of the ESEC chambers are fabricated and assembled.

(4) Achievable Heat transfer performance among different ESEC chambers is then conducted at an open loop system in the open environment.

(5) Models regarding to the ESEC chambers for numerical simulation of the electrostatic field distribution are established and run using the COMSOL Multiphysics software.

(6) The spatial electrical field intensity distribution and the surface charge distribution at the tip of the micronozzles are analyzed.

(7) The data from measurement results of heat transfer performance and the numerical electrostatic modeling results are compared to discuss the heat transfer performance differences among the ESEC chambers.

The electrostatic field modeling investigations are discussed in 5.4, and the experimental investigations are discussed in 5.5.

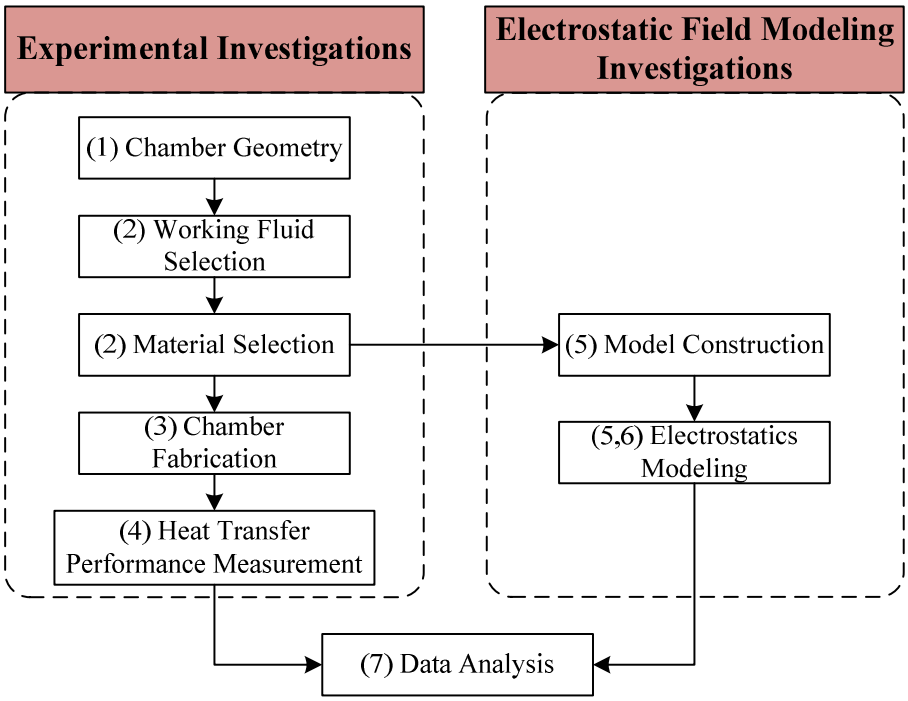

Figure 5-7. *Schematic flowchart showing the design procedures for the ESEC chambers.*

5.3 Experimental Apparatus for the ESEC Chambers

5.3.1 Experimental Apparatus

Figure 5-8 shows the experimental apparatus for heat transfer characteristic investigation of the ESEC chambers. The apparatus is composed of four major units, including a custom-designed testing platform, microchannel-based fluid chambers, working fluid supply unit, and high DC potential supply unit. These four major units are discussed in more detail as follows.

5.3.1.1 Custom-Designed Testing Platform

Figure 5-9 shows the schematic diagram of the custom-designed testing platform. The platform consists of a thermal insulation block, an AC electrical heater, a layer of ceramic-based thermal compound, a collecting electrode, four plastic screws, and four K-type thermocouples. The dimensions of the thermal insulation block are 44 mm (L) × 44 mm (W) × 40 mm (H). The thermal insulation block is made of Teflon. Night holes were drilled into the sidewalls of the

thermal insulation block. Four holes are used to position the electrically insulated thermocouples which are used to measure temperature inside the thermal exchange plate (collecting electrode). Four holes are used to secure the collecting electrode by the plastic screws (made of Teflon). One hole is used to ground the collecting electrode through an electric wire. Assuming at moderate heat flux generated from the heater, the estimated heat loss from the peripheral surfaces and the bottom surface of the thermal insulation block was calculated to be less than 5% and 1%, respectively.

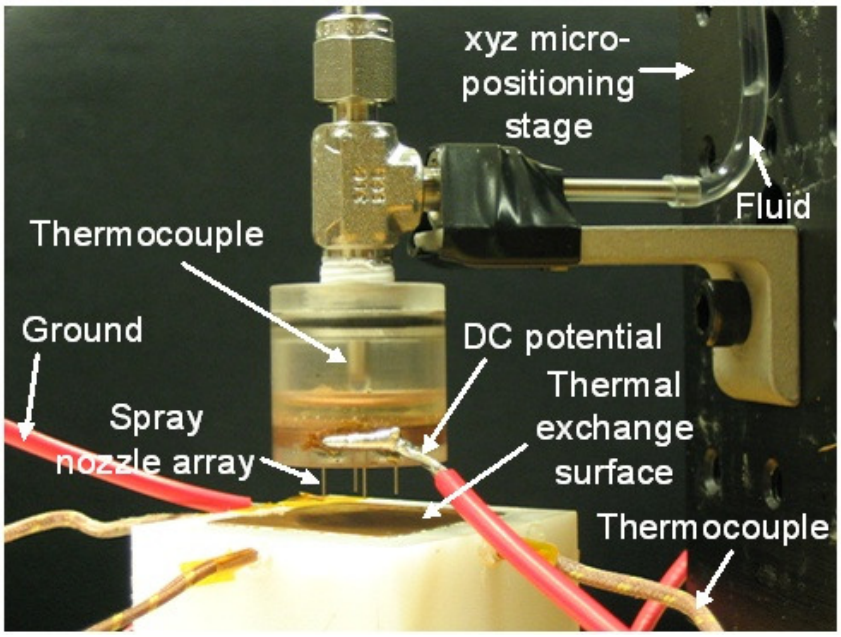

Figure 5-8. *The experimental apparatus for the heat transfer performance measurement of the ESEC chambers.*

The collecting electrode is made of copper, and its dimension is 30 mm (L) × 30 mm (W) × 4 mm (H). Eight holes were drilled on the four sidewall of the copper plate for the insertion of four thermocouples and plastic screws. One thermocouple was placed directly under the center of the collecting electrode, and the rest of the thermocouples were positioned 7 mm deep into the collecting electrode from the remaining sidewalls (Figure 5-10).

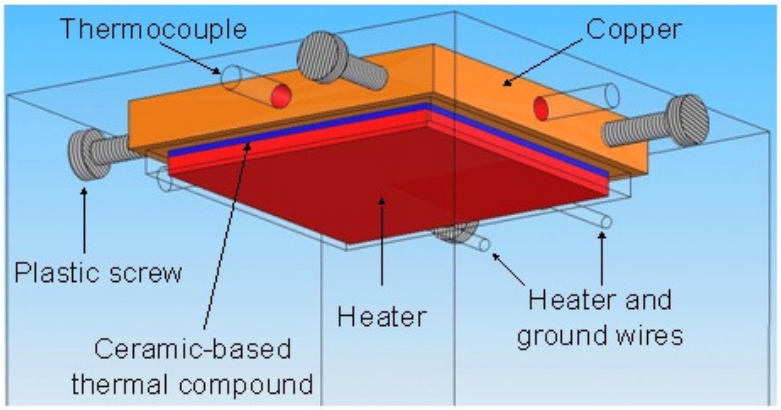

Figure 5-9. *Schematic diagram of the testing platform for heat transfer enhancement measurement of the ESEC chambers. The platform consists of an electrical and thermal insulation block (transparent), an AC electrical heater (red), a layer of ceramic-based thermal compound (blue), a collecting electrode (orange), four plastic screws (gray), and four electrically insulated K-type thermocouples (transparent tubes).*

To position the collecting electrode in place and to minimize the heat loss from its peripheral surfaces, the collecting electrode was clamped using four plastic screws inside the thermal insulation block. Only the top surface of the collecting electrode was exposed to the surrounding environment. During the experiment, the collecting electrode was connected in series with a resistor to a ground.

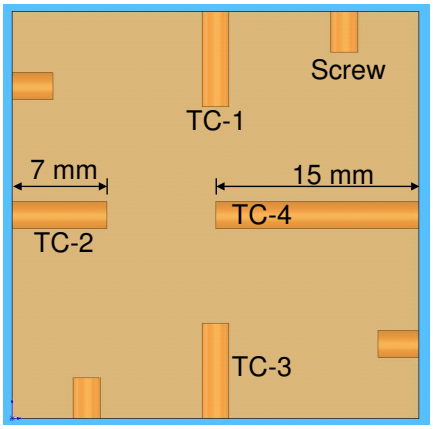

Figure 5-10. *Schematic diagram of the thermocouple placement inside the thermal exchange surface.*

Figure 5-11 shows the snapshot of the AC electrical heater which is a square (1 in × 1 in) Kapton (Polyimide) Thermofoil^{TM} heater made by Minco Corporation. The heater is driven by an

AC voltage power source (ELGAR CW1251). The relationship among the driving voltage, the corresponding heat flux, and the temperature inside the collecting electrode (TSE, thermal exchange surface) is shown in Figure 5-12. The correlation is expressed as follows.

$$q'' = 27.0732 + 3.1091\exp\left(0.5253V_h\right) \tag{5.1}$$

$$T_i = -9.89 + 16.5633V_h \tag{5.2}$$

where V_h is the driving AC voltage on the heater, and T_i is the temperature inside the thermal exchange surface (TSE). In general, the temperature inside the thermal exchange surface grows linearly when the driving AC potential is raised from 3 V to 9 V. The growth behavior of the corresponding heat flux of the heater with respect to the driving AC voltage is exponential. During the experiment, the electrical heater was connected in series with a resistor to an AC power supply (CW 1251).

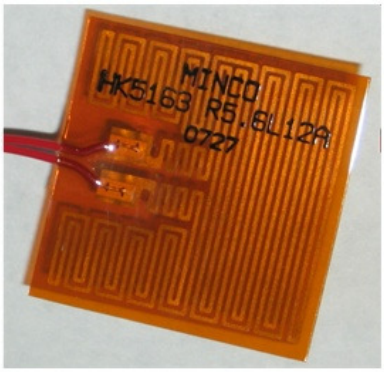

Figure 5-11. *The photograph of the Kapton ThermofoilTM heater.*

A ceramic-based thermal compound layer was placed between the collecting electrode and the electrical heater to ensure that no electrical conduction path exists in between, as well as to minimize the interfacial thermal resistance.

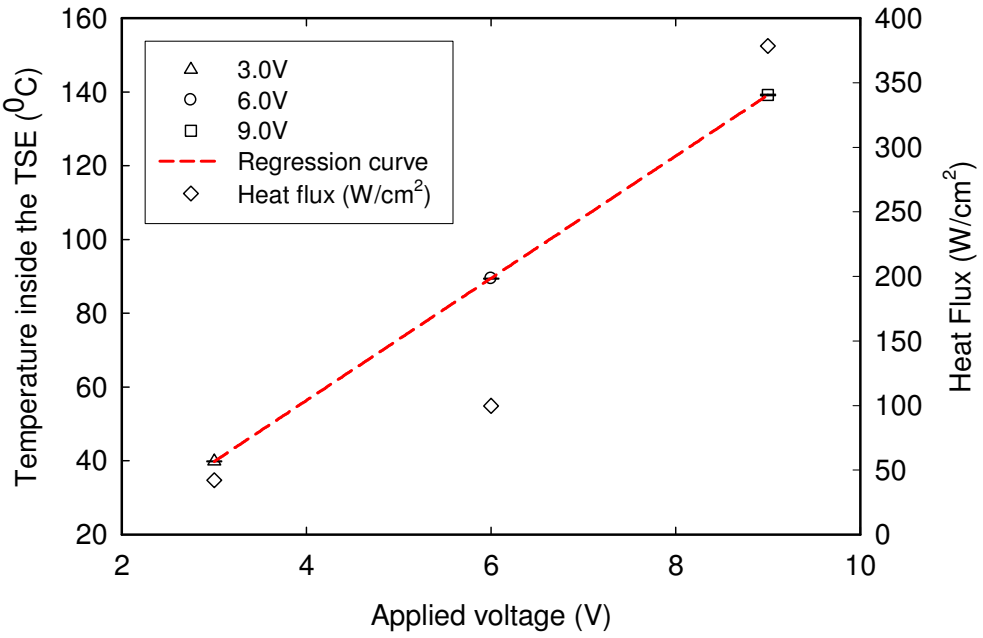

Figure 5-12. *The temperature and heat flux characteristic of the square Kapton heater at different AC voltages.*

A correlation between the surface temperature (T_s) and the temperature (T_i) inside the thermal exchange surface was established using a T-type thermocouple attached on top of the center of the thermal exchange surface to measure temperature on the thermal exchange surface at certain driving voltages on the heater. All temperatures were collected at the steady state condition, which is defined as a temperature fluctuation of less than ± 0.5 °C, and the temperatures lasted for at least 5 minutes. Figure 5-13 shows the temperature difference (Δ_t) between the temperature inside the thermal exchange surface and the temperature on the thermal exchange surface. The correlation is regressed as follows.

$$\Delta_t = T_i - T_s = 1.2592 + 0.2410\exp\left(0.0316T_i\right) \tag{5.3}$$

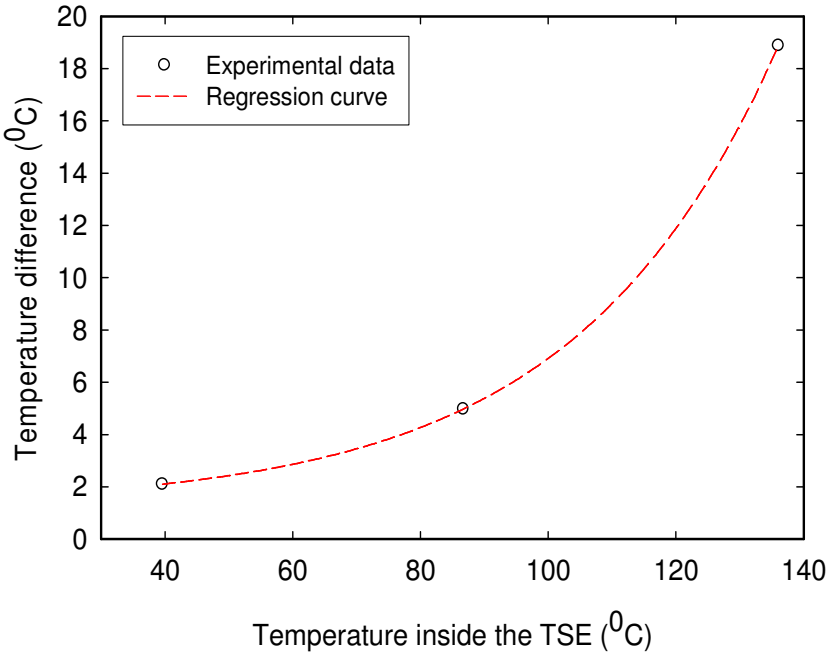

Figure 5-13. *The temperature correlation between the surface temperature and the temperature inside the thermal exchange surface.*

5.3.1.2 Fluid Chamber

As the flow rate per nozzle investigated is relatively low compared to the flow rate used for conventional spray cooling technologies, to achieve considerable heat transfer performance, the 1-nozzle, 4-nozzle, and 8-nozzle ESEC chambers are designed.

As shown in Figure 5-4, the inner diameter of the ESEC chamber is 20 mm, the height of the chamber is 20 mm, and the thickness of the chamber is 2 mm. One end of the ESEC chamber was placed with the circular copper plate drilled with certain microchannels through the plate for three kinds of chambers. During the experiment, the copper plate was connected to a high DC voltage supply unit with positive polarity. Microchannels were connected by micronozzles with an inner diameter (ID) of 210 µm, an outer diameter (OD) of 410 µm, and a length of 9.98 mm.

5.3.1.3 Fluid Supply Unit

The working fluid, ethanol alcohol, was pumped into the fluid chamber using a syringe pump (Figure 5-14), a syringe, and plastic tube. The NE-1000 Programmable Syringe Pump

from New Era Pump Systems, Inc. has the ability to meet the requirement of ultralow flow rate control. Since the syringe pump can automatically control the defined flow rate, calibration for the flow rate is omitted.

Figure 5-14. *The Photograph of the syringe pump.*

5.3.1.4 High DC Potential Supply Unit

The high DC potential supply unit should be capable of supplying voltage covering ranges from the onset voltage of the EHD processes to the voltage causing complete breakdown. Polarity is an important factor which might affect the nature characteristic of the EHD process and its efficiency. For example, the amount of the ozone induced during the EHD process in the air with negative polarity is larger than that with positive polarity [139-141]. Furthermore, positive polarity is more efficient for the EHD process in the air, in terms of induced wind velocity [142]; therefore, positive polarity is chosen for the ESEC chambers. Spellman SL150 is used for a high DC potential supply unit, which can offer positive potential from 0 to 150 kV.

5.3.1.5 Data Acquisition Unit

Data is acquired by a LabVIEW program on a desktop computer through a USB-interface 8-channel compact device (NI cDAQ-9172) with a temperature measurement module (NI 9211). Four K-type thermocouples and one T-type thermocouple are connected to the temperature measurement module. The sampling rate for temperature is set to 3 Hz.

5.3.2 Experimental Parameters

Table 5.4 shows the experimental parameters investigated in this dissertation. Ethyl alcohol has a lower surface tension, which allows for: (1) electrospray generated at a lower applied potential, and (2) a higher applied potential before breakdown occurs. A broad range of operating potentials allows for transitions between different EHD functioning modes, in order to achieve optimal heat transfer performance for the ESEC chambers. To maintain the multi-jet EHD functioning mode for the ESEC chambers throughout all experiments, lower total flow rate is necessary. In this way, the electric force at the micronozzle tip is kept much stronger than the intermolecular forces, which maintains the same multi-jet EHD functioning mode for all chambers at the operating conditions shown in Table 5.4. Therefore, four different total flow rates of 1, 2, 4, and 8 cm^3/hr were chosen for this investigation.

Table 5.4. *Summary of the experimental parameters investigated in this dissertation.*

Total liquid flow rate (cm^3/hr)	Potential (kV)	Gap (mm)	Heater driving voltage (V)	Fluid chamber	
				1 nozzle	0 mm spacing
1 2 4 8	4 5 6 7 7.7	2.5 5.0 7.5	6 7 8 9	4 nozzles	4mm spacing 5mm spacing 6mm spacing
				8 nozzles	4mm spacing 5mm spacing 6mm spacing

The breakdown voltage for each ESEC chamber is different according to our experimental observation. All ESEC chambers should not be operated close to the breakdown voltage. The heater driving voltage is from 6 V to 9 V to generate different heat fluxes for the heat transfer performance measurement of the ESEC chambers. The gaps between the tip of the micronozzles and the thermal exchange surface are 2.5 mm, 5.0 mm, and 7.5 mm. The gap is controlled by a micro positioning xyz optical stage. The 1-nozzle chamber, 4-nozzle chamber, and 8-nozzle ESEC chambers with different geometry were designed.

5.3.3 Procedures

The experimental procedures for heat transfer characteristic measurement of the ESEC chambers are as follows.

(1) The electrical heater is turned on to reach the steady state surface temperature at driving voltage of 6 V. For higher driving voltage, the actual temperature inside the thermal exchange surface is correlated using Eq. (5.2).

(2) The ESEC chamber is turned on at a specific DC potential and liquid flow rate for a given gap to reach a new steady state temperature condition.

(3) The thermal exchange surface temperature for the natural convection and electrospray-induced convection is correlated using Eq. (5.3).

(4) By calculating the surface temperature difference between the natural and electrospray-induced convection conditions, the heat transfer performance of the ESEC device can then be analyzed.

(5) The temperature of the working fluid, ethanol alcohol, is monitored by a T-type thermocouple installed inside the fluid chamber. Since the ESEC chamber is connected to a high DC potential, the temperature monitoring of the working fluid during the experiment is unavailable; therefore, the fluid temperature inside the ESEC chamber is only measured before and after the experiment.

To identify the EHD modes of the ESEC chambers at various testing conditions, a DSLR camera with micro-lens is used to capture the electrospray modes at different potentials.

5.3.4 Data Reduction

5.3.4.1 Enhancement Ratio

The general form describing the average corresponding convection heat transfer coefficients is

$$h = \frac{q''}{T_s - T_\infty} \tag{5.4}$$

where q'' is the heat flux, T_s is the average thermal exchange surface temperature, and T_∞ is the ambient temperature. The heat flux (q'') was assumed to be uniform over the entire thermal exchange surface, and it is expressed as

$$q'' = \frac{IV}{A_s} \tag{5.5}$$

where I is the current from the heater, V is the applied AC voltage on the electric heater, and A_s is the surface area of the thermal exchange surface, which is 900 mm^2 (30 mm × 30 mm) and faces the micronozzles.

During the experiments, the heat flux from the heater was kept as a constant. Therefore, the enhancement ratio (ER) of the average corresponding convection heat transfer coefficient is

$$\text{ER} = \frac{\overline{h_1}}{\overline{h_0}} = \frac{T_{0,s} - T_{0,\infty}}{T_{1,s} - T_{1,\infty}} \tag{5.6}$$

where $\overline{h_0}$ and $\overline{h_1}$ are average corresponding convection heat transfer coefficients calculated at non-electrospray and electrospray conditions, respectively. $T_{0,s}$ and $T_{0,\infty}$ are the surface and environmental temperatures during non-electrospray condition, respectively. $T_{1,s}$ and $T_{1,\infty}$ are the surface and environmental temperatures during electrospray conditions, respectively.

At the steady state condition, the total heat (Q_t) is transferred through thermal conduction to the thermal exchange surface, and is then transferred by convection (Q_{conv}), vaporization (Q_v) and thermal radiation (Q_{rad}) at the thermal exchange surface. Therefore, heat removed by the ESEC device, Q_{ESEC}, was calculated and expressed as

$$Q_{ESEC} = Q_{conv} + Q_v = Q_t - Q_{rad} - Q_l \tag{5.7}$$

where Q_l is the heat loss of the thermal stand. In the analysis, according to the design data of the thermal stand, the maximum heat loss was assumed to be approximately 5% of the total heat flux.

5.3.4.2 Average Thermal Resistance

Thermal resistance (TR) is the temperature difference across a structure when a unit of heat energy flows through it in unit time. From Newton's law of cooling, average thermal resistance for convection heat transfer is expressed as

$$\mathrm{TR} \equiv \frac{T_s - T_\infty}{q} = \frac{1}{hA} \tag{5.8}$$

where T_s is the thermal exchange surface temperature, T_∞ is the environmental temperature, q is the heat generated from the thermal exchange surface, h is the convective heat transfer coefficient, and A is the thermal exchange surface area. Lower thermal resistance represents higher convective heat transfer coefficient as the thermal exchange area remains the same.

5.3.4.3 Average Cooling Rate

To thoroughly understand how fast different ESEC chambers can transfer heat from the thermal exchange surface, the average cooling rate (CR) was defined as

$$\mathrm{CR} \equiv \frac{\Delta T}{\Delta t} \tag{5.9}$$

where ΔT is the temperature difference between the starting temperature and the steady state temperature, and Δt is the time required for the chambers to reach the steady state temperature from a defined starting temperature.

Figure 5-15 shows the definition of the average cooling rate. The average cooling rate means that time required for the ESEC chamber to cool the thermal exchange surface from a certain specific temperature to a final steady state temperature.

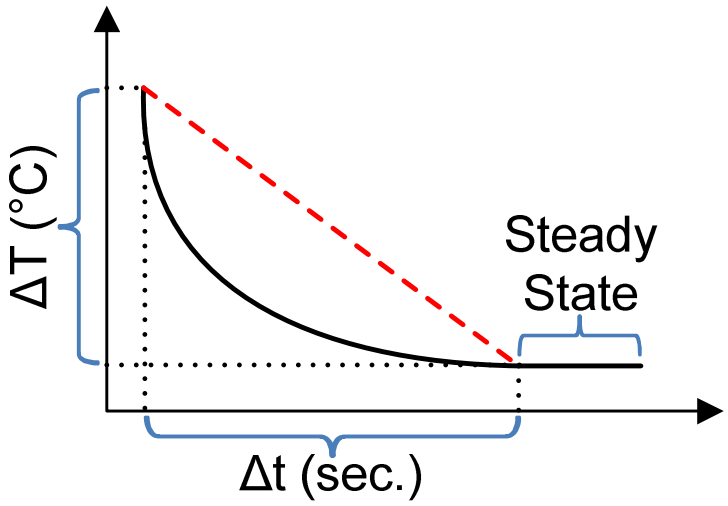

Figure 5-15. *Schematic diagram showing the definition of the average cooling rate for the proposed ESEC chambers.*

5.3.5 Uncertainty Analysis

The uncertainties in this investigation are due to the measurement of the following parameters: the micronozzle length, the DC voltage, the temperature measurement on the thermal exchange surface, the ambient temperature measurement, the AC voltage to the heater, and the current from the heater. The error in micronozzle length measurement is around ± 0.25 mm. The DC voltage output error is 1.00% of the scale reading. The error in temperature measurement on the thermal exchange surface is around 0.75% (from a K-type thermocouple). The ambient temperature measurement error is around 0.75% (from a T-type thermocouple). The AC voltage output error is ± 1.00% of the scale reading, and its current measurement is ± 2.00% of the scale reading.

According to Eq. (5.4) and Eq. (5.5), the uncertainty in heat transfer coefficient estimation (U_h/h) is expressed as follows [143].

$$\left(\frac{U_h}{h}\right)^2 = \left(\frac{U_I}{I}\right)^2 + \left(\frac{U_V}{V}\right)^2 + \left(\frac{U_{\Delta T}}{\Delta T}\right)^2$$
$$= \left(\frac{0.02}{0.88}\right)^2 + \left(\frac{0.02}{9.0}\right)^2 + \left(\frac{0.01}{105.1}\right)^2 \quad (5.10)$$

Therefore, the maximum total uncertainty for the heat transfer coefficient estimation ($(U_h/h)_{\max}$) is less than 2.28%. The uncertainty for the temperature measurement and current measurement is calculated from the experimental data, while the uncertainty for the AC voltage is from the instrument's specifications.

5.4 Electrostatic Field Simulation of the ESEC Chambers

5.4.1 Modeling Parameter Analysis

The major factor affecting the performance of electrospray-based applications is the spatial distribution of the electric field intensity. The motivation is that we expect the heat transfer performance of the ESEC chambers to be highly determined by the electric field intensity as well and can be enhanced by improving the spatial distribution of the electric field distribution. Therefore, the optimization of the electric field distribution of the ESEC chambers will enhance their heat transfer performance.

Figure 5-16 shows that the micronozzle material, the quantity of micronozzles, the micronozzle arrangement, the micronozzle length, the working fluid, the gap, the spacing, and charged droplet transportation trajectory are the primary parameters that influence the electric field intensity of ESEC chambers. Among these parameters, optimization of the electric field intensity of ESEC chambers is focused on the quantity of micronozzles, the micronozzle arrangement, and the spacing in order to optimize the electric field intensity and surface charge density distribution at the tip of the micronozzles of ESEC chambers.

Since the direct modeling of the electric field intensity under the full multiphysics behind the ESEC chamber is currently unavailable, the electromagnetic module built on the COMSOL Multiphysics software is used to model the effect of the quantity of micronozzles, the

micronozzle arrangement, and the spacing on the electric field intensity distribution of the proposed ESEC chambers.

5.4.2 Modeling Procedures

The general procedures of using COMSOL Multiphysics software are establishing geometries of the model, setting up physical properties, applying appropriate boundary conditions, generating and refining the mesh, solving the model, and processing the data.

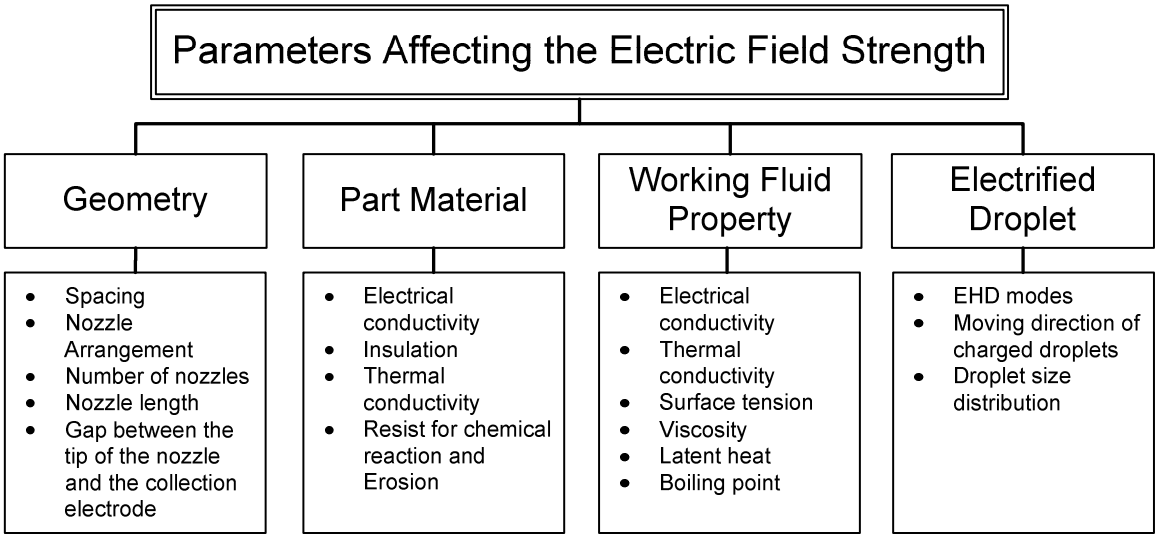

Figure 5-16. *Schematic diagram showing the parameters affecting the electric field intensity of the proposed ESEC chambers.*

5.4.3 Theoretical Background

The classic Poisson's equation is derived by the combination of the definition of potential with Gauss' law and the equation of continuity. Under static conditions, the electrical potential, *V*, is defined by the relationship

$$\boldsymbol{E} = -\nabla V \tag{5.1}$$

where $\boldsymbol{E}$ is the electric field. Besides, the electrical displacement field ($\boldsymbol{D}$) can be expressed as

$$\boldsymbol{D} = \varepsilon_0 \boldsymbol{E} + \boldsymbol{P} \tag{5.2}$$

where ε_0 and $\boldsymbol{P}$ are permittivity of vacuum and the electrical polarization, respectively. By combining Eq. (5.1) and Eq. (5.2), the Gauss' law can be modified as Poisson's equation by the constitutive relationship between $\boldsymbol{E}$ and $\boldsymbol{D}$.

$$-\nabla \cdot \left(\varepsilon_0 \nabla V - \boldsymbol{P}\right) = \rho \tag{5.3}$$

where ρ is space-charge density. For the axisymmetric electrostatics application mode, since the field and geometry are axially symmetric, the electrical potential is constant in the φ direction, implying that the electric field is tangential to the rz-plane. In cylindrical coordinates, multiplying Eq. (5.3) by r to avoid singularities at $r = 0$, the equation becomes

$$-\begin{bmatrix} \dfrac{\partial}{\partial r} \\ \dfrac{\partial}{\partial z} \end{bmatrix} \cdot \left(r\varepsilon_0 \begin{bmatrix} \dfrac{\partial V}{\partial r} \\ \dfrac{\partial V}{\partial z} \end{bmatrix} - r\boldsymbol{P} \right) = r\rho \tag{5.4}$$

5.4.4 Boundary Conditions

Figure 5-17 shows the entire geometry of the electrostatic model established in the COMCOL Multiphysics software. Three boundary conditions were applied to the model, including zero charge/symmetry, ground, and electrical potential. The general physical meaning of these boundary conditions is briefly described in the following.

Zero charge/Symmetry. This boundary condition illustrates the normal component of the electric displacement equals zero and is expressed as

$$\boldsymbol{n} \cdot \boldsymbol{D} = 0 \tag{5.5}$$

Ground. This boundary condition is a special case of the electric potential, specified as zero potential at some boundary in the geometry.

Electric Potential. This boundary condition specifies the voltage at a boundary. In general, the value of the potential is defined at some boundary in the geometry and is expressed as

$$V = V_0 \tag{5.6}$$

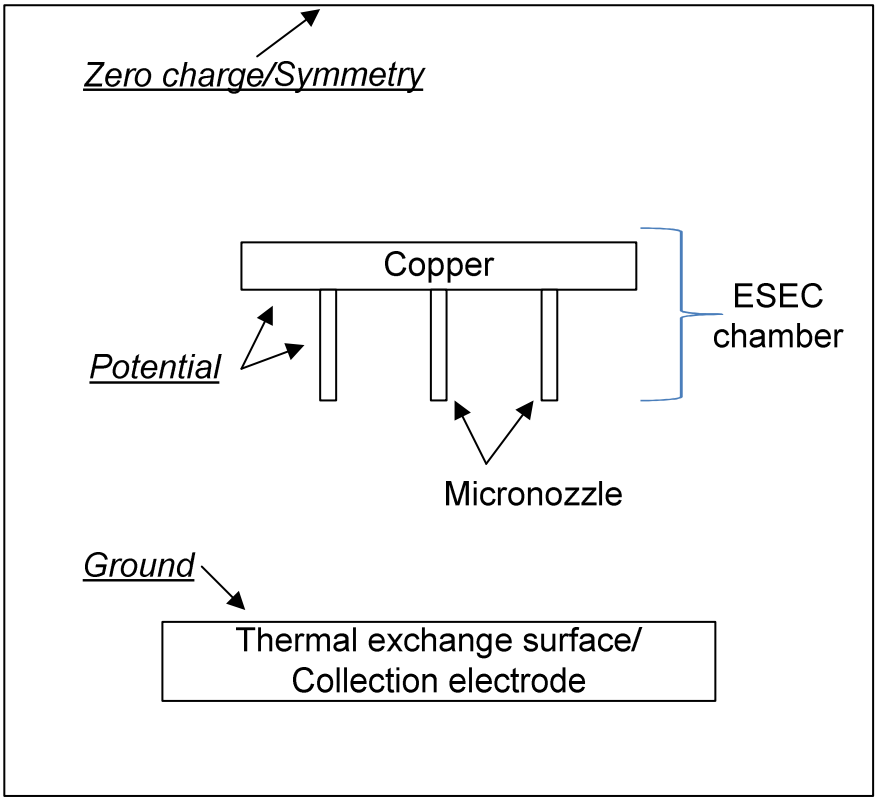

Figure 5-17. *Schematic diagram showing the boundary conditions applied on the electrostatic field model of the ESEC chamber. (not to scale)*

As indicated in Figure 5-17, the zero charge/symmetry boundary condition was applied to the exterior boundaries of the model to eliminate the effect of the geometry of the model on the simulation results. In addition, since the positive potential was adopted, the ground and the electric potential boundary conditions were applied on a copper plate, which is also a thermal exchange surface, and an electrospray chamber, respectively. Table 5.5 shows the summary of the boundary conditions applied on the numerical model of the ESEC chamber. The detailed geometry and dimension of the copper plate and the ESEC chambers are described in 5.3.

Table 5.5. *Summary of the boundary conditions applied on the numerical model of the ESEC chamber.*

Boundary condition	Component of the model
Zero charge/symmetry	• Exterior boundaries of the model
Positive potential	• Microfluidic chamber • Micronozzles
Ground	• Thermal exchange surface or Collecting electrode

5.4.5 Modeling Result Analysis

5.4.5.1 Surface Charge Distribution

Figure 5-18 (a), (b), and (c), respectively, show the surface charge distribution over the tip of one of the micronozzles of the 1-nozzle ESEC chamber, 4-nozzle ESEC chamber (5 mm spacing), and the 8-nozzle ESEC chamber (5 mm spacing) at the applied potential of 7.0 kV. The results show that the surface charge distribution close to the inner diameter of the micronozzle is more uniform, while that close to the outer diameter of the micronozzle is highly non-uniform.

Additionally, the higher surface charge distribution at the outer diameter of the tip of the micronozzle of the 1-nozzle ESEC chamber is more uniform than those of the 4-nozzle chamber with 5 mm spacing and the 8-nozzle ESEC chamber with 5 mm spacing. The difference of the non-uniform distribution of the space charge over the tip of one of the micronozzles of the ESEC chambers is mostly because of the influence of the adjacent micronozzles. The relative geometric orientation among the micronozzles, the micronchannel-based copper plate, and the collecting electrode directly under the micronozzles is also another factor influencing the distribution of the surface charge at the tip of the micronozzle of the ESEC chambers.

When an electrospray chamber is operated in the multi-jet EHD functioning mode, the distribution of the droplet diameters are from submicron meter to several hundred micron meter [68]. The observation of all the electrified jets through photography becomes complicate. Figure 5-19 shows the multi-jet EHD functioning mode achieved by the 4-nozzle chamber with 5 mm spacing at the applied potential of 7.0 kV and total flow rate of 2 cc/hr. Three obvious electrified ethyl alcohol jets are formed at the tip of one of the micronozzles of the 4-nozzle ESEC chamber. The number of the electrified jets observed is very close to the number of the regions where local surface charge density is relatively higher (Figure 5-18 (b)).

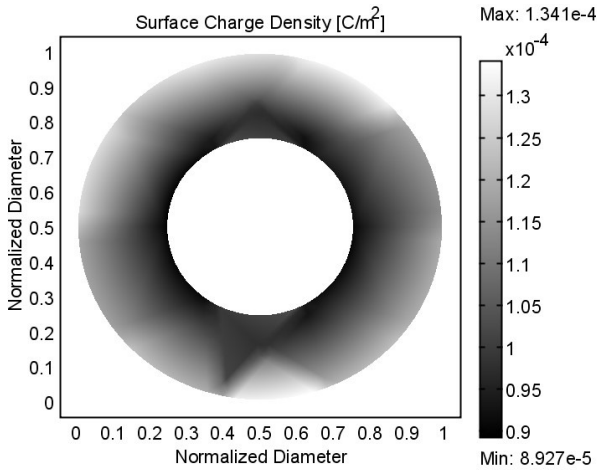

(a) the 1-nozzle ESEC chamber

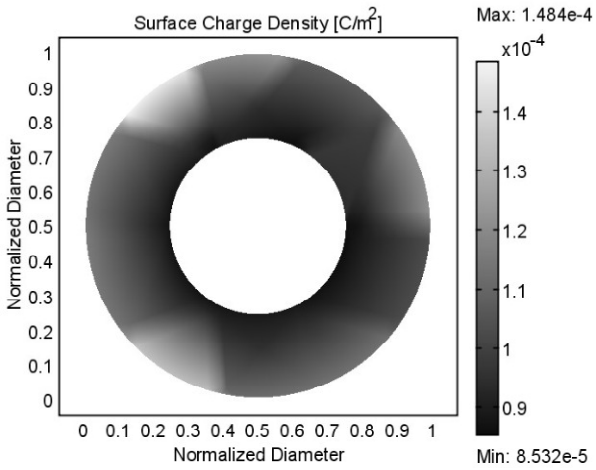

(b) the 4-nozzle ESEC chamber with 5 mm spacing

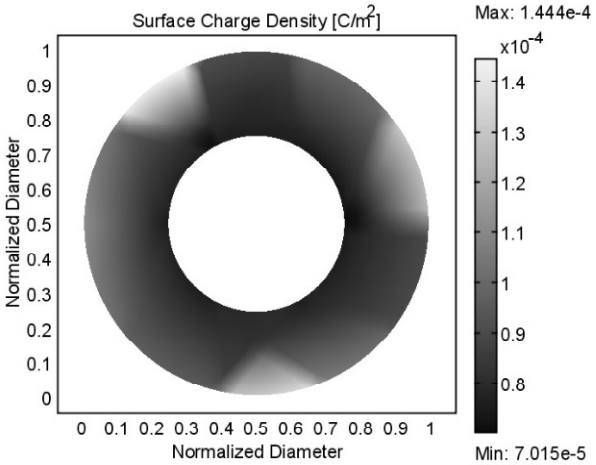

(c) the 8-nozzle ESEC chamber with 5 mm spacing

Figure 5-18. *Simulation results of the surface charge distribution at the tip of one of the micronozzles of the 1-nozzle chamber, 4-nozzle chamber, and 8-nozzle chamber at the potential of 7.0 kV.*

Although the formation of the local higher surface charge density regions from the simulation results could explain the formation of the electrified jets of the multi-jet EHD functioning mode, the actual number of the electrified jets from experiments might not be exactly the same as the number of the regions where the local surface charge density is relatively higher from the simulation results due to an assumed ideal model. The experimental observation highly depends on the fabrication and integration of the components of the ESEC chambers. A slightly deviation on the length of the micronozzles and the inclination angle between the tip of

the micronozzles and the collecting electrode is also the major factor affecting the EHD functioning mode near the tip of all the micronozzles. To obtain more accurate modeling results regarding the formation of the electrified jets, a complete multiphysics numerical model, including electrostatic, fluid mechanism, and heat transfer modes, is necessary.

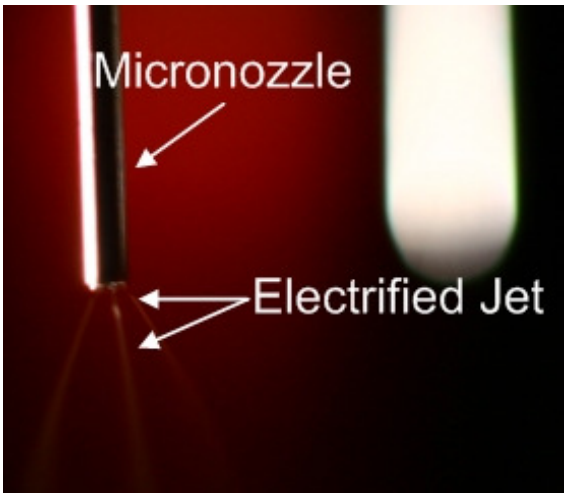

Figure 5-19. *Multi-jet EHD mode of the 4-nozzle ESEC chamber (5 mm spacing) operated at the potential of 7.0 kV and the flow rate of 2 cc/hr. Three obvious ethyl alcohol jets are electrified close to the tip of one of the micronozzles of the chamber. (color picture is available in digital copy)*

Figure 5-20 shows the average surface charge at the tip of the micronozzle of three ESEC chambers. As the applied DC potential is increased, the average surface charge is raised linearly for all the three ESEC chambers as well. Additionally, although the average surface charge of the 1-nozzle chamber and 4-nozzle chamber is almost identical, while that of the 8-nozzle chamber is relatively lower than the others, the total surface charge of the 8-nozzle chamber is the highest, which indicates that more charges can distribute to each micronozzle to efficiently electrify the fluid at the tip of the micronozzle. Furthermore, the higher total surface charge at the tip of the micronozzles means more charge can be carried by the electrified droplets. The charged droplets with higher amount of the charge can be accelerated faster toward the thermal exchange surface, which induces the convective heat transfer rate near the thermal exchange surface, although the majority of the heat transfer is due to the phase change of the fluid on the thermal exchange surface.

5.4.5.2 Electrostatic Field Intensity

Figure 5-21 (a) shows the numerical modeling results of the distribution of the potential of all the three ESEC chambers. This distribution of the potential is along the r axis (defined in Figure 5-21 (b)) from the centerline of the tip of one of the micronozzles to the distance 3 mm away from the tip centerline in the radial direction of the chambers and in the direction parallel to the collecting electrode. The applied potential is 7.0 kV for all the three ESEC chambers. The result shows that at a certain distance away from the centerline of the micronozzle tip, the 8-nozzle ESEC chamber still retains a higher potential than the other two chambers. This is attributed to the fact that the effect of the adjacent micronozzles of the 8-nozzle ESEC chambers is stronger than that of the 4-nozzle ESEC chamber.

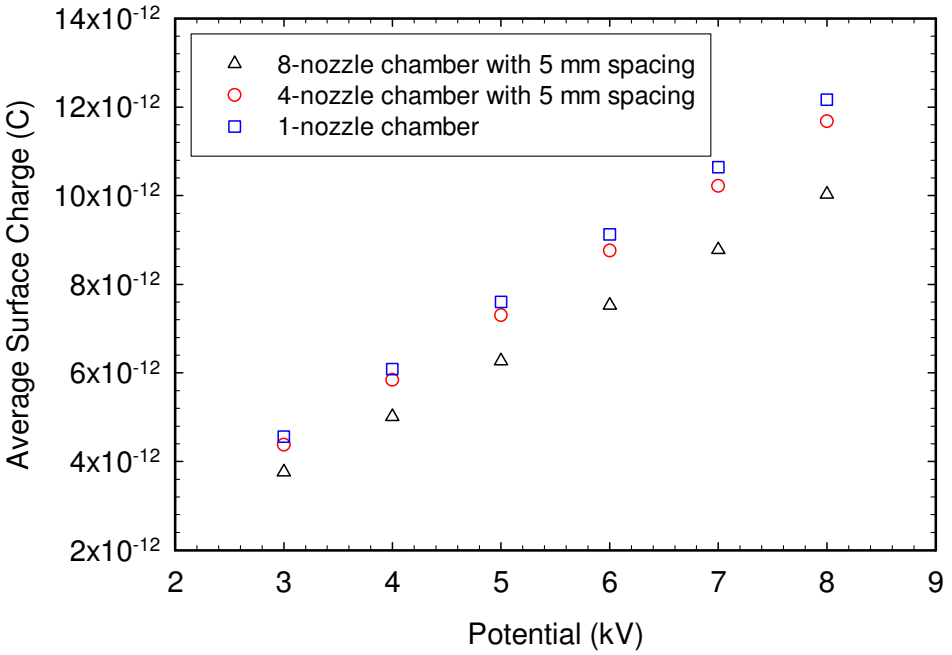

Figure 5-20. *Simulation results showing the amount of the average surface charge at the tip of the micronozzles of each ESEC chamber at different DC potential.*

Additionally, although the geometric orientation of the centerline of the micronozzle of the 1-nozzle ESEC chamber and the 4-nozzle ESEC chamber to the centerline of the respective ESEC chambers is different, Figure 5-21 (a) indicates that the electrostatic field distribution of the 1-nozzle ESEC chamber and the 4-nozzle ESEC chamber in the horizontal direction is almost identical as the distance is within 1.5 mm. This phenomenon implies that although there are four

micronozzles consisting of the 4-nozzle ESEC chamber, the electrostatic field intensity of the individual micronozzles of the 4-nozzle ESEC chamber is almost the same as that of the 1-nozzle ESEC chamber. Therefore, the electrostatic field of each of the micronozzles of the 4-nozzle ESEC chamber near the outer diameter of the tip of the micronozzle can be regarded as an isolated unit.

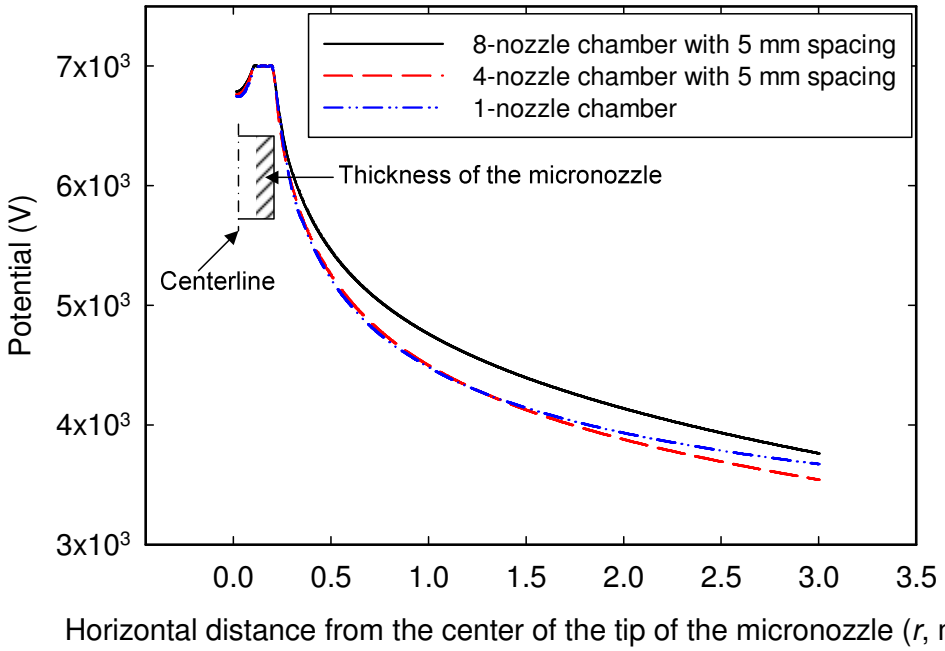

(a) Simulation results

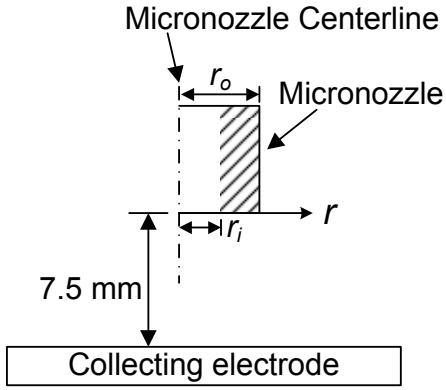

(b) Schematic showing where the electrostatic field is presented in (a)

Figure 5-21. *Simulation results showing the distribution of the potential of all three ESEC chambers from the centerline of tip of the micronozzle to the distance 3 mm away from the tip centerline in the radial direction of the chambers and the direction parallel to the collecting electrode. The applied potential for these three ESEC chambers is 7.0 kV. r_0 and r_i are the outer radius and inner radius of the micronozzle, respectively.*

However, as the distance is beyond 1.5 mm, the decline slope of the potential for the 4-nozzle ESEC chamber and the 8-nozzle ESEC chamber is almost the same, i.e. at the distance of 3.0 mm shown in Figure 5-21 (a). The decline slope is even larger than that of the 1-nozzle chamber. This is because of the geometric position of the micronozzle to the centerline of the ESEC chamber, as shown in Figure 5-6. Therefore, the greater the amount of the micronozzles is used, the wider the equi-potential distribution around the micronozzles would be. For example, the 5.0 kV potential for the 1-nozzle ESEC chamber and the 4-nozzle ESEC chamber is 0.5 mm away from the centerline of the micronozzle, while that for the 8-nozzle camber extends to around 0.8 mm away from the centerline of the micronozzle. The broadened equi-potential distribution results in a wider electrospray angle between the centerline of the micronozzle and the tangential direction of the electrified jet at the outer diameter of the tip of the micronozzle when the electrospray is operated in the multi-jet EHD functioning mode. Figure 5-22 shows the definition of the electrospray angle.

To estimate the average electrostatic field intensity of the ESEC chambers, we modified the analytical model describing the electrostatic field intensity of a hyperboloid-to-plane EHD configuration [86, 144] to fit our electrostatic field intensity modeling results. Some physical parameters, such as the distance of 7.5 mm between the tips of the micronozzle and the thermal exchange surface, as well as the diameter of the micronozzle, are fixed values, while the only variable for modeling is the applied potential on three ESEC chambers.

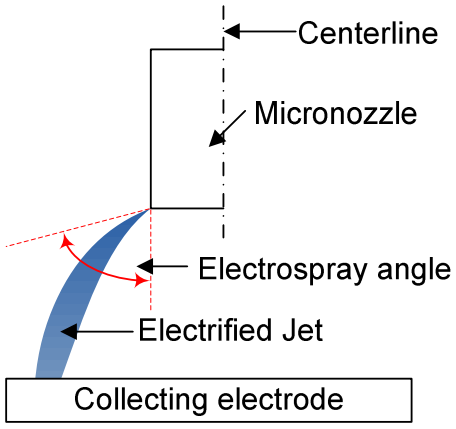

Figure 5-22. *Schematic diagram showing the definition of the electrospray angle in the multi-jet EHD functioning mode.*

The general form describing the electrostatic field intensity of a hyperboloid-to-plane EHD configuration is [144, 145]

$$E_0 = \frac{AV}{r_0 \ln\left(4H/r_0\right)} \tag{5.7}$$

where r_0 is the outer radius of the hyperboloid object, and H is the distance between the tip of the hyperboloid object and the thermal exchange surface. The constant A is determined from experimental results of different EHD configurations [80, 146, 147]. For the ESEC chambers, r_0 is the outer radius of the micronozzle. There are two reasons why we chose r_0 (outer radius of the micronozzle) as the key parameter. First, the operation of the ESEC chamber primarily depends on the potential distribution between the tips of the micronozzles and the collecting electrode (thermal exchange surface). The outer diameter of the micronozzle affects the potential distribution between the tips of the micronozzles and the collecting electrode. Second, although the electrostatic field modeling results shown in Figure 5-21 (a) indicates that there is a potential distribution inside the micronozzle, for the practical operating of the ESEC chamber, the working fluid fills the entire inner part of the micronozzle; therefore, the potential gradient inside the micronozzle should be smaller in comparison to the potential gradient outside the micronozzle.

For the hyperboloid-to-plane EHD configuration, the constant A usually ranges from $\sqrt{2}$ to 2. However, the estimation of the electrostatic field intensity of the 1-nozzle ESEC chamber using the previously determined A results in an electrostatic field intensity 50 times higher than that generated by the numerical modeling results, because the analytical model is based on the tip radius of the hyperboloid needle which is much smaller than the outer radius of the micronozzle of the 1-nozzle ESEC chamber. Therefore, we suggest that the constant A of the simplified analytical model for the geometry of the micronozzle-based 1-nozzle ESEC chamber is modified as 2.89×10^{-2}, two orders lower than that of the previously determined values [80, 146, 147].

Figure 5-23 shows the plot of the average electrostatic field intensity of the hyperboloid-to-plane EHD configuration analytical model with the modified constant A of 2.89×10^{-2}. The

average electric field intensity of the 1-nozzle ESEC chamber, the 4-nozzle ESEC chamber (5 mm spacing), and the 8-nozzle ESEC chamber (5 mm spacing) with respect to different applied DC potentials is also plotted for comparison. As the applied DC potential is increased, the average electrostatic field intensity of the 8-nozzle chamber is always higher than that of the 4-nozzle chamber and the 1-nozzle chamber. The average electrostatic field intensities of the 1-nozzle chamber and the 4-nozzle chamber are very close to each other, especially at a lower applied potential. This result can be used to explain the difference in the experimental heat transfer performance of the three ESEC chambers (1-nozzle chamber, 4-nozzle chamber with 5 mm spacing, and 8-nozzle chamber with 5 mm spacing) discussed in 5.5.

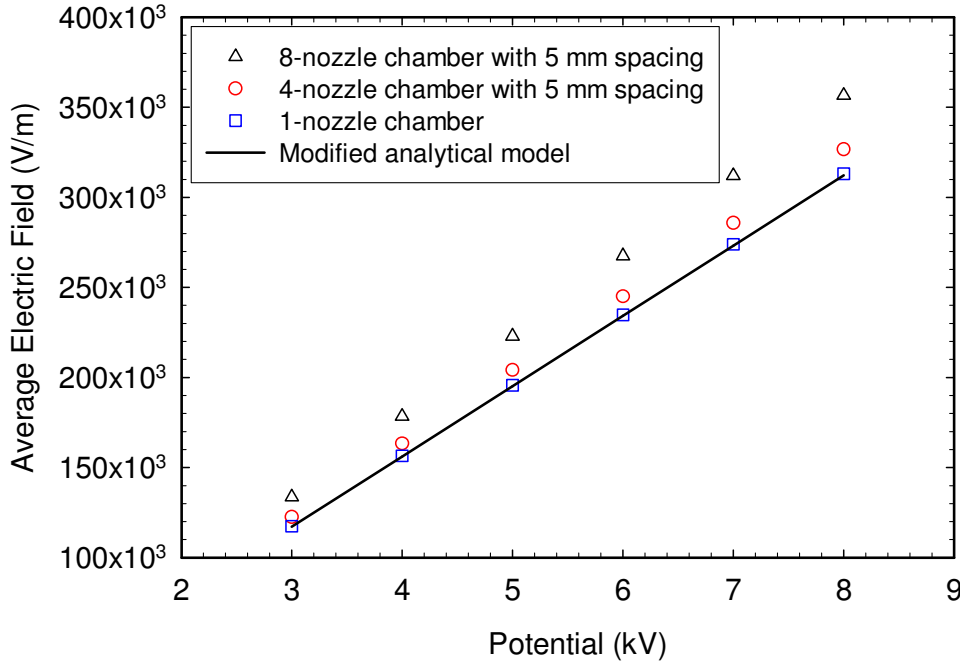

Figure 5-23. *Simulation results of the average electrostatic field intensity at the central line of three ESEC chambers. The central line is parallel to the micronozzles of the three chambers. The electrostatic field intensity of the modified hyperboloid-to-plane EHD configuration is also plotted to fit the numerical result of electrostatic field intensity of the 1-nozzle ESEC chamber.*

5.5 Heat Transfer Characterization of the ESEC Chambers

5.5.1 Demonstration of the Heat Transfer Cooling Effect

Figure 5-24 shows the cooling effect achieved by the 1-nozzle ESEC chamber by using a thermal image camera (Fluke Ti55FT). Blue and red color represents high and low temperatures, respectively, while others are in between. Before turning on the ESEC chamber, shown schematically in Figure 5-24 (a), the thermal exchange surface was kept at steady state temperature of approximately 90°C. After turning on the ESEC chamber (Figure 5-24 (b)-(d)), the temperature of the thermal exchange surface under the electrospraying micronozzle has been noticeably lowered at the DC potential of 4 kV and flow rate of 1 cc/hr, which means the ESEC chamber has successfully demonstrated the heat removal ability over the heated thermal exchange surface experimentally.

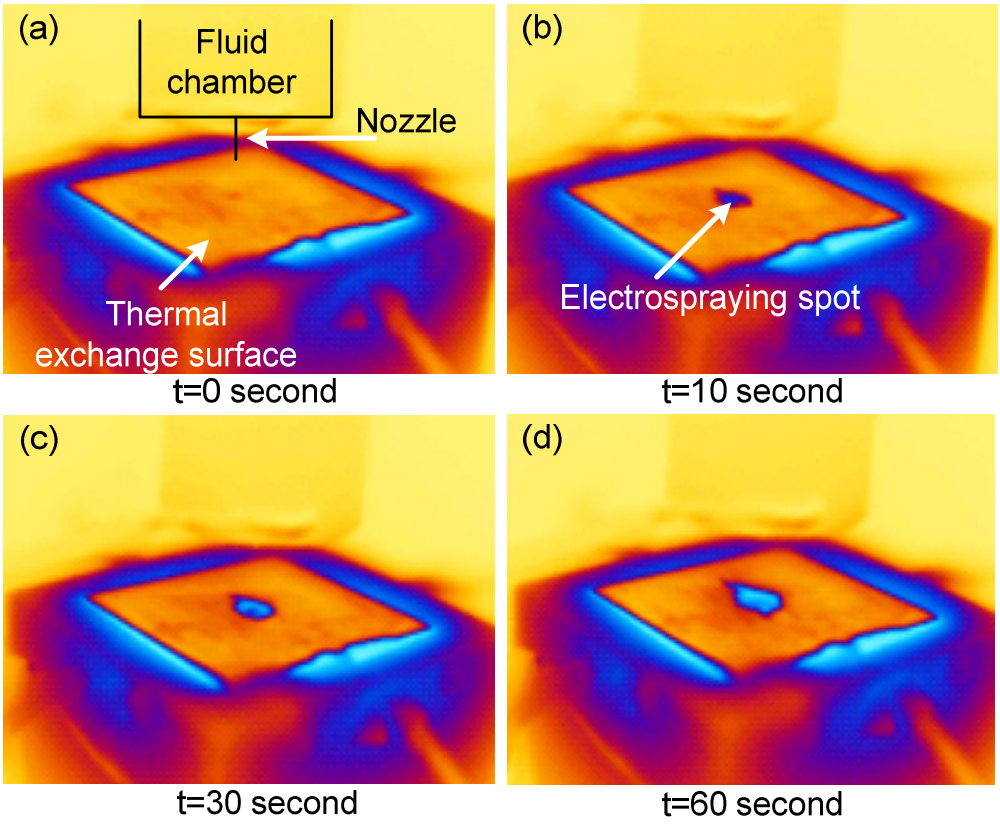

Figure 5-24. *Thermal images show the cooling effect of the ESEC chamber. Red and blue color represents high and low temperatures, respectively, while others are in between. (color pictures are available in digital copy)*

5.5.2 Gap Effect

The effect of gaps between the tip of the micronozzle of the ESEC chambers and the thermal exchange surface is discussed at the DC potential of 3.5 kV. Although the DC potential was kept as a constant, the electrostatic field intensity variation due to the gaps resulted in different EHD functioning modes. For example, according to our experimental observation for the operation of the 1-nozzle ESEC chamber at 3.5 kV, the stable cone-jet mode occurs when the gap is 7.5 mm, while the multi-jet mode occurs when the gap is 2.5 mm.

For the 1-nozzle ESEC chamber, the EHD functioning mode changes due to the variation in the gap results in a slight increase in the enhancement ratio for all flow rates per nozzle, except for the flow rate of 1.00 cc/hr per nozzle, as shown in Figure 5-25.

For the 4-nozzle ESEC chamber (5 mm spacing), increasing the gap also slightly increases the enhancement ratio except for the flow rate of 2.00 cc/hr per nozzle, as shown in Figure 5-26. The enhancement ratios for the flow rate of 2.00 cc/hr per nozzle decrease as the gap is increased.

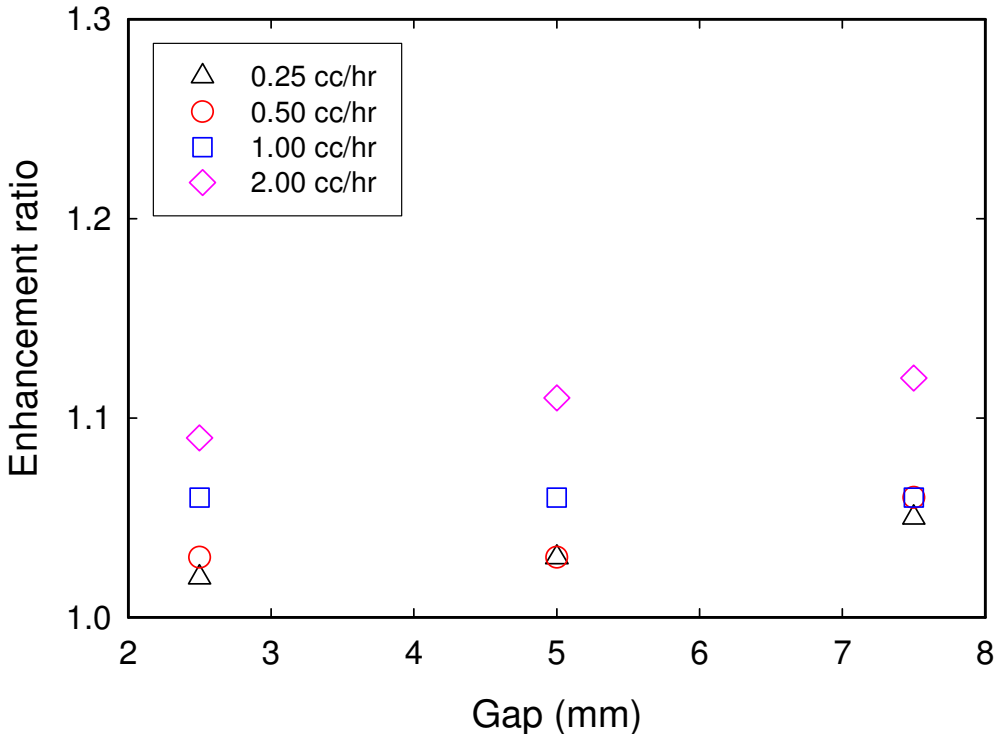

Figure 5-25. *Average corresponding enhancement ratios achieved by the 1-nozzle ESEC chamber at different gaps and flow rates per nozzle.*

Figure 5-27 shows the comparison of the enhancement ratios achieved by the 1-nozzle chamber and the 4-nozzle chamber (5 mm spacing) at the same total flow rates but with different gaps. Noticeably, the enhancement ratios achieved by the 4-nozzle chamber (5 mm spacing) are always higher than those achieved by the 1-nozzle chamber, meaning that increasing the quantity of micronozzles but decreasing the flow rate per nozzle is an appropriate way of improving the enhancement ratio of the ESEC chambers.

Since most of the higher enhancement ratios occurred at a gap of 7.5 mm, this gap was adopted for the rest of the investigation to better understand the heat transfer performance of different ESEC chambers at different experimental parameters set in Table 5.4.

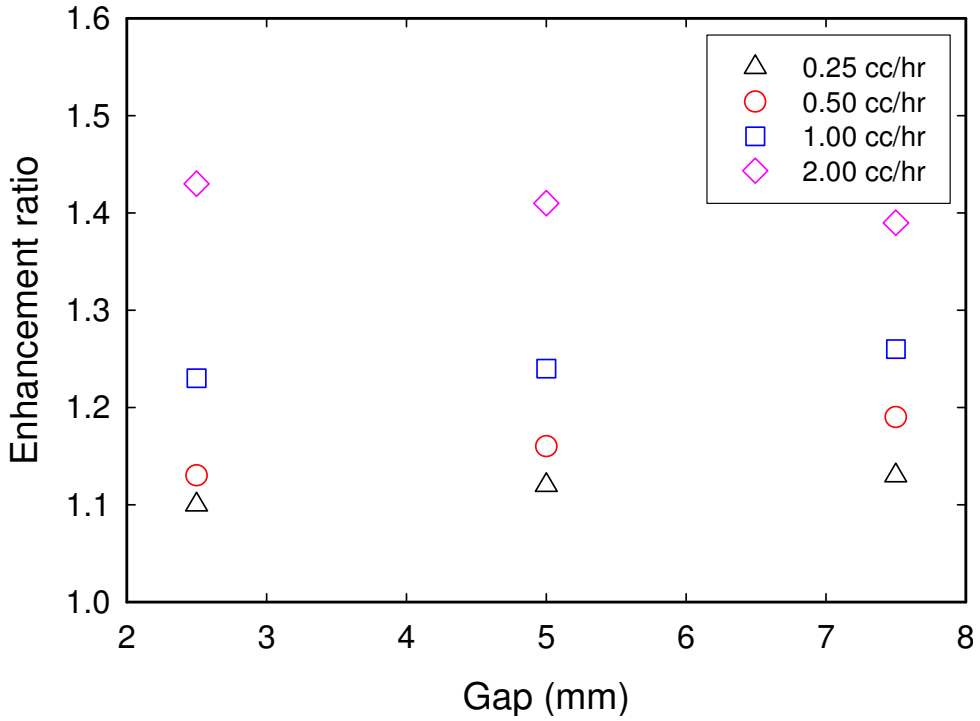

Figure 5-26. *Average corresponding enhancement ratio achieved by the 4-nozzle ESEC chamber (5 mm spacing) at different gaps and flow rates per nozzle.*

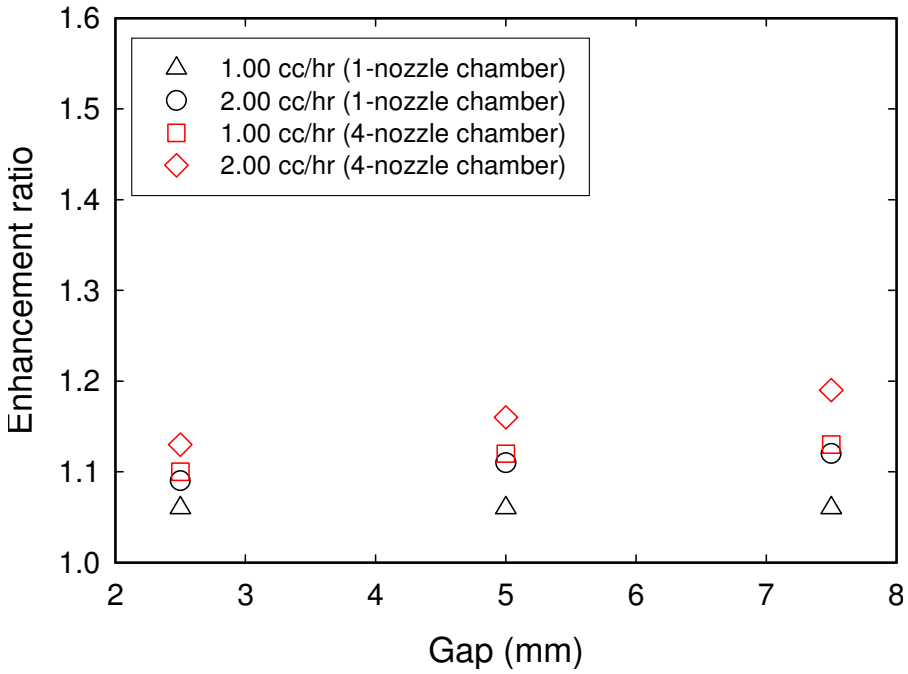

Figure 5-27. *Comparison of the average corresponding enhancement ratio of the 1-nozzle chamber and the 4-nozzle chamber at the same total flow rates but with different gaps.*

5.5.3 Effect of the Quantity of Micronozzles on the ESEC Chamber

The 1-nozzle ESEC chamber, the 4-nozzle ESEC chamber with 5 mm spacing, and the 8-nozzle ESEC chamber with 5 mm spacing are discussed in this section.

5.5.3.1 Enhancement Ratio of Convection Heat Transfer Coefficient

At a heat flux of 4,384.40 W/m^2, Figure 5-28 shows the relationship between the enhancement ratio and the mass flow rate of the 8-nozzle ESEC chamber (5 mm spacing) at different applied potentials. At the fixed mass flow rate, a higher applied potential results in a higher enhancement ratio. At the fixed potential, increasing the mass flow rate enhances the enhancement ratio. The 4-nozzle ESEC chamber (5 mm spacing) and the 1-nozzle ESEC chamber show the same relationship between the enhancement ratio and the mass flow rate as well.

Figure 5-29 shows that at the constant heat flux (4,384.40 W/m^2) and a potential of 7.0 kV, the enhancement ratio increases as the mass flow rate of the fluid is increased. At the same mass

flow rate, the highest enhancement ratio was achieved by the 8-nozzle ESEC chamber (5 mm spacing), which indicates that the higher the quantity of the micronozzles, the more efficient the fluid can be distributed to cover a larger surface area of the thermal exchange surface for heat transfer.

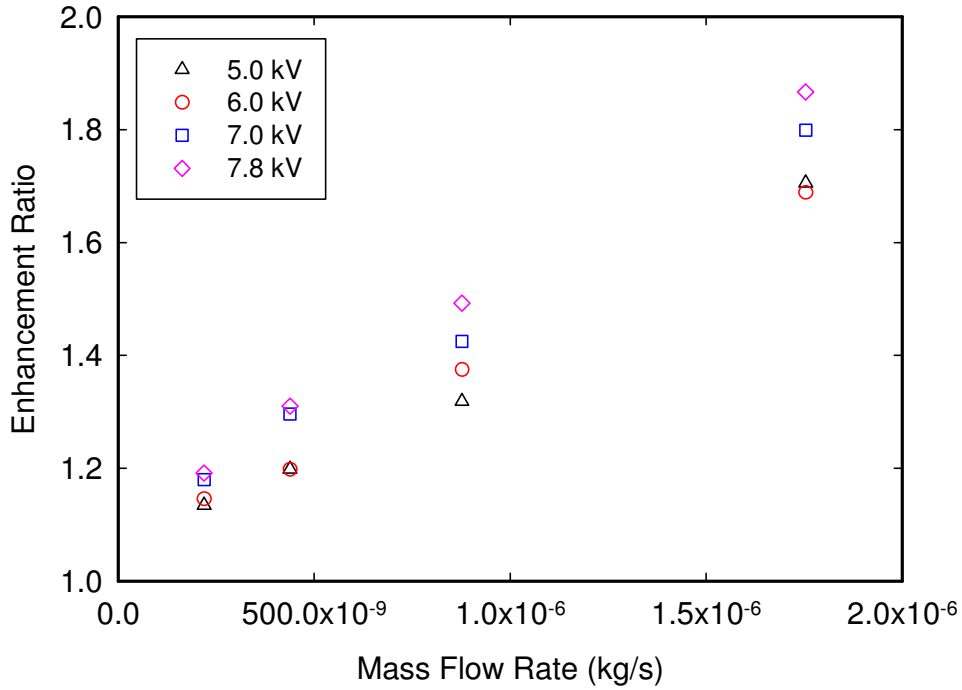

Figure 5-28. *The relationship between the mass flow rate and the enhancement ratio of the 8-nozzle ESEC chamber with 5 mm spacing at different potentials. The heat flux is 4,384.40 W/m^2.*

At the heat flux of 4,3843.40 W/m^2, Figure 5-30 shows the relationship between the enhancement ratio and the average electrostatic field of the three ESEC chambers at a total flow rate of 8 cc/hr. In general, at the same average electrostatic field, the 8-nozzle ESEC chamber with 5 mm spacing has the highest enhancement ratio, followed by the 1-nozzle ESEC chamber and the 4-nozzle ESEC chamber with 5 mm spacing.

To compare the enhancement ratio achieved by the three ESEC chambers with different average electrostatic fields, we use linear curve regression to discuss the relationship between the average electrostatic field and the enhancement ratio of the three ESEC chambers.

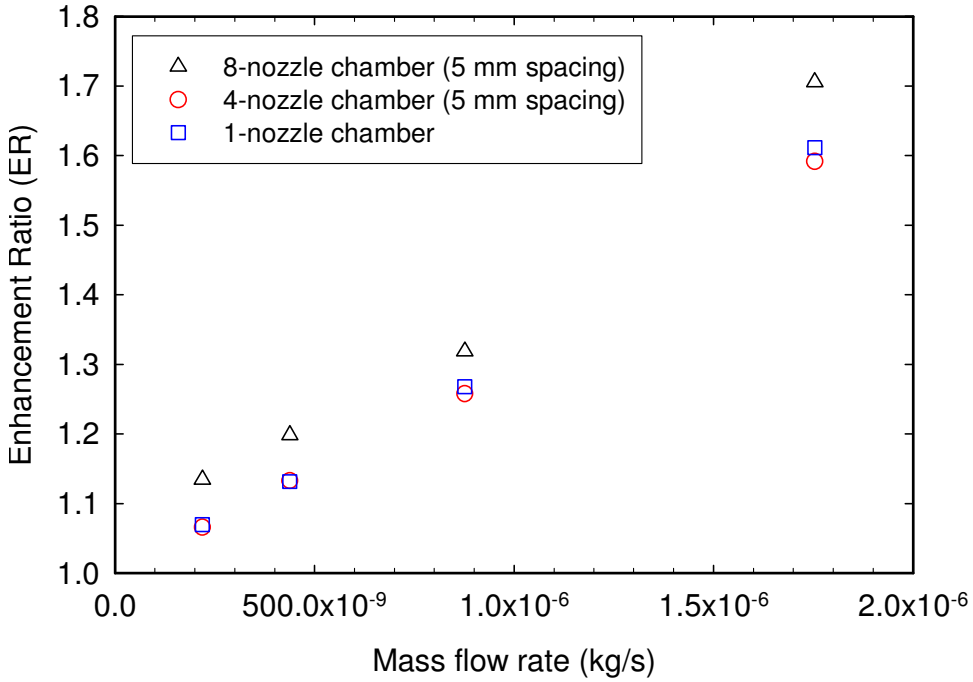

Figure 5-29. *The relationship between the mass flow rate and the enhancement ratio achieved by three ESEC chambers at constant heat flux (4,384.40 W/m^2) and 7.0 kV DC potential.*

For the 8-nozzle ESEC chamber with 5 mm spacing, the regression curve is

$$\mathrm{ER} = 1.3678 + 1.3897\times10^{-6}\times\bar{E} \tag{5.1}$$

For the 4-nozzle ESEC chamber with 5 mm spacing, the regression curve is

$$\mathrm{ER} = 1.4625 + 6.7105\times10^{-7}\times\bar{E} \tag{5.2}$$

For the 1-nozzle ESEC chamber, the regression curve is

$$\mathrm{ER} = 1.4050 + 1.1498\times10^{-6}\times\bar{E} \tag{5.3}$$

where $\bar{E}$ is the average electrostatic field, and ER is the enhancement ratio.

The regression curve slope for the 1-nozzle chamber and the 8-nozzle chamber with 5 mm spacing are in the same order, which indicates that the increase of the average electrostatic field on these two chambers should result in the same increasing rate in the enhancement ratio. In addition, our experimental enhancement ratios are within ± 5.0% deviation of the linearly

regressed curve for the three ESEC chambers, which indicates that choosing linear curve regression should provide us enough information regarding the average electrostatic field and the corresponding enhancement ratio for practical ESEC chamber design.

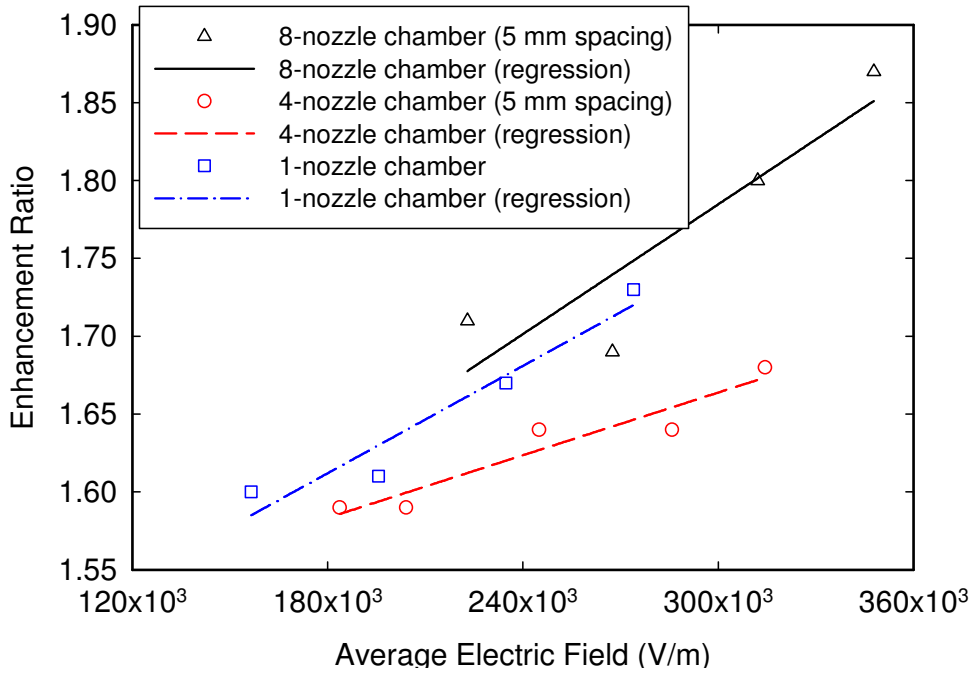

Figure 5-30. *The relationship between the average electrostatic field and the enhancement ratio among three different ESEC chambers at a flow rate of 8 cc/hr and a heat flux of 4,384.40 W/m^2.*

Figure 5-31 (a) shows enhancement ratios achieved by each ESEC chamber at potential of 7.0 kV, flow rate of 8 cc/hr, and four different heat fluxes. At each heat flux, the 8-nozzle ESEC chamber always achieves the highest enhancement ratio, followed by the 1-nozzle ESEC chamber and the 4-nozzle ESEC chamber. The reason why the highest enhancement ratio was achieved by the 8-nozzle ESEC chamber is because the potential distribution near one of the tips of the micronozzle is higher than that of the other two ESEC chambers (Figure 5-21 (a)). In this operating condition, the electrified jets are forced to eject at a higher electrospray angle, resulting in the fact that the electrified jets can cover larger portions of the thermal exchange surface, which allows for larger heat transfer performance and significantly lowers the surface temperature of the thermal exchange surface.

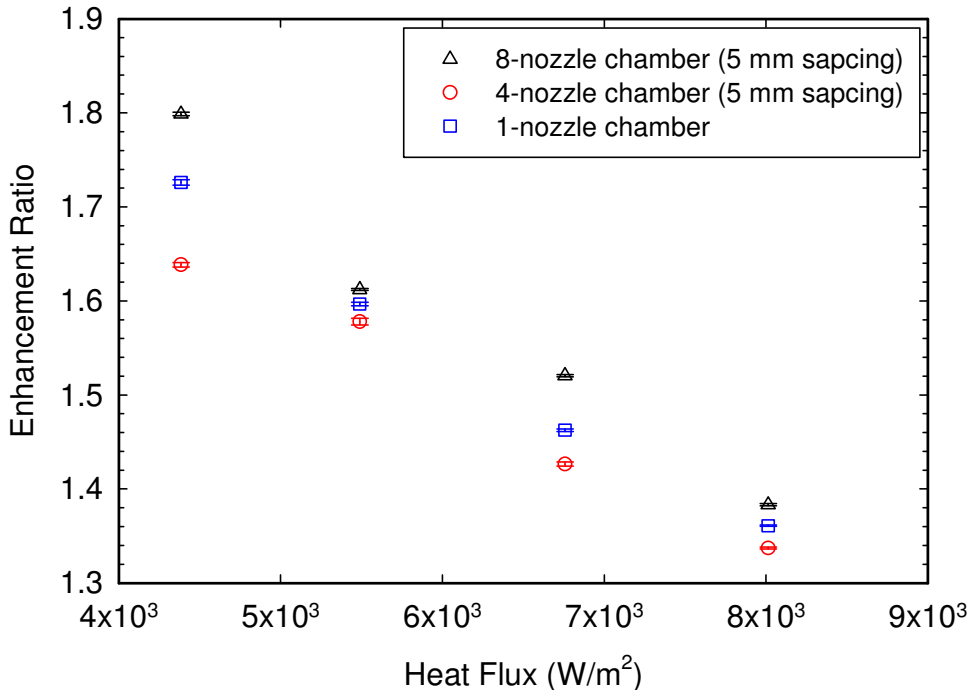

(a) 7.0 kV

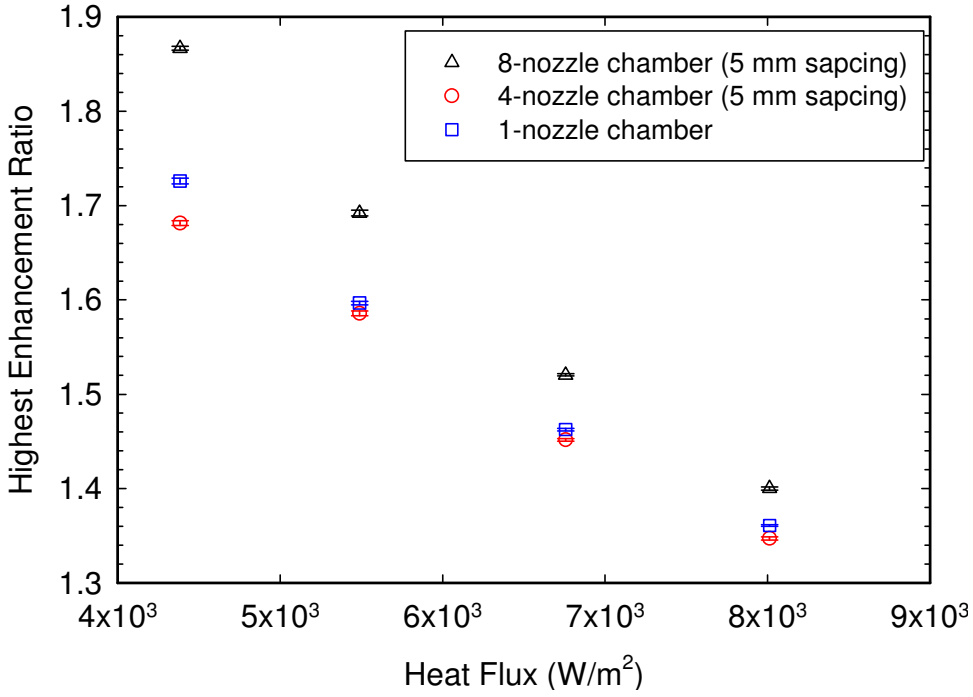

(b) Highest respective achievable potential

Figure 5-31. *Enhancement ratios achieved by the three chambers at different heat fluxes. The highest enhancement ratios occur at the flow rate of 8 cm^3/hr.*

In addition, for the same ESEC chamber, increasing the heat flux results in a decreased enhancement ratio. Enhancement ratio differences among the three ESEC chambers become noticeable when the ESEC chambers are operated in a lower heat flux condition. At a lower heat flux, the temperature difference between the temperature of the ethyl alcohol and the thermal exchange surface is small, resulting in lower heat transfer rate by conduction from the thermal exchange surface to the ethyl alcohol film accumulated on the thermal exchange surface. The ethyl alcohol film does not absorb enough heat to vaporize on the thermal exchange surface. Furthermore, the amount of the coming ethyl alcohol from the ESEC chamber is larger than that of the vaporized ethyl alcohol on the thermal exchange surface. Therefore, the surface temperature of the thermal exchange surface is largely lowered by the net increased amount of the ethyl alcohol on the thermal exchange surface. The accumulation of the electrified ethyl alcohol on the thermal exchange surface decreases as the heat flux becomes higher. This phenomenon occurs at all heat flux conditions.

Figure 5-31 (b) shows the highest enhancement ratio achieved by each ESEC chamber at the highest achievable potential, the highest flow rate of 8 cc/hr, and the four different heat fluxes. The highest achievable potential is the potential before the happening of the breakdown between the ESEC chamber and the collecting electrode and, therefore, the highest achievable is different for all the three ESEC chambers. The highest achievable potential for the 1-nozzle chamber, 4-nozzle chamber, and 8-nozzle ESEC chamber is 7.0 kV, 7.7 kV, and 7.8 kV, respectively. The corresponding average electrostatic field intensity for the 1-nozzle chamber, 4-nozzle chamber, and 8-nozzle ESEC chamber is 2.74×10^5 (V/m), 3.14×10^5 (V/m), and 3.48×10^5 (V/m), respectively.

The maximum enhancement ratio of 1.87 was achieved by the 8-nozzle chamber at the highest achievable potential and lowest heat flux of 7.8 kV and 4,384.40 W/m^2, respectively. The same tendency that the maximum enhancement ratio occurs at the lowest heat flux and the highest potential was also presented by Feng *et al.* [86].

Furthermore, Figure 5-31 (b) also shows that for heat flux higher than 5,000 W/m2, the highest enhancement ratio achieved by the 1-nozzle ESEC chamber is slightly higher than that achieved by the 4-nozzle ESEC chamber. Although the average electrostatic field of the 4-nozzle ESEC chamber is higher than that of the 1-nozzle ESEC chamber, the potential distribution close

to the tip of the micronozzle of the ESEC chambers dominates the enhancement ratio of each ESEC chamber.

Therefore, we conclude that the potential distribution close to the tip of the micronozzle dominates the enhancement ratio of all the ESEC chambers investigated. Although a universal criterion that correlates the average electrostatic field and the enhancement of the ESEC chamber with different geometry is still not available, the modeling results regarding the potential distribution near the tip of the micronozzle of the ESEC chambers could point out the relative magnitude of the enhancement ratio among the ESEC chambers.

To understand the effect of the potential increasing rate and the total mass flow rate increasing rate on the enhancement ratio, the potential, the total mass flow rate, and the enhancement ratio are normalized for analysis. Figure 5-32 shows the effect of the potential increasing rate on enhancement ratio increasing rate achieved by the three different ESEC chambers at the heat flux of 4,384.40 W/m^2. The slope of the regression curves among the three ESEC chambers indicate that at the same potential increasing rate, the 8-nozzle ESEC chamber with 5 mm spacing achieves the fastest increasing rate in the enhancement ratio, followed by the 1-nozzle ESEC chamber and the 4-nozzle ESEC chamber with 5 mm spacing. The same performance behavior among the three ESEC chambers regarding to the total mass flow rate increasing rate and the enhancement ratio increasing rate is shown in Figure 5-33.

Additionally, for the same ESEC chamber and heat flux, Figure 5-32 and Figure 5-33 indicates that to achieve a higher enhancement ratio increasing rate, increasing the applied potential is more efficient than increasing the total mass flow rate.

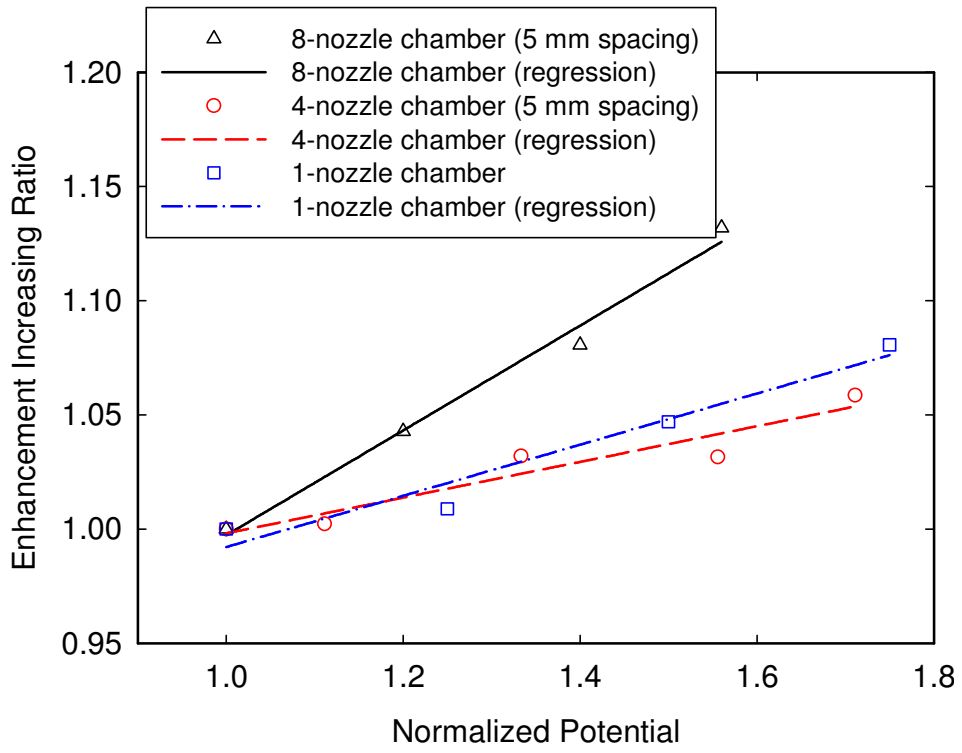

Figure 5-32. *The enhancement ratio increasing rate due to the increased potential among the three ESEC chambers. The heat flux is 4,384.40 W/m^2.*

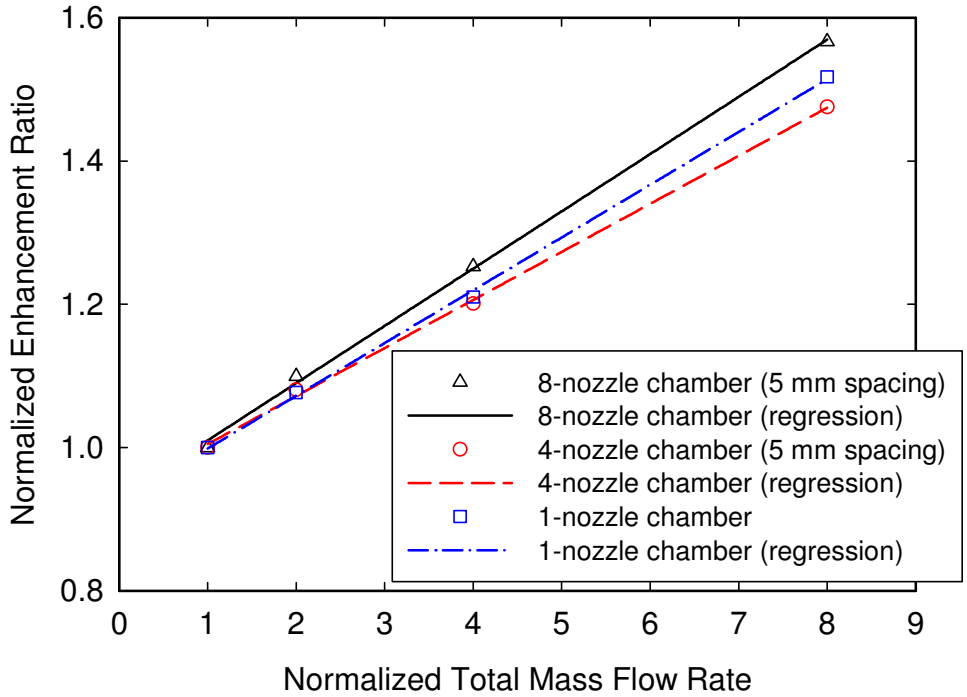

Figure 5-33. *The enhancement ratio increasing rate due to the increased total mass flow rate among the three ESEC chambers. The heat flux is 4,384.40 W/m^2.*

5.5.3.2 Thermal resistance

At the same heat flux and applied potential, Figure 5-34 shows that increasing the mass flow rate decreases the average thermal resistance. At the same mass flow rate and heat flux, increasing the applied potential reduces the average thermal resistance.

At a heat flux of 4,3843.40 W/m^2, Figure 5-35 shows the relationship between the average thermal resistance and the average electrostatic field of the three ESEC chambers at the total flow rate of 8 cm^3/hr. At the same average electrostatic field, the 8-nozzle ESEC chamber with 5 mm spacing has the lowest average thermal resistance, followed by the 1-nozzle chamber and the 4-nozzle ESEC chamber with 5 mm spacing. The regression curves regarding the relationship between the average electrostatic field and the average thermal resistance for all three ESEC chambers are described next.

For the 8-nozzle ESEC chamber with 5 mm spacing, the regression curve is

$$\mathrm{TR} = 10.7140 - 5.7514 \times 10^{-6} \times \bar{E} \tag{5.4}$$

For the 4-nozzle ESEC chamber with 5 mm spacing, the regression curve is

$$\mathrm{TR} = 11.4809 - 6.4028 \times 10^{-6} \times \bar{E} \tag{5.5}$$

For the 1-nozzle ESEC chamber, the regression curve is

$$\mathrm{TR} = 11.5910 - 8.1000 \times 10^{-6} \times \bar{E} \tag{5.6}$$

where $\bar{E}$ is the average electrostatic field, and TR is the average thermal resistance. Unlike the behavior between the average electrostatic field and the enhancement ratio, the slope of the regression curve of the three ESEC chambers investigated in this dissertation are in the same order, indicating that increase the average electrostatic field results in the same increasing rate of the average thermal resistance.

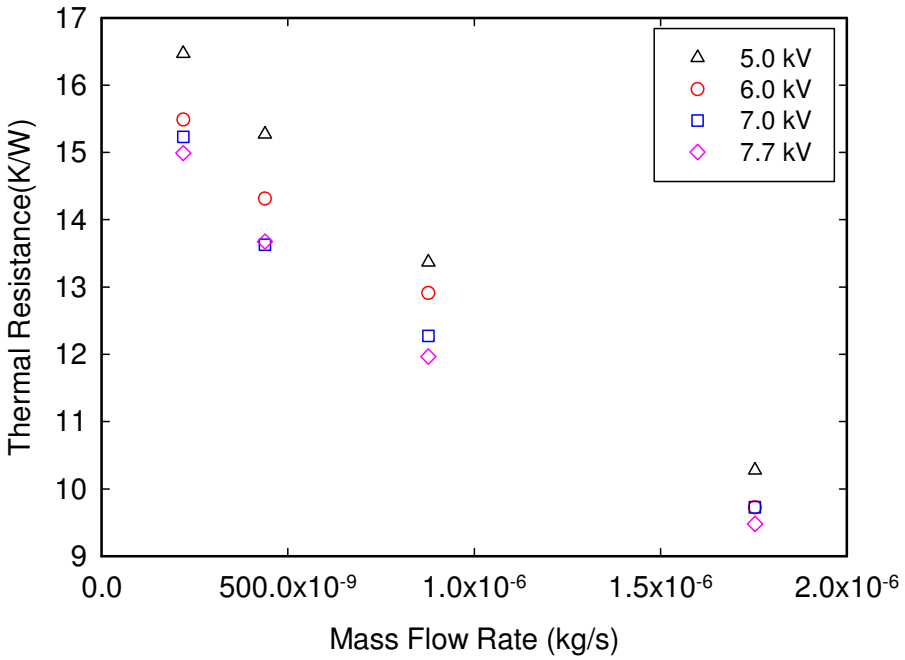

Figure 5-34. *The relationship between the mass flow rate and the average thermal resistance of the 4-nozzle ESEC chamber (5 mm spacing) at different potentials. The heat flux is 4,384.40 W/m^2.*

Figure 5-36 shows the lowest thermal resistance achieved by the three chambers at the highest respective achievable potential, flow rate, and four different heat fluxes. In general, at all heat flux conditions, the average lowest thermal resistance achieved by the three chambers increases as the heat flux increases.

Additionally, at each heat flux, the 8-nozzle ESEC chamber with 5 mm spacing achieves the lowest average thermal resistance, while the other two ESEC chambers almost achieve the same average thermal resistance. The potential distribution close to the tip of the micronozzle of the ESEC chamber, as shown in Figure 5-21 (a), can explain the difference of the thermal resistance among the three ESEC chambers. The average electrostatic field intensity with respect to different applied potentials shown in Figure 5-23 can also be used to explain the difference of the thermal resistance among the three ESEC chambers. Therefore, we conclude that the average thermal resistance is dominated by the potential distribution near the tip of the micronozzle of the ESEC chambers.

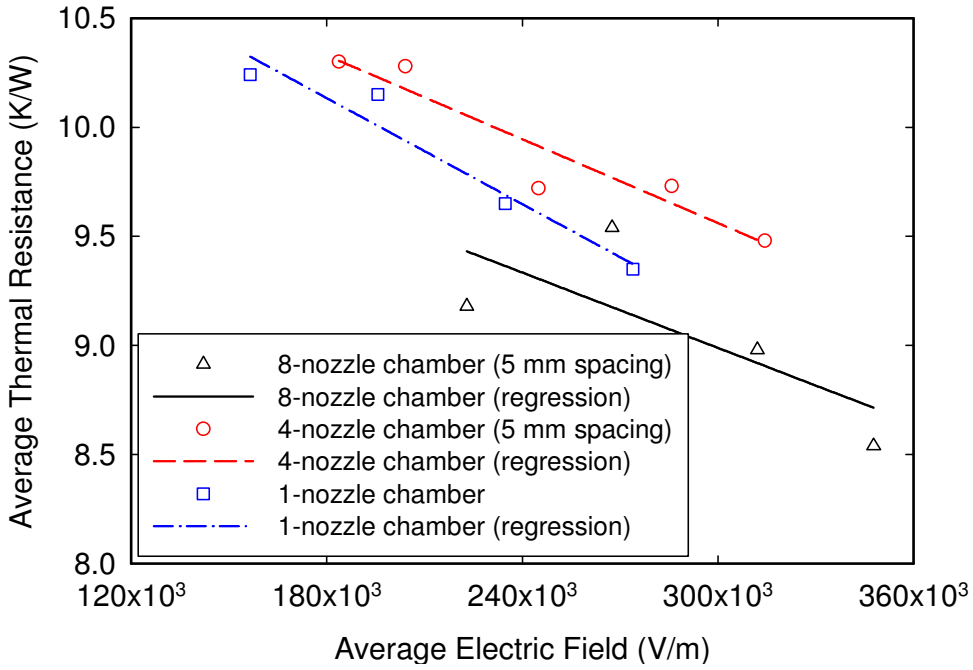

Figure 5-35. *The relationship between the average electrostatic field and the average thermal resistance among three different ESEC chambers at the flow rate of 8 cm^3/hr and the heat flux of 4,384.40 W/m^2.*

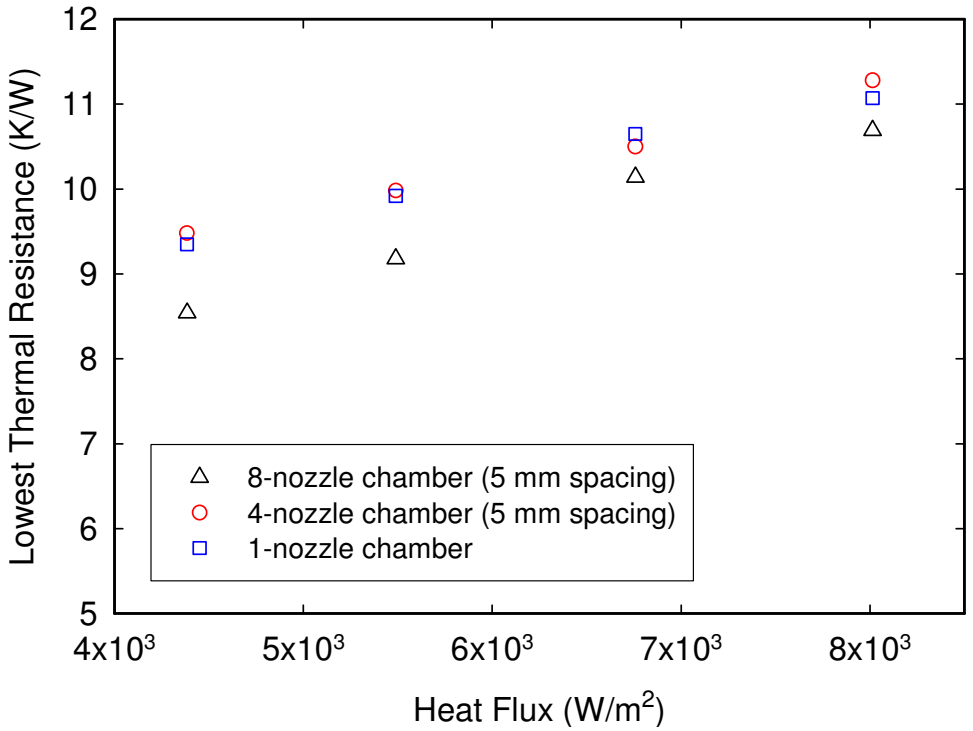

Figure 5-36. *The lowest thermal resistance achieved by the three ESEC chambers at different heat fluxes. The lowest thermal resistance occurs at the highest achievable potential of each chamber and flow rate of 8 cm^3/hr.*

5.5.3.3 Cooling Rate

Figure 5-37 shows that the 8-nozzle ESEC chamber with 5 mm spacing might not be able to achieve better average cooling rate at higher applied potential or higher mass flow rate. For example, at the mass flow rate of 8.77×10^{-7} kg/s, the 8-nozzle ESEC chamber achieves the maximum average cooling rate of 7.56×10^{-3} °C/s when the applied potential is 5 kV, while the minimum average cooling rate of 2.00×10^{-3} °C/s is achieved when the applied potential is 7.8 kV. In addition, the maximum average cooling rate of 8.75×10^{-3} °C/s is achieved by the chamber at an applied potential of 7.0 kV instead of 7.8 kV.

For the first five minutes after the ESEC cooling device is started, Figure 5-38 shows the transient relationship between the average electrostatic field and the average cooling rate of all the three ESEC chambers at the heat flux of 4,384.40 W/m^2 and the total flow rate of 8 cc/hr. In general, increase the average electrostatic field results in the increase in the average cooling rate. For all the three ESEC chambers, the slopes between the average electrostatic field and the average cooling rate are approximately 5.0×10^{-8} K/s per average electrostatic field intensity.

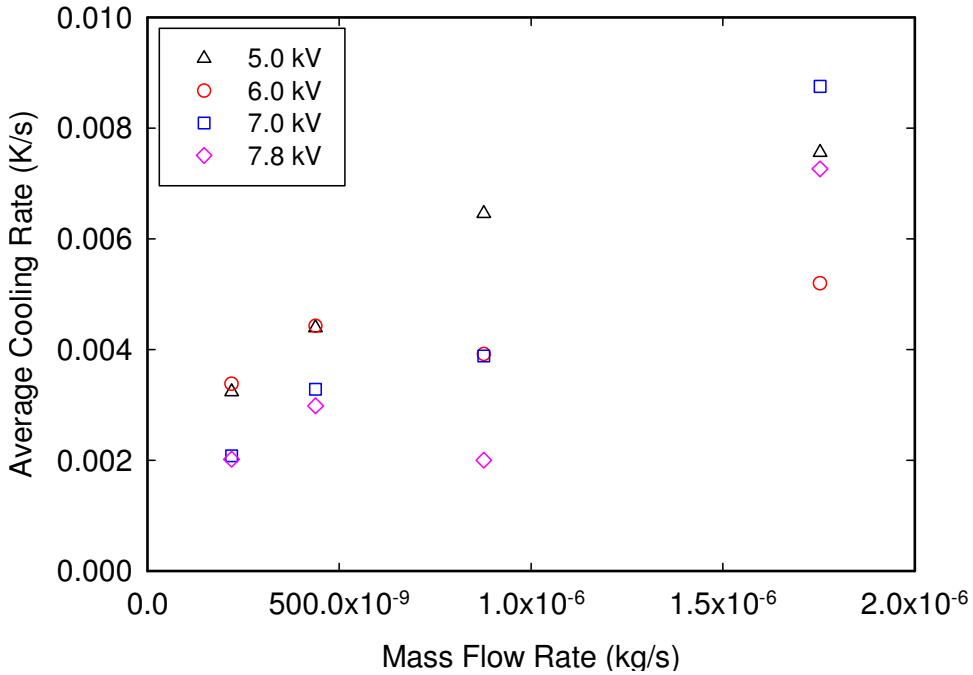

Figure 5-37. *The relationship between the mass flow rate and the average cooling rate of the 8-nozzle ESEC chamber with 5 mm spacing at different potentials. The heat flux is 4,384.40 W/m^2.*

At the same average electrostatic field, the average cooling rate of the 1-nozzle ESEC chamber is the highest, followed by the 4-nozzle chamber with 5 mm spacing and the 8-nozzle chamber with 5 mm spacing. The average cooling rates of the 4-nozzle chamber with 5 mm spacing and the 8-nozzle chamber with 5 mm spacing are 11.74 % and 21.82 %, respectively, lower than that of the 1-nozzle ESEC chamber at the same average electrostatic field. At these conditions, the corresponding potentials applied on the 4-nozzle chamber and the 8-nozzle ESEC chamber are 4.00 % and 12.13 %, respectively, lower than that applied on the 1-nozzle ESEC chamber.

Neither the potential distribution close to the tip of the micronozzle of the ESEC chambers nor the average surface change on the tip of the micronozzle can explain different behavior in the average cooling rate achieved by the three ESEC chambers. The most possible reason is due to the EHD functioning mode. Although all of the ESEC chambers were operated in the multi-jet mode, the amount of the applied potential still dominates the number of the electrified jets, the electrospray angle (defined in Figure 5-22) of each jet, the corresponding distribution of the droplet diameter, the spatial distribution of the droplets, and possible presence of gas ions due to the electrical discharge at a higher applied potential. Further quantitative investigations regarding to these effects through experiments and full multiphysics modeling are necessary.

At the steady state condition, Figure 5-39 shows the relationship between the highest cooling rate and the heat fluxes among the three ESEC chambers. In general, the highest cooling rate of the three ESEC chambers at different heat fluxes ranges from 8×10^{-3} K/s to 1.4×10^{-3} K/s. Furthermore, the results show that the 4-nozzle chamber with 5 mm spacing could deal with a wider range of heat flux while still keep the highest average cooling rate over the 1-nozzle chamber and the 8-nozzle ESEC chamber with 5 mm spacing.

Additionally, although the actual highest cooling rates of the 4-nozzle ESEC chamber with 5 mm spacing and the 1-nozzle ESEC chamber are not the same, the average difference of the highest cooling rate between the 4-nozzle ESEC chamber with 5 mm spacing and the 1-nozzle ESEC chamber at different heat fluxes is approximately 3×10^{-3} K/s. The potential distribution close to the tip of the micronozzle of the 1-nozzle ESEC chamber and the 4-nozzle ESEC chamber with 5 mm spacing is also applicable to point out the tendency of the highest cooling rate of the 4-nozzle ESEC chamber with 5 mm spacing and the 1-nozzle ESEC chamber at different heat fluxes.

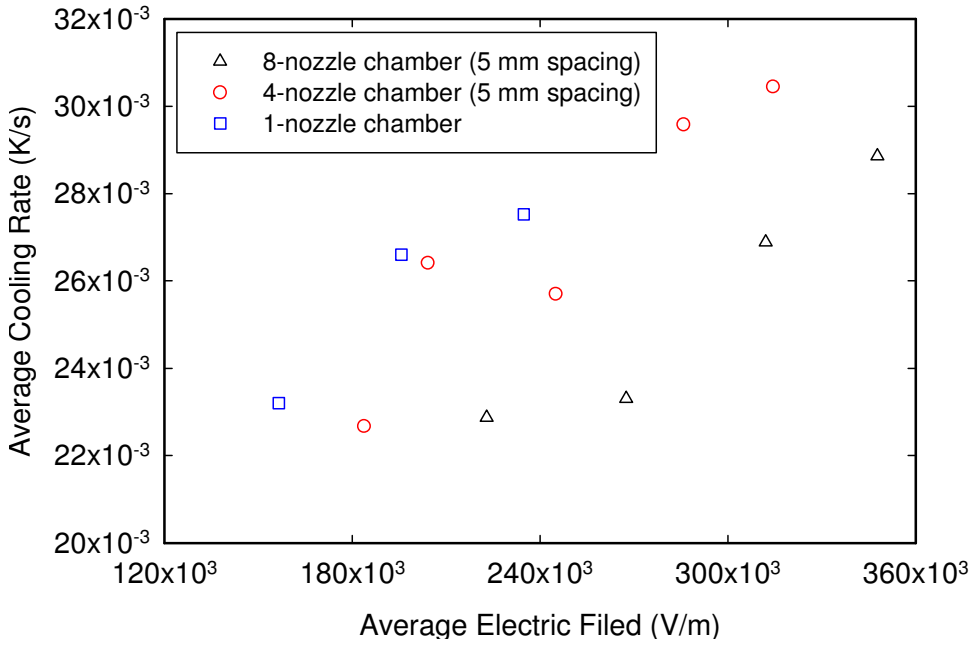

Figure 5-38. *The relationship between the average electrostatic field and the average cooling rate among three different ESEC chambers at a total flow rate of 8 cm^3/hr and a heat flux of 4,384.40 W/m^2.*

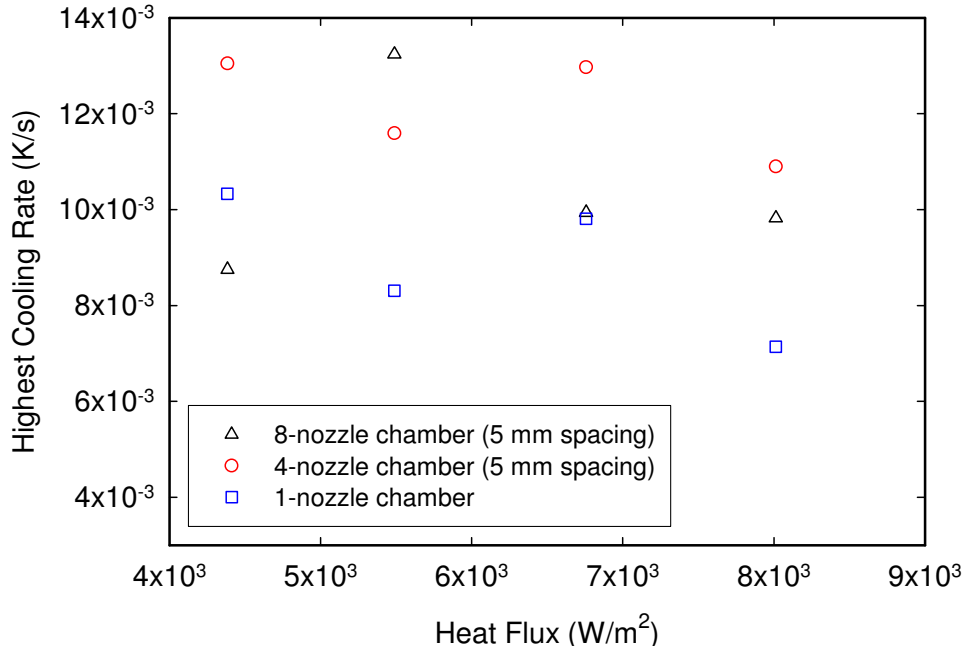

Figure 5-39. *Highest cooling rate achieved by the three ESEC chambers at different heat fluxes.*

5.5.4 Optimization Methodology of the ESEC Chambers

5.5.4.1 Enhancement Ratio

Figure 5-40 shows the relationship between the enhancement ratio and the ratio of the We_E to We for the 1-nozzle ESEC chamber. The applied potential was from 4 kV to 7 kV. At the same Weber number, higher applied potentials results in higher enhancement ratios. At the same applied potential (the same We_E), increasing the working fluid flow rate (higher Weber number) results in a higher enhancement ratio. Additionally, at the same heat flux, the highest enhancement in the heat transfer performance always occurs at the highest flow rate and highest achievable potential. This phenomenon is especially obvious at the lower heat flux. For example, at the heat flux of 4,384 W/m^2, the difference between the highest achievable enhancement ratio and lowest one is 0.66, while the difference between the highest achievable enhancement ratio and lowest one at the heat flux of 8,014 W/m^2 reduces to 0.32.

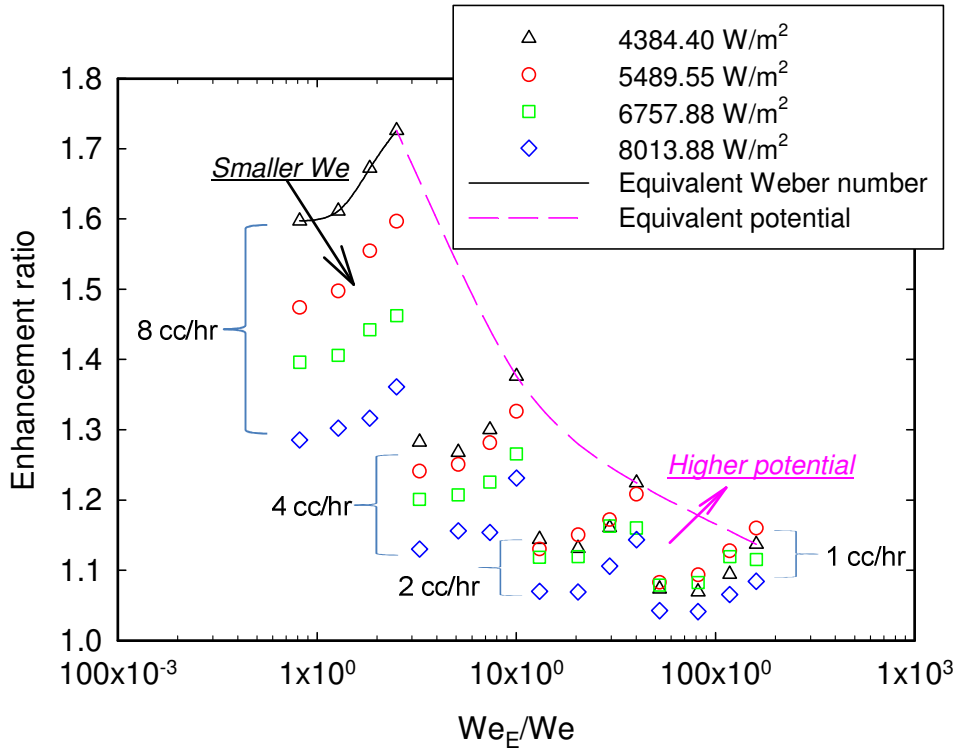

Figure 5-40. *Relationship between the electric Weber number, the Weber number, and the enhancement ratio achieved by the 1-nozzle ESEC chamber at different heat fluxes.*

The decrease in the enhancement ratio for all chambers at the lowest volumetric flow rate is due to the bulk heating of the formed liquid thin film on the thermal exchange surface. The thermal boundary layer reaches the free surface of the wall jet. The same phenomenon was also observed for different arrays of traditional impinging liquid jets [62].

Figure 5-41 and Figure 5-42, respectively, show the enhancement ratios achieved by the 4-nozzle chamber with 6 mm spacing and the 8-nozzle chamber with 5 mm spacing at different heat fluxes. For the same Weber number ranges, the enhancement ratio distribution trend achieved by these two ESEC chambers are similar to that achieved by the 1-nozzle ESEC chamber (Figure 5-40); that is, at the same heat flux, the enhancement ratios increase when both the Weber number and electric Weber number increase. The highest enhancement ratios achieved by the 4-nozzle (6 mm spacing) ESEC chamber and 8-nozzle (5 mm spacing) ESEC chamber occur at the lowest heat flux investigated. The 4-nozzle chamber with 4 mm spacing and the 4-nozzle chamber with 5 mm spacing also shows the same trend on the enhancement ratio, and so do the 8-nozzle chamber with 4 mm spacing and the 8-nozzle chamber with 6 mm spacing.

Figure 5-43 shows the relationship between the enhancement ratio and the total mass flow rate of three different sorts of ESEC chambers at 5 kV and 4,384 W/m^2 heat flux. In terms of the quantity of micronozzles, the 8-nozzle ESEC chambers of different spacing achieve enhancement ratios of higher than those achieved by the 4-nozzle ESEC chambers of different spacing. Additionally, Figure 5-43 indicates that the chamber with the higher quantity of micronozzles might not be able to achieve higher enhancement ratios. For example, the enhancement ratios achieved by the 4-nozzle chamber with 5 mm spacing are nearly the same as those achieved by the 1-nozzle ESEC chamber, and in some cases, the enhancement ratio achieved by the 4-nozzle chamber with 5 mm spacing are even lower than those achieved by the 1-nozzle ESEC chamber. Furthermore, for the 4-nozzle chamber with 6 mm spacing and the 8-nozzle chamber with 6 mm spacing, they achieve nearly the same enhancement ratios, meaning that as long as the spacing is large enough, increasing the quantity of the micronozzles does not enhance the potential gradient near the tip of the micronozzle [1], which results in higher enhancement ratios.

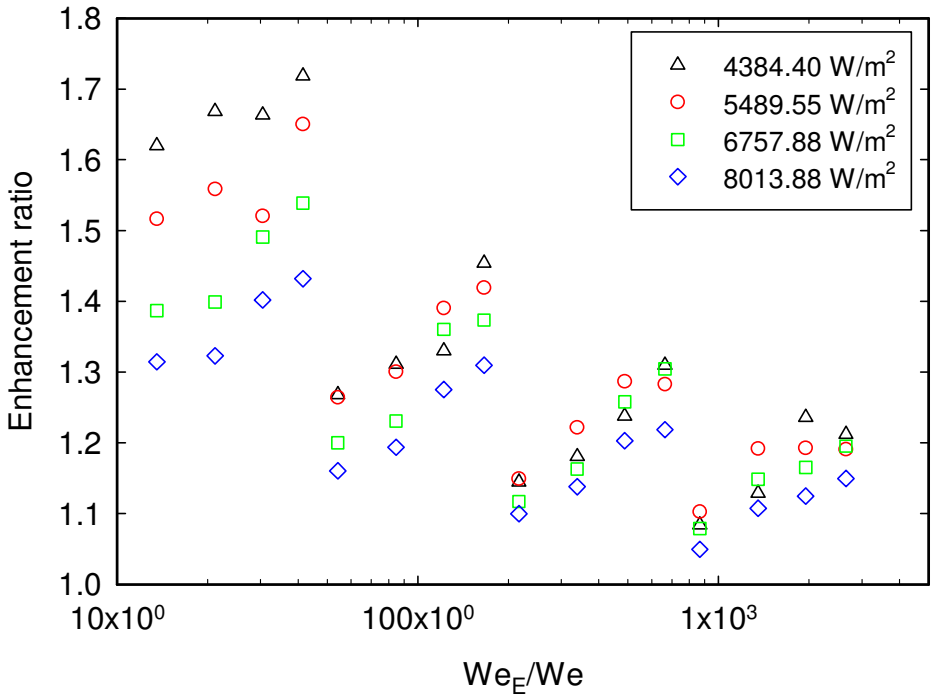

Figure 5-41. *Relationship between the electric Weber number, the Weber number, and the enhancement ratio achieved by the 4-nozzle ESEC chamber with 6 mm spacing at different heat fluxes.*

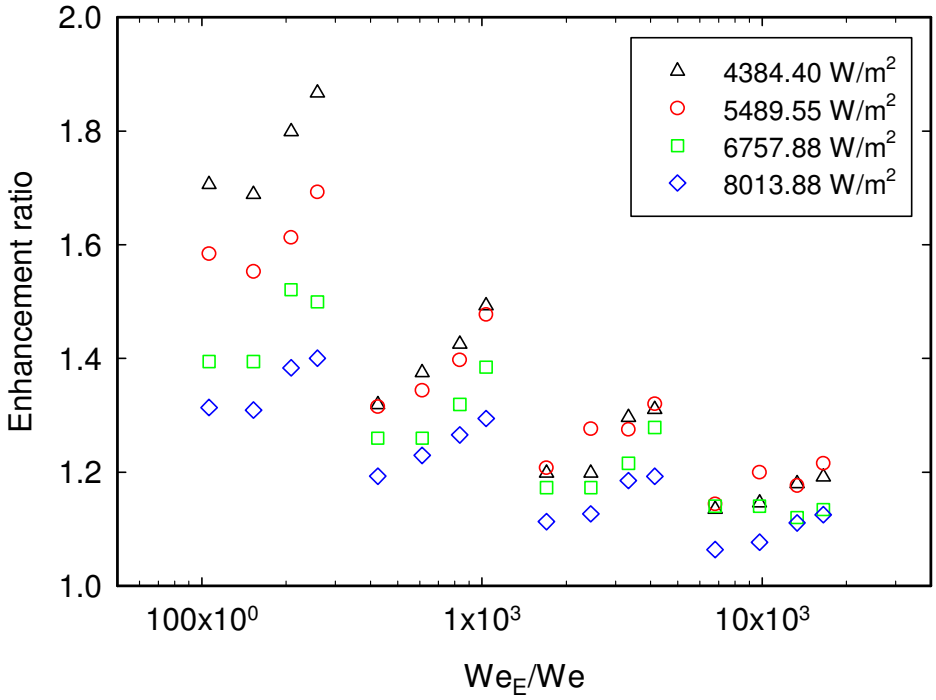

Figure 5-42. *Relationship between the electric Weber number, the Weber number, and the enhancement ratio achieved by the 8-nozzle ESEC chamber with 5 mm spacing at different heat fluxes.*

Figure 5-43 also shows that, for the same quantity of micronozzles, ESEC chambers of different spacing have great influence on the achievable enhancement ratio. This phenomenon was not observed for cases using impinging liquid jets from an array of nozzles over a chip-scale heated surface [62]. The application of the potential on the ESEC chamber creates the non-uniform potential distribution between the tip of the micronozzle and the thermal exchange surface. The intensity of the potential distribution determines the EHD functioning mode [42, 43] of the ESEC chambers, which then determines the heat transfer performance of the ESEC chambers.

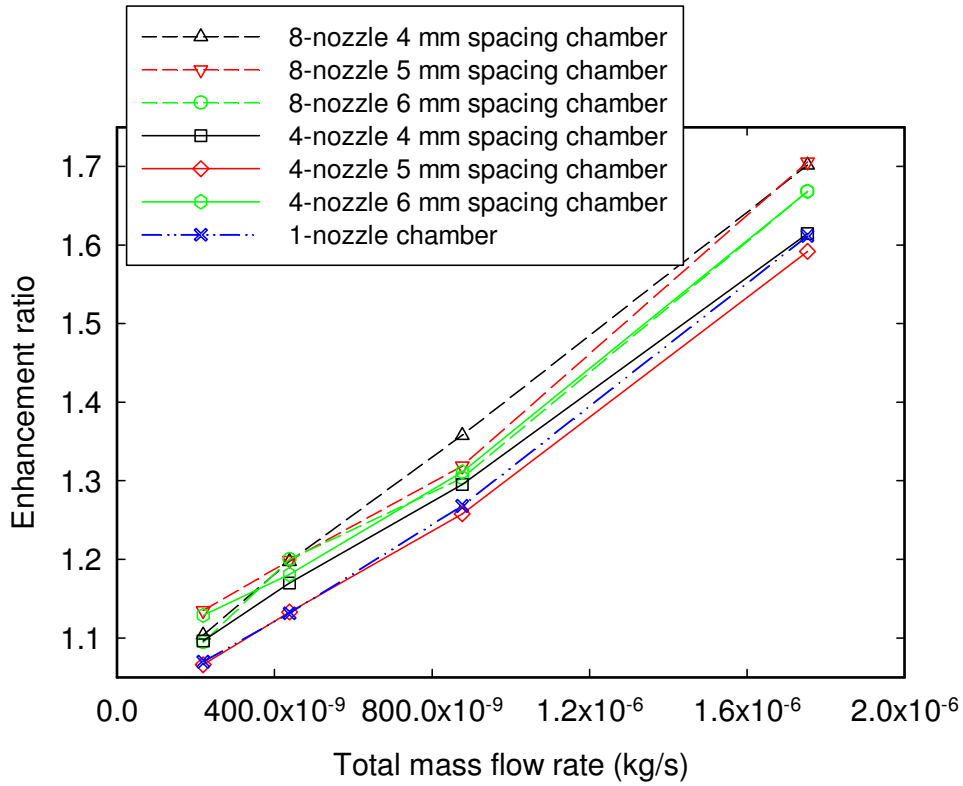

Figure 5-43. *Relationship between the total mass flow rate and the enhancement ratio achieved by three different types of ESEC chambers. The applied potential is 5 kV, and the heat flux is 4,384.40 W/m^2.*

Figure 5-44 shows the highest enhancement ratios achieved by the 4-nozzle ESEC chambers of different spacing at different heat fluxes. Highest enhancement ratios always occur at the highest achievable potential and flow rate. Although the maximum enhancement ratio of 1.72

was achieved by the 4-nozzle chamber with 6 mm spacing at the lowest heat flux, this maximum enhancement ratio is slightly lower than that achieved by the 1-nozzle ESEC chamber at the same heat flux. When the 4-nozzle ESEC chambers were operated at a heat flux higher than 5,000 W/m^2, the highest enhancement ratios achieved by the 4-nozzle chamber with 6 mm spacing was higher than that of the 1-nozzle ESEC chamber, while the highest enhancement ratios achieved by the 4-nozzle chamber with 4 mm spacing and 4-nozzle chamber with 5 mm spacing were lower than that of the 1-nozzle ESEC chamber.

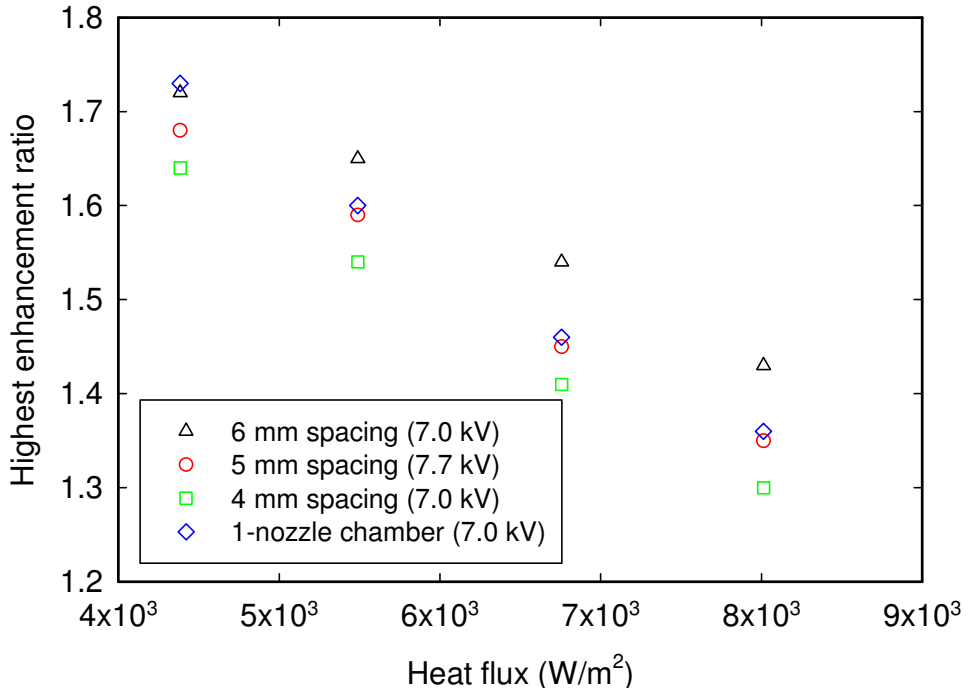

Figure 5-44. *Highest enhancement ratios achieved by 4-nozzle chambers of different spacing at different heat fluxes.*

The transient electrospray behavior of the 4-nozzle ESEC chambers in the beginning of the electrospray process determines the enhancement ratio difference among 4-nozzle ESEC chambers. For the 4-nozzle chamber with 6 mm spacing, the electrified droplets broadly distribute to cover a larger thermal exchange surface area in the beginning of the electrospray process, which results in a larger temperature decrease on the thermal exchange surface within the same time scale.

Figure 5-45 shows the highest enhancement ratios achieved by the 8-nozzle ESEC chambers of different spacing at different heat fluxes. Unlike the 4-nozzle ESEC chambers, the maximum

enhancement ratio of 1.87 achieved by the 8-nozzle chamber with 5 mm spacing is higher than that of the 1-nozzle ESEC chamber at the same lowest heat flux. Additionally, throughout the heat fluxes investigated, the highest enhancement ratios achieved by the 8-nozzle chamber with 5 mm spacing is higher than those of the 1-nozzle ESEC chamber. The highest enhancement ratios achieved by the 8-nozzle chamber with 6 mm spacing and the 8-nozzle chamber with 4 mm spacing are similar to those of the 1-nozzle chamber, except for the highest heat flux condition.

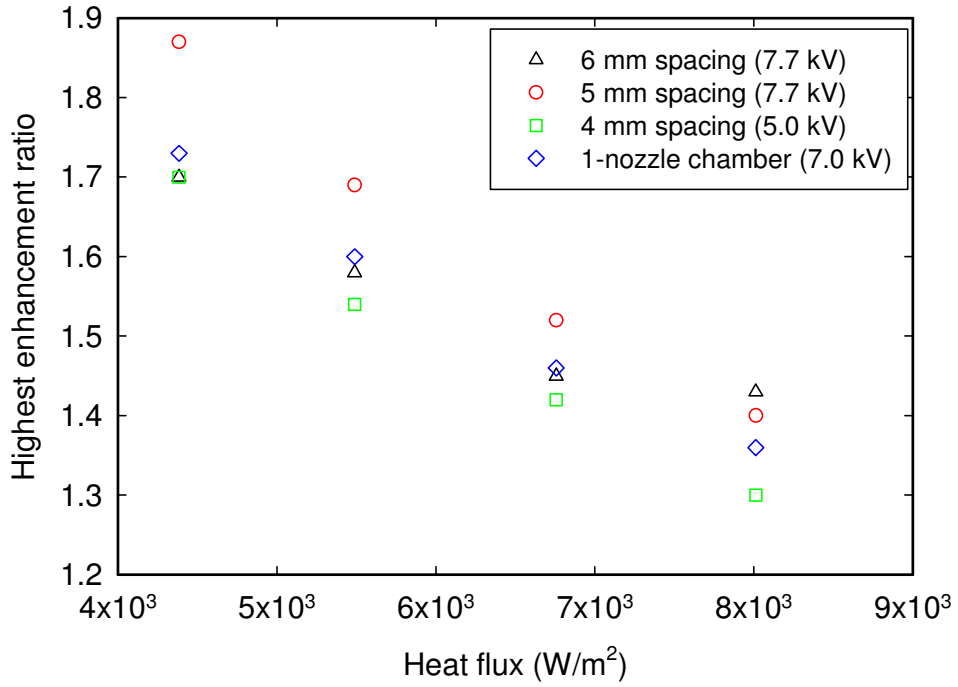

Figure 5-45. *Highest enhancement ratios achieved by 8-nozzle chambers of different spacing at different heat fluxes.*

When we compare Figure 5-44 and Figure 5-45, it shows that, at steady state conditions, increasing the quantity of electrospray nozzles does not have an obvious improvement on the maximum achievable enhancement ratio because of the formation and accumulation of a liquid thin film over the thermal exchange surface at steady state conditions. At the lower heat flux condition, if the thermal exchange surface temperature is below the ethanol alcohol's boiling point, the entire thermal exchange surface is almost covered with the liquid thin film. The mass transfer phenomenon is not obvious. At higher heat flux conditions, when the thermal exchange surface temperature is higher than 78.3 ºC, the boiling phenomenon occurs at the liquid-solid interface where a liquid thin film accumulates. The obvious mass transfer also occurs at the

liquid-gas interface where phase change occurs. The boiling phenomenon and mass transfer give rise to larger heat transfer rates.

Figure 5-44 and Figure 5-45 also indicate that the highest enhancement ratios achieved by the 4-nozzle chamber with 4 mm spacing and the 8-nozzle chamber with 4 mm spacing at different heat fluxes are almost the same, and those values are the lowest compared to other ESEC chambers investigated in this dissertation.

5.5.4.2 Average Thermal Resistance

Figure 5-46 shows the average thermal resistance achieved by three different ESEC chambers at 7 kV, 4,384 W/m^2 heat flux and different total mass flow rates. Data for the 8-nozzle chamber with 4 mm spacing is unavailable, because this chamber's maximum applicable potential before breakdown is 5.0 kV. The 4-nozzle 6 mm spacing ESEC chamber and the 8-nozzle 5 mm spacing ESEC chamber achieved better average thermal resistance than that achieved by the 1-nozzle ESEC chamber for the investigated total mass flow rates. At total mass flow rates lower than 8.8×10^{-7} kg/s, although some ESEC chambers achieve better average thermal resistance than that achieved by the 1-nozzle ESEC chamber, they cannot achieve average thermal resistance better than the 1-nozzle ESEC chamber at total mass flow rates higher than 8.8×10^{-7} kg/s. Therefore, in terms of the average thermal resistance, although both the quantity of micronozzles and the spacing between them has great impact on the achievable average thermal resistance, there is no noticeable trend indicating what factor dominates the achievable average thermal resistance of the ESEC chamber.

At different heat fluxes, Figure 5-47 shows the lowest average thermal resistance achieved by the 4-nozzle ESEC chambers of different spacing. In general, for the same 4-nozzle ESEC chamber, higher heat flux results in higher average thermal resistance, which means that heat transfer performance becomes worse at higher heat flux.

Among 4-nozzle ESEC chambers, the chamber with 6 mm spacing has the lowest average thermal resistance at all heat fluxes, which means that the chamber with 6 mm spacing has better heat transfer performance in terms of the lowest average thermal resistance. In addition, Figure 5-47 also indicates that the lowest average thermal resistance of the 4-nozzle chamber with 5 mm

spacing is nearly the same as that of the 1-nozzle ESEC chamber. The 4-nozzle chamber with 4 mm spacing has the highest average thermal resistance at all heat flux conditions.

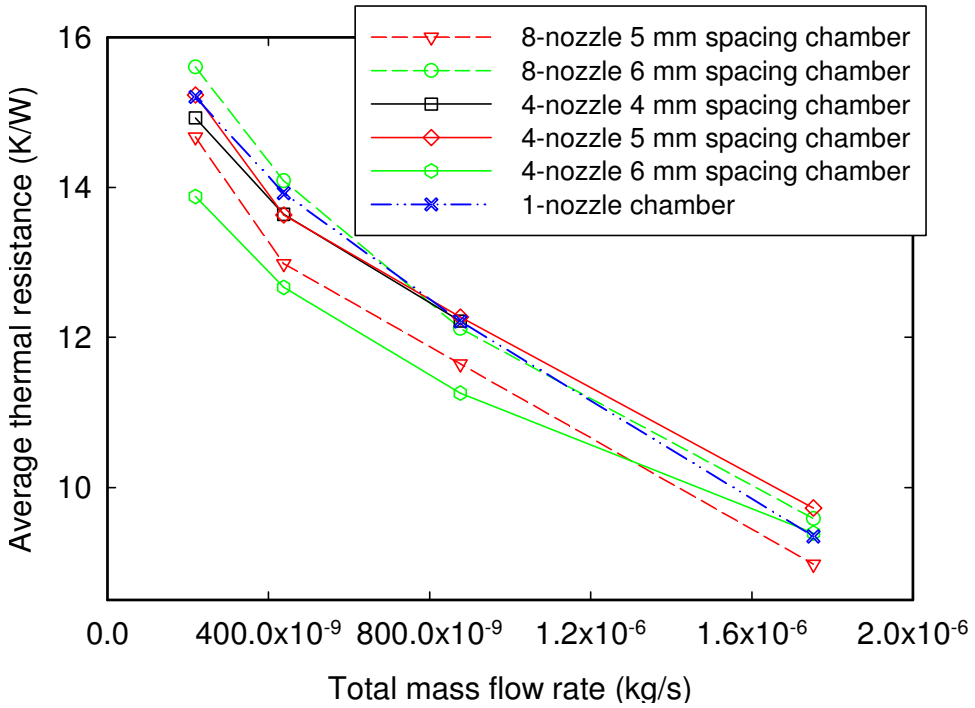

Figure 5-46. *Relationship between the total mass flow rate and average thermal resistance achieved by three different types of ESEC chambers. The applied potential is 7 kV, and the heat flux is 4,384.40 W/m^2.*

Figure 5-48 shows the lowest average thermal resistance achieved by 8-nozzle ESEC chambers of different spacing at different heat flux. The 8-nozzle chamber with 5 mm spacing achieves the lowest average thermal resistance among the 8-nozzle ESEC chambers.

Among the 8-nozzle ESEC chambers, the 8-nozzle chamber with 5 mm spacing almost achieves the lowest thermal resistance at the investigated heat fluxes. The average thermal resistance achieved by the 8-nozzle chamber with 4 mm spacing and 8-nozzle chamber with 6 mm spacing is higher than that achieved by the 1-nozzle ESEC chamber.

Therefore, in terms of average thermal resistance, the 4-nozzle chamber with 6 mm spacing and the 8-nozzle chamber with 5 mm spacing achieved better performance.

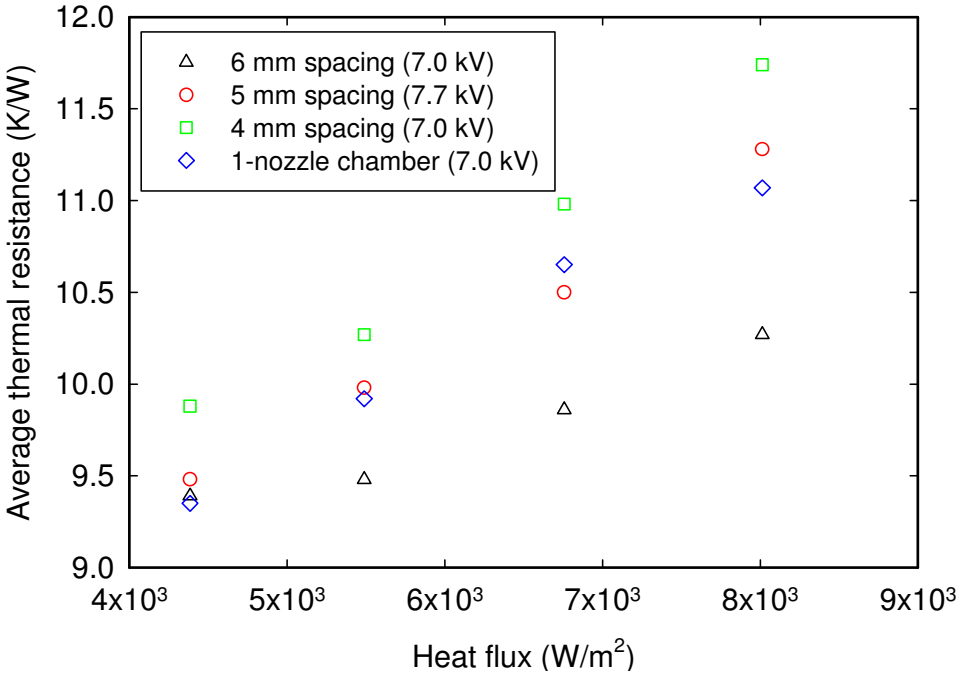

Figure 5-47. *The lowest average thermal resistance achieved by the 4-nozzle ESEC chambers of different spacing at different heat fluxes.*

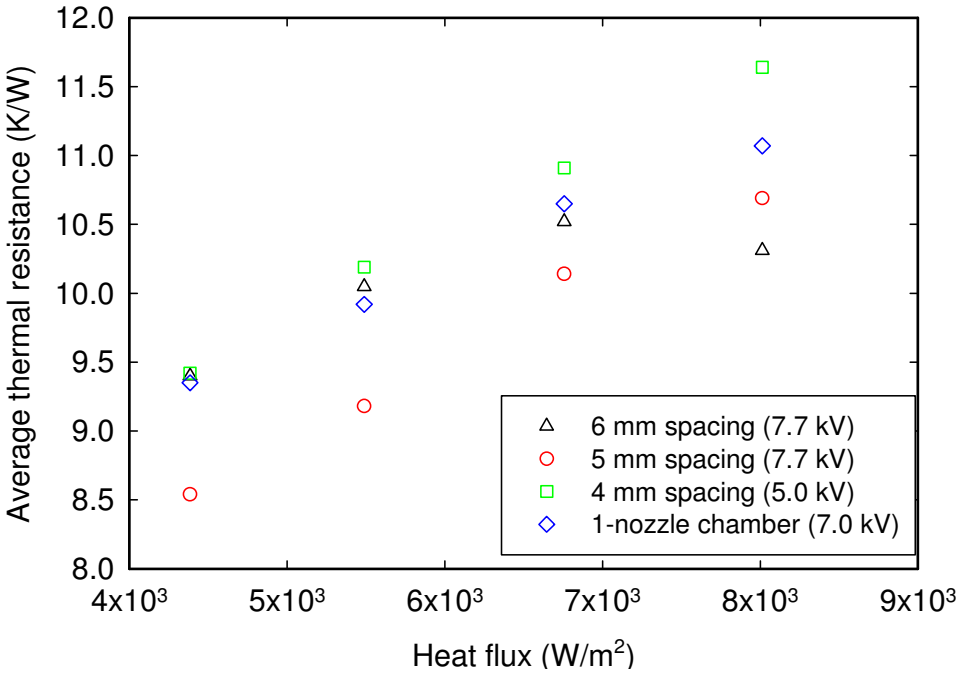

Figure 5-48. *The lowest average thermal resistance achieved by the 8-nozzle chambers of different spacing at different heat fluxes.*

5.5.4.3 Cooling Rate

Unlike the enhancement ratio and average thermal resistance achieved by these ESEC chambers at the steady state condition, these chambers achieve different transient heat transfer performance. Figure 5-49 shows the average cooling rate achieved by three different types of ESEC chambers at 5 kV, 4,384 W/m^2 heat flux, and different total mass flow rates. Like how the quantity and spacing of the micronozzles affect the steady state heat transfer performance of ESEC chambers, these two factors also affect the transient average cooling rate. For the 8-nozzle ESEC chambers, the 8-nozzle chamber with 4 mm spacing achieves the highest average cooling rate at the investigated total mass flow rate range. In addition, the average cooling rate achieved by the 8-nozzle chamber with 5 mm spacing and the 8-nozzle chamber with 6 mm spacing at different total mass flow rates is nearly the same. The difference is around 2.3×10^{-3} K/s at the investigated total mass flow rates.

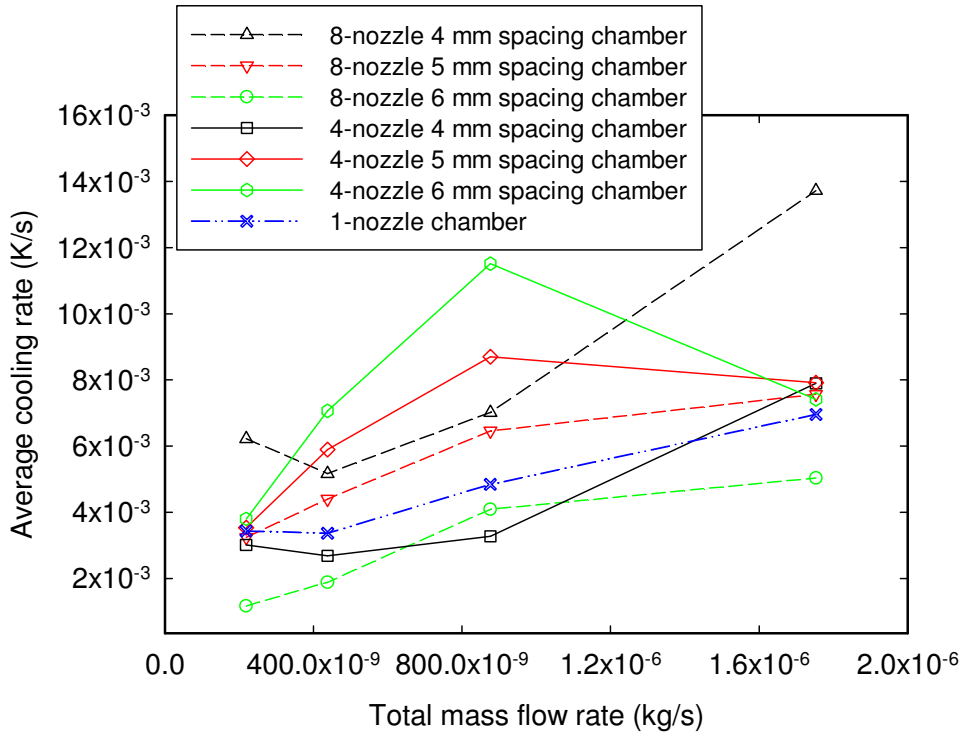

Figure 5-49. *Relationship between the total mass flow rate and the average cooling rate achieved by three different types of ESEC chambers. The applied potential is 5 kV, and the heat flux is 4,384.40 W/m^2.*

Unlike 8-nozzle ESEC chambers, the 4-nozzle chamber with 4 mm spacing achieves the lowest average cooling rate among 4-nozzle ESEC chambers at the investigated total mass flow rates. The 4-nozzle chamber with 5 mm spacing and the 4-nozzle chamber with 6 mm spacing achieve different maximum average cooling rates at the total mass flow rate of 8.8×10^{-7} kg/s.

Furthermore, in terms of the spacing, ESEC chambers of the same spacing show the same trend in the distribution of the average cooling rate, with respect to the total mass flow rate. For example, for the 8-nozzle chamber with 4 mm spacing and the 4-nozzle chamber with 4 mm spacing, they both achieve the minimum average cooling rate at the total mass flow rate of approximately 4.4×10^{-7} kg/s.

Although the 8-nozzle chamber with 6 mm spacing achieves a transient average cooling rate lower than that achieved by the 1-nozzle ESEC chamber, its steady state heat transfer performance (Figure 5-43) is higher than that of the 1-nozzle ESEC chamber. The 4-nozzle chamber with 5 mm spacing also has a completely different steady state and transient heat transfer performance. Therefore, to enable ESEC chambers for the thermal management of microelectronics, different applications require different design and optimization scenarios.

Figure 5-50 shows the highest average cooling rate achieved by the 4-nozzle chambers of different spacing at different heat fluxes. Among 4-nozzle chambers, the 4-nozzle chamber with 6 mm spacing almost achieves the highest cooling at all the heat fluxes. The achievable highest average cooling rate increases as the heat flux is increased. Additionally, the cooling rate achieved by the 4-nozzle chambers of different spacing at different heat fluxes is almost higher than that reached by the 1-nozzle chamber, which means that increasing the quantity of electrospray nozzles is an effective way of enhancing the transient cooling rate of ESEC chambers.

Figure 5-51 shows the highest cooling rate achieved by the 8-nozzle chambers of different spacing at different heat fluxes. For the 8-nozzle chamber with 6 mm spacing, the highest average cooling rate increases with respect to the increase in heat fluxes. For the 8-nozzle chamber with 5 mm spacing, the maximum highest average cooling rate occurs at the heat flux of 5,490 W/m^2. Further increase or decrease in heat flux results in the decrease in the highest average cooling rate. For the 8-nozzle chamber with 4 mm spacing, the highest average cooling rate with respect to the heat flux is similar to that of the 1-nozzle chamber. The highest average cooling rate occurs at the lowest heat flux; a further increase in the heat flux results in the

decrease in the highest average cooling rate. In addition, Figure 5-51 shows that regardless of the spacing of the 8-nozzle chambers, the achievable highest average cooling rates at all heat fluxes are almost higher than those achieved by the 1-nozzle ESEC chamber, which means that increasing the quantity of electrospray nozzles remains an effective way of enhancing the average cooling rate of the ESEC chambers.

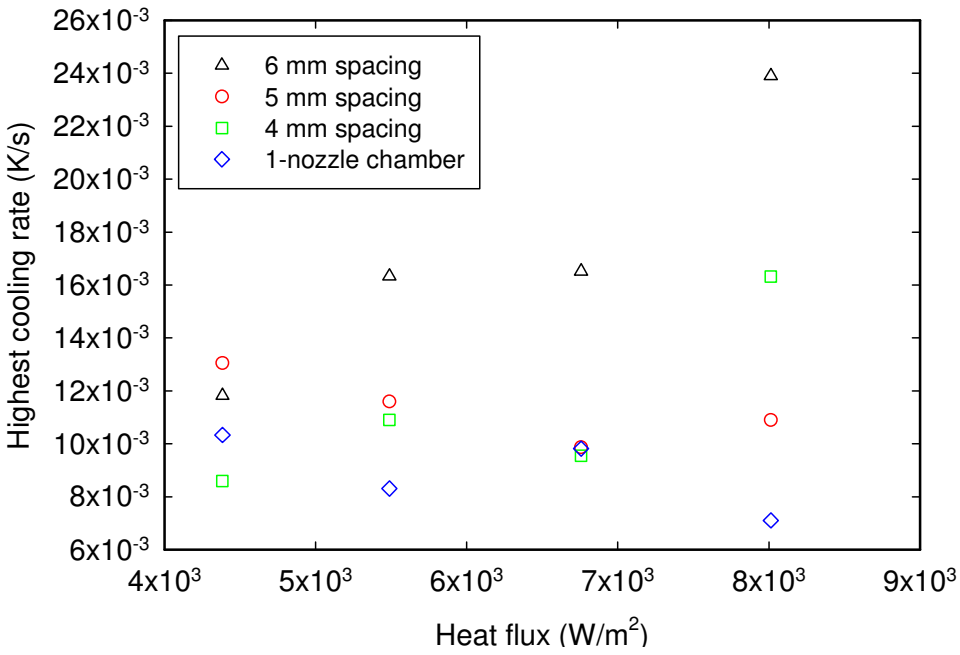

Figure 5-50. *The average cooling rate achieved by the 4-nozzle chambers of different spacing at different heat fluxes.*

Figure 5-50 and Figure 5-51 also show that the 4-nozzle chamber with 6 mm spacing achieves a higher maximum highest average cooling rate than that achieved by the 8-nozzle chamber with 6 mm spacing. When we compare the maximum achievable enhancement ratio achieved by these two chambers, the 4-nozzle chamber with 6 mm spacing still achieves a higher maximum enhancement ratio than that achieved by the 8-nozzle chamber with 6 mm spacing. However, when we compare the achievable enhancement ratio achieved by these two chambers (Figure 5-43), they achieves similar enhancement ratios. Therefore, the transient heat transfer performance (highest average cooling rate) of the ESEC chamber is independent on its enhancement ratio.

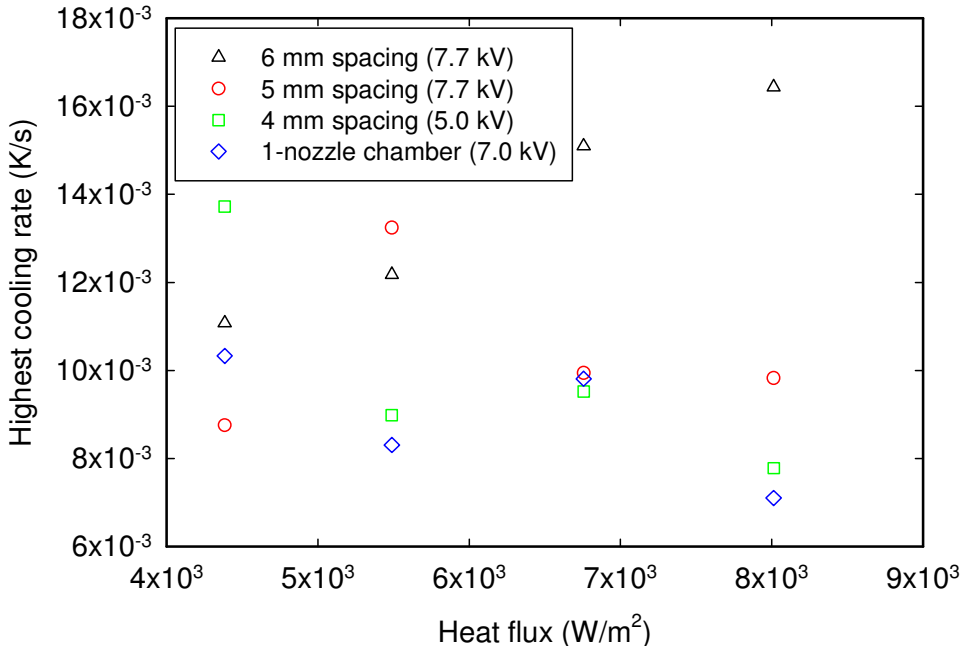

Figure 5-51. *The average cooling rate achieved by 8-nozzle chambers of different spacing at different heat fluxes.*

5.6 Empirical Heat Transfer Models of the ESEC Chambers

Empirical heat transfer correlations to design the electrospray evaporative cooling (ESEC) chambers are current unavailable. Wang *et al.* [1] observed that when ESEC chambers operate in multi-jet electrohydrodynamics (EHD) mode, the shape of the electrified liquid jet on the tip of the micronozzle is similar to that of the traditional liquid impinging jet [62, 63]. Therefore, we regarded that empirical heat transfer correlations for traditional free-surface liquid impinging jets are a viable starting point to approximate heat transfer correlations for ESEC chambers.

This chapter discusses empirical heat transfer correlations of ESEC chambers, in terms of the number of the micronozzles, the spacing between the centerlines of the micronozzles and the centerline of the chamber, the applied potentials, the flow rates, and the heat fluxes. These correlations are extended from traditional impinging liquid jets, with the addition of the electric field effect. The data used to formulate the correlations are reported in [3, 6, 110, 148].

5.6.1 Definition of Characteristic Length

The application of EHD on an ESEC chamber complicates the characteristic length selection for the heat transfer performance analysis. The process of choosing the characteristic length for a chamber is not only influenced by the number of micronozzles [62, 149], but also the spacing between the micronozzles (defined in Figure 5-6) and the length of the micronozzles. These parameters are important to determine how EHD influences the thermal management performance of an ESEC chamber.

The electric field gradient, found at the tip of the micronozzle, controls the electrospray process. The factors that affect the electric field gradient include: the spatial position (with respect to the closest adjacent micronozzle), the micronozzle length, the distance between the micronozzle tip center and the closest edge of the collecting electrode, the distance between the micronozzle tip center and the closest corner of the collecting electrode, and the spacing between the centerline of the micronozzle and the centerline of the chamber. The different characteristic lengths (L^*) associated with three ESEC chamber types (i.e., 8-nozzle, 4-nozzle, 1-nozzle chambers) are shown in Figure 5-52. For 8-nozzle chambers, shown in Figure 5-52 (a), L^* is defined as

$$L^* = \sqrt{L_{1,8}^2 + L_{2,8}^2} \tag{5.7}$$

$$L_{1,8} = \left(L_1 + L_2 + L_3 + L_4\right)/4 \tag{5.8}$$

$$L_{2,8} = L_9 = \sqrt{(D_c - s)^2 + L_t^{\,2}} \tag{5.9}$$

$$L_1 = L\sqrt{2}/2 - s \tag{5.10}$$

$$L_2 = L/2 - \left(s/\sqrt{2}\right) \tag{5.11}$$

$$L_3 = \sqrt{\left(L/2\right)^2 + (L/2 - s)^2} \tag{5.12}$$

$$L_4 = L/2 - s \tag{5.13}$$

where s is the spacing, D_c is the radius of the chamber, L_t is the length of the micronozzle, and L is the length of the square thermal exchange surface. For 4-nozzle chambers, shown in Figure 5-52 (b), L^* is defined as

$$L^* = \sqrt{L_{1,4}^2 + L_{2,4}^2} \tag{5.14}$$

$$L_{1,4} = \left(L_5 + L_6\right)/2 \tag{5.15}$$

$$L_{2,4} = L_9 = \sqrt{(D_c - s)^2 + L_t^{\,2}} \tag{5.16}$$

$$L_5 = L\sqrt{2}/2 - s \tag{5.17}$$

$$L_6 = L/2 - \left(s/\sqrt{2}\right). \tag{5.18}$$

For 1-nozzle chambers, shown in Figure 5-52 (c), L^* is defined as

$$L^* = \sqrt{L_{1,1}^2 + L_{2,1}^2} \tag{5.19}$$

$$L_{1,1} = \left(L_7 + L_8\right)/2 = \left(L\sqrt{2}/2 + L/2\right)\Big/2 \tag{5.20}$$

$$L_{1,2} = L_9 = \sqrt{D_c^{\,2} + L_t^{\,2}} \tag{5.21}$$

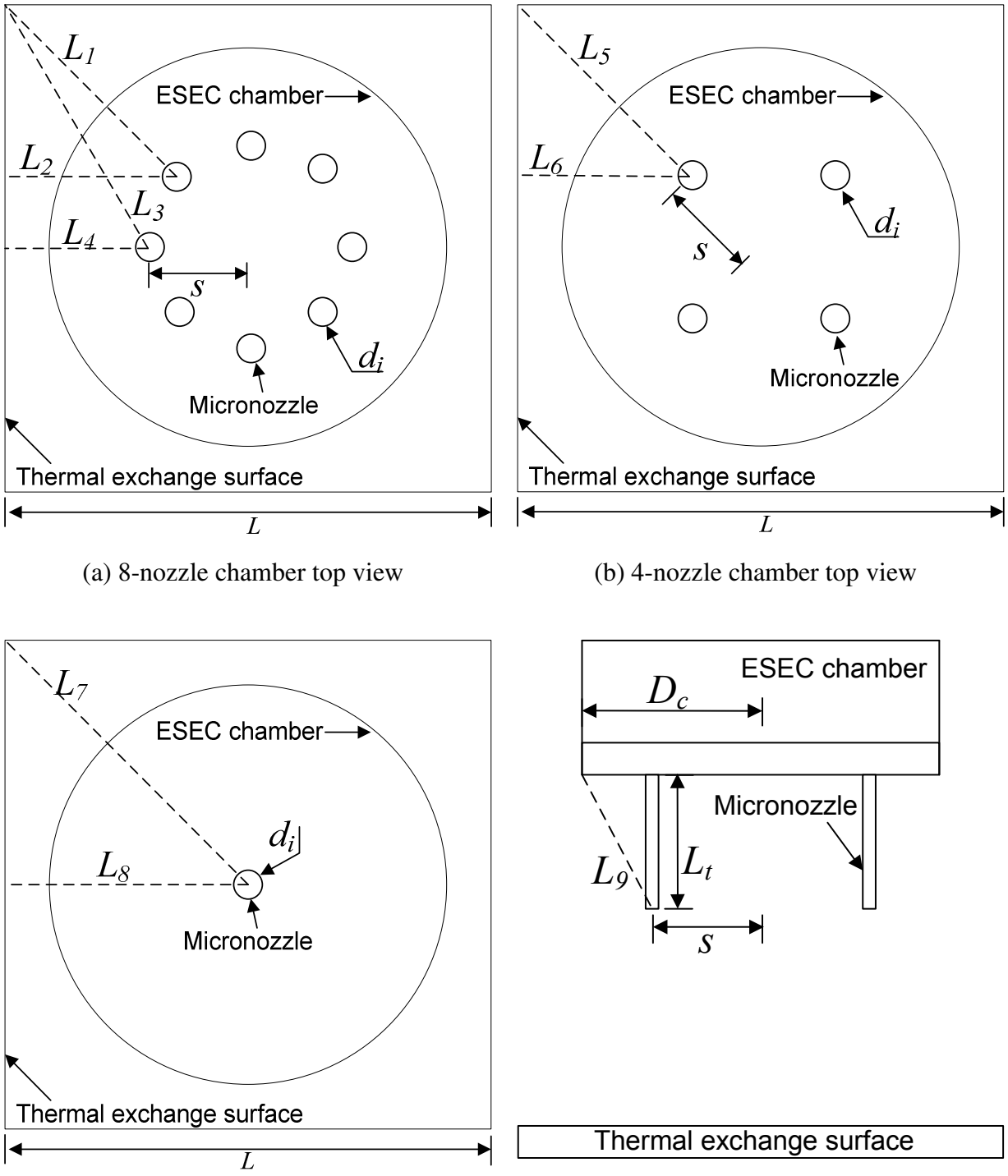

(a) 8-nozzle chamber top view

(b) 4-nozzle chamber top view

(c) 1-nozzle chamber top view

(d) ESEC chamber side view

Figure 5-52. *Definition of the characteristic length for ESEC chambers with different geometry. L is the length of the side of the square heater.*

5.6.2 Electric Field Approximations

It is undesirable to directly measure the electric field intensity at a voltage as high as 7.0 kV. We used the COMSOL Multiphysics numerical electrostatic modeling module to estimate the average electric field intensity for the three ESEC chambers discussed in this investigation. The number of micronozzles and the spacing between the micronozzles (Figure 5-6) are the two factors that determine the difference in the average electric field intensity between the tips of the micronozzles and the thermal exchange surface. Therefore, the electric field approximation of an ESEC chamber is regressed as a function of the number of micronozzles and the spacing between them.

The analytical model for the electric field intensity of a hyperboloid-to-plane EHD configuration was derived from the Laplace equation, and is expressed as [144, 145]

$$E_0 = \frac{AV}{r_0 \ln(4H/r_0)} \tag{5.22}$$

where V is the applied potential, r_0 is the outer radius of the micronozzle, and H is the distance between the tip of the micronozzle and the thermal exchange surface. This equation is also used by Feng *et al.* [86] to estimate the average electric field intensity for multi-nozzle electrospray cooling devices, without modifying the constant A. However, for an EHD configuration using a constant diameter nozzle electrode, Wang *et al.* [1] suggest one should modify the constant A approximately two order of magnitudes less than the hyperboloid-to-plane EHD configuration to fit the numerical electric field modeling result. This is because the analytical model, represented by Eq. (5.22), is based on the hyperboloid needle's tip radius, which is much smaller than the outer radius of a constant diameter nozzle electrode. Therefore, the form of Eq. (5.22) is used in this investigation to estimate the average electric field intensity of ESEC chambers for empirical heat transfer correlation analysis.

To approximate the average electric field intensity, Eq. (5.22) is adapted by modifying A as a function of the number of micronozzles and the spacing between them, while the other

parameters remain unchanged. The modified analytical model for a chamber using constant diameter nozzles is expressed as

$$E_0(s,N) = \frac{A(s,N)\times V}{r_e \ln(4H/r_e)} \tag{5.23}$$

where s is the spacing between the center of the chamber and the micronozzles (Figure 5-6), N is the number of micronozzles, r_e is the effective radius of each micronozzle, and r_e is defined as

$$r_e = \sqrt{N} r_0 \tag{5.24}$$

The chamber's effective radius of the micronozzle represents the corresponding nozzle tip surface area when only using a single nozzle. The corresponding nozzle tip surface area is the summation of the nozzle tip surface area of every single nozzle consisting of a multi-nozzle ESEC chamber. Figure 5-53 shows the simulated average electric field intensity for all ESEC chambers. By using Eq. (5.23), the constant ($A(s,N)$) as a function of the number of micronozzles and the spacing between them for ESEC chambers is regressed as

$$\begin{gathered} A(s,N) = 0.31\exp\left\{-0.50\left[\left(N_e\right)^2 + \left(s_e\right)^2\right]\right\} \\ N_e = \left(N - 8.02\right)/4.80 \\ s_e = \left(s + 7.67\times10^{-2}\right)/5.48\times10^{-2} \end{gathered} \tag{5.25}$$

where s is the spacing between the center of the chamber and the micronozzles (Figure 5-6), and N is the number of micronozzles.

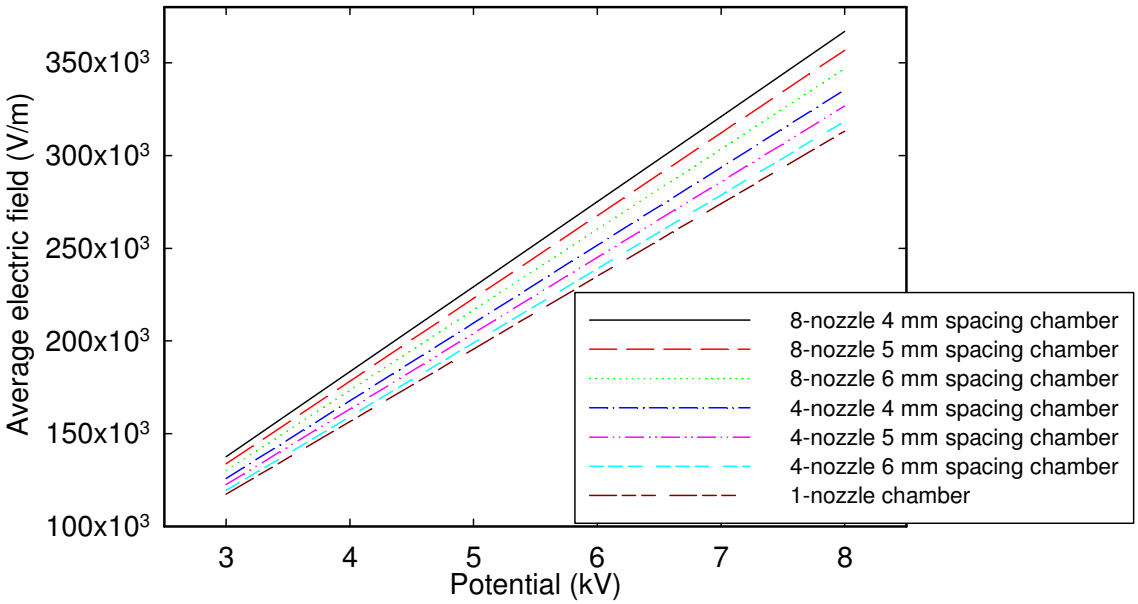

Figure 5-53. *Simulated average electric field intensity for the ESEC chambers.*

5.6.3 Empirical Heat Transfer Correlations

5.6.3.1 Enhancement Ratio Correlations

The enhancement ratio (ER) of an ESEC chamber depends on the geometry type, the electric field intensity distribution, the fluid properties, the flow rate, and so on. Based on these parameters, the general ER correlation form for each ESEC chamber follows the function

$$\mathrm{ER} = f\left(N, \frac{L^*}{D_i}, \mathrm{We_E}, \mathrm{We}, \mathrm{Re}_{D_i}\right) = a\mathrm{We_E}^{b}\mathrm{We}^{c}\,\mathrm{Re}_{D_i}{}^{d}\left(N \times \frac{L^*}{D_i}\right)^{e} \tag{5.26}$$

where a, b, c, d, and e are mathematically determined coefficients, and L^* is the characteristic length (discussed in Section 5.6.1). These coefficients are iteratively determined from -1 to 1, in 0.001 intervals. To approximate the ER correlations, some assumptions are made: (i) that the difference between the experimental ER and the calculated ER is less than ± 10%, and (ii) that more than 75% of the experimental ERs should be covered.

The incrementally determined coefficients of the ER correlation, Eq. (5.26), for the three chamber geometry types over the ranges $4.0\times10^{-2} \leq \mathrm{We_E} \leq 2.5\times10^{-1}$, $1.4\times10^{-5} \leq \mathrm{We} \leq 6.0\times10^{-2}$, $1.3\times10^{-2} \leq \mathrm{Re}_{D_i} \leq 9.0\times10^{-1}$, $70 \leq L^*/D_i \leq 104$, and $1 \leq N \leq 8$ are shown in Table 5.6.

Table 5.6. *Coefficients of the enhancement ratio correlation Eq. (5.26) for three different ESEC chamber geometry types.*

ESEC chamber	*a*	*b*	*c*	*d*	*e*
1-nozzle chamber	1.243	0.11	-0.255	0.648	-0.05
4-nozzle chambers	1.243	0.11	-0.255	0.648	-0.001
8-nozzle chambers	1.243	0.11	-0.255	0.648	-0.001

Although many values between -1 and 1 are applicable to the developed ER correlation, we apply the criterion that all coefficients are regressed to be the same values, except for coefficient *e*. Coefficient *a* is a constant term that can either represent the flow condition inside each micronozzle or the operated EHD mode. According to the operating conditions, the flow condition (discussed later) and the operated EHD mode (discussed in Section 2.2.3) remain the same for all ESEC chambers. Therefore, coefficient *a* is kept the same value for all ESEC chambers.

The parameters, with respect to coefficients *b*, *c*, and *d*, represent the flow condition, the applied potential, and the fluid properties. These three coefficients are kept at the same value for all ESEC chambers for several reasons. First, ethyl alcohol is the only working fluid; therefore, the fluid properties remain the same. Second, according to the Reynolds number for the internal flow inside a circular tube with [87], the flow condition inside the micronozzle is laminar flow. The application of the potential on the micronozzle does not influence the flow condition inside the micronozzle [67]. This is because only pressure and viscous forces inside the micronozzle creates a pressure drop to overcome viscous losses. Electrohydrodynamic stress due to the applied potential only influences the flow condition at the micronozzle tip where the liquid meniscus forms. Additionally, although the ESEC chamber consists of multiple micronozzles, the flow (Hagen-Poiseille flow) condition inside each micronozzle should be the same as long as the electric field intensity does not vary significantly from nozzle to nozzle [67, 150]. Our electrostatic field numerical modeling results show that the electric field intensity's variation

from nozzle to nozzle is less than 0.20%. Therefore, it is appropriate to assume that the flow condition inside all micronozzles remains the same.

According to Eq. (5 the parameters related to the coefficient *e* represent how the chamber's geometry affects the achievable ER. The results show that for a chamber with multiple micronozzles, coefficient *e* can be regressed to be the same value (-0.001), whereas *e* for a chamber with only one micronozzle is different (-0.05). Although the characteristic lengths (L^*) for each geometry type are remarkably similar, the multiple of *N* results in a higher NL^*/D_i for chambers that have more micronozzles under the same operating conditions. Therefore, the smaller coefficient, *e,* for a multiple micronozzle ESC chamber is expected to approximate the experimental ERs.

For an ESEC chamber operated at different flow rates and at different heat sources, Figure 5-54 shows the comparison between the calculated enhancement ratio and the experimental data for the 4-nozzle chamber with 6 mm spacing between the centerline of micronozzles and the centerline of the chamber. As can be derived from the ER ratio data, 95% of the experimental enhancement ratios are within ± 10% of the derived correlation. The data that deviates from the correlation by more than ± 10% occurs at a lower heat source and with a higher flow rate (8 cm^3/hr). Other ESEC chambers have been found to have this phenomenon as well. The following discusses three possible reasons attributed to this deviation. First, at a lower heat source condition, the bulk heat acting on the thin film (over the thermal exchange surface) is not noticeable. Lower heat causes the accumulation of liquid, which in turn results in a thicker thin film that causes the average electric field intensity to alternate between the tip of the micronozzle and the collecting electrode. Second, the average electric field estimation between the micronozzle tip and the thermal exchange surface could be miscalculated. The average electric field is obtained from the numerical electrostatic field simulation results. Detailed numerical electrostatic field modeling is discussed in [148]. Real average electric field intensity is highly affected by several parameters like the inconsistent nozzle length, the orientation of these micronozzles to the centerline of an ESEC chamber, and so on. For example, the length of a micronozzle can vary within ± 0.25 mm, and the orientation of a micronozzle (with respect to the thermal exchange surface) is not perfectly perpendicular. These imperfections influence the actual electric field of an ESEC chamber, and possibly affect the flow condition inside each micronozzle. If we increase the modeled average electric field by 10%, deviations between all

the experimental enhancement ratios and correlated data would collapse to within ± 10% deviation from the derived ER correlation. Third, for ESEC chambers with multiple micronozzles, some of the micronozzles are not parallel with each other as they were installed on the chamber. This factor results in a non-similar distribution of electric field intensity at each micronozzle tip. In some cases, the non-similar electric field intensity results in different flow conditions inside each micronozzle. In other cases, the non-similar electric field intensity results in different EHD modes at the micronozzle tip. Different EHD mode alternates the space charge distribution and the formed liquid meniscus shape close to the micronozzle tip, which changes the transport trajectory of charged droplets. The changed charged droplet trajectory then influences the heat transfer performance as the electrified jets reach the thermal exchange surface. Different flow conditions inside each micronozzle, as well as different EHD modes could cause coefficients *a*, *b*, *c*, and *d* to change; these changed values might better approximate the enhancement ratio correlation.

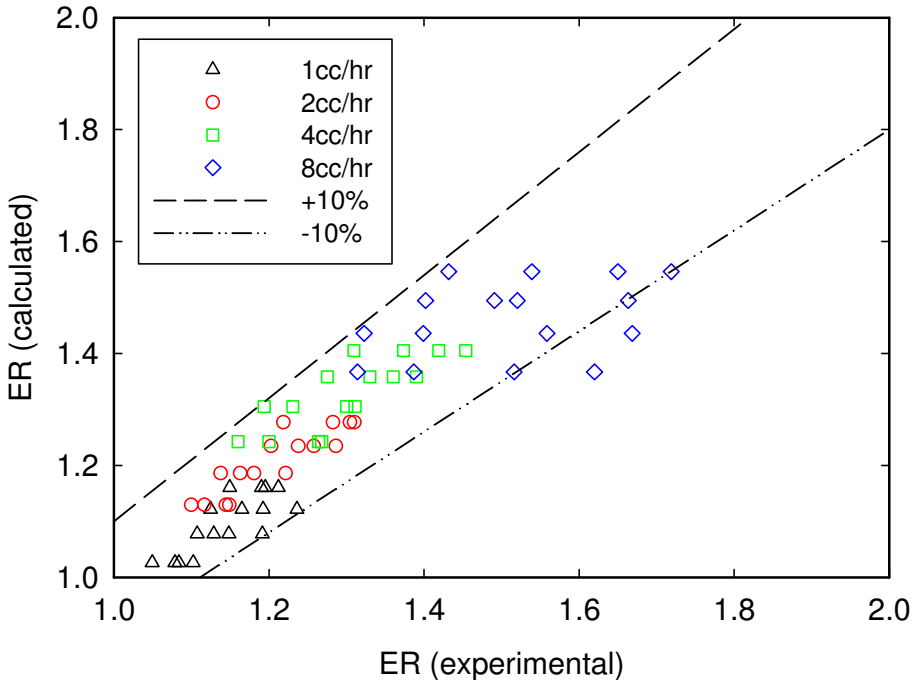

Figure 5-54. *Correlation between calculated ER and experimental data for the 4-nozzle 6 mm spacing ESEC chamber.*

The relationship between the correlated enhancement ratio and the experimental data for each 8-nozzle ESEC chamber (i.e., chambers with 4 mm, 5 mm, and 6 mm spacing between the

centerline of micronozzles and the centerline of the chambers) is shown in Figure 5-55. For 8-nozzle chambers, the enhancement ratio correlation collapses more than 83% of the experimental enhancement ratios, within ± 10% deviation from the derived correlation. Additionally, the 8-nozzle chamber with 5 mm spacing had both the maximum achievable enhancement ratio (1.87) and the largest deviation of data when operating at 7.7 kV (with a flow rate of 8 cm^3/hr), as shown in Figure 5-55. The following outlines two reasons for why there was a larger deviation in the data regression. First, the maximum achievable enhancement ratio is determined by the transient electrospray behavior that occurs at the beginning of the electrospray process. The 8-nozzle chamber (with 5 mm spacing) has the largest portion of the thermal exchange surface covered at the beginning of the electrospray process, which results in the largest temperature decrease within the same time scale. Second, if the thermal exchange surface temperature is below the ethyl alcohol's boiling point, almost the entire thermal exchange surface is covered with the liquid thin film. This occurs because the thermal exchange surface cannot supply enough heat to cause a large amount of evaporation at the liquid-gas interface.

However, at higher heat source conditions (i.e., when the thermal exchange surface temperature is higher than 78.3 ºC), a boiling phenomenon occurs. More heat provided by the thermal exchange surface causes evaporation to occur at the liquid-gas interface. This evaporation lowers the amount of liquid accumulation, resulting in a thinner liquid film covering a small portion of the thermal exchange surface. Consequently, the 8-nozzle chamber (with 5 mm spacing) has a bad heat transfer rate at higher heat source conditions.

Figure 5-56 shows how sensitive the enhancement ratios are to variations in potential (We_E), flow rate (We and Re_{D_i}), and geometry (L^*/Di). The 4-nozzle ESEC chambers are used for analysis. By using Eq. (5.26), the analysis shows that the enhancement ratio is sensitive to variations in applied potential and flow rate, whereas the enhancement ratio is independent of different geometric factors of the same ESEC type. Among the parameters investigated, the variation in applied potential has the most influence on the enhancement ratio change. This phenomenon is supported when the relationship between the enhancement ratio and applied potential, and the relationship between the enhancement ratio and flow rate are compared [3, 6, 148]. The same results are also obtained for the 1-nozzle ESEC chamber and 8-nozzle ESEC chambers.

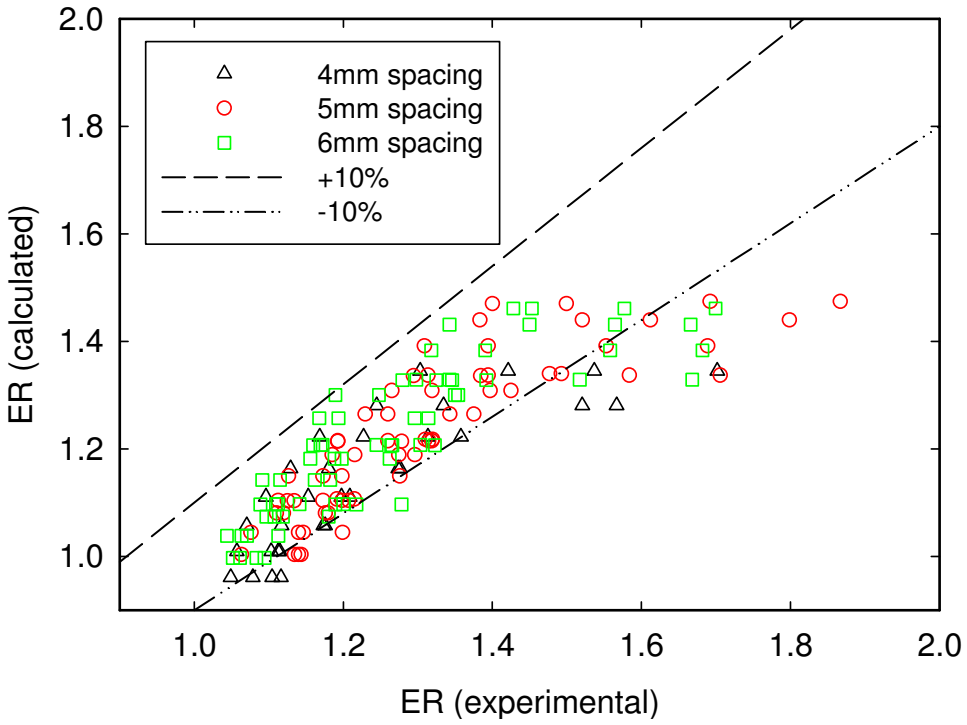

Figure 5-55. *The correlation between the calculated ER and experimental data for 8-nozzle ESEC chambers with three different types of spacing.*

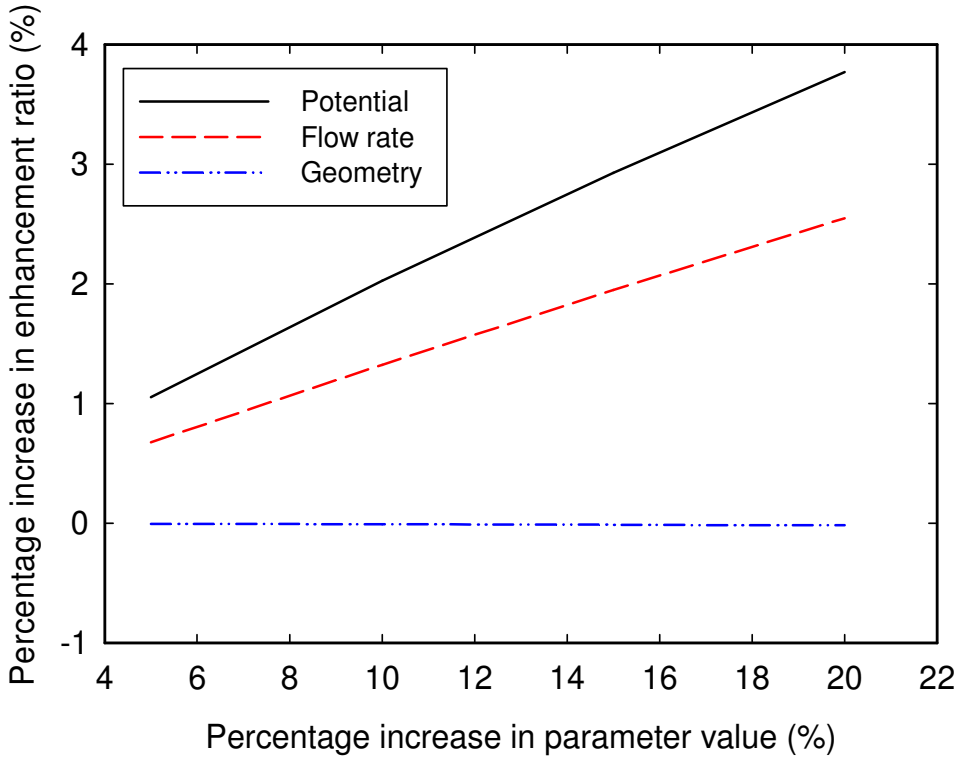

Figure 5-56. *Enhancement ratio variation due to change of potential, flow rate, and geometry (for 4-nozzle ESEC chambers).*

5.6.3.2 Nusselt Number (Nu_L) Correlations

Like the enhancement ratio, the Nusselt number for an ESEC chamber depends on the geometry type, the electric field intensity, the fluid properties, the flow rate, and so on. The enhancement ratio is the dimensionless form of the Nusselt number. Therefore, based on the enhancement ratio correlation shown in Eq. (5.26), the general Nusselt number correlation for different ESEC chamber types is expressed as

$$\frac{\mathrm{Nu}_L}{\mathrm{Pr}^g} = f\left(N, \frac{L^*}{D_i}, \mathrm{We}_\mathrm{E}, \mathrm{We}, \mathrm{Re}_{D_i}\right) = a \times \mathrm{We}_\mathrm{E}^b \mathrm{We}^c \, \mathrm{Re}_{D_i}^d \left(N \times \frac{L^*}{D_i}\right)^e \tag{5.27}$$

where a, b, c, d, e, and g are mathematically determined coefficients. Coefficients b, c, d, and e are the same as the values used in Eq. (5.26), because they are the same parameters. Coefficient a and g, however, are mathematically determined new coefficients. The coefficients to approximate the Nusselt number correlation, Eq. (5.27), over the ranges $4.0\times10^{-2} \le \mathrm{We_E} \le 2.5\times10^{-1}$, $1.4\times10^{-5} \le \mathrm{We} \le 6.0\times10^{-2}$, $1.3\times10^{-2} \le \mathrm{Re}_{D_i} \le 9.0\times10^{-1}$, $70 \le L^*/D_i \le 104$, $1 \le N \le 8$, and Pr = 16 are listed in Table 5.7. More information for how coefficients b, c, d, and e are determined can be found in Section 5.6.3.1. Moreover, because coefficient g relates to the properties of the working fluid (which remained the same for all investigated ESEC chambers), the geometry of the chamber should not influence this value. However, further investigations that use different fluid properties in the same ESEC chambers might have differing values for coefficient g.

Table 5.7. *Coefficients that fit the Nusselt number correlation Eq. (5.27) with respect to three different ESEC chamber types.*

ESEC chamber	*a*	*b*	*c*	*d*	*e*	*g*
1-nozzle chamber	0.312	0.11	-0.255	0.648	-0.05	1.39
4-nozzle chambers	0.310	0.11	-0.255	0.648	-0.001	1.39
8-nozzle chambers	0.335	0.11	-0.255	0.648	-0.001	1.39

A comparison between the calculated Nusselt number and the experimental data for 8-nozzle chambers (with 5 mm spacing) is shown in Figure 5-57. According to the developed

empirical Nusselt number correlation, approximately 88% of the experimental Nusselt number is within ± 10% deviation from the derived correlation. The possible reasons for a deviation of more than -10% under the same conditions (i.e., a low heat source, a high flow rate, and a high potential of 7.7 kV) are discussed in Section 5.6.3.1, in relation to Figure 5-54.

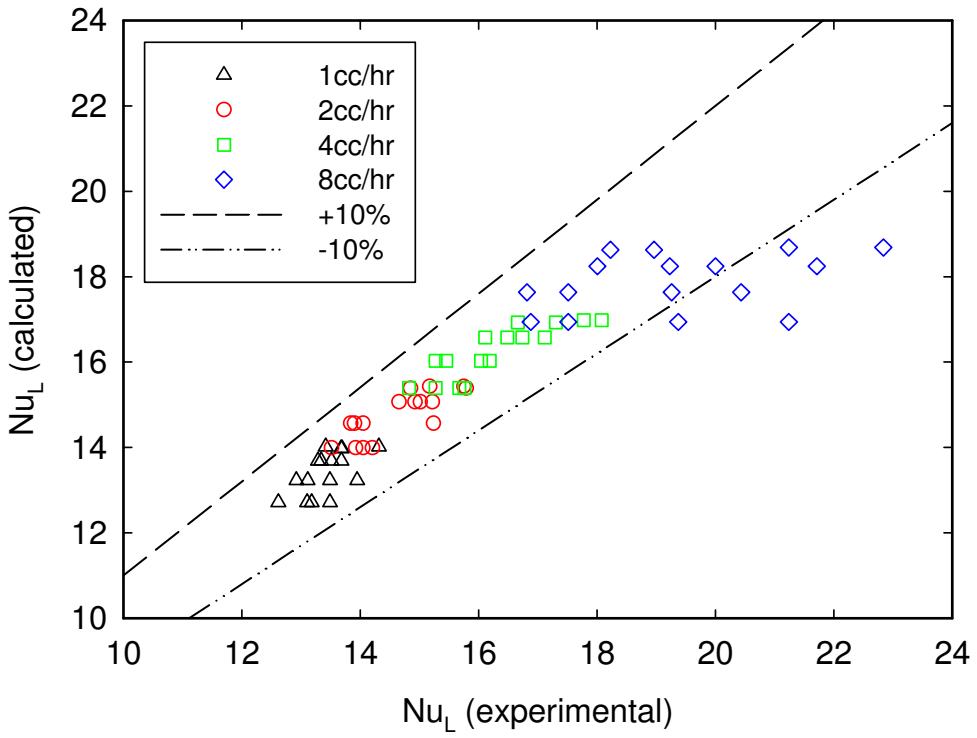

Figure 5-57. *The correlation between the calculated Nu_L and the experimental data for the 8-nozzle chamber with 5 mm spacing.*

The relationship between the correlated Nusselt number and the experimental data (for 4-nozzle chambers of 4 mm, 5 mm, and 6 mm spacing between the centerline of micronozzles and the centerline of the chambers) is shown in Figure 5-58. The Nusselt number correlation collapses more than 89% of the experimental Nusselt number, within ± 10% deviation from the derived correlation. Additionally, 4-nozzle chambers with 5 mm spacing and 6 mm spacing achieve the maximum Nusselt number at a lower heat source, 8 cm^3/hr flow rate, and 7.7 kV. This phenomenon indicates that, for 4-nozzle chambers, increasing the spacing between the micronozzles does not noticeably improve the heat transfer performance, which is also concluded in sensitivity analysis for the enhancement ratio shown in Figure 5-56. According to the ESEC chamber design methodology [1] we presented, the electric field intensity near the

micronozzle tip (within 3 mm) determines the heat transfer performance. The 4-nozzle ESEC chamber with 5 mm spacing's electric field intensity near the micronozzle tip is not highly influenced by adjacent micronozzles, and each micronozzle on this ESEC chamber can be considered as an isolated micronozzle. This is also true for the 4-nozzle ESEC chamber with 6 mm spacing because of the larger spacing between micronozzles. The electric field intensity of the same applied potential at the micronozzle tip for the 4-nozzle ESEC chamber with 6 mm spacing would be similar to that of the 4-nozzle ESEC chamber with 5 mm spacing, because the electric field intensity at the micronozzle tip for each micronozzle is an isolated object, which results in the same electric field intensity at the micronozzle tip. In this way, the same electric field intensity at the micronozzle tip indicates the same heat transfer performance.

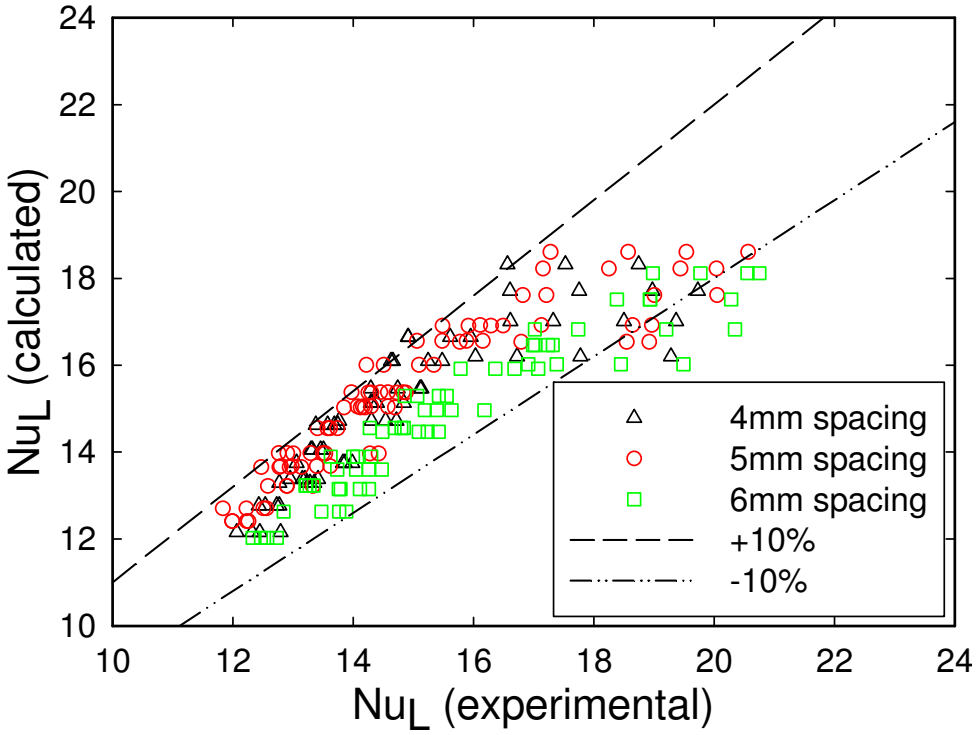

Figure 5-58. *Correlation between the calculated Nu_L and the experimental data for 4-nozzle ESEC chambers with three different spacing amounts.*

5.6.4 Natural Convection at Low Rayleigh Number

To calculate the achievable enhancement ratio for an ESEC chamber, it is imperative to investigate the natural convection Nusselt number correlation for the customized thermal testing

platform [1, 6]. One way we obtained the natural convection correlation, according to the operating heat sources of the testing platform, is to use the empirical natural convection correlations in [87]. In general, the natural convection correlation for a horizontal plate is

$$\overline{\mathrm{Nu}}_l = a\mathrm{Ra}_l^b \tag{5.28}$$

where Ra_l is the Rayleigh number.

To improve the correlation's accuracy, Goldstein *et al.* [151] and Lloyd *et al.* [152] recommended the use of characteristic length l, as defined by

$$l \equiv \frac{A_s}{P} \tag{5.29}$$

where A_s and P are surface area and perimeter of the plate, respectively. We used the characteristic length defined in Eq. (5.29) to apply a natural convection correlation associated with the appropriate Rayleigh number range. The characteristic length, l, of the thermal testing platform, Figure 5-9 (a), is 7.5×10^{-3} m, and the corresponding Rayleigh number ranges from 1,000 to 3,000.

Currently, the natural convection correlation for a horizontal plate is only applicable for a Rayleigh number (Ra) higher than 10^4; when the Rayleigh number is lower than 10^4, there are no appropriate correlations available. When a horizontal plate is heated on the upper surface and is insulated on the button surface, the applicable correlation is

$$\overline{\mathrm{Nu}}_l = 0.54\mathrm{Ra}_l^{1/4} \quad \left(10^4 \le \mathrm{Ra}_l \le 10^7\right) \tag{5.30}$$

Applying Eq. (5.30) for this investigation's designed thermal testing platform results in an average natural convection heat transfer coefficient that is 5 times lower than that obtained from the experimental data. Therefore, developing a new natural convection correlation for the designed thermal testing platform is necessary.

As found in our investigation, the relationship among the Rayleigh number (Ra), the Nusselt number (Nu), and the average natural convection heat transfer coefficient is shown in Figure 5-59. The Rayleigh number and the Nusselt number calculations are based on the film temperature, which is the average temperature between the environmental temperature and the thermal exchange surface temperature. Based on this data, we suggest that for a Rayleigh number between 1,500 and 2,200, the empirical Nusselt number correlation for the natural convection on the thermal exchange surface of the thermal testing platform is

$$\overline{\mathrm{Nu}}_l = 11.1043\mathrm{Ra}_l^{0.0571} \quad (1{,}500 < \mathrm{Ra}_l < 2{,}200) \tag{5.31}$$

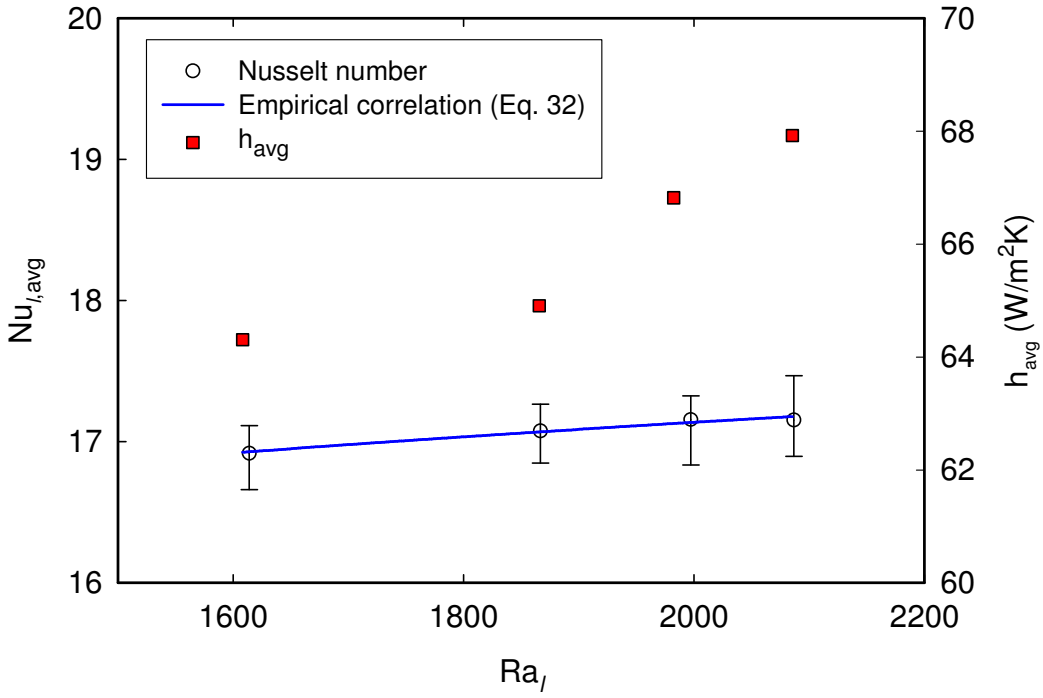

Figure 5-59. *The relationship among the Rayleigh number, the Nusselt number, and the average natural convection coefficient. The Rayleigh number is from 1,600 to 2,200. The error bars show the maximum and the minimum average Nusselt number at each Rayleigh number.*

5.7 ESEC Practical Design Overview

This section discusses certain ESEC practical design issues. An Apple MacBook 13" Series laptop is used to demonstrate how an ESEC chamber could be used as a thermal management solution.

5.7.1 Battery life-time of Small Form Factor Electronics

The Li-Polymer battery provides 5600 mAh or 61 W for the laptop. To dissipate 100 W of heat, the required volumetric flow rate of ethanol alcohol is 9.13 cc/min. According to the scaling law on the generated current and volumetric flow rate of a working fluid of an electrospray device developed by Ganan-Calvo *et al.* [85], the corresponding current of the electrospray device is around 0.4 μA. If the electrospray device is operated at the potential of 7 kV, the power consumption of the electrospray device is 2.8 mW, which is three orders less than that of a start-of-the-art laptop cooling module which is composed of a rotary fan and heat pipe. Assuming that 10% of the battery power is used to drive the ESEC cooling device with the power consumption of 2.8 mW, the ESEC cooling device can work in the laptop for more than 2,000 hours.

5.7.2 High Voltage Supply Unit

High voltage supply unit, typically around 2 to 7 kV, is required for an ESEC cooling device in order to operate the cooling device in different modes. Some high voltage supply units have been on the market for a while. For example, the Q series (i.e., Q50-5) ultra-miniature DC to high voltage DC converter from EMCO is an excellent high voltage supply unit source. The power output of this converter is around 50 mW, and the output voltage range is 2.5 kV to 5 kV. The package dimensions of the Q50-5 are 12.7 mm × 12.7 mm × 12.7 mm. The power supply efficiency is approximately 80% when operated at full load. Although the packaged size of this converter is around 2.0 cm^3, most of this volume is not used, as the same standard package is utilized by EMCO for a large number of power modules; therefore, we think the integration of the voltage supply unit in a laptop is a non-critical issue [153].

5.7.3 Working Fluid Supply

The choice of the solvent depends on several factors, including how much heat from the electronics needs to be dissipated, the electronics' operating temperature, the internal pressure of a cooling device, and the solvent's physical properties (i.e., specific heat and boiling point). The

following shows a scenario of how much solvent is required for an electrospray cooling device. The working fluid is 99.99% pure ethanol (the one we used for this investigation). The required heat dissipation rate is 100 W, and the internal pressure of the cooling device is 0.6 atmospheres, which indicates that the boiling point of ethanol is around 67 °C. Electronics has to be operated at the steady state temperature of 70 °C. Based on these conditions, the required solvent is around 9.13 mL/min.

The ESEC chambers investigated in this dissertation are open loop devices, meaning that a user has to refill the device after a period of time and the solvent will not be able to be recycled. One possible way to recycle the solvent in the current open loop device is to have a suction duct on top of the thermal exchange to gather vapor to a condenser to cool down the vapor to be liquid solvent again. However, for practical application, the chamber needs to be designed as an independent and disposable closed loop device, and the working liquid evaporates and condenses inside the cooler. In this way, there is no need to refill working liquid during normal operation. In addition, when the working fluid evaporates over the thermal exchange surface, the vapor will go through a microchannel-based vapor condenser in order to condense to be liquid for another round of heat exchange.

5.7.4 Closed Loop ESEC Device

A conceptual drawing of the closed loop ESEC device is shown in Figure 5-60. Like conventional spray cooling technologies, ESEC works by utilizing an array of nozzles to enable droplet impingement over a thermal exchange surface (TES). When the droplets reach the TES, two-phase heat transfer occurs. A significant amount of heat is dissipated on the TES during the phase change from liquid to vapor. The vapor is sent to the vapor condenser where the working fluid becomes liquid again by ejecting heat to the coolant that flows through the vapor condenser. The vapor condenser is controlled by the amount of coolant that flows in and out of the vapor condenser. Then, a mechanical pump or micropump pushes the liquid flow back to the fluid reservoir again for another round of the heat transfer cycle. The detailed closed loop design depends highly on practical applications, which are beyond the scope of this dissertation.

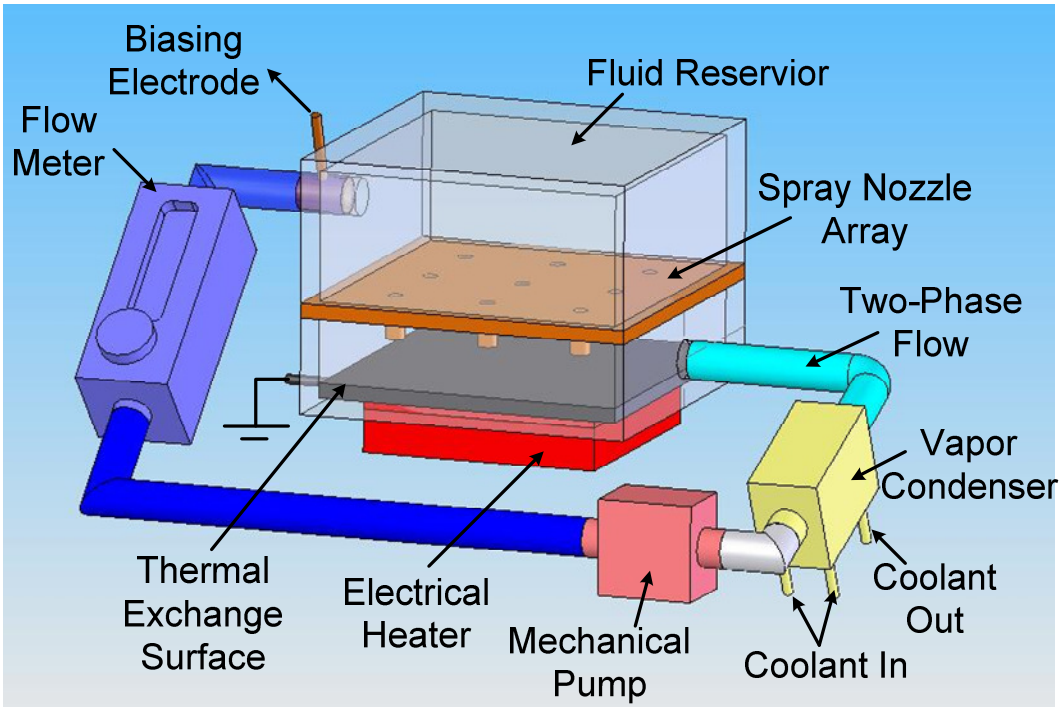

Figure 5-60. *A conceptual drawing of the closed loop ESEC device.*

5.7.5 Working Fluid Selection and Heat Capacity

The inner pressure of the ESEC cooling chamber is reduced to maintain the surface temperature of electronics at 50 °C so that a working fluid can be operated at the phase change condition to transfer large amounts of heat from the thermal exchange surface. Table 5.3 shows the physical properties of four selected working fluids for analysis. In general, the relationship between the heat dissipation rate and the amount of the volumetric flow rate of a working fluid is linear, and the slope of the linear curve is the heat of vaporization of the working fluid. At the same heat dissipation rate, the amount of the volumetric flow rate of water is always the smallest followed by that of ethanol alcohol, whereas that of engineered fluids is always the highest. Although water is beneficial to the ESEC chamber design in terms of the required amount of volumetric flow rate, the power required to drive the ESEC chamber using water is the highest, as shown in Figure 5-61. This is because water has the highest surface tension, which requires a higher onset voltage [78] to start the electrospray process.

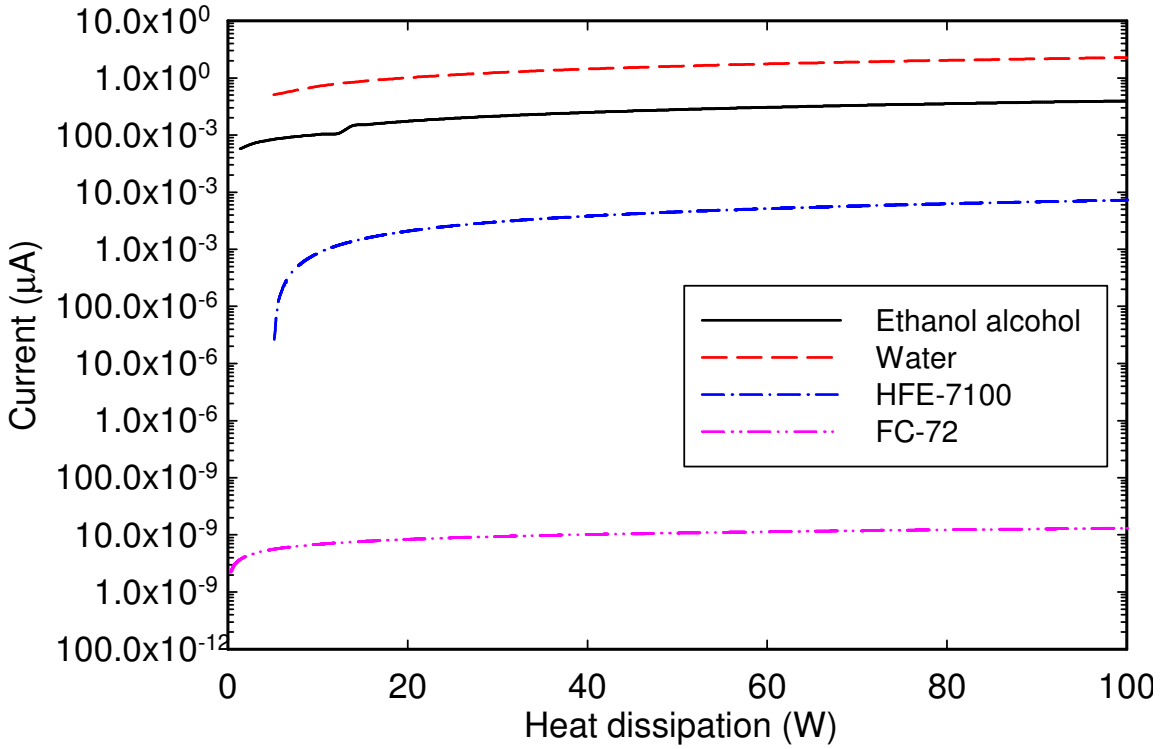

Figure 5-61. *The amount of volumetric flow rate required for a working fluid to dissipate different amount of heat generated for the thermal exchange surface of electronics.*

5.7.6 Heat Transfer Performance Degradation

ESEC chambers rely on liquid fluid to complete a thermal cycle to dissipate heat from a hot thermal exchange surface to the ambient. Factors that might result in heat transfer performance degradation are briefly discussed next.

For a closed loop ESEC chamber, factors affecting heat transfer performance degradation of the ESEC chamber including purity of a working fluid and physical and chemical property variation of the working fluid due to thermal cycles. Even the purest solvents contain residues that would deposit on the thermal exchange surface of the ESEC attached to the surface being cooled down. The deposits due to the impurity of the working fluid might not destroy the ESEC chamber, but might change the ESEC chamber's heat transfer characteristics. The deposit might also take place on electrospray nozzles, which is expected to be an important issue, as electrospray nozzles are in the micro-scale. In addition, when the working fluid has been operated for a certain period of time, the working fluid's physical and chemical properties may change, and may cause erosion on components of the ESEC chambers (i.e., electrospray nozzle,

micro-channel of a vapor condenser, component bonding interfaces, etc.). This is an important topic for engineered fluids [154] developed for the thermal management of electronics. Although further investigations on lifetime estimation and heat transfer performance degradation of ESEC chambers due to thermal cycles will be valuable for practical design, we expect that the ESEC chamber's heat transfer performance will not degrade noticeably after being operated for 30,000 hours. This will make the ESEC chambers competitive to traditional liquid cooling modules (i.e., heat pipes [155]).

5.8 Conclusion

The design methodology focuses on the relationship between the electrostatics field intensity and the heat transfer performance of ESEC chambers. We have adopted the direct simulation results of electrostatic field intensity to design the ESEC chambers and have discussed the impact of the electrostatic field intensity difference close to the tips of the designed ESEC chambers' micronozzles on the chambers' heat transfer performance. The numerical results show that the surface charge distribution at the tip of the micronozzle of the chambers has an indirect effect on the heat transfer performance of the ESEC chambers, while the potential distribution close to the tip of the micronozzle of the ESEC chambers has great influence on the thermal characteristics of the ESEC cooling chambers. Additionally, the results indicate that increasing the quantity of the micronozzles of the ESEC chambers might not be an effective way of improving the heat transfer performance of the ESEC cooling chamber. The enhancement ratio and the average thermal resistance of the 1-nozzle chamber are even better than those of the 4-nozzle chamber with 5 mm spacing, demonstrating that the numerical electrostatic field modeling result is applicable to pre-estimate the heat transfer performance difference among ESEC chambers with different quantities of micronozzles.

The optimization methodology focuses on three different kinds of ESEC chambers with different spacing to investigate their optimal heat transfer performance in terms of the steady state heat transfer performance (the enhancement ratio and the average thermal resistance) and the transient heat transfer performance (the average cooling rate). The experimental results show that for the same kind of ESEC chamber, the heat transfer performance at different heat fluxes is distinct. At the same heat flux, the enhancement ratio increases when the working fluid flow rate

(Weber number) and applied potential (electric Weber number) are increased. The 4-nozzle chamber with 6 mm spacing achieves the maximum enhancement ratio of 1.72 among the 4-nozzle chambers. The 8-nozzle chamber with 5 mm spacing achieves the maximum enhancement ratio of 1.87 among the 8-nozzle chambers. Furthermore, among all ESEC chambers, the maximum enhancement ratio of 1.87 was achieved by the 8-nozzle chamber with 5 mm spacing at the lowest heat flux. According to the average thermal resistance, regardless of the micronozzle's spacing on the ESEC chamber, higher heat flux results in higher average thermal resistance. The lowest average thermal resistance of 8.5 K/W was achieved by the 8-nozzle chamber with 5 mm spacing. The average cooling rate analysis shows that the 4-nozzle chamber with 6 mm spacing achieves the maximum cooling rate of 1.5 times higher than that achieved by the 8-nozzle chamber with 6 mm spacing. The comparison between the achievable enhancement ratio and the maximum cooling rate among ESEC chambers indicates that the average cooling rate is not directly related to the achievable enhancement ratio. Although increasing the spacing and quantity of micronozzles on the ESEC chamber does not have an obvious improvement on the maximum achievable enhancement ratio and the lowest average thermal resistance, increasing the spacing and quantity of micronozzles noticeably improves the highest transient cooling rate.

The developed enhancement ratio correlations in this dissertation indicate that more than 83% of the experimental enhancement ratios are within ± 10% deviation from the derived correlation. The correlated enhancement ratio also shows that the heat transfer performance of the chamber highly depends on its geometry type. Additionally, 89% of the experimental Nusselt number data is within ± 10% of the correlated data, according to the developed Nusselt number correlations. For the same type of ESEC chambers, the analysis of how the enhancement ratios are sensitive to the parameters indicates that the variation in the enhancement ratio is sensitive to that of applied potential and flow rate, whereas the variation in the enhancement ratio is not sensitive to that of the geometry of the same ESEC type. The same result is also proven by experimental data. Furthermore, we suggest a new natural convection correlation for lower Rayleigh number ranges below 3,000.

Chapter 6 **Conclusions and Future Work**

6.1 Conclusions

This dissertation investigates the design and application of sensors and actuators with a fringing electric field in dielectric material property measurement and the thermal management of electronics. A systematical circuit calibration methodology was presented to accurately calibrate individual stages of the measurement circuit of the sensor systems, which significantly reduces the measurement deviation of the relative dielectric permittivity of the air to 0.5% from 30% in non-calibration mode, at 1 kHz. In addition, the sensor system demonstrates that its capability to identify different classes of explosive granular by using the granular materials' dielectric signatures in the frequency domain.

Electrostatic field numerical modeling was conducted to design and optimize the multichannel concentric fringing electric field sensor for the coating thickness measurement of a multi-layer coating stack-up on an aircraft. A material property estimation algorithm was also developed to relate the sensor's electrical impedance to variations in the coating thickness and loading of interest. The experimental results demonstrate the sensor's capability for in-process coating layer thickness and loading measurements. Data analysis shows that the coating loading measurement accuracy is better than 1.5%, and the coating thickness measurement accuracy is better than 0.1 mm.

For the fringing electric field actuator, the electrospray evaporative cooling (ESEC) chamber, a design and optimization methodology for the actuator for the thermal management of electronics was presented. This design methodology uses numerical electrostatic field modeling to indirectly estimate the heat transfer performance difference of three different ESEC chambers. The results of the numerical electrostatic field modeling and heat transfer experiments indicate that the potential distribution near the tip of the micronozzle of the ESEC chamber dominates the heat transfer performance of the ESEC cooling devices, demonstrating that the numerical electrostatic field modeling result is applicable to pre-estimate the heat transfer performance difference among ESEC chambers with different quantities of micronozzles. Additionally, the results indicate that increasing the quantity of micronozzles of the ESEC chambers might not be an effective way of improving the heat transfer performance of the ESEC cooling chamber.

The optimization methodology focuses on the geometry type effect, the quantity of micronozzles, and the spacing between them, on three different kinds of ESEC chambers' optimal heat transfer performance, in terms of the steady state enhancement ratio, the average thermal resistance, and the transient average cooling rate. The geometry types affect the ESEC chambers' heat transfer performance in different ways. The comparison between the achievable enhancement ratio and the maximum cooling rate among ESEC chambers indicates that the average cooling rate is not directly related to the achievable enhancement ratio. Increasing the spacing and quantity of micronozzles noticeably improves the highest transient cooling rate, although increasing the spacing and quantity of micronozzles on the ESEC chamber does not have an obvious improvement on the maximum achievable enhancement ratio and the lowest average thermal resistance.

The ESEC chambers are highly sensitive to local variations in the electrostatic field intensity, which makes the optimization methodology not able to indicate an obvious way of optimizing the heat transfer performance of the ESEC chambers for practical applications. This dissertation develops the enhancement ratio correlations to design practical ESEC chambers. The results indicate that more than 83% of the experimental enhancement ratios are within ± 10% deviation from the derived correlation. The correlated enhancement ratio also shows that the heat transfer performance of the chamber highly depends on its geometry type. Additionally, 89% of the experimental Nusselt number data is within ± 10% of the correlated data, according to the developed Nusselt number correlations. For the same type of ESEC chambers, the analysis of how the enhancement ratios are sensitive to the parameters indicates that the variation in the enhancement ratio is sensitive to that of applied potential and flow rate, whereas the variation in the enhancement ratio is not sensitive to that of geometry of the same ESEC type. The experimental data also proves the same result. Furthermore, we suggest a new natural convection correlation for lower Rayleigh number ranges below 3,000.

6.2 Future Work

6.2.1 Sensors with Fringing Electric Field

Future work for sensors with fringing electric fields (FEFs) should be focused on the development of handheld instruments. Fringing electric field sensors have been investigated in many applications, e.g., coating thickness measurement and granular material property measurement. To push FEF sensors toward industrial applications, portable and handheld instruments with integrated functions are necessary. Algorithm development is also one of the core hearts of handheld instruments. This will require elaborate future research efforts to develop complete algorithms for different applications. For example, for in-process coating applications and coating thickness validation, future work should focus on the development of algorithms that measure multiple individual layers of an aircraft's multi-layer coating stack-up.

6.2.2 Actuators with Fringing Electric Field

Future work for the development of electrospray evaporative cooling (ESEC) chambers will focus on the development of numerical models and applications. The focuses of these two areas are provided below:

Applications. The ESEC cooling chambers developed in this dissertation are open-loop devices, which are not appropriate for practical applications; therefore, closed-loop ESEC chambers should be developed for practical applications. In addition, for practical designs, the cooling chambers' energy efficiency and chambers with higher micronozzle density operated in the stable cone-jet EHD mode should be investigated. Furthermore, since ESEC cooling chambers involves droplet manipulation concepts, these chambers should be integrated with other droplet manipulation technologies as novel cooling modules, which have the capability to optimize the heat transfer performance for the thermal management of future microelectronics.

Numerical Model Development. Although empirical heat transfer correlation models have been investigated in this dissertation, it is necessary to extend these heat transfer correlations to cover additional parameters for different thermal management applications. For example, one can use the imaging processing methodology to photograph the shape of the electrified jets of ESEC

chambers to improve the accuracy of the empirical correlations by including the area-weighted factor to the correlations developed in this dissertation. In addition, analytical current scaling laws should be developed for the unstable multi-jet EHD mode operated in this dissertation. Currently, analytical current scaling laws are for the stable cone-jet EHD mode. Furthermore, to minimize the costs for the experiment and to assist practical device designs for applications in different heat transfer performance, it is imperative to develop several numerical models regarding multiphysics behind ESEC chambers as much as possible. Analytical models should also be developed to support the lack of full multiphysics models.

References

[1] H. C. Wang and A. V. Mamishev, "Design Methodology of the micronozzle-based electrospray evaporative cooling devices," *Journal of Electronics Cooling and Thermal Control,* vol. 2, pp. 17-31, 2012.

[2] H. C. Wang and A. V. Mamishev, "Optimization methodology for electrospray evaporative cooling chambers," *Journal of Electrostatics,* vol. 70, pp. 384-392, 2012.

[3] H. C. Wang and A. V. Mamishev, "Optimal heat transfer performance of the microfluidic electrospray cooling devices," in *27th Annual IEEE Semiconductor Thermal Measurement and Management Symposium (SEMI-THERM 2011)* 2011, pp. 35-42.

[4] H. C. Wang and A. V. Mamishev, "Methodology for estimation of heat transfer in multi-jet electrospray evaporative coolers," in *2nd ISNPEDADM Conference* Noumea, New Caledonia, 2011.

[5] H. C. Wang and A. V. Mamishev, "Heat transfer correlation models for electrospray evaporative cooling chambers of different geometry types," *Applied Thermal Engineering,* vol. 40, pp. 91-101, July 2012 2012.

[6] H. C. Wang, A. V. Mamishev, and C. P. Hsu, "The enhancement ratio of corresponding convection heat transfer coefficient using electrospray evaporative cooling system," in *ASME Summer Heat Transfer Conference* San Francisco, California USA, 2009, pp. 1013-1020

[7] H. C. Wang, V. Inclan, A. Zyuzin, N. Donnangelo, and A. Mamishev, "Material property measurement of granular materials using a calibrated dielectric spectroscopy system," in *2011 The Conference on Electrical Insulation and Dielectric Phenomena (CEIDP)* Cancun, Mexico, 2011.

[8] H. C. Wang, V. Inclan, A. Zyuzin, N. C. Donnangelo, and A. V. Mamishev, "Calibration methodology for the dielectric spectroscopy system measuring dielectric properties of granular materials," *Submitted to IEEE Sensors Journal for publication,* 2012.

[9] H. C. Wang, V. Inclan, A. Zyuzin, and A. V. Mamishev, "Measurement of coating thickness using concentric fringing electric field sensors," *Submitted to IEEE Sensors Journal for publication,* 2012.

[10] S. D. Senturia, N. F. Sheppard, H. L. Lee, and D. R. Day, "In-situ measurement of the properties of curing systems with microdielectrometry," *Journal of Adhesion,* vol. 15, pp. 69-90, 1982.

[11] N. T. Smith and D. D. Shepard, "Dielectric cure analysis," *European Coatings Journal,* pp. 4pp-4pp, 1995.

[12] J. W. Gardner, A. Pike, N. F. de Rooij, M. Koudelka-Hep, P. A. Clerc, A. Hierlemann, and W. Gopel, "Integrated array sensor for detecting organic solvents," *Sensors and Actuators, B: Chemical,* vol. B26, pp. 135-139, 1995.

[13] E. S. Kolesar Jr and J. M. Wiseman, "Interdigitated gate electrode field effect transistor for the selective detection of nitrogen dioxide and diisopropyl methylphosphonate," *Analytical Chemistry,* vol. 61, pp. 2355-2361, 1989.

[14] J. Bing and A. Mamishev, "Robotic monitoring of power systems," *IEEE Transactions on Power Delivery,* vol. 19, pp. 912-918, 2004.

[15] B. Jiang, P. Stuart, M. Raymond, D. Villa, and A. V. Mamishev, "Robotic platform for monitoring underground cable systems," in *2002 Asia Pacific IEEE/PES Transmission and Distribution Conference and Exhibition* 2002, pp. 1105-1109 vol.2.

[16] A. V. Mamishev, S. X. Short, K. Ta-Wei, and B. D. Russell, "Nonintrusive sensing techniques for the discrimination of energized electric cables," *IEEE Transactions on Instrumentation and Measurement,* vol. 45, pp. 457-461, 1996.

[17] G. Niebling and A. Schlachter, "Qualitative and quantitative gas analysis with non-linear interdigital sensor arrays and artificial neural networks," *Sensors and Actuators, B: Chemical,* vol. B27, pp. 289-292, 1995.

[18] A. P. Washabaugh, A. Mamishev, Y. Du, and M. Zahn, "Dielectric measurements of semi-insulating liquids and solids," in *12th International Conference on Conduction and Breakdown in Dielectric Liquids (ICDL 1996)* 1996, pp. 381-384.

[19] C. P. Hsu, N. E. Jewell-Larsen, I. A. Krichtafovitch, and A. V. Mamishev, "Heat-transfer-enhancement measurement for microfabricated electrostatic fluid accelerators," *Journal of Microelectromechanical Systems,* vol. 18, pp. 111-118, Feb 2009.

[20] C. P. Hsu, N. E. Jewell-Larsen, I. A. Krichtafovitch, S. W. Montgomery, J. T. Dibene, and A. V. Mamishev, "Miniaturization of electrostatic fluid accelerators," *Journal of Microelectromechanical Systems,* vol. 16, pp. 809-815, Aug 2007.

[21] C. P. Hsu, N. E. Jewell-Larsen, A. C. Rollins, I. A. Krichtafovitch, S. W. Montgomery, J. T. Dibene II, and A. V. Mamishev, "Miniaturization of electrostatic fluid accelerators," in *ASME International Mechanical Engineering Congress and Exposition (IMECE 2006)* Chicago, IL, United States, 2006, pp. 165-170.

[22] N. E. Jewell-Larsen, C. P. Hsu, I. A. Krichtafovitch, S. W. Montgomery, J. T. Dibene, and A. V. Mamishev, "CFD analysis of electrostatic fluid accelerators for forced convection cooling," *IEEE Transactions on Dielectrics and Electrical Insulation,* vol. 15, pp. 1745-1753, Dec 2008.

[23] N. E. Jewell-Larsen, S. V. Karpov, I. A. Krichtafovitch, V. Jayanty, C. P. Hsu, and A. V. Mamishev, "Modeling of corona-induced electrohydrodynamic flow with COMSOL multiphysics," in *Proc. ESA Annual Meeting Electrostatics*, 2008, p. E1.

[24] N. E. Jewell-Larsen, D. A. Parker, I. A. Krichtafovitch, and A. V. Mamishev, "Numerical simulation and optimization of electrostatic air pumps," in *2004 Annual Report Conference on Electrical Insulation and Dielectric Phenomena*, 2004, pp. 106-109.

[25] N. E. Jewell-Larsen, H. Ran, Y. Zhang, M. K. Schwiebert, K. A. Honer, and A. V. Mamishev, "Electrohydrodynamic (EHD) cooled laptop," in *25th Annual IEEE Semiconductor Thermal Measurement and Management Symposium (SEMI-THERM 2009)*, 2009, pp. 261-266.

[26] N. E. Jewell-Larsen, E. Tran, I. A. Krichtafovitch, and A. V. Mamishev, "Design and optimization of electrostatic fluid accelerators," *IEEE Transactions on Dielectrics and Electrical Insulation,* vol. 13, pp. 191-203, 2006.

[27] N. E. Jewell-Larsen, P. Q. Zhang, C. P. Hsu, I. A. Krichtafovitch, and A. V. Mamishev, "Coupled-physics modeling of electrostatic fluid accelerators for forced convection cooling," in *9th AIAA/ASME Joint Thermophysics and Heat Transfer Conference* San Francisco, California USA, 2006, pp. AIAA 2006-3607.

[28] I. A. Krichtafovitch, V. L. Gorobets, S. V. Karpov, and A. V. Mamishev, "Electrostatic fluid accelerator and air purifier – The second wind," in *Annual Meeting of the Electrostatics Society of America* Edmonton, Canada, 2005, pp. 1-13.

[29] F. Yang, N. E. Jewell-Larsen, D. L. Brown, K. Pendergrass, D. A. Parker, I. A. Krichtafovitch, and A. V. Mamishev, "Corona driven air propulsion for cooling of electronics," in *XIIIth International Symposium on High Voltage Engineering*, 2003.

[30] D. P. Rizzetta and M. R. Visbal, "Effect of plasma-based control on low-Reynolds-number flapping airfoil performance," *AIAA Journal,* vol. 50, pp. 131-147, 2012.
[31] D. P. Rizzetta and M. R. Visbal, "Numerical investigation of plasma-based control for low-reynolds-number airfoil flows," *AIAA Journal,* vol. 49, pp. 411-425, 2011.
[32] D. P. Rizzetta and M. R. Visbal, "Large eddy simulation of plasma-based control strategies for bluff body flow," *AIAA Journal,* vol. 47, pp. 717-729, 2009.
[33] T. Tungkavet, D. Pattavarakorn, and A. Sirivat, "Bio-compatible gelatins (Ala-Gly-Pro-Arg-Gly-Glu-4Hyp-Gly-Pro-) and electromechanical properties: effects of temperature and electric field," vol. 19, pp. 1-9, 2012.
[34] X. Rottenberg, S. Brebels, P. Ekkels, P. Czarnecki, P. Nolmans, R. P. Mertens, B. Nauwelaers, R. Puers, I. D. Wolf, W. D. De Raedt, and H. A. C. Tilmans, "An electrostatic fringing-field actuator (EFFA): application towards a low-complexity thin-film," *Journal of Micromechanics and Microengineering,* vol. 17, p. S204, 2007.
[35] P. E. Morgan, D. P. Rizzetta, and M. R. Visbal, "Large-eddy simulation of separation control for flow over a wall-mounted hump," *AIAA Journal,* vol. 45, pp. 2643-2660, 2007.
[36] ASTM, "ASTM D150-98 Standard Test Methods for AC Loss Characteristics and Permittivity (Dielectric Constant) of Solid Electrical Insulation," 2004.
[37] U. C. Hasar, "Calibration-independent method for complex permittivity determination of liquid and granular materials," *Electronics Letters,* vol. 44, pp. 585-586, 2008.
[38] T. J. Kelleners, D. A. Robinson, P. J. Shouse, J. E. Ayars, and T. H. Skaggs, "Frequency dependence of the complex permittivity and its impact on dielectric sensor calibration in soils," *Soil Science Society of America Journal,* vol. 69, pp. 67-76, 2005/1 2005.
[39] T. J. Kelleners, R. W. O. Soppe, D. A. Robinson, M. G. Schaap, J. E. Ayars, and T. H. Skaggs, "Calibration of Capacitance Probe Sensors using Electric Circuit Theory," *Soil Science Society of America Journal,* vol. 68, pp. 430-439, 2004/3 2004.
[40] G. Ramm and H. Moser, "Calibration of electronic capacitance and dissipation factor bridges," *IEEE Transactions on Instrumentation and Measurement,* vol. 52, pp. 396-399, 2003.
[41] N. Sakamoto and Y. Nakamura, "Calibration method for large capacitances using a current comparator with an inductive voltage divider," in *2010 Conference on Precision Electromagnetic Measurements (CPEM)* 2010, pp. 412-413.
[42] M. Cloupeau and B. Prunetfoch, "Electrohydrodynamic spraying functioning modes - a critical review," *Journal of Aerosol Science,* vol. 25, pp. 1021-1036, Sep 1994.
[43] A. Jaworek and A. Krupa, "Classification of the modes of EHD spraying," *Journal of Aerosol Science,* vol. 30, pp. 873-893, Aug 1999.
[44] A. M. Ganan-Calvo, J. C. Lasheras, J. Davila, and A. Barrero, "Electrostatic spray emitted from an electrified conical meniscus," *Journal of Aerosol Science,* vol. 25, pp. 1121-1142, 1994.
[45] R. P. A. Hartman, D. J. Brunner, D. M. A. Camelot, J. C. M. Marijnissen, and B. Scarlett, "Electrohydrodynamic atomization in the cone-jet mode: Physical modeling of the liquid cone and jet," *Journal of Aerosol Science,* vol. 30, pp. 823-849, 1999.
[46] O. Lastow and W. Balachandran, "Numerical simulation of electrohydrodynamic (EHD) atomization," *Journal of Electrostatics,* vol. 64, pp. 850-859, Nov 2006.
[47] O. Lastow and W. Balachandran, "Novel low voltage EHD spray nozzle for atomization of water in the cone jet mode," *Journal of Electrostatics,* vol. 65, pp. 490-499, Jul 2007.

[48] J. M. Lopez-Herrera, A. M. Ganan-Calvo, and M. Perez-Saborid, "Non-linear deformation and breakup of charged capillary jets," *Journal of Aerosol Science,* vol. 27, pp. S183-S184, 1996.

[49] J. M. Lopez-Herrera, A. M. Gañán-Calvo, and M. Perez-Saborid, "One-dimensional simulation of the breakup of capillary jets of conducting liquids. Application to EHD spraying," *Journal of Aerosol Science,* vol. 30, pp. 895-912, 1999.

[50] P. K. Notz and O. A. Basaran, "Dynamics of drop formation in an electric field," *Journal of Colloid and Interface Science,* vol. 213, pp. 218-237, May 1 1999.

[51] A. K. Sen, J. Darabi, and D. R. Knapp, "Simulation and parametric study of a novel multi-spray emitter for ESI-MS applications," *Microfluidics and Nanofluidics,* vol. 3, pp. 283-298, Jun 2007.

[52] J. S. Shrimpton, "Dielectric charged drop break-up at sub-Rayleigh limit conditions," *IEEE Transactions on Dielectrics and Electrical Insulation,* vol. 12, pp. 573-578, Jun 2005.

[53] J. S. Shrimpton, "Modeling dielectric charged drop break up using an energy conservation method," *IEEE Transactions on Dielectrics and Electrical Insulation,* vol. 15, pp. 1471-1477, Oct 2008.

[54] S. S. Yoon, S. D. Heister, J. T. Epperson, and P. E. Sojka, "Modeling multi-jet mode electrostatic atomization using boundary element methods," *Journal of Electrostatics,* vol. 50, pp. 91-108, Jan 2001.

[55] J. Sjodahl, J. Melin, P. Griss, A. Emmer, G. Stemme, and J. Roeraade, "Characterization of micromachined hollow tips for two-dimensional nanoelectrospray mass spectrometry," *Rapid Communications in Mass Spectrometry,* vol. 17, pp. 337-341, 2003.

[56] B. Q. T. Si, D. Byun, and S. Lee, "Experimental and theoretical study of a cone-jet for an electrospray microthruster considering the interference effect in an array of nozzles," *Journal of Aerosol Science,* vol. 38, pp. 924-934, Sep 2007.

[57] G. A. Schultz, T. N. Corso, S. J. Prosser, and S. Zhang, "A fully integrated monolithic microchip electrospray device for mass spectrometry," *Analytical Chemistry,* vol. 72, pp. 4058-4063, Sep 1 2000.

[58] J. Doshi and D. H. Reneker, "Electrospinning Process and Applications of Electrospun Fibers," *Journal of Electrostatics,* vol. 35, pp. 151-160, Aug 1995.

[59] A. M. Ganan-Calvo and A. Barrero, "A global model for the electrospraying of liquids in steady cone-jet mode," *Journal of Aerosol Science,* vol. 27, pp. S179-S180, Sep 1996.

[60] J. Zeng, D. Sobek, and T. Korsmeyer, "Electro-hydrodynamic modeling of electrospray ionization: CAD for a μfluidic device-mass spectrometer interface," in *12th International Conference on Transducers, Solid-State Sensors, Actuators and Microsystems (2003)*, 2003, pp. 1275-1278.

[61] S. Zhao, K. Adamiak, and G. S. P. Castle, "The implementation of Poisson field analysis within FLUENT to model electrostatic liquid spraying," in *Canadian Conference on Electrical and Computer Engineering (CCECE 2007) 2007* 2007, pp. 1456-1459.

[62] D. J. Womac, F. P. Incropera, and S. Ramadhyani, "Correlating equations for impingement cooling of small heat sources with multiple circular liquid jets," *Transactions of the ASME Journal of Heat Transfer,* vol. 116, pp. 482-486, May 1994.

[63] D. J. Womac, S. Ramadhyani, and F. P. Incropera, "Correlating equations for impingement cooling of small heat-sources with single circular liquid jets," *Transactions of the ASME Journal of Heat Transfer,* vol. 115, pp. 106-115, Feb 1993.

[64] K. Sundara-Rajan, A. V. Mamishev, and M. Zahn, "Fringing electric and magnetic field sensors," in *Encyclopedia of Sensors*. vol. X, C. A. Grimes, E. C. Dickey, and M. V. Pishko, Eds., 2006, pp. 1-12.
[65] A. V. Mamishev, K. Sundara-Rajan, Y. Fumin, D. Yanqing, and M. Zahn, "Interdigital sensors and transducers," *Proceedings of the IEEE,* vol. 92, pp. 808-845, 2004.
[66] A. S. Zyuzin, "Measurement fundamentals of the three-channel dielectric spectroscopy meter DS-1," Illionix, LLC, Seattle, WA, Report No.: 909-01, 2010.
[67] W. W. Deng, J. F. Klemic, X. H. Li, M. A. Reed, and A. Gomez, "Increase of electrospray throughput using multiplexed microfabricated sources for the scalable generation of monodisperse droplets," *Journal of Aerosol Science,* vol. 37, pp. 696-714, Jun 2006.
[68] Y. Tatemoto, R. Ishikawa, M. Takeuchi, T. Takeshita, K. Noda, and T. Okazaki, "An electrospray method using a multi-capillary nozzle emitter," *Chemical Engineering & Technology,* vol. 30, pp. 1274-1279, Sep 2007.
[69] A. G. Bailey, *Electrostatic spraying of liquids*: Research Studies Press Ltd., 1988.
[70] J. Zeleny, "The electrical discharge from liquid points, and a hydrostatic method of measuring the electric intensity at their surfaces," *Physical Review,* vol. 3, p. 69, 1914.
[71] J. Rutkowski, "Foundations of balancing at mobile phase interface," *Arch. Thermodyn.,* vol. 2, pp. 75-108, 1981.
[72] O. Wilhelm, L. Madler, and S. E. Pratsinis, "Electrospray evaporation and deposition," *Journal of Aerosol Science,* vol. 34, pp. 815-836, Jul 2003.
[73] N. Frossling, "Ueber die Verdunstung fallender tropfen," *Gerlands Beitrage zur Geophysik,* vol. 52, pp. 170-216, 1938.
[74] K. V. Beard and H. R. Pruppacher, "A wind tunnel investigation of the rate of evaporation of small water drops falling at terminal velocity in air," *Journal of the Atmospheric Sciences,* vol. 28, pp. 1455-1464, 2011/08/16 1971.
[75] R. Clift, J. R. Grace, and M. E. Weber, *Bubbles, droplets, and particles*. New Yark, 1978.
[76] W. E. Ranz and J. W. R. Marshall, "Evaporation from drops," *Chemical Engineering Progress,* vol. 48, pp. 173-180, 1952.
[77] W. A. Sirignano, *Fluid dynamics and transport of droplets and sprays*: Cambridge University Press, 1999.
[78] A. R. Jones and K. C. Thong, "Production of charged monodisperse fuel droplets by electrical dispersion," *Journal of Physics D-Applied Physics,* vol. 4, pp. 1159-1168, 1971.
[79] G. Taylor, "Disintegration of water drops in electric field," *Proceedings of the Royal Society of London Series a-Mathematical and Physical Sciences,* vol. 280, pp. 383-+, 1964.
[80] D. P. H. Smith, "The electrohydrodynamic atomization of liquids," *IEEE Transactions on Industry Applications,* vol. 22, pp. 527-535, May-Jun 1986.
[81] D. R. Chen, D. Y. H. Pui, and S. L. Kaufman, "Electrospraying of conducting liquids for monodisperse aerosol generation in the 4 nm to 1.8 μm diameter range," *Journal of Aerosol Science,* vol. 26, pp. 963-977, 1995.
[82] M. Drötboom, H. Fichtner, and H. Fissan, "Current measurement in an electrospray system," *Journal of Aerosol Science,* vol. 28, pp. S535-S536, 1997.
[83] J. F. De La Mora and I. G. Loscertales, "The current emitted by highly conducting Taylor cones," *Journal of Fluid Mechanics,* vol. 260, pp. 155-184, Feb 10 1994.

[84] A. M. Ganan-Calvo, "The surface charge in electrospraying: Its nature and its universal scaling laws," *Journal of Aerosol Science,* vol. 30, pp. 863-872, Aug 1999.
[85] A. M. Ganan-Calvo, J. Davila, and A. Barrero, "Current and droplet size in the electrospraying of liquids: Scaling laws," *Journal of Aerosol Science,* vol. 28, pp. 249-275, Mar 1997.
[86] X. Feng and J. E. Bryan, "Application of electrohydrodynamic atomization to two-phase impingement heat transfer," *Transactions of the ASME Journal of Heat Transfer,* vol. 130, p. 072202, July 2008.
[87] F. P. Incropera, D. P. DeWitt, T. L. Berqman, and A. S. Lavine, *Introduction to heat transfer*, 5 ed.: John Wiley & Sons, Inc., 2006.
[88] I.-D.-E. T. Comm., "Recommended international standard for dimensionless parameters used in electrohydrodynamics," *IEEE Transactions on Dielectrics and Electrical Insulation,* vol. 10, pp. 3-6, Feb 2003.
[89] J. S. Eow, M. Ghadiri, and A. Sharif, "Deformation and break-up of aqueous drops in dielectric liquids in high electric fields," *Journal of Electrostatics,* vol. 51, pp. 463-469, May 2001.
[90] V. K. Varadan, V. V. Varadan, and X. Q. Bao, "Integration of interdigital transducers, MEMS, and antennas for smart structures," San Diego, CA, USA, 1996, pp. 95-106.
[91] P. A. von Guggenberg and M. C. Zaretsky, "Estimation of one-dimensional complex-permittivity profiles: a feasibility study," *Journal of Electrostatics,* vol. 34, pp. 263-277, 1995.
[92] A. Mamishev and M. Zahn, "Techniques for semi-empirical characterization of material and sensor properties in interdigital dielectrometry," in *Conference Record of the 1996 IEEE International Symposium on Electrical Insulation*, 1996, pp. 486-489 vol.2.
[93] A. V. Mamishev, Y. Du, J. H. Bau, B. C. Lesieutre, and M. Zahn, "Evaluation of diffusion-driven material property profiles using three-wavelength interdigital sensor," *IEEE Transactions on Dielectrics and Electrical Insulation,* vol. 8, pp. 785-798, 2001.
[94] A. V. Mamishev, C. Lin, Y. Du, B. C. Lesieutre, and M. Zahn, "Improvement of algorithms for on-line interdigital dielectrometry measurement of material properties," in *Conference Record of the 1998 IEEE International Symposium on Electrical Insulation*, 1998, pp. 444-447 vol.2.
[95] U. Kaatze, "Reference liquids for the calibration of dielectric sensors and measurement instruments," *Measurement Science and Technology,* vol. 18, p. 967, 2007.
[96] A. S. Zyuzin, "Circuit design of single-channel dielectric spectroscopy meter for high voltage applications," Illionix, LLC, Seattle, WA, Internal Report No.: 210-02, 2010.
[97] C. C. Coleman and W. G. Steele, *Experimentation and Uncertainty Analysis for Engineers*, 3rd ed. New York: Wiley, 2009.
[98] S. D. Pawar, P. Murugavel, and D. M. Lal, "Effect of relative humidity and sea level pressure on electrical conductivity of air over Indian Ocean," *Journal of Geophysical Research-Atmospheres,* vol. 114, Jan 2009.
[99] A. J. B. de Oliveira and M. T. de Melo, "Measuring the dielectric properties of granular and liquid materials in the microwave range," in *Proceedings of the 2001 SBMO/IEEE MTT-S International Microwave and Optoelectronics Conference (IMOC 2001)*, 2001, pp. 141-143 vol.1.
[100] S. O. Nelson, "Density-permittivity relationships for powdered and granular materials," *IEEE Transactions on Instrumentation and Measurement,* vol. 54, pp. 2033-2040, 2005.

[101] S. Trabelsi, A. W. Kraszewski, and S. O. Nelson, "Microwave dielectric sensing of bulk density of granular materials," *Measurement Science and Technology,* vol. 12, p. 2192, 2001.
[102] J. Barber, J. C. Weatherall, B. T. Smith, S. Duffy, S. J. Goettler, and R. A. Krauss, "Millimeter wave measurements of explosives and simulants," in *Passive Millimeter-Wave Imaging Technology XIII*, Orlando, Florida, USA, 2010, pp. 76700E-7.
[103] A. S. Zyuzin, "Measurement of dielectric permittivity of commercial aircraft coating sheet," Illionix, LLC, Seattle, WA, Report No.: 709-01, 2010.
[104] A. V. Mamishev, B. C. Lesieutre, and M. Zahn, "Optimization of multi-wavelength interdigital dielectrometry instrumentation and algorithms," *IEEE Transactions on Dielectrics and Electrical Insulation* vol. 5, pp. 408-420, 1998.
[105] A. V. Mamishev, A. R. Takahashi, Y. Du, B. C. Lesieutre, and M. Zahn, "Assessment of performance of fringing electric field sensor arrays," in *2002 Annual Report Conference on Electrical Insulation and Dielectric Phenomena*, 2002, pp. 918-921.
[106] C. Delahunt, "Metrics to assess clustering of data vectors: RMS and kNN," Illionix, LLC, Seattle, WA 2010.
[107] P. A. Walsh, V. Egan, R. Grimes, and E. J. Walsh, "Scaling of flow characteristic and power consumption with profile height for miniature centrifugal fans," in *Proceedings of the Fifth International Conference on Nanochannels, Microchannels and Minichannels* Puebla, Mexico, 2007, pp. ICNMM2007-30136.
[108] E. Stanford, "Power delivery challenges in computer platforms," Intel, 2006.
[109] N. E. Jewell-Larsen, S. V. Karpov, H. Ran, P. Savalia, and K. A. Honer, "Investigation of dust in electrohydrodynamic (EHD) systems," in *26th Annual IEEE Semiconductor Thermal Measurement and Management Symposium (SEMI-THERM 2010)* 2010, pp. 249-255.
[110] H. C. Wang, N. E. Jewell-Larsen, and A. V. Mamishev, "Thermal management of microelectronics with electrostatic fluid accelerators," *Applied Thermal Engineering,* vol. 51, pp. 190-211, 2013.
[111] E. A. Silk, J. Kim, and K. Kiger, "Spray cooling of enhanced surfaces: Impact of structured surface geometry and spray axis inclination," *International Journal of Heat and Mass Transfer,* vol. 49, pp. 4910-4920, Dec 2006.
[112] A. C. Cotler, E. R. Brown, V. Dhir, and M. C. Shaw, "Chip-level spray cooling of an LD-MOSFET RF power amplifier," *IEEE Transactions on Components and Packaging Technologies,* vol. 27, pp. 411-416, 2004.
[113] S. V. Garimella, "Advances in mesoscale thermal management technologies for microelectronics," *Microelectronics Journal,* vol. 37, pp. 1165-1185, 2006.
[114] T. Widerski, E. Raj, and Z. Lisik, "Cooling microstructure for automotive electronic module," in *The International Conference on "Computer as a Tool"*, 2007, pp. 1429-1432.
[115] V. Khanikar, I. Mudawar, and T. Fisher, "Flow boiling in a micro-channel coated with carbon nanotubes," *IEEE 11th Intersociety Conference on Thermal and Thermomechanical Phenomena in Electronic Systems (ITHERM 2008)* pp. 960-969, 2008.
[116] J. Schutze, H. Ilgen, and W. R. Fahrner, "An integrated micro cooling system for electronic circuits," *IEEE Transactions on Industrial Electronics,* vol. 48, pp. 281-285, Apr 2001.

[117] J. Lee and I. Mudawar, "Fluid flow and heat transfer characteristics of low temperature two-phase micro-channel heat sinks - Part 1: Experimental methods and flow visualization results," *International Journal of Heat and Mass Transfer,* vol. 51, pp. 4315-4326, Aug 2008.

[118] J. Lee and I. Mudawar, "Low-temperature two-phase micro-channel cooling for high-heat-flux thermal management of defense electronics," *IEEE 11th Intersociety Conference on Thermal and Thermomechanical Phenomena in Electronic Systems (ITHERM 2008)* pp. 132-144, 2008.

[119] Y. J. Kim, Y. K. Joshi, and A. G. Fedorou, "An absorption based miniature heat pump system for electronics cooling," *International Journal of Refrigeration-Revue Internationale Du Froid,* vol. 31, pp. 23-33, Jan 2008.

[120] L. N. Jiang, J. Mikkelsen, J. M. Koo, D. Huber, S. H. Yao, L. Zhang, P. Zhou, J. G. Maveety, R. Prasher, J. G. Santiago, T. W. Kenny, and K. E. Goodson, "Closed-loop electroosmotic microchannel cooling system for VLSI circuits," *IEEE Transactions on Components and Packing Technologies,* vol. 25, pp. 347-355, Sep 2005.

[121] N. R. Jankowski, L. Everhart, B. R. Geil, C. W. Tipton, J. Chaney, T. Heil, and W. Zimbeck, "Stereolithographically fabricated aluminum nitride microchannel substrates for integrated power electronics cooling," *IEEE 11th Intersociety Conference on Thermal and Thermomechanical Phenomena in Electronic Systems (ITHERM 2008)* pp. 180-188, 2008.

[122] V. Chiriac and F. Chiriac, "An overview and comparison of various refrigeration methods for microelectronics cooling," *IEEE 11th Intersociety Conference on Thermal and Thermomechanical Phenomena in Electronic Systems (ITHERM 2008)* pp. 618-625, 2008.

[123] V. Singhal and S. V. Garimella, "Induction electrohydrodynamics micropump for high heat flux cooling," *Sensors and Actuators A-Physical,* vol. 134, pp. 650-659, Mar 15 2007.

[124] M. Stubbe, M. Holtappels, and J. Gimsa, "A new working principle for ac electro-hydrodynamic on-chip micro-pumps," *Journal of Physics D-Applied Physics,* vol. 40, pp. 6850-6856, Nov 7 2007.

[125] C. K. Lee, A. J. Robinson, and C. Y. Ching, "Development of EHD ion-drag micropump for microscale electronics cooling," in *IEEE 13th International Workshop on Thermal Investigation of ICs and Systems (THERMINIC 2007)* 2007, pp. 1-6.

[126] J. Darabi and H. X. Wang, "Development of an electrohydrodynamic injection micropump and its potential application in pumping fluids in cryogenic cooling systems," *Journal of Microelectromechanical Systems,* vol. 14, pp. 747-755, Aug 2005.

[127] J. Darabi, M. M. Ohadi, and D. DeVoe, "An electrohydrodynamic polarization micropump for electronic cooling," *Journal of Microelectromechanical Systems,* vol. 10, pp. 98-106, Mar 2001.

[128] J. Darabi and K. Ekula, "Development of a chip-integrated micro cooling device," *Microelectronics Journal,* vol. 34, pp. 1067-1074, Nov 2003.

[129] S. Chowdhury, J. Darabi, M. Ohadi, and J. Lawler, "Chip integrated micro cooling system for high heat flux electronic cooling applications," in *IEEE 8th Intersociety Conference on Thermal and Thermomechanical Phenomena in Electronic Systems (ITHERM 2002)* 2002, pp. 1-9.

[130] K. Adamiak, A. Mizuno, and M. Nakano, "Electrohydrodynamic flow in optoelectrostatic micropump: experiment versus numerical simulation," *IEEE Transactions on Industry Applications,* vol. 45, pp. 615-622, 2009.
[131] A. E. Bergles, "Evolution of cooling technology for electrical, electronic, and microelectronic equipment," *IEEE Transactions on Components and Packaging Technologies,* vol. 26, pp. 6-15, Mar 2003.
[132] R. C. Chu, R. E. Simons, M. J. Ellsworth, R. R. Schmidt, and V. Cozzolino, "Review of cooling technologies for computer products," *IEEE Transactions on Signal Processing,* vol. 4, pp. 568-585, 2004.
[133] P. J. Halvorson, "On the heat transfer characteristics of spray cooling," Georgia Institute of Technology, 1994.
[134] M. J. Morgan, W. S. Chang, M. R. Pais, and L. C. Chow, "Comparison of high heat-flux cooling applications," in *High Heat Flux Engineering*, 1992, pp. 17-28.
[135] I. Mudawar, "Assessment of high-heat-flux thermal management schemes," *IEEE Transactions on Components and Packing Technologies,* vol. 24, pp. 122-141, 2001.
[136] D. P. Rini, R. H. Chen, and L. C. Chow, "Bubble behavior and nucleate boiling heat transfer in saturated FC-72 spray cooling," *Transactions of the ASME Journal of Heat Transfer,* vol. 124, pp. 63-72, 2002.
[137] W. Deng and A. Gomez, "Electrospray cooling for microelectronics," *International Journal of Heat and Mass Transfer,* vol. 54, pp. 2270-2275, 2011.
[138] A. Bar-Cohen, M. Arik, and M. Ohadi, "Direct liquid cooling of high flux micro and nano electronic components," *Proceedings of the IEEE,* vol. 94, pp. 1549-1570, Aug 2006.
[139] H. Kawamoto, "Ozone generation in corona discharge at pin electrode of electrophotographic charger," *Journal of Imaging Science and Technology,* vol. 44, pp. 452-456, Sep-Oct 2000.
[140] J. H. Chen and J. H. Davidson, "Ozone production in the negative DC corona: The dependence of discharge polarity," *Plasma Chemistry and Plasma Processing,* vol. 23, pp. 501-518, Sep 2003.
[141] J. H. Chen and J. H. Davidson, "Ozone production in the positive DC corona discharge: Model and comparison to experiments," *Plasma Chemistry and Plasma Processing,* vol. 22, pp. 495-522, Dec 2002.
[142] H. Kalman and E. Sher, "Enhancement of heat transfer by means of a corona wind created by a wire electrode and confined wings assembly," *Applied Thermal Engineering,* vol. 21, pp. 265-282, Feb 2001.
[143] H. W. Coleman and W. G. Steele, *Experimentation, Validation, and Uncertainty Analysis for Engineers*, Third ed. New Jersey: John Wiley & Sons, Inc., 2009.
[144] H. Watanabe, T. Matsuyama, and H. Yamamoto, "Experimental study on electrostatic atomization of highly viscous liquids," *Journal of Electrostatics,* vol. 57, pp. 183-197, Feb 2003.
[145] C. F. Eyring, S. S. Mackeown, and R. A. Millikan, "Field currents from points," *Physical Review,* vol. 31, pp. 900-909, 1928.
[146] X. F. Zhong, R. Yi, A. E. Holliday, and D. D. Y. Chen, "Field distribution in an electrospray ionization source determined by finite element method," *Rapid Communications in Mass Spectrometry,* vol. 23, pp. 689-697, Mar 2009.

[147] A. R. Jones and K. C. Thong, "Production of charged monodisperse fuel droplets by electrical dispersion," *Journal of Physics D-Applied Physics,* vol. 4, pp. 1159-&, 1971.
[148] H. C. Wang and A. V. Mamishev, "Thermal management of microelectronics," University of Washington, Seattle, Internal report No. 65-5342, 2010.
[149] E. A. Browne, G. J. Michna, M. K. Jensen, and Y. Peles, "Experimental investigation of single-phase microjet array heat transfer," *Transactions of the ASME Journal of Heat Transfer,* vol. 132, p. 041013, Apr 2010.
[150] R. T. Kelly, J. S. Page, I. Marginean, K. Tang, and R. D. Smith, "Nanoelectrospray emitter arrays providing interemitter electric field uniformity," *Analytical Chemistry,* vol. 80, pp. 5660-5665, 2011/11/28 2008.
[151] R. J. Goldstein, E. M. Sparrow, and D. C. Jones, "Natural convection mass transfer adjacent to horizontal plates," *International Journal of Heat and Mass Transfer,* vol. 16, pp. 1025-1035, 1973.
[152] J. R. Lloyd and W. R. Moran, "Natural convection adjacent to horizontal surface of various planforms," *Transactions of the ASME Journal of Heat Transfer,* vol. 96, pp. 443-447, 1974.
[153] N. E. Jewell-Larsen, H. Ran, Y. Zhang, M. K. Schwiebert, K. A. H. Tessera, and A. V. Mamishev, "Electrohydrodynamic (EHD) cooled laptop," in *25th Annual IEEE Semiconductor Thermal Measurement and Management Symposium (SEMI-THERM 2009)*, 2009, pp. 261-266.
[154] "http://solutions.3m.com/wps/portal/3M/en_US/3MNovec/Home/."
[155] http://www.1-act.com/resources/heat-pipe-design-guide.php.